Advanced Electron Tomography to Investigate the Growth and Stability of Complex Metal Nanoparticles

Geavanceerde Elektronentomografie om de Groei en Stabiliteit van Complexe Metallische Nanodeeltjes te Onderzoeken

Proefschrift voorgelegd tot het behalen van de graad van

Doctor in de Wetenschappen: Fysica

aan de Universiteit Antwerpen, te verdedigen door

Mikhail Mychinko

Promotor:

Prof. Dr. Sara Bals

Antwerpen, 2024

Doctoral Committee

Chair

Prof. Dr. Vera Meynen, University of Antwerp, Belgium

Promotor

Prof. Dr. Sara Bals, University of Antwerp, Belgium

Members

Prof. Dr. Milorad Milošević, University of Antwerp, Belgium

Prof. Dr. Sofie Cambré, University of Antwerp, Belgium

Prof. Dr. Luis M. Liz-Marzán, Ikerbasque, The Basque Foundation for Science, Spain and CIC BiomaGUNE, Basque Research and Technology Alliance, Spain

Prof. Dr. Johan Hofkens, Catholic University of Leuven, Belgium

Contact information

Mikhail Mychinko

University of Antwerp – Department of Physics

EMAT – Electron Microscopy for Materials Science

Groenenborgerlaan 171

B-2020 Antwerpen

Belgium

mikhail.mychinko@uantwerpen.be

Contents

List of abbreviations

2D	Two-dimensional
3D	Three-dimensional
4D	Four-dimensional
AR	Aspect ratio
BF	Bright field
BINAMINE	1,1′-Binaphthyl-2,2′-diamine
CBED	Convergence Beam Electron Diffraction
CCD	Charge-coupled device
CD	Circular dichroism
CNN	Convolutional neural network
CTAB	Cetyltrimethylammonium bromide
CTAC	Cetyltrimethylammonium chloride
Cys	Cysteine
DART	Discrete algebraic reconstruction technique
DFT	Density functional theory simulations
ED	Electron diffraction
EDX	Energy dispersive X-ray spectroscopy
EELS	Electron energy loss spectroscopy
EM	Expectation-maximization
ET	Electron tomography
fcc	Face-centered cubic
FIB	Focused Ion Beam
HAADF	High-angle annular dark field
iDPC	Integrated differential phase contrast

LipoCYS	2-amino-N-decyl-3-mercaptopropanamide
LSPR	Localized surface plasmon resonance
MD	Molecular dynamics
MEMS	Micro-electromechanical systems
NBP	Nanobipyramid
NIR	Near-infrared
NP	Nanoparticle
NR	Nanorod
NS	Nanosphere
OCT	Octahedron
PT	Pentatwinned
SC	Single-crystalline
SIRT	Simultaneous iterative reconstruction technique
SNR	Signal-to-noise ratio
SP	Sphere
SSR	Sparce spheres reconstruction
STEM	Scanning transmission electron microscopy/microscope
TVM	Total variation minimization
UV	Ultraviolet
WBP	Weighted back-projection

Chapter 1. Introduction to metallic chiral and bimetallic core-shell nanoparticles

1.1 Plasmonic nanoparticles: properties and application

Significant advancements and breakthroughs in the field of nanotechnology have occurred in recent decades, following the introduction of the concept by an American physicist and Nobel laureate Richard Feynman in 1959.[1] This period has witnessed the emergence of nanomaterials as integral components of our daily lives. For instance, Ag nanoparticles (NPs) have been employed to impede the reproduction of odor-causing bacteria in shoes and clothing, harnessing their antibacterial properties.[2,3] Metallic NPs can be also integrated into textiles enabling ultraviolet shielding, self-cleaning capabilities, and electrical conductivity, in addition to antistatic, wrinkle-resistant, and flame-retardant properties, all without altering the fundamental characteristics of the textile.[4]

Localized Surface Plasmon Resonance (LSPR) is a remarkable optical property exhibited by metallic NPs which deserves a more detailed description in the framework of this thesis. LSPR arises from the resonant oscillations of conduction electrons within the NPs when they interact with electromagnetic radiation, particularly in the visible or near-infra-red (NIR) light range (as illustrated in Figure 1.1a).[5–7] This unique phenomenon has propelled the field of nanoplasmonics, where plasmonic NPs hold significant promise for a range of applications such as photocatalysis,[6,8] sensing,[9,10] data storage,[11] and solar energy conversion (Figure 1.1b).[12,13] Nanoplasmonics has also demonstrated particular potential in the field of medicine. One notable aspect is the ability of nanoplasmonic NPs to generate localized heat at the nanoscopic scale upon exposure to NIR laser radiation. By delivering these NPs to specific areas within an organism and subsequently subjecting them to laser irradiation (organic tissues are partially transparent to NIR light), it becomes possible to selectively destroy tumor cells while minimizing damage to healthy tissue.[14–16] This approach holds promise for

targeted and localized cancer therapy, offering a potential avenue for more effective treatments.
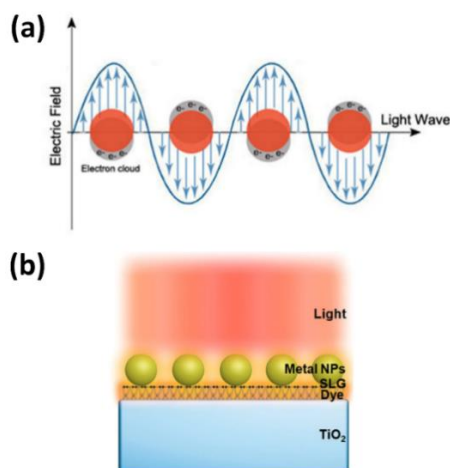
Figure 1.1 (a) The oscillation of conduction band electron caused by the interaction with the incident electromagnetic wave. (b) Schematic representation of substrate-induced interfacial plasmonics for photoexciting a layer of dyes between a TiO2 dielectric substrate and single-layer graphene.[13] Image is taken from open access article distributed under the terms of the Creative Commons CC BY license (Copyright © 2015, Springer Nature Limited).

The advancement of plasmonic-based technologies requires the development of synthetic techniques capable of producing metallic NPs with precise control over their shapes, sizes, and compositions. Among the various synthetic approaches, the wet chemical (colloidal) method, also known as seed-mediated crystal growth, has attracted significant attention and has undergone substantial progress in recent decades. This method has demonstrated its capacity to reliably produce a wide range of mono- and bimetallic NPs (as depicted in Figure 1.2).[17–19] The key advantage of the seed-mediated crystal growth method lies in its ability to finely regulate the directions of crystal growth. This is achieved, for instance, by reducing metal ions (e.g., Au^+, Ag^+) in a solution onto the surface of seed particles. The control over crystal growth directions is achieved by carefully manipulating experimental parameters such as temperature, component concentrations, pH, and reaction time.[20] The nature of the seed particles,

whether single-crystalline (SC) or pentatwinned (PT), as well as the choice of reducing agent (e.g., ascorbic acid), further influence the growth process.[21,22]
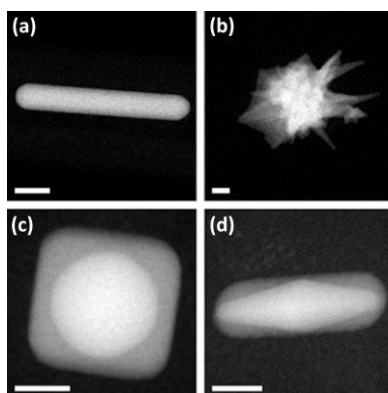
Figure 1.2 (a,b) Examples of various Au NPs: a nanorod (NR) and a highly asymmetric nanostar. The contrast difference due to the thickness variation in the specimen can be seen in (c). (c,d) Bimetallic core-shell Au@Ag NPs, where shapes of both core and shell with various degree of symmetry can be achieved. Higher and lower intensities observed in (c,d) correspond to pure Au and Au due to the Z-contrast of HAADF-STEM. All scale bars are 20 nm.

However, to ensure crystal growth along specific directions, an additional component is required. These surfactants, typically organic molecules like cetyltrimethylammonium chloride (CTAC) or bromide (CTAB), possess a structure with a polar, hydrophilic 'head' (e.g., an ionized atom) and a lengthy aliphatic hydrophobic 'tail,' as depicted in Figure 1.3a. Due to their configuration, these molecules can self-assemble into various forms, such as spherical micelles, when introduced, for example, in water (Figure 1.3b). In this scenario, the polar heads of the resulting spherical micelles will be directed towards the water phase (polar solvent) and the hydrophobic tails self-assemble, creating a more hydrophobic core. When a phase boundary exists between polar and nonpolar components, such as the 'water-air' phase boundary, surfactant molecules can arrange themselves into layered structures based on 'polar-polar' and 'nonpolar-nonpolar' interactions (Figure 1.3c). Certain surfactants that possess atoms with lone pairs of electrons (acting as a Lewis base) can adhere to the

surface of metallic NPs (acting as Lewis acid) creating coordination complexes. In this arrangement, the hydrophilic head of the surfactant molecule, containing -SH or -NH$_2$ groups, functions as ligands, forming a surface layer on the metallic nanoparticles. Consequently, a second layer of surfactant molecules aligns in a 'tail-to-tail' manner, positioning the hydrophilic section of the second layer toward the water solution (as depicted in Figure 1.3d). In the case of ionic surfactants, e.g. CTAC or CTAB molecules containing -NH$_4^+$ head group, this arrangement results in the development of an electrostatic bilayer formed by surfactant molecules, giving rise to repulsion forces between the individual double-layered micelles. These repulsive forces originate from the surface charge of the same sign, significantly enhancing nanoparticle stability and preventing agglomeration. Furthermore, micelles can serve as nanoreactors, providing a confined environment conducive to controlled nanoparticle growth. The capability to arrange surfactant molecules into asymmetric micelles can be strategically combined with other synthetic factors, e.g. the incorporation of shape-directing additives (metal ions or halides), enabling the synthesis of diverse asymmetric NPs, such as nanorods (NRs).[23] This intricate interplay of factors enhances the versatility of the synthesis process.[23,24]
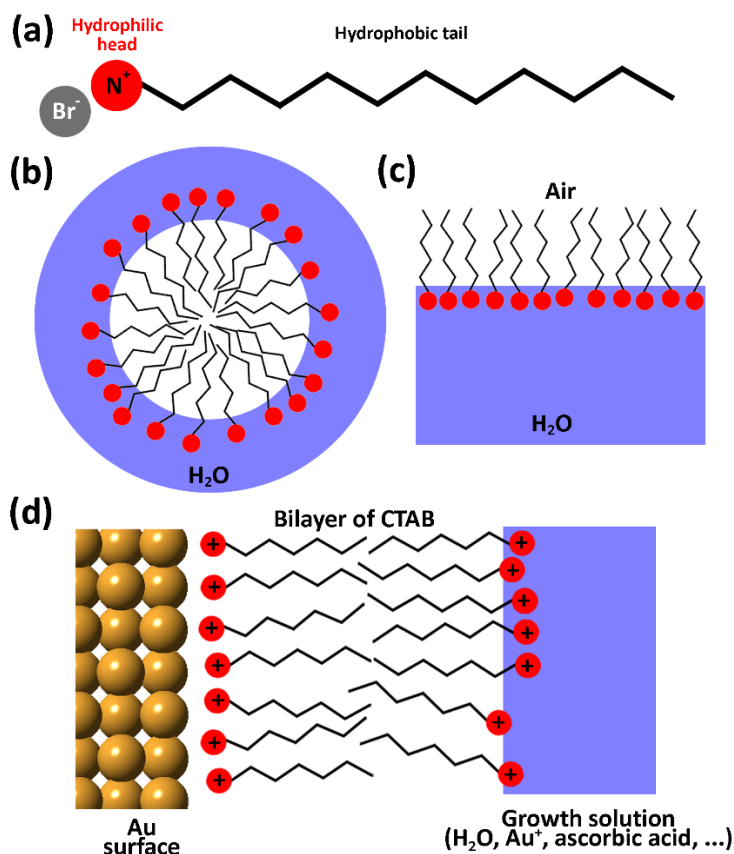
Figure 1.3 (a) Schematic representation of surfactant molecule, consisting of consist of a hydrophilic (water-attracting) "head" and a hydrophobic (water-repelling) "tail". (b,c) Visual representation of surfactant molecules self-assemblies, demonstrating the formation of spherical micelles in water and layered structures at the water-air interface. (d) The formation of surfactant bilayer on the surface of Au NP in nanocrystal growth solution.

Due to significant advancements in synthetic protocols, comprehensive studies of the optical properties of specifically tailored nanoplasmonic materials have become possible, leading to notable improvements in their applicability. An example of this progress is the ability to tune the LSPR wavelength over a broad range of electromagnetic irradiation wavelengths, ranging from ultraviolet (UV) to visible and IR regions, by utilizing NPs with different compositions, where the position, width, and

symmetry of plasmon adsorption (or, more precisely, extinction) band is characteristic for each element (as illustrated in Figure 1.4a).[12] For more precise control over the LSPR wavelength, Ag nanocubes (NCs) with varying sizes can be employed (as shown in Figure 1.4b).[12] By adjusting the size of the NCs, finer tuning of the LSPR shift can be achieved.[12] It is worth noting that, in addition to shifting the LSPR peak, it is also possible to observe its splitting into two components. This phenomenon can occur for asymmetric Au, e.g. nanorods (NRs) or nanowires (NWs), where the resonant oscillations of valence electrons differ significantly along the longitudinal and transverse directions due to the difference in confinement distances within the elongated NP (Figure 1.4c).[12] The aspect ratio (AR) of the NR, which represents the ratio of its length to width, plays a crucial role in determining this splitting effect. Besides, beneficial properties of individual elements can be combined to improve the plasmonic properties by the production of bimetallic NPs.[25] This enables tailoring the plasmonic response to specific wavelength ranges for desired applications. Overall, these advancements in nanoplasmonics allow for precise control over the optical properties, enhancing the versatility and potential applications of nanoplasmonic materials.
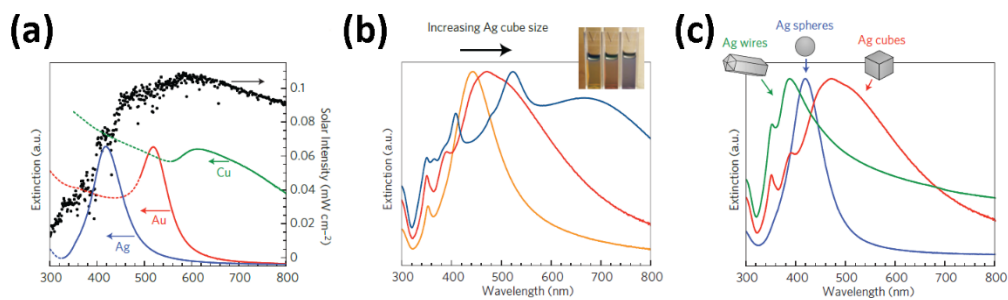
Figure 1.4 (a) Normalized extinction spectra of spherical Ag, Au, Cu NPs.[12] (b) Normalized extinction spectra for Ag NCs as a function of size. The inset shows a photograph of the three NCs samples suspended in ethanol.[12] (c) Normalized extinction spectra for Ag wire, cube and sphere nanoparticles.[12] It can be seen, that the position, shape, and number of LSPR adsorption peaks can be routinely adjusted by modifying the chemical composition and size-related aspects of metallic nanoparticles. Reproduced with permission from Springer Nature. (Copyright © 2011 Macmillan Publishers Limited).

1.2 Chiroptical properties and chiral nanoparticles

A class of nanoplasmonic particles that recently received increasing attention are those with a helical morphology, leading to what is called chiral NPs. The significance of chirality in both biological and non-biological systems cannot be understated, as it exerts a profound influence on various aspects of life. The term "chirality" derives from the Ancient Greek word for "hand" and describes objects that cannot be superimposed on their mirror image. A simple way to understand chirality is by observing one's own hands, which despite having the same types and quantities of constituent elements, cannot be perfectly aligned due to their distinct geometric orientation. In the field of chemistry, certain elements and their chemical bonding can lead to the formation of chiral asymmetry centers, resulting in different configurations known as enantiomers. Figure 1.5a illustrates this concept of two amino acids that share the same composition but differ in the arrangement of the functional groups attached to the chiral carbon atom. Chirality plays a crucial role in DNA molecules (depicted in Figure 1.5b), which are fundamental building blocks of all living organisms. The chiral nature of DNA can have unexpected implications on the human body, particularly when interacting with different enantiomers of the same chemical compound. A well-known example of this is the case of R- and S-thalidomide, also known as Rectus and Sinister thalidomide (referring to right- and left-handedness, respectively). R-thalidomide has been identified as the clinically active component, whereas the left-handed enantiomer was unknowingly administered to pregnant women in the 1960s to alleviate morning sickness. This led to the birth of over 10,000 children with severe birth defects, such as phocomelia.[26] Another, less drastic example of chiral effects is observed in the distinct aromas of R-carvone (minty smell) and S-carvone (spicy aroma resembling caraway seeds).[27]
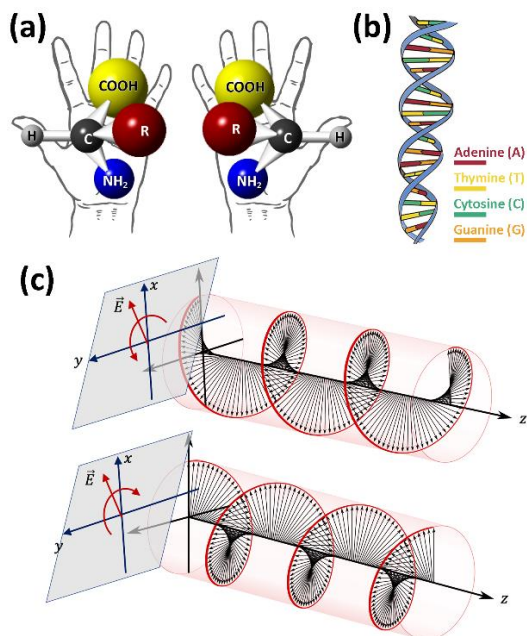
Figure 1.5 (a) Left and right-handed amino acids. (b) The helical structure of DNA molecule. (c) Left and right-handed circularly polarized light. Adapted from Wikipedia - The Free Encyclopedia. (Copyright © Creative Commons Attribution-ShareAlike 4.0 International License.

The provided examples highlight the significance of meticulous synthesis and analysis of drugs and other organic compounds. The pronounced interaction between nanoplasmonics and electromagnetic irradiation offers promising opportunities for the fabrication of chiral structures and exploration of their interaction with circularly polarized light (Figure 1.5c), which opens up opportunities for utilizing spectroscopy based on differential absorption of left- and right-handed circularly polarized light. This technique, known as circular dichroism (CD), is widely employed to investigate and detect a vast range of chemical compounds. The most common measure to quantitatively describe the optical properties of chiral materials is so-called dissymmetry factor or g-factor, which can be defined as follows (Equation 1.1):

$$g = k \cdot \frac{I_L - I_R}{\frac{1}{2}(I_L + I_R)}, \tag{1.1}$$

where I_L and I_R are the absorption intensities for left- and right-handed circularly polarized light, k – constant determined by used CD spectrometer.[28,29] This factor is a dimensionless quantity useful when the signs and the magnitudes of CD signals are compared among various kinds of samples, conditions, and excitation wavelengths.[29]

High chiroptical activity of asymmetric nanoplasmonics can be advantageous for enhancing the CD signal of trace amounts of chiral molecules and shifting it to the visible range, facilitating detection and analysis of chiral compounds.[30] Furthermore, the optical activity of chiral nanomaterials can be modulated through coupling with other physical stimuli, such as magnetic fields.[31] Despite significant progress in the investigation of chiral nanomaterials, there is still considerable scope for further advancement, particularly in the development of reliable and flexible synthetic methods. A comprehensive understanding of the mechanisms governing chiral growth is essential to achieve precise control over the synthesis process and obtain desired chiral nanostructures with predefined optical properties.

1.3 Properties and stability of bimetallic nanoparticles

An alternative approach to enhance and broaden the application of nanoplasmonics is the synthesis of bimetallic NPs, which combine the advantageous properties of multiple elements within a single particle, often resulting in optimized properties compared to monometallic counterparts. An illustrative example is the synthesis of Au-Ag NPs, which have been extensively studied because of their unique optical properties.[32] The similar lattice constants and face-centered cubic (*fcc*) crystal structure of gold and silver hereby facilitate the synthesis of various Au-Ag alloy/core-shell structures.[33–35] The LSPR wavelengths for spherical Au and Ag NPs are around 520 nm and 400 nm, respectively.[36] By combining these two metals into a single NP, the LSPR absorption can be continuously tuned in the ultraviolet (UV), visible, and NIR regions. Compared to Au, Ag nanostructures exhibit a shorter LSPR wavelength and stronger near-field enhancement for comparable sizes.[37–39] However, Au demonstrates better resistance to oxidative degradation, thereby enhancing the stability of resulting Au-Ag NPs. The distribution of elements within the volume of the bimetallic particle plays a crucial role

in determining its properties. Indeed, the arrangement and distribution of gold and silver atoms within the particle influence its optical and catalytic characteristics, making it essential to carefully control the elemental distribution during synthesis.[33,40–42]

It is important to note that the carefully synthesized distribution of elements inside a bimetallic NP might change once the NP is exposed to realistic conditions, such as elevated temperatures, by alloying or mutual diffusion (interdiffusion).[43,44] Heat-induced interdiffusion of components occurs through the hopping of individual atoms into interstitial and vacant sites of a crystal lattice typical for most solid structures (Figure 1.6), e.g. Ni-Al[45] or Au-Ag alloys.[46] At elevated temperatures the energy required for atoms or particles to move through the bulk volume of a material is transferred. This energy is called as an volume diffusion activation barrier playing a significant role in determining the rate of diffusion within the material. The rate of diffusion can be expressed using the diffusion constant, quantifying how quickly particles move or spread through a medium over time due to thermal motion or concentration gradients. In addition to temperature dependence, the dynamics and mechanism of these processes strongly depend on various aspects, e.g. NP composition,[43,47,48] size[43,46] or shape.[44,49] Additionally, a difference in core-shell interfacial facets[49] or the presence of twin boundaries, such as those in PT NPs, may also play a role.[50,51] Understanding the influence of these parameters is thus of great importance, since alloying can alter the physicochemical and optical properties of bimetallic NPs.[52] On the other hand, precise control over thermal or irradiation conditions may also be beneficial, for instance, leading to dramatically improved monodispersity in Au NPs,[53] superior catalytic performance of Au-Pd alloyed nanospheres,[54] or the development of novel data storage technologies.[11] In the particular case of Au-Ag NRs, alloying has been reported to lead to enhanced chemical stability in harsh environments, preserving improved LSPR properties in comparison to Au@Ag core@shell structures.[55–57] Despite recent progress concerning the investigation of bimetallic systems using various experimental and simulation techniques, understanding of the mechanisms behind atomic diffusion at the single NP level is still far from complete. In fact, the diffusion dynamics are expected to be different at the nanoscale compared to the bulk, as indicated by diffusion coefficients for Au-Ag NPs

with sizes smaller than 5 nm, that are orders of magnitude higher when compared to their bulk counterparts.[58] Thus, a detailed understanding of nano-alloying processes and their dependence on relevant external stimuli and NP parameters is crucial for further improvement of NP properties and applications. In order to obtain such understanding, I will combine ET with the dedicated *in situ* heating tomography holder based on microelectromechanical system-based (MEMS) devices. MEMS heating devices are designed at a microscale, allowing for precise control and efficient heat generation suitable for TEM studies.[59] In this study, MEMS-based DENSsolutions Wildfire heating chips was utilized operating on the principle of a 4-probe configuration. These chips incorporate two probes designated as current-carrying electrodes, responsible for generating heat, while the other two probes serve as voltage-sensing electrodes, enabling precise temperature measurement.
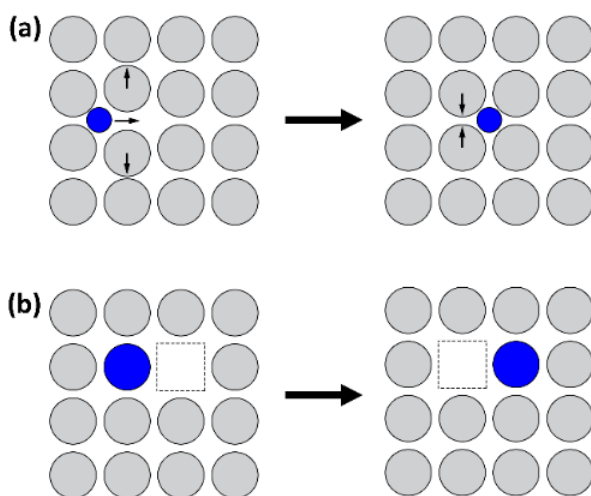
Figure 1.6 Site exchange in crystalline metals: (a) interstitial diffusion, (b) vacancy mechanism. The diffusion in solid matter via interstitial sites requires high energy (e.g., heating) to overcome the potential energy barriers that occur due to the dense packing of atoms within the crystal lattice. The diffusion can be facilitated by introducing vacancies or lattice distortions, resulting in lower diffusion activation energies or faster diffusion kinetics.

Another competing process, surface diffusion can also happen at elevated temperatures and should be taken into account.[60–62] Due to the high surface energy, characteristic for all nanomaterials, NPs tend to decrease the surface-to-volume ratio by reshaping into more symmetric (spherical or cubic) shapes under temperatures as low as 100 °C (Figure 1.7). Thus, surface diffusion activation energy for metallic NPs is significantly lower compared to volume diffusion, where higher temperatures are required for atoms of the material to move through the crystal lattice (typically above 300 °C).[44] Surface diffusion processes can complicate the analysis of elemental redistribution within the volume of bimetallic NPs, where different approaches to prevent the thermal reshaping of asymmetric NPs should be used. For example, plasmonic NPs can be coated with mesoporous silica (m-SiO$_2$), which is rigid enough to preserve the surface morphology and has additional useful properties, for instance, optical transparency, high biocompatibility, chemical and colloidal stability, and controllable porosity. [63]
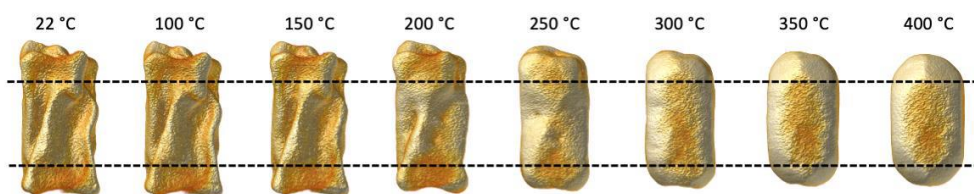
Figure 1.7 ET reconstructions of a twisted Au nanorod at different times during an *in situ* heating procedure. During heating, a gradual smoothing of the surface becomes apparent, attributed to the redistribution of Au atoms across the surface. This reshaping phenomenon is propelled by the reduction of the energetically unfavorable high surface-to-volume ratio.

1.4 Thesis motivation and outline

Nanotechnology has significantly influenced our society in recent decades, impacting various aspects of our daily lives, spanning from food production to advancements in medicine. Anticipated advancements in nanotechnology are aimed at addressing significant challenges of modern society, including mitigating greenhouse gas emissions and discovering more effective cancer treatments. To ensure further progress

and enhance existing nanotechnology, a comprehensive understanding and precise manipulation of the properties of underlying nanomaterials stand as pivotal requirements.

The advancements made in the synthesis of various metallic NPs represent a significant stride in nanotechnology. However, further enhancement in this field can be achieved by synthesizing novel types of asymmetric NPs, leveraging a deeper comprehension of the underlying growth mechanisms. Deep understanding of these growth mechanisms will enable the tailoring of nanoparticles with meticulous control over their size, shape, and optical properties. By exploring and manipulating these mechanisms at atomic level, new pathways emerge for designing nanoparticles with enhanced functionalities and tailored characteristics suitable for diverse applications. This deeper insight not only broadens the spectrum of nanoparticle possibilities but also lays the foundation for more precise and efficient synthesis methods, paving the way for innovative and impactful advancements in nanotechnology.

Advancements in electron tomography (ET) have made comprehensive characterization of nanomaterials possible, allowing retrieval of morphology and structural information of various NPs in three dimensions (3D). For instance, advanced ET has facilitated the atomic-level investigation of relatively symmetric Au and Au@Ag NPs, enabling precise determination of each atom's position within these structures.[64–66] However, implementing such techniques for a broader range of materials and morphologies, such as highly asymmetric Au NPs, presents challenges. In these cases, multiple parameters need serious consideration for reliable characterization of complex nanomaterials. Firstly, optimizing experimental conditions during tomography series acquisition is crucial to obtain maximum structural information without damaging samples due to excessive electron beam irradiation. Secondly, analysing highly irregular morphologies, e.g. determining surface faceting, remains challenging even with achievable 3D reconstruction at atomic resolution. Often studied NPs may not be suitable for high-resolution ET studies, requiring alternative strategies to gain deeper insights into the synthesized NPs' morphology and the underlying mechanisms of nanocrystal growth. My research was motivated by the aim to implement and enhance advanced ET

techniques, particularly high-resolution ET, for the investigation of complex Au NPs, especially those with high asymmetry. This pursuit aimed to deepen our understanding of their properties and synthetic mechanisms.

Thus, **Part 1** of my PhD research is dedicated to the study of chiral growth mechanisms and the structural analysis of novel types of chiral nanostructures that requires the utilization of various ET techniques. Advanced three-dimensional characterization methods are essential for accurate determination of the surface faceting of intermediate particles.

In **Chapter 4**, I will use atomic resolution tomography to provide input that can be used for DFT calculations to obtain insights into the interaction of chiral inducer molecules of amino acids (cysteine, Cys) with the specific surface facets of Au NP during the chiral growth at the atomic level. In **Chapter 5**, the mechanism of chiral growth of wrinkled Au NPs is studied in presence of BINAMINE-CTAC micelles. In this case, I have visualized a thin Pd layer that was deposited between the core and the wrinkled shell of studied NP, therefore, obtaining the valuable information about the interaction of surfactant micelles with specific facets of Au seeds. **Chapter 6** of this thesis focuses on the characterization of both twisted and wrinkled chiral structures obtained through the implementation of a modified surfactant (LipoCYS), that combines the chiral properties of amino acids with long aliphatic tails, facilitating the formation of micelles. The characterization of these chiral structures is carried out using a combination of ET based on HAADF-STEM and Electron Diffraction Tomography (3D-ED), enabling an accurate analysis of the surface facets, where the adsorption of chiral inducer molecules predominantly occurs.

An alternative approach to enhance the applicability of complex mono and bimetallic NPs involves a deeper comprehension of their stability under real application conditions. It is important to note that most (S)TEM investigations of nanomaterials are conducted in high vacuum and at room temperature, often in 2D. These conditions are inadequate to fully understand the behavior of NPs in realistic environment, particularly for asymmetric NPs. Therefore, a more comprehensive understanding of particles

stability can only be achieved through a combination of advanced ET techniques and specialized TEM equipment. An additional challenge in these investigations involves the intricate interplay among multiple parameters, including the sample's structure, the experimental conditions utilized in (S)TEM, and the competing processes—surface versus volume diffusion. Isolating each parameter for the study of their individual influences is often far from straightforward and requires careful choice of studied samples and experimental conditions.

In the **Part 2** of this PhD research, I investigated the influence of various parameters on heat-induced alloying in bimetallic core-shell NPs, including size, aspect ratio, core shape, and the presence of twin boundaries. To gain a comprehensive understanding of this phenomenon, I employed fast HAADF-STEM tomography in combination with *in situ* heating holders, demonstrating advantages of this method. This approach enabled real-time observation of the alloying process in different NPs while they were subjected to controlled heating. The development and improvement of fast tomography is hereby crucial to enable the 3D investigation of several particles under same experimental conditions during one microscopy session, thus, providing us with reliable information on the alloying dynamics in different NPs. This method and its advantages will be explained in more detail in **Part 2** of my thesis.

In **Chapter 8** of this work, I will provide both a detailed qualitative and quantitative analysis of the heat-induced alloying in bimetallic core-shell NPs. I will describe the observed changes in the NP morphologies, compositions, and elemental distributions during the alloying process. By analysing different individual NPs with varying sizes, aspect ratios, core shapes, and the presence of twin boundaries, I aimed to identify the key factors that govern the alloying kinetics and outcomes. In addition to fast HAADF-STEM tomography, I also utilized high-resolution *in situ* heating ET techniques to track the elemental redistribution of individual atoms during the alloying process. In **Chapter 8**, I will explore the challenges related to obtaining reliable 3D reconstructions that enable the visualization of individual Au and Ag atoms in core-shell and alloyed Au-Ag NPs.

Chapter 2. Introduction to Electron Tomography

2.1 Introduction to electron microscopy

The understanding of nanomaterials' physical properties relies heavily on an accurate characterization of their particle size, morphology, chemical composition, and atomic structure.[67–69] Such knowledge is crucial for optimizing the synthesis process to produce nanomaterials with desired properties[70] and may eventually guide the design of new applications. However, nanomaterials cannot be observed by the naked eye or conventional light microscopes due to their lack of spatial resolution. The resolution of light microscopes typically reaches approximately 0.22 μm with the best available objective lenses.[71]

In 1927, Davisson and Germer conducted an experiment that demonstrated the wave-particle duality of electrons, confirming Louis de Broglie's proposal.[72] They observed the diffraction pattern of a metallic object using electrons emitted from a heated filament and accelerated through a potential difference of 50 V. The electron wavelength in this experiment was approximately 0.17 nm, comparable to the lattice parameters of crystalline objects. Around the same time, Ernst Ruska and Max Knoll began developing a cathode-ray oscillograph, focusing on magnetic lenses to concentrate the electron beam emitted from the cathode-ray.[73] This work eventually led to the development of the transmission electron microscope (TEM), which was capable of producing images of metallic arrangements at magnifications of up to 14.4x at that time. By accelerating the electrons through a potential difference of 75 kV, a resolution of 0.22 nm was expected. However, achieving this resolution was challenging due to the presence of aberrations caused by electromagnetic lenses. E. Ruska produced the first commercial electron microscope at Siemens in 1938. Manfred von Ardenne, also at Siemens, added scanning coils to the instrument in 1938, leading to the development of the first scanning transmission electron microscope (STEM).[72] In 1970, Albert Victor Crewe and his colleagues constructed the first dedicated STEM equipped with an annular-dark field (ADF) detector.[72,74,75] This instrument enabled the simultaneous acquisition of chemical and morphological information at high resolution.

2.2 Evolution of electron microscopy

Subsequent advancements in lenses, detectors, electron sources, and high-tension supplies allowed the visualization of objects, including biological and crystalline materials, at the atomic scale using both TEM and STEM. The invention of aberration correctors in 1998 further improved the resolution of (S)TEM instruments.[76] Nowadays, with aberration correction, typical (S)TEM instruments can achieve a resolution limit of 0.05 nm at an accelerating voltage of 300 kV.[77] The ability to discern individual atomic columns has enabled comprehensive crystallographic studies, the examination of defect origination and proliferation, the analysis of crystal surface faceting, and the in-depth investigation of interfacial interactions within the materials under investigation.[78] It is noteworthy that both TEM and STEM are based on distinct techniques that register different types of signals, and consequently, each possesses its unique set of strengths and limitations.

The most wide-spread imaging modality employed in TEM is bright field (BF) imaging. Thereby, a parallel incoming beam is utilized for sample illumination. The contrast within the resulting images stems from two primary mechanisms. Mass thickness contrast (or absorption contrast) is dominant for amorphous samples which means that thicker regions of the sample appear darker in the image. Conversely for crystalline samples, diffraction contrast arising from elastic Bragg scattering is dominant. This form of contrast is profoundly sensitive to the orientation of the sample relative to the incident electron beam. Consequently, bright field imaging serves as ат important tool for characterizing the atomic structure in materials, as the acquired projection images yield critical insights into the periodicity of the atomic lattice.

The STEM mode involves the interaction of a focused electron beam with the specimen. The resulting image is generated by scanning the beam across the region of interest. The spatial resolution of STEM is determined by the size of the electron probe, which can achieve 50 pm in modern aberration-corrected microscopes. Dedicated detectors, as depicted in Figure 2.1a, are employed to capture scattered electrons with different angular directions. Each type of detector has specific acceptance angle ranges: typically

50-190 mrad for High-angle annular dark field (HAADF) detectors, 10-50 mrad for annular dark field (ADF) detectors, and 0-10 mrad for BF detectors.[79] The HAADF detector selectively detects electrons scattered at large angles, effectively reducing diffraction contrast and primarily capturing incoherent elastically scattered electrons. In this regime, electron scattering is dominated by Rutherford scattering, proportional to the thickness and Z^n (Z – atomic number, $1.6 < n < 2$). Consequently, HAADF-STEM images exhibit contrast variations based on specimen thickness and chemical composition, where heavier atoms scatter electrons to higher angles compared to lighter atoms due to Coulomb interaction. Thus, mass-thickness contrast plays a dominant role during the formation of HAADF-STEM images (Figure 2.1b). By adjusting the camera length (distance from the specimen to the projected image indicated by double arrow in Figure 2.1) or by using a detector with a smaller radius and correspondingly smaller acceptance angles, the acceptance angles of the detector can be modified (low angle annular dark field, LAADF, Figure 2.1c). This modification may reveal contrast variations caused by diffraction scattering events and, for example, demonstrate the presence of lattice defects.
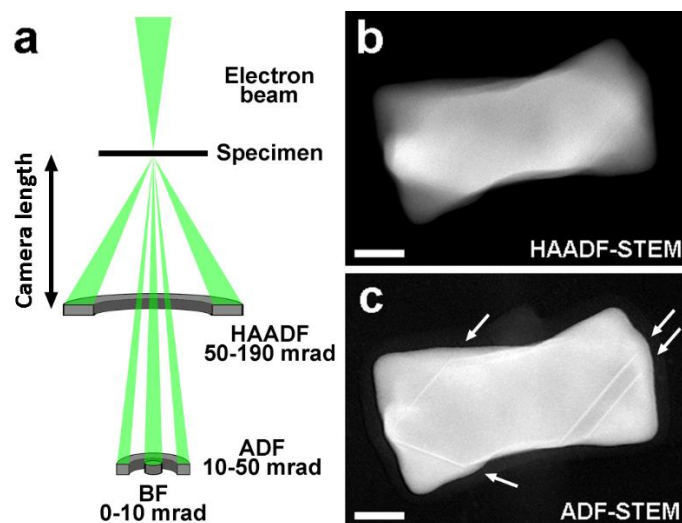

Figure 2.1 (a) Scheme illustrating the electron scattering by the specimen and detection geometry, (b,c) HAADF and ADF-STEM images of the chiral Au NP, depicting the contribution of mass-thickness and diffraction contrast respectively. White arrows in (c) represent the positions of twin boundaries. All scalebars are 25 nm.

It is worth mentioning, that along with the registration of elastically scattered electrons, used in (S)TEM, the registration of inelastically scattered electrons can be highly gainful. For instance, electron energy loss spectroscopy (EELS) enables the determination of specimen thickness, composition, bonding and oxidation state of constituent elements.[80,81] The development of Wien type monochromators has allowed to achieve an extremely narrow energy spread of electron beam and an ultrahigh energy resolution with spectroscopy (up to ~10 meV of spectral resolution).[82–84] In that manner, the ultra-low loss spectroscopy became possible enabling the studies of the optical and electronic properties, e.g., mapping of localized surface plasmons in metallic nanoparticles.[85,86] Another technique called energy dispersive X-ray spectroscopy (EDX), enabling the qualitative and quantitative analysis of composition, will be discussed in more detail in **Section 2.4.2**.

Additionally, the development of new types of electron detectors can be used to retrieve more information about the studied materials. For example, in four-dimensional (4D) STEM, a full 2D diffraction pattern can be captured at each pixel position on a STEM map, producing maps of local crystal orientation, structural distortions, or crystallinity.[87,88] The speed and sensitivity of 4D data combined with direct electron detectors enables the control over the incident electron dose and, therefore, the investigation of beam sensitive materials.[88–90] Another recent development, integrated differential phase contrast (iDPC-STEM) technique is capable of imaging light and heavy elements simultaneously even at low electron doses.[91,92] In contrast to typical annular detectors used in STEM (Figure 2.2a) which display the integrated intensities of these electrons at each scan position of the incident probe, in iDPC-STEM a segmented detector, e.g., composed of four segments, is used (Figure 2.2b).[92,93] In this manner, by measuring the angle and the direction of the beam deflection the mapping of electrostatic potential fields of the specimen can be performed, thus, resulting in a direct phase imaging,[94] beneficial for the visualization of heavy and light elements even in beam-sensitive materials.[95]
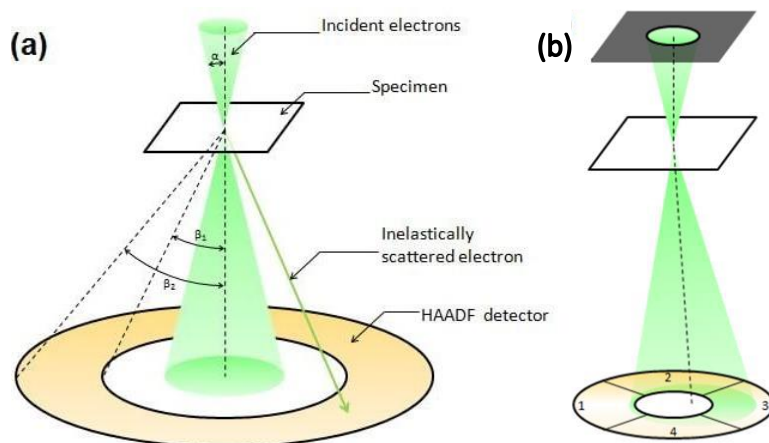
Figure 2.2 (a) Schematic of integrated scattered electrons detections in HAADF-STEM. (b) Schematic of detection of the electron beam deflection in a specimen using a segmented detector (The electron beam is deflected by a specimen). Images from Glossary of TEM terms, JEOL (Copyright © 2006-2023 JEOL Ltd).

Considerable efforts to improve the spatial and spectral resolution of (S)TEM techniques, coupled with the evolution of novel detector technologies, have drastically expanded the variety of the samples that can be investigated in (S)TEM and enriched the depth of information attainable from such experiments. However, these methods only provide 2D information about the subjects under scrutiny, thus, limiting the examination of asymmetric samples, such as chiral metallic NPs. In the following sections, I will give an overview on the electron tomography, enabling to overcome these constraints.

2.3 Introduction to electron tomography

ET is a powerful technique for characterizing nanostructures, but its limitation lies the in fact that it conventionally only provides 2D projected information of a 3D object. This hampers interpreting the morphology of nanomaterials based on a single projection image. For instance, the HAADF-STEM image of a chiral Au NP in Figure 2.3 may erroneously suggest an hourglass shape instead of actual 4-fold twisted morphology revealed through the application of electron tomography (ET). Characterizing the

morphology of nanomaterials is crucial for a comprehensive understanding of their physical properties, as emphasized in **Chapter 1**. ET serves as a valuable technique for acquiring such 3D information. By utilizing a mathematical algorithm, this method enables the reconstruction of an object's morphology and internal structure from multiple 2D projection images, acquired over a large tilt range. In the next section, I therefore elaborate on this technique.
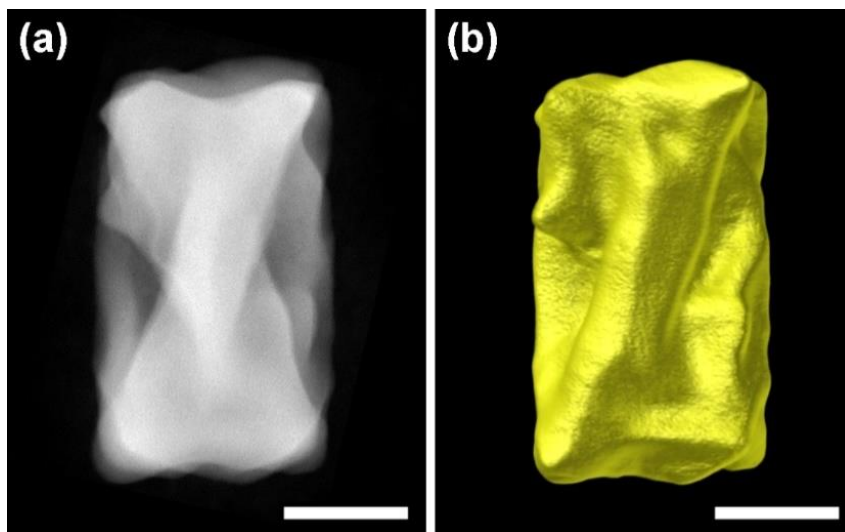
Figure 2.3 (a) 2D HAADF-STEM image of chiral Au NPs, (b) 3D reconstruction revealing actual twisted morphology of the studied nanoparticle. Scalebars are 50 nm.

2.3.1 Basic principles of electron tomography

In 1917, Radon developed a mathematical theory that describes how an 3D object can be reconstructed from a series of 2D projections.[96] The theory states that when an object, denoted as $f(x, y)$, in real space D is projected along an inclined direction with respect to the reference axis (x,y) by an angle θ, the resulting projection $p_\theta(r)$ can be represented by the Radon transform R (Figure 2.4). The Radon transform is defined as the integral of the object $f(x, y)$ along line integrals through all possible lines L:

$$p_\theta(r) = Rf = \int_L f(x,y)ds \tag{2.1}$$

where ds represents the unit length along the line L. Alternatively, the object $f(x, y)$ can be reconstructed by applying the inverse Radon transform to a series of different projections $p_\theta(r)$. This fundamental concept forms the basis of tomographic reconstruction. The definition of the Radon transform implies that the intensity of the projection images should be a monotonic function of the physical quantity to be reconstructed. This property is known as the projection requirement of tomography.[96]
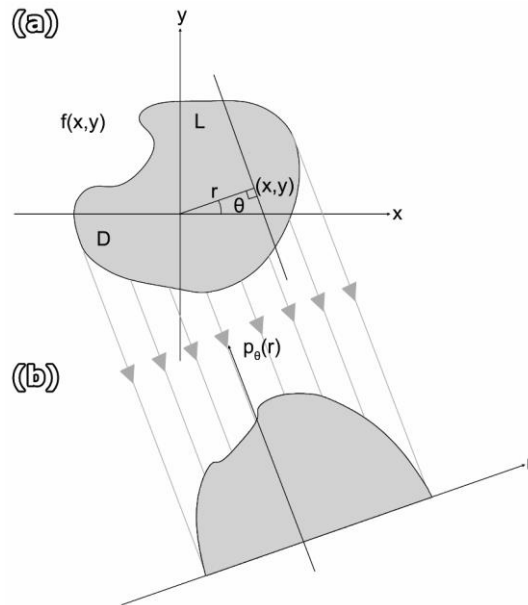
Figure 2.4 (a) Object $f(x, y)$ represented in real space. The projection $p_\theta(r)$ of such object can be obtained through the sampling of the object by solving line integrals of all possible lines L (b). The orientation of the projection of the function $f(x,y)$ is represented by the grey lines with arrows. By combining all the possible projections along different angles θ, the object $f(x, y)$ can be fully recovered.[97]

The Radon operator R transforms the coordinate system of the object in real space to the Radon space (l, z), where l represents the direction perpendicular to the projection direction and is given by $l = r \cdot \cos \theta$, and z represents the direction parallel to the projection direction ($z = r \sin \theta$). Here, θ denotes the projection angle (Figure 2.5.a). To simplify the mathematical description, polar coordinates (r, ϕ) are often used instead

of Cartesian coordinates for representing the object in real space. The polar coordinates are defined as $r = \sqrt{x^2 + y^2}$ and $\phi = \tan^{-1}(y/x)$.

Figure 2.5 illustrates that a projection of the complete object in Radon space corresponds to a sinusoidal-shaped line, which is why the projections in Radon space are commonly referred to as sinograms. Complete sampling of the object is achieved by recording projections at all possible projection angles, as demonstrated for the Shepp-Logan phantom in Figure 2.5.b, in both real and Radon space. In practise, however, reconstruction approaches based on Radon transform are often implicit, because the projection data are always sampled at discrete angles leaving regular gaps in the Fourier space. The Radon transform calculations intrinsically require a continuous function, and therefore, radial interpolation is required to fill the gaps in the Fourier space. Thus, the quality of the reconstruction is significantly affected by the type of implemented interpolation, where the smearing, data loss and creation of a non-unique solution from unique input data can be observed.[98]
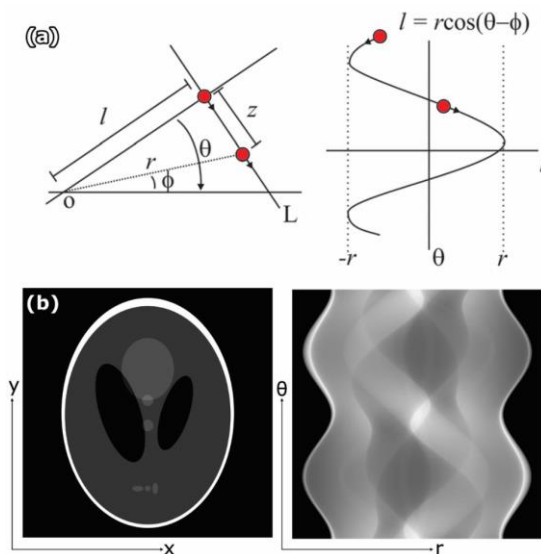
Figure 2.5 Geometrical relationship between polar (r,ϕ) and Radon (l, θ) space. (a) The trajectory of the red circle on the right panel corresponds to the dislocation of the red circle of the left panel.[99] (b) Illustration of the same principle in (a) for the Shepp-Logan phantom.[100]

2.3.2 Back-projection

A straightforward approach to obtain a reconstruction is through back-projection. This technique involves taking all the sinogram values and re-projecting them back into the object space along the corresponding line. Mathematically, the concept of back-projection can be expressed as:

$$f_b(x, y) = \int_0^\pi p(\theta, x\cos(\theta) + y\sin(\theta))d\theta \tag{2.2}$$

However, this approach often results in a blurred version of the object (Figure 2.6a,b). The underlying problem becomes evident when examining the Radon transform in the frequency domain. The projection can be described as:

$$p(x) = \int_{-\infty}^{+\infty} f(x, y)dy \tag{2.3}$$

The Fourier transform of the object is given by:

$$F(u, v) = \int_{-\infty}^{+\infty} \int_{-\infty}^{+\infty} f(x, y)e^{-2\pi i(ux+vy)}dxdy \tag{2.4}$$

The central slice perpendicular to the projection direction through this Fourier transform is represented by:

$$F(u, 0) = \int_{-\infty}^{+\infty} \left[\int_{-\infty}^{+\infty} f(x, y)dy\right] e^{-2\pi i(ux)}dx \; = \; \int_{-\infty}^{+\infty} p(x)e^{-2\pi i(ux)}dx \tag{2.5}$$

which is equal to the Fourier transform of the measured projection, $p(x)$. In other words, it implies that the 1D Fourier transform of a projection of a 2D object corresponds to a line passing through the 2D Fourier transform of the imaged object. This line intersects the origin of the Fourier space and is perpendicular to the projection direction. This concept is known as the central slice theorem. From Figure 2.7, it is evident that lower frequencies are overestimated when combining all the projection slices. This oversampling of the lower frequencies can be compensated by employing a weighting filter, leading to the weighted back-projection (WBP) reconstruction technique (Figure 2.6c).
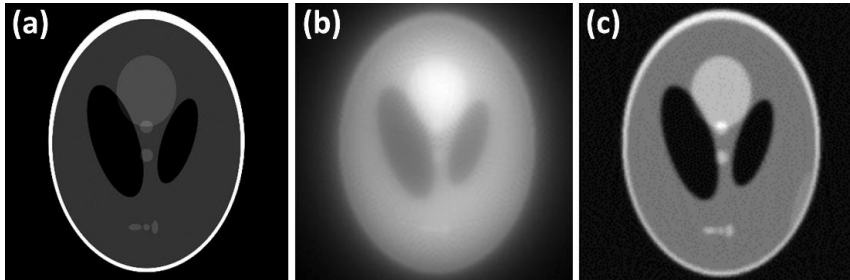
Figure 2.6 (a) Shepp-Logan phantom, reconstruction using (b) back projecting and (c) WBP.
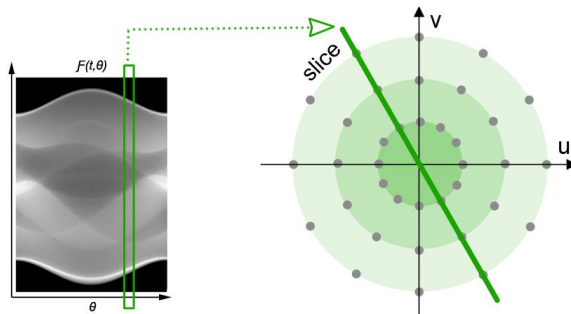
Figure 2.7 Illustration of the Fourier slice theorem which states that a projection at a certain angle at the space domain corresponds to a central section through the Fourier transform of that object.[97]

2.4 Imaging modes for electron tomography

As discussed in **Section 2.3.1**, the projection requirement states that the intensity observed in a projection image should exhibit a monotonic relationship with a specific physical property of the object being studied, integrated throughout its thickness along the direction of projection.[101] In light of this requirement, it is imperative to perform a careful selection of an appropriate imaging modality. For instance, BF TEM proves particularly well-suited for the examination of amorphous materials[102] and biological structures,[103] owing to the prevalence of absorption-based contrast as the primary contrast mechanism. Consequently, the intensity observed in the projection image is

directly correlated with the thickness of the specimen in such cases. However, BF TEM fails to provide reliable information about the thickness of crystalline samples, where the strong diffraction contrast becomes dominant, leading to the disconnection between the acquired intensity and the thickness of the specimen. In the next section, I will review the different imaging modes that can be employed for tomography of metallic NPs, studied in this thesis.

2.4.1 STEM imaging

STEM is a powerful imaging technique used in electron microscopy that provides detailed structural and compositional information about nanoobjects at the atomic level. As discussed in **Section 2.2**, mass-thickness contrast plays a dominant role during the formation of HAADF-STEM images and satisfies the projection requirement.[104] In that manner, ET based on HAADF-STEM imaging has proven itself as a valuable technique for the investigation of various complex nanostructures in 3D.[101,105]

The growing complexity of synthesized NPs may require the investigation of structural defects in 3D, that could be achieved with LAADF-STEM tomography. However, the ability of LAADF-STEM to yield the superior information on the location of crystal defects, e.g., twin planes, is undermined by the significant shape and volume errors, arising from the projection requirement violation.[106] To overcome this limitation, acquiring the tilt series by simultaneously using different detectors can be performed, allowing to obtain the 3D information on the actual morphology of the particle (HAADF-STEM, Figure 2.8a) and the position of crystal lattice defects (LAADF-STEM, Figure 2.8b). To obtain a better visualization of the defects from the LAADF-STEM reconstruction, a manual segmentation is typically performed. Because the acquisition is performed simultaneously, the alignment parameters for both series are identical, two reconstructions can be superimposed in a straightforward manner (Figure 2.9).[106] This approach is called "multimode ET" and has proven itself as a powerful method to investigate the presence of defects in NPs.[22,106]
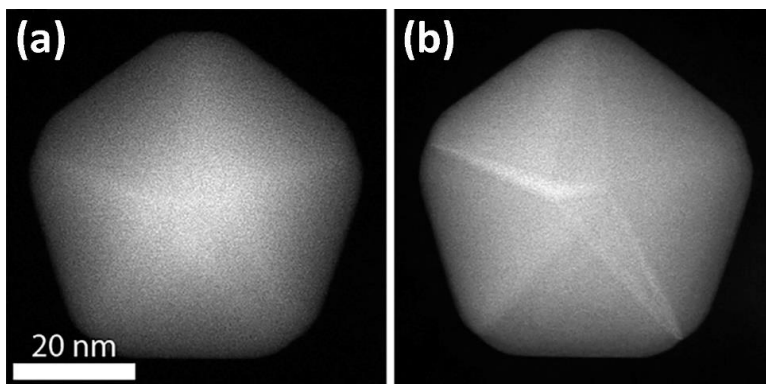
Figure 2.8 (a) HAADF-STEM and (b) LAADF-STEM projections of Au decahedron, taken simultaneously.[106] Image is adapted from open access article distributed under the terms of the Creative Commons CC BY license (Copyright © 2018 American Chemical Society.
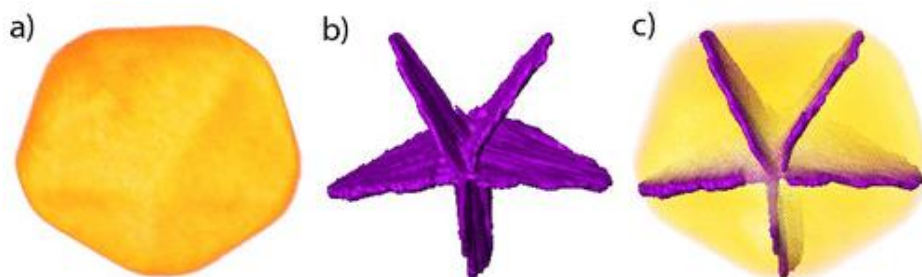
Figure 2.9 3D visualization of the HAADF-STEM reconstruction (a) and the twin planes segmented from the LAADF-STEM reconstruction (b) of an Au decahedron. Both volumes are superimposed to evaluate the position of the twin planes in the correct volume (c).[106] Image is adapted from open access article distributed under the terms of the Creative Commons CC BY license (Copyright © 2018 American Chemical Society).

2.4.2 Energy dispersive x-ray spectroscopy

For HAADF-STEM imaging, the chemical composition of specimens can typically be inferred when there is a significant difference in atomic masses between chemical species. On the other hand, HAADF-STEM only provides relative intensity values and prior knowledge of present elements may be needed. In addition, for chemical elements

with very similar atomic number Z or in the case of alloying, spectroscopic methods are necessary to accurately characterize the specimen's chemical nature. In a transmission electron microscope, this information can be for example obtained through EDX.[107–109] STEM-EDX is commonly employed to record the X-ray signals emitted during inelastic scattering events, and semiconductor-based detectors are used to capture these signals. When X-rays interact with the detector, electron-hole pairs are generated and translated into charge pulses. As the X-ray energies are typically above 1 keV, multiple electron-hole pairs are created, and the quantity is directly proportional to the energy of the detected X-ray. Unfortunately, in most cases the application of EDX tomography is severely limited by the typically very low signal-to-noise ratio (SNR) in the 2D elemental maps. The poor SNR is caused by the combination of the fundamentally low probability of characteristic X-rays generation and low efficiency of their detection due to the size constraints on the EDX detector inside a TEM.[110] To improve the SNR of EDX maps, a Super-X detector, consisting of four detectors, can be employed, ensuring the more effective collection of X-rays (as shown in Figure 2.9a).[111] Each pixel within the region of interest can be assigned an energy spectrum (Figure 2.9b). By fitting the spectrum across the entire region of interest, a 2D chemical map of the region can be generated, as exemplified by an Au@Ag@m-SiO$_2$ PT NR (Figure 2.9c). To accurately quantify the chemical composition of a spectral map obtained from EDX spectroscopy, various methods can be employed, including the Cliff-Lorimer ratio technique[110,112,113] and the ζ-factor methodology.[114] Achieving statistically significant results requires multiple scans over the region of interest to enhance the SNR ratio.
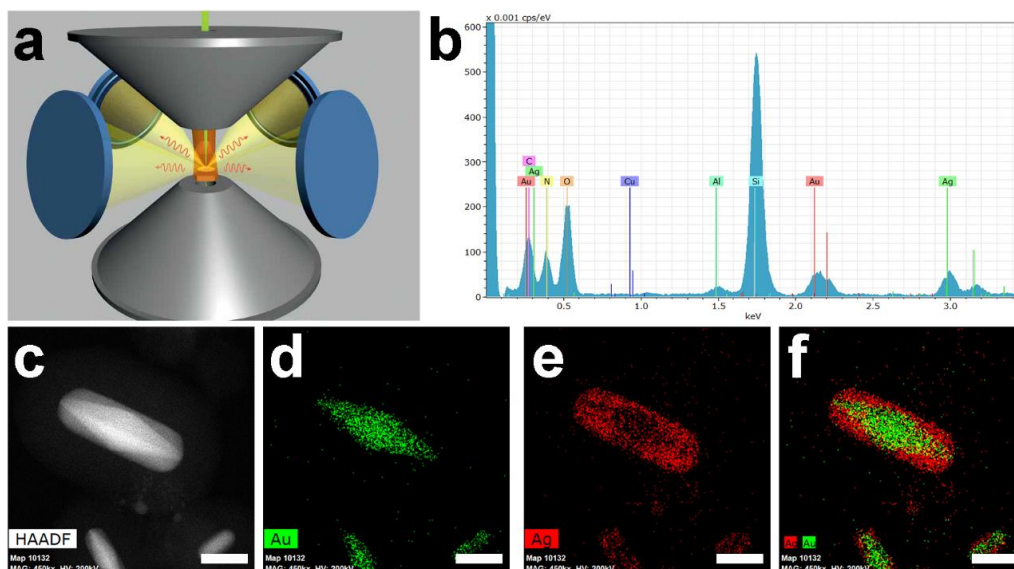
Figure 2.9 (a) Design of the Super-X detector (blue) for the detection of x-rays emitted by the specimen (orange).[115] (b) Typical spectrum obtained by EDX spectroscopy of an Au@Ag@m-SiO$_2$ PT nanorod. (c-f) HAADF-STEM image and 2D chemical maps (Au, Ag and the superposition of both) of the same nanorod investigated in (b). Scalebars are 40 nm.

The EDX spectroscopic technique can be extended to three dimensions, as the detection of X-rays is directly related to the volume of the chemical element within the specimen. This satisfies the projection requirement for tomographic reconstructions.[116] Nonetheless, owing to the poor SNR inherent to EDX maps, the duration needed for acquiring a single STEM-EDX projection may extend beyond 10 minutes, which drastically increases the total duration of tilt series acquisition and, in parallel, imposes substantial electron doses, rendering this approach unsuitable for beam-sensitive materials. Typically, EDX maps are acquired for only a few projections to minimize exposure time and prevent radiation damage-induced structural modifications. In this approach, a tomographic series is simultaneously obtained using the HAADF-STEM mode, covering on as wide tilt range as possible, and the spectroscopic data is incorporated during the tomographic reconstruction process.[108,109] Recent studies conducted in our laboratory have demonstrated that combining the ζ-factor

methodology with 3D characterization of nanomaterials yields more precise quantification compared to the Cliff-Lorimer ratio.[117] This distinction arises from the capability of the ζ-factor method to provide data on the specimen's thickness at each discrete analysis point in conjunction with compositional information.[118] In contrast, the accurate execution of Cliff-Lorimer analysis necessitates both a uniform specimen thickness and the capacity to derive individual element-specific k-factors, typically obtained from standard samples.[119] It is also worth mentioning that deep learning-based denoising method was developed at EMAT, based on the establishing an extensive database of realistic nanoparticle structures and simulated noisy and clean EDX maps, which was used for training and quantitative evaluation of various data-driven image processing, analysis, and reconstruction methods for nanoparticles.[120] Based on these data, a deep neural network with U-net architecture was trained for denoising elemental maps.[120] This method is allowing for more than an order of magnitude reduction in electron dose and acquisition time for EDX tomography without compromising the analysis of elemental distribution in nanoparticles.[120]

In addition to the Z-contrast of elastically scattered electrons or X-ray signals generated during inelastic scattering events, other signals resulting from the interaction of an electron beam with matter and satisfying the projection requirement can be detected in modern electron microscopes and utilized for tomography reconstructions. For instance, electron holography relies on the formation of an interference pattern or 'hologram', facilitating the recovery of the phase shift of the electron wave.[121] As the phase shift is sensitive to local variations in magnetic and electrostatic potential, the technique can be used to obtain quantitative information about magnetic and electric fields in 3D.[122,123] Another example is Energy Filtered Transmission Electron Tomography (EFTEM), which employs EELS technique based on the detection of inelastically scattered electrons.[124,125] This technique is typically applied for the three-dimensional characterization of the chemical nature and oxidation states of various nanomaterials.[126,127] Furthermore, the development of novel techniques enables to obtain 3D information about nanomaterials, as in case of 4D-STEM based MultiSlice Electron Tomography (MSEM) which can be applied to a wide variety of materials, including radiation-sensitive samples and materials containing light elements.[128,129.]

2.5 Practical aspects of electron tomography

In this section, a comprehensive overview of every practical step involved in a tomography experiment is provided.

2.5.1 Image acquisition

In an ET experiment, a tilt series of multiple projection images is acquired. The acquisition process involves using a dedicated single tilt tomography holder (Figure 2.10a). The images are captured over a large tilt range, typically with a constant tilt increment of 1–3°. Ideally, the acquisition should cover a tilt range from -90° to +90°. However, even with a dedicated holder design, a maximum tilt angle of only ±80° can be achieved (Figure 2.10b). This limitation creates a "missing wedge" of information in the acquired data, leading to artifacts in the reconstruction process. These artifacts manifest as blurring and elongation of the reconstructed image along the direction of the optical axis. The impact of these "missing wedge" artifacts can be observed in Figure 2.11.
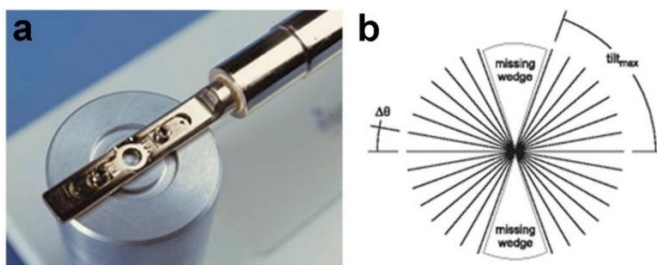
Figure 2.10 (a) Fischione 2022 tomography holder. (b) Representation of the missing information during the tomography acquisition.
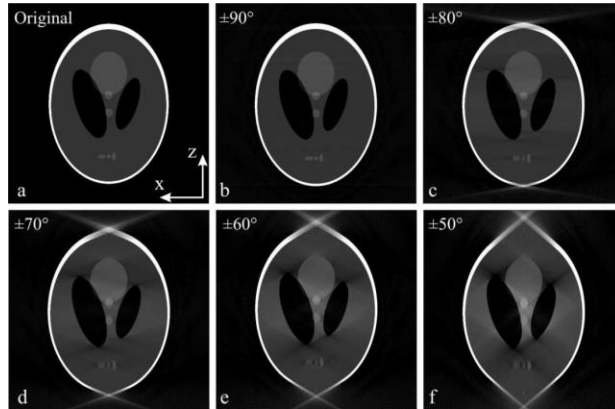
Figure 2.11 Series of phantom images showing the missing wedge artifact. a) The original image. b-f) The reconstructed object for an increasing missing wedge along the z-direction.[130]

The utilization of Focused Ion Beam (FIB, a precision instrument used in microscopy and microfabrication employing a focused beam of ions, e.g. Ga ions)[131] to mill or section a sample to create thin specimens for analysis in conjunction with an on-axis tomography holder (Figure 2.12a) offers significant advantages in acquiring tilt series encompassing a full tilt range of ±180°, thereby eliminating missing wedge artifacts. This approach is only applicable in studies for which a needle shaped sample can be prepared, e.g. self-supporting needle-like structures. Additionally, the supporting matrix can accommodate various nanostructures, such as the combination of zirconia and polymer,[132] carbon nanotubes and silica,[133] or porous $La_2Zr_2O_7$ films (Figure 2.12b,c).[134] Subsequently, FIB treatment and ET investigations can be performed, effectively avoiding the occurrence of missing wedge artifacts. It is important to note, however, that the FIB milling process can introduce traces of Pt and Ga within the sample, potentially altering its initial morphology. Careful consideration should be given to these effects when utilizing FIB sample preparation for tomography experiments. Another significant constraint to consider is the stability of the sample throughout the acquisition of the tilt series. This stability may decrease as the size of the needle-shaped specimen is reduced, especially when aiming for the acquisition of high-resolution (S)TEM projection images.[135] As a result, this method is employed in only a limited

number of studies due to the challenging preparation of needle-shaped specimens for arbitrary samples, such as nanoparticles.[136,137]
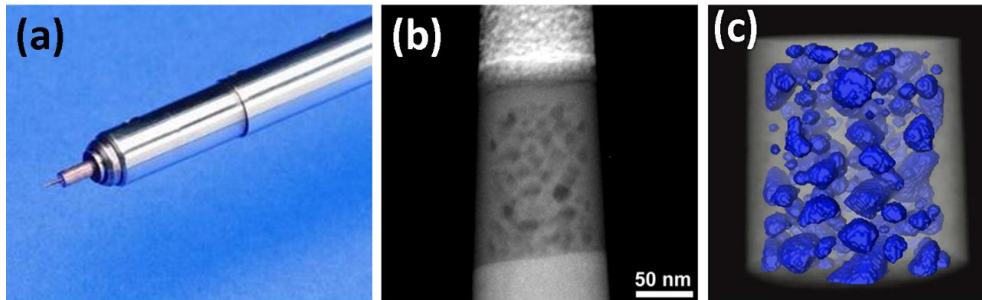
Figure 2.12 (a) Fischione 2050 on-axis rotation tomography holder allowing ±90° tilt. (b) 2D projection image of a needle-shaped pillar and (c) the visualisation of the 3D reconstruction obtained for a porous layer of $La_2Zr_2O_7$.[134] (Copyright © 2011 IOP Publishing Ltd)

2.5.2 Alignment of a tilt series

The next step in ET is image alignment to compensate for any residual shifts between consecutive projection images. Despite efforts to bring the region of interest into the field of view during the acquisition, there can still be a small residual shift of a few nm between images. To obtain an accurate 3D representation of the specimen, it is crucial to align the series of projection images, preferably with subpixel precision. One common approach for image alignment is to use cross-correlation, which measures the degree of similarity between two consecutive images (Figure 2.13). The cross-correlation is derived by calculating the inverse Fourier transform of the product of the Fourier transform of the first projection and the complex conjugate of the Fourier transform of the second image (Figure 2.13a-c). The location of the maximum intensity in the cross-correlation image indicates the displacement between the two original projection images (represented by red circle Figure 2.13c). The derived displacement position can be further adjusted until it aligns with the center of the resulting cross-correlation image, thereby ensuring the minimization of the shift between the two projections. Consequently, by calculating the cross-correlation function, it becomes possible to determine the degree of shift between each pair of images.
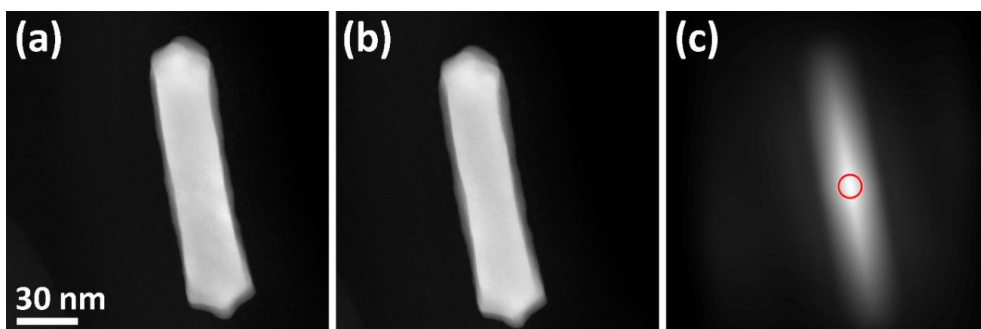
Figure 2.13 Cross-correlation (c) between two images of Au NP acquired at different tilt angles (a: 0°, b: 3°) was calculated. Red circle in (c) represents the position of the maximum intensity in the cross-correlation and, thus, the relative shift between the two original projections. When two projections are optimally aligned, the position of maximum intensity (red circle) will coincide with the center of the image.

Once the images are aligned, it is necessary to adjust the tilt axis before proceeding with tomographic reconstruction. This adjustment is essential because the projection geometry employed by reconstruction algorithms demands that the rotation axis be precisely vertical and intersect the center of each projection (as indicated by the red line in Figure 2.14a). However, the actual rotation axis of the acquired tilt series often deviates from this required position. This deviation is typically caused by the experimental setup parameters, such as the scanning directions in STEM. Thus, the goal is to determine the optimal tilt axis for the tomography series, which minimizes artifacts in the reconstructed slices. This can be achieved by reconstructing three slices along the object at the top and bottom (blue and green lines in Figure 2.14a) and examining the presence of "arc" artifacts (highlighted by dashed lines in Figure 2.14). To minimize the arc artifacts, the position and inclination of the tilt axis can be manually adjusted during the data processing step. When the tilt axis is properly aligned, more accurate tomographic reconstructions are obtained (Figure 2.14b), showing no indication of strong arc artifacts. If there is a rotation of the tilt axis, only slices above and below the central slice will show arc artifacts, pointing in opposite directions (Figure 2.14c, dashed lines). If there is a misalignment in the position of the tilt axis, an arc artifact will be

observed in all slices, pointing in the same direction (Figure 2.14d, dashed lines). As can be seen, an incorrect estimation of the tilt axis results in a loss of information in the final reconstruction. After the rotation axis is aligned, the series of aligned images can be used as input for the tomographic reconstruction process.
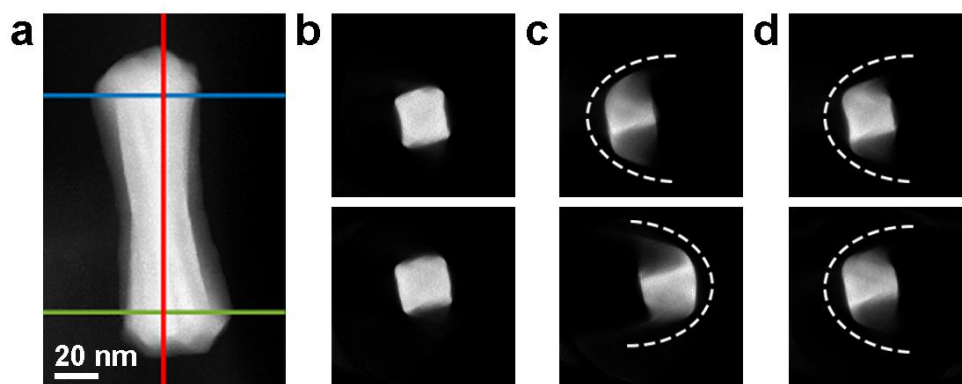
Figure 2.14 Alignment of the tit axis of a tomograph. (a) 0° projection of the studied Au NP. The red line represents the position of the tilt axis, whereas the blue and green lines depict the positions of top and bottom slices through the 3D reconstructions corresponding to the top and bottom images in (b,c,d). In (b), the presence of arc artifacts is minimized due to the correct alignment of the tilt axis. In (c), an incorrect rotation of the tilt axis leads to the formation of arc artifacts, pointing to the opposite directions. In (d), a shift of the tilt axis results in the creation of arc artifacts, pointing to the same direction. White dashed lines correspond to arc artifacts.

2.5.3 Reconstruction methods

Following the discussion of the Fourier slice theorem, it is possible to execute tomographic reconstruction in real space. One frequently employed technique is weighted back-projection (WBP), which operates on the same principles as the Fourier slice theorem but is conducted in real space. In cases where a substantial number of projection angles is unavailable, WBP results in reconstructions of poor quality due to inadequate sampling. To address this limitation, iterative methods are employed. A commonly used technique is the simultaneous iterative reconstruction technique

(SIRT). SIRT involves refining the reconstruction at each iteration by solving the minimization problem:

$$\hat{x} = argmin_x \|A\boldsymbol{x} - \boldsymbol{b}\|_2^2, \tag{2.6}$$

where $\boldsymbol{x}$ is the vector that represents the reconstructed object, A denotes the projector operator, and $\boldsymbol{b}$ symbolizes the vector that represents the projection images. The initial iteration is obtained by applying the back projection method. Subsequently, images based on the first reconstructed volume are generated at the same projection angles and compared with the input images for reconstruction. The relative error, or residual, between the input and the generated projection image is computed simultaneously for each tilt angle and used to generate a new reconstructed volume. This iterative process continues until convergence is achieved in minimizing the residual, as depicted in Figure 2.15. For a typical SNR in HAADF-STEM tilt series of metallic NPs (SNR $\approx$ 8), it was reported that this method will converge after approximately 20 to 30 iterations.[138] Another reconstruction approach known as the Expectation-Maximization (EM) algorithm is employed for maximum likelihood estimation, particularly advantageous in scenarios involving missing variables, which can arise due to factors like the missing wedge in tilt series collection.[139] The EM algorithm operates by initially estimating the values of these missing variables and subsequently optimizing the reconstructed object. This two-step process of expectation (E) and maximization (M) is repeated iteratively until convergence is achieved. It is important to note that the SIRT algorithm can also be demonstrated to converge towards a maximum likelihood solution, but it is only suitable for situations where the noise in the input data is Gaussian distributed. An advantage of EM is the adaptability to handle input data characterized by a Poisson distribution, experimentally arising from discrete number of events at each measured point – such as the number of scattered electrons in HAADF STEM, that makes EM algorithm a very popular practical method for obtaining electron tomography reconstructions.
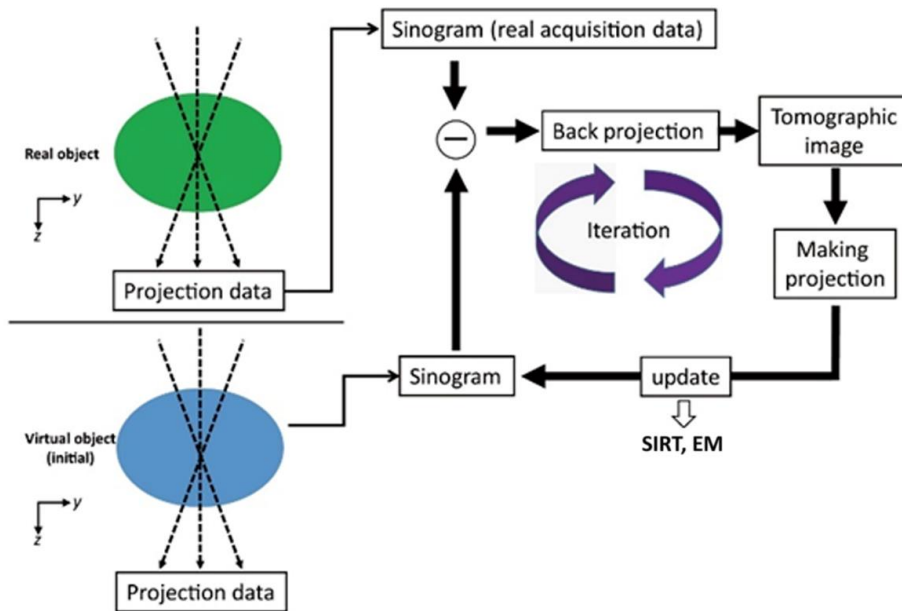
Figure 2.15 Flowchart showing the principle of the iterative reconstruction methods.[140] Image is adapted from open access article distributed under the terms of the Creative Commons CC BY license (Copyright 2016 IntechOpen).

Recently, significant advancements have been made in the development of more advanced algorithms that leverage prior knowledge in tomographic reconstructions. Two notable examples are the Discrete Algebraic Reconstruction Technique (DART)[141] and Total Variation Minimization (TVM)[142] algorithms. The DART algorithm operates under the assumption that only a limited number of materials exist, represented by a discrete set of grey values, within the reconstruction. During the iterative process, the DART algorithm performs segmentation of the reconstruction, enabling a direct quantifiable reconstruction (Figure 2.16). On the other hand, the TVM reconstruction algorithm is based on the principles of compressed sensing. In this method the prior knowledge that the boundary of the specimen is sparse is used. By incorporating such prior knowledge, these advanced algorithms contribute to the improvement of tomographic reconstruction, but they are highly computationally demanding and require careful choice of reconstruction parameters, e.g. threshold intensity values for DART reconstruction.
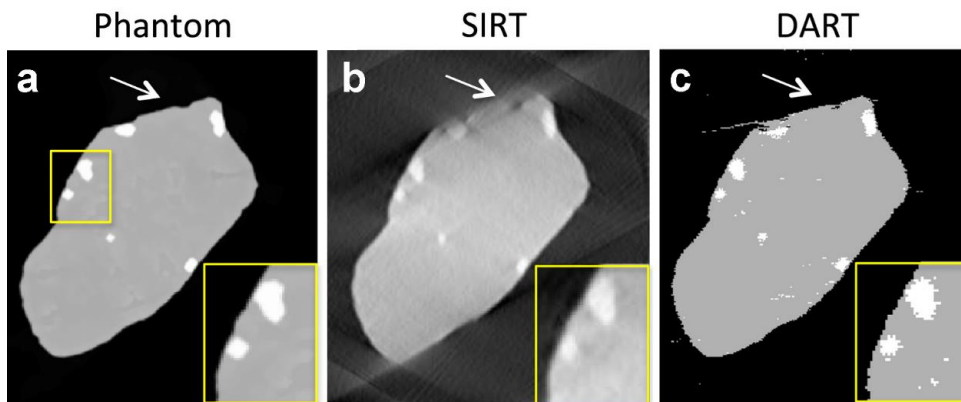
Figure 2.16 Numerical tomography simulations of (a) a phantom object and its reconstructions performed for a ±60° tilt range with 2° increments obtained using (b) WBP, (c) SIRT and (d) DART.[143] Adapted with permission from Elsevier (Copyright © 2017 Elsevier B.V.)

2.5.4 3D visualization and quantification

Three primary techniques are employed for visualization: orthoslices, isosurfaces, and volume rendering using voxels (voltex rendering). Orthoslices are essentially cross-sectional slices obtained from the reconstruction, enabling examination of the internal structure of the nanoparticle along various directions. These orthoslices are considered the most objective visualization method since they do not require a (manual) threshold. In addition, slices through the reconstruction can be used to analyse the inner structure of studied objects, e.g., the presence of twin boundaries in Au NPs (bright lines in Figure 2.17a). Apart from orthoslices aligned with the original x, y, and z directions of the 3D reconstruction, oblique slices, taken along arbitrary orientations, can also be employed to offer greater flexibility in visualizing specific features of interest.
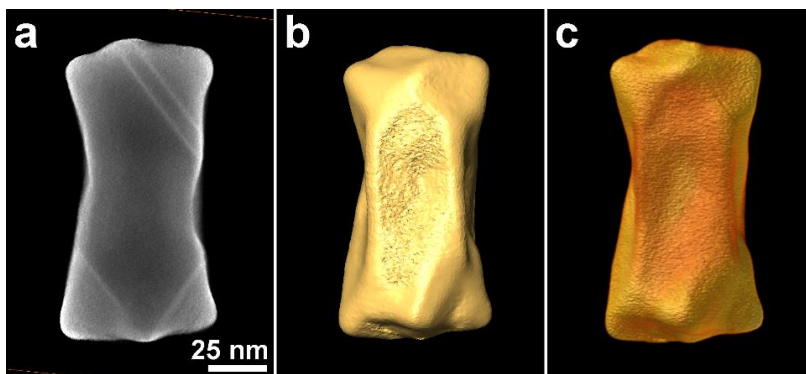
Figure 2.17 Example of 3D reconstruction representations of chiral Au NP: (a) central slice through the reconstruction, (b) isosurface and (c) voltex rendering. Retrieving consecutive slices facilitates the examination of the internal structure of a NP, offering insight into features like defects or voids. Conversely, isosurface and volume rendering enable the manipulation of the entire NP volume. These techniques allow for actions such as rotating the NP to various viewing angles, providing the means to analyze surface features effectively.

In contrast, both isosurfaces and voltex rendering (Figure 2.17b,c) involve selecting a threshold prior to their calculation. Only intensities surpassing the threshold are taken into consideration. For isosurfaces, voxels with identical intensities are connected to form a connected surface, effectively reducing the 3D volume to a 2D surface. This reduction significantly benefits calculation time. Additionally, isosurface can be easily extracted for the utilization as an input for, e.g. simulation of electromagnetic properties (for more detail see **Section 2.5.5**). Conversely, voltex rendering projects the entire 3D volume onto the computer screen, allowing the manipulation of intensity, color, and transparency of the 3D reconstruction to emphasize specific details.

2.5.5 Electron tomography as an input for atomistic and electromagnetic simulations

The structural information of various nanomaterials, obtainable directly through (S)TEM techniques, has demonstrated its significance in both fundamental and material

sciences. However, atomic-resolution data about nanomaterials (particularly in 3D) acquired via electron microscopy, can also be integrated with or utilized as input for theoretical modelling methods. This synergy can substantially enhance the scientific insights gained in the field of material sciences, augmenting the overall outcome of conducted researches.

One particular example is Molecular Dynamics (MD) simulations based on the idea of classical mechanics, which is the study of the dynamical response of objects under applied forces.[144,145] MD simulations can allow researchers to observe atomic-scale dynamics, as well as conformational transitions under different conditions, such as changes in temperature or pressure.[3,4] In that light, the processes at nanoscale experimentally observed by using high resolution and *in situ* (S)TEM methodologies can be incorporated with the MD simulations, as was demonstrated for different nanomaterials at EMAT. [146,147]

For instance, the laser-light-induced atomistic rearrangements in Au NRs, causing shape deformations and defect generation was demonstrated by combined atomic-resolution ET and MD simulations.[146] In this work, based on the determined surface facets of the Au NR using ET (Figure 2.18a), model-like input structures of Au NRs were constructed to have {110} and {100} lateral facets, and a combination of {100},{110}, {111} facets at its tips.[148–150] Next, mesoporous silica shell was created around the created Au NR models,[151] followed by the structural relaxation of the created mesoporous silica-coated Au NR models in vacuum and at room temperature before the MD simulations for laser heating. It should be mentioned, that while keeping ARs of Au NRs models similar to those obtained in the ET experiment, the diameter was reduced to 4 nm as the high computational cost limit the size range and time scales of MD simulations. During the MD simulations, Embedded Atom Model (EAM)[152] was used for the interaction between Au atoms, whereas the inter-atomic potential of Vashishta et al.[153] was defined for the interaction between the atoms of silica. [146] For the interaction between the Au atoms and the mesoporous silica coating, the Lennard-Jones potential was applied.[154] Then the MD simulations for femtosecond laser excitation were performed (Figure 2.18b). In this way, atomistic rearrangements upon

femtosecond laser irradiation causing shape deformation and defect generation were unravelled by performing MD simulations based on experimentally measured surface morphology.
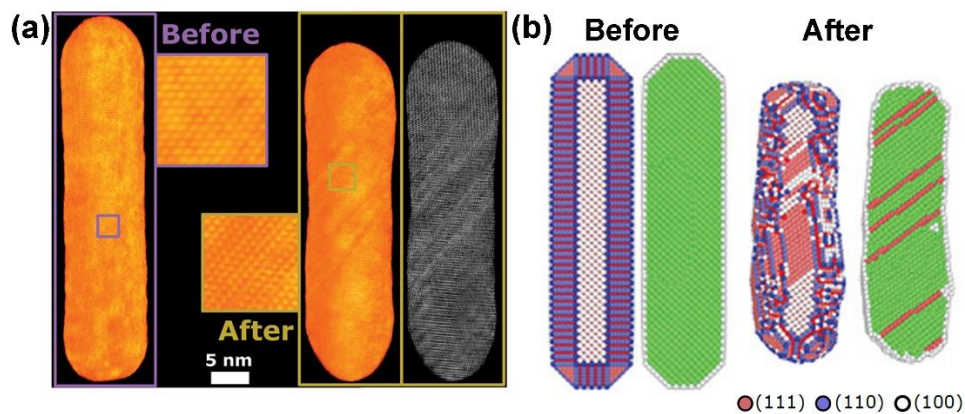
Figure 2.18 (a) Atomic resolution ET of the same silica-coated Au NR before and after femtosecond laser excitation: 3D visualization before and after excitation along the same viewing direction. A magnified visualization shows the SC nature of the particle before laser excitation. After excitation, a magnified visualization and a slice through the middle of the NR (right box) confirm TB defects. (b) MD simulations of laser-heated Au NR: Side views (left sides) and interior structure (right sides) before and after simulated laser pulse excitation and the calculated temperature profiles. For these simulations, particle of a smaller size but with a similar aspect ratio to the NP from (a) was utilized. The silica coating is omitted in the visualizations in both (a) and (b).[146] Adapted with permission from Wiley Materials (Copyright © 2021 Wiley-VCH GmbH).

Additionally, combined ET and MD simulations can be also performed to investigate the elemental diffusion in bimetallic systems. One of the examples is the diffusion in Au@Pt NPs, where the thermal migration of Au atoms from the core through the interface to the outer surface were reported using of *in situ* heating ET.[147] This behaviour was further confirmed by MD simulations, showing that diffusion of Au atoms to the surface leads to a thermodynamically favourable structure compared to initial unstable Au@Pt NPs (Figure 2.18b).[147] In this work,[147] the input structure of Au NRs were

constructed to have eight {520} lateral facets and {100}, {110}, {111} facets at its tips based on the experimentally determined surface facets.[155] Then the created Au NR was placed at the center of the created Pt structure.[156] Since using the actual size of the experimental NPs in MD simulations requires vast computational power, overall sizes of the created Au@Pt NRs were scaled down, whereas for all the other parameters, such as aspect ratio and Pt/Au ratios, experimentally determined values were used.[147] The following simulations were carried out with the EAM potential.[155] First, the conjugate gradient energy minimization was applied to all input structures of NRs by imposing a maximum distance that an atom can move in a one-time step (0.01 Å).[147] Afterward, the systems were relaxed at room temperature for 20 ns in a canonical ensemble with Nosé–Hoover thermostat (NVT ensemble) and a damping factor of 0.1. Then, the temperature of each system was increased with the NVT ensemble up to 200 °C with a constant heating rate of 0.5 K/ps, and the NRs were relaxed for 20 ns at each temperature.[147]

Another powerful theoretical approach for the investigation of materials at the nanoscale are Density Functional Theory (DFT) simulations. The underlying principle of DFT is that the electron density is the fundamental quantity to describe the ground state properties of the many-body system.[156] However, instead of solving the Schrödinger equation for the many-electron system, which is computationally infeasible for large systems, certain approximations are used in DFT. For instance, the approximations based on Kohn-Sham equations[157] can be applied, enabling the replacement of original many-body problem with an auxiliary system of independent particles, moving in an effective potential.[158] The Kohn-Sham equations must be solved self-consistently, but the group of parameters related to the interaction of the particles with the effective potential remains fundamentally unknown, related to the interaction of the particles, not accounted in the non-interacting Kohn-Sham approach.[158] These parameters are known as exchange-correlation parameters and can be determined using local density[157,159] and generalised gradient[160] approximations (LDA and GGA) to the exchange-correlation energy of studied system. In addition, the van der Waals density functional (vdW-DF) method[161] can be used to enable the simulation of van der Waals interactions between the atoms in the simulation. In that manner, the DFT calculations combined with UV–vis spectrometry demonstrated the preferential coordination of aminopropanol through

the amino group on the surface of Pd NPs, controlling the particle shape through a selective blocking of (100) facets, which promote the growth on the (111) facets.[162] Given the ability of DFT simulations to predict the interaction of various nanomaterials with organic molecules, complex studies can be envisioned, where the information on the surface faceting of various NPs, obtained from ET experiments, can be corroborated with DFT calculations. I will demonstrate this concept in **Chapter 4** of my thesis, where I will show how surface faceting information was obtained through ET and was subsequently utilized as input data for DFT calculations, specifically focused on the facet-specific adsorption of Cys molecules on the surface of Au NPs.

To investigate the chiral nature of various metallic NPs electromagnetic modeling of the optical properties can be performed based on the numerical resolution of Maxwell's equations.[163] This method is typically used to understand experimental measurements of plasmon resonance modes, using idealized models that resemble as close as possible the experimental morphology of interest.[163] The 3D objects retrieved from electron tomography reconstructions are more reliable models that can be used directly as the input for such simulations. However, the typical methods of electromagnetic simulations, e.g. discrete-dipole approximation[164] or frequency-domain finite-element methods,[165] yield reliable analytical solution of Maxwells's equations only for higher symmetric geometries.[166] To achieve reliable electromagnetic modeling of complex nanostructures, full-wave frequency-domain methodology based on boundary-element parametrizations (surface integral equation-method of moments, SIE-MoM) was proposed and utilized by the groups of F. Obelleiro and J.M. Taboada.[166] In this approach only the material boundaries (i.e., two dimensional surfaces) must be parametrized, thereby drastically reducing the resulting algebraic problem size if compared with conventional volumetric approaches.[166] In this manner, the 3D volume obtained from ET (Figure 3.7a)[167] can be converted into a mesh object representing the surface (Figure 3.8b), that can be used as an input for SIE-MOM simulations of chiroptical properties. Although suitable reproduction of the observed morphologies can still be challenging, given the intricate network of wrinkles covering the chiral Au NR surface, more accurate morphologies can be created, mimicking the size/AR of the studied NPs and the regions with wrinkles displaying different angles (Figure 3.7c).[167]

The comparison of simulated (Figure 3.7d) and experimental (Figure 3.7e) chiroptical activity of the wrinkled Au NPs demonstrates an excellent agreement of experimentally measured CD spectroscopy results with electromagnetic simulations, that underscores the utility of electron tomography data as valuable input for these simulations.[167]
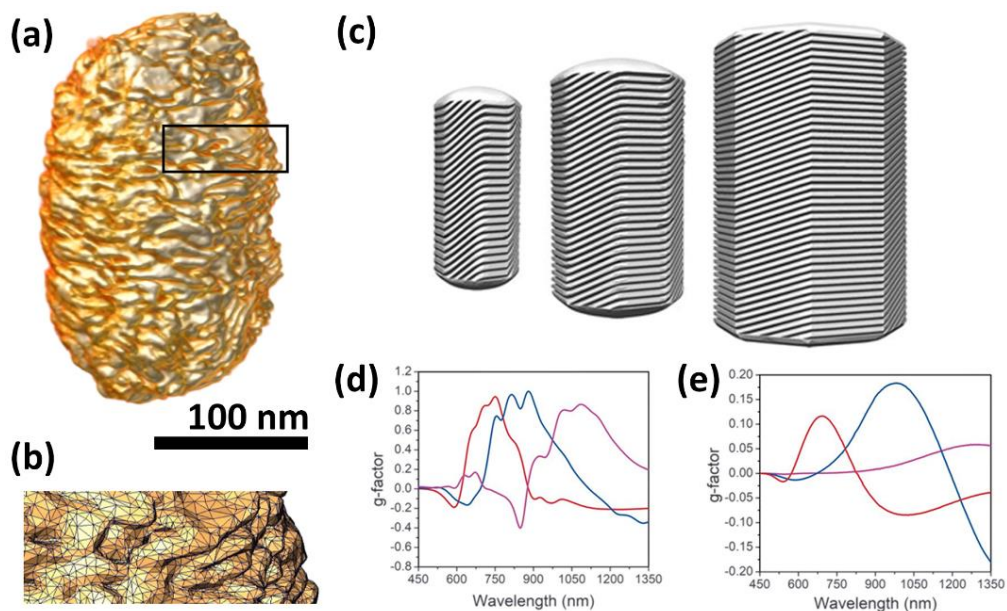
Figure 2.19 (a) Tomography reconstruction of a Au NP grown in an (R)-BINAMINE-CTAC mixture, (b) Magnified part of the surface of the chiral Au NP (black square in a), represented as triangular meshes. (c) Idealized models of chiral gold NRs (resembling experimental morphology) used to simulate the chiral plasmonic properties (from left to right: 165×73, 210×112, and 270×175 nm). (d) Calculated anisotropy factor spectra (red, blue, and magenta respectively). (e) CD-spectral evolution of the anisotropy factor for chiral Au NRs with the comparable average dimensions.[167] Adapted under the terms of the Science Journals Default License (Copyright © 2020 American Association for the Advancement of Science).

Part 1

3D characterization of chiral NPs

Chapter 3. Introduction to the synthesis of chiral NPs

The synthesis of chiral nanostructures can be divided into two main approaches. The first one, the top-down approach[168] is based on the local elimination of material from a larger object or film to obtain the desired shape, layout, and properties, using technologies such as direct laser writing (DLW), focused ion beam etching, and optical or electron-beam lithography. For example, Wegener's group obtained corkscrew-shaped gold helix arrays using DLW (Figure 3.1).[169] However, most studies have focused on assemblies of similar nano-objects placed in a 2D plane either at random positions or ordered on a regular 2D array.[170,171] Although well-defined 3D nanostructures can be produced by lithographic techniques (and more generally top-down approaches), they often require multistep processes of layer-by-layer deposition and expensive vacuum-based equipment.[170] In particular, the building blocks need to have subwavelength dimensions, i.e., of the order of tens of nanometers for applications in the visible and UV range, which is challenging, even for e-beam lithography.[170]
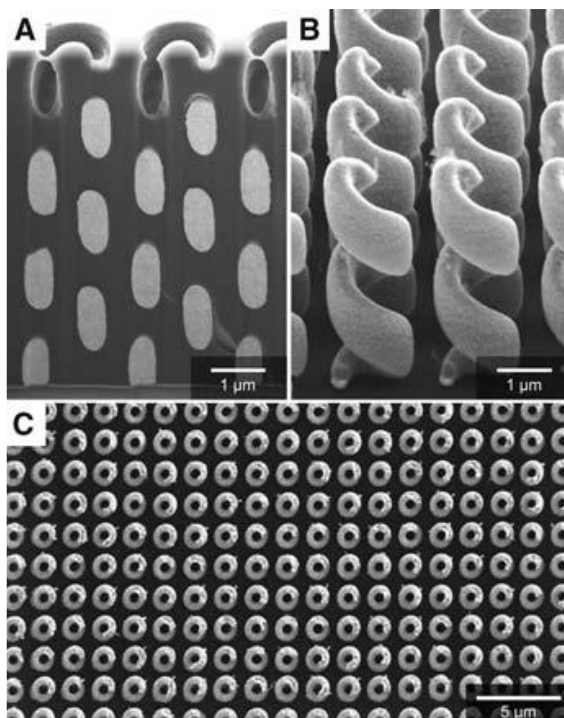
Figure 3.1 (A) Focused-ion-beam (FIB) cut of a polymer structure partially filled with gold by electroplating. (B) Oblique view of a left-handed helix structure after removal of the polymer by plasma etching. (C) Top-view image revealing the circular cross-section of the helices and the homogeneity on a larger scale.[169] Adapted under the terms of the Science Journals Default License (Copyright © 2009 American Association for the Advancement of Science).

Alternatively, bottom-up approaches can be employed to manipulate nanoparticles and arrange them into hierarchical structures or assemblies. One example of such assemblies is the self-assembly of nanoparticles facilitated by their physical interaction with chiral templates, such as DNA origami or chiral nanofibers (Figure 3.2).[172–174] This self-assembly process results in the formation of chiral nanostructures, where the nanoparticles are adsorbed onto the surface of a chiral template, thus adopting a helical arrangement. The optical properties of these chiral assemblies are determined by their complex structure, which can give rise to multiple LSPR modes that may spectrally overlap with each other.[168] This overlapping of LSPR modes can complicate the

interpretation of CD spectra (Figure 3.2d).[175] Additionally, the chiroptical behavior, which refers to the optical activity resulting from the anisotropic coupling between the assembled nanoparticles, can be significantly degraded in multilayer structures where the individual particles are in close proximity and interact with each other.[176] These limitations in the self-assembly of nanoparticles on chiral templates can hinder their application in certain contexts. To overcome these challenges, it is necessary to synthesize individual nanoparticles with their own inherent chirality. By directly introducing chirality into the nanoparticles during their synthesis, it becomes possible to achieve well-defined chiral properties without the complications arising from assembly processes.
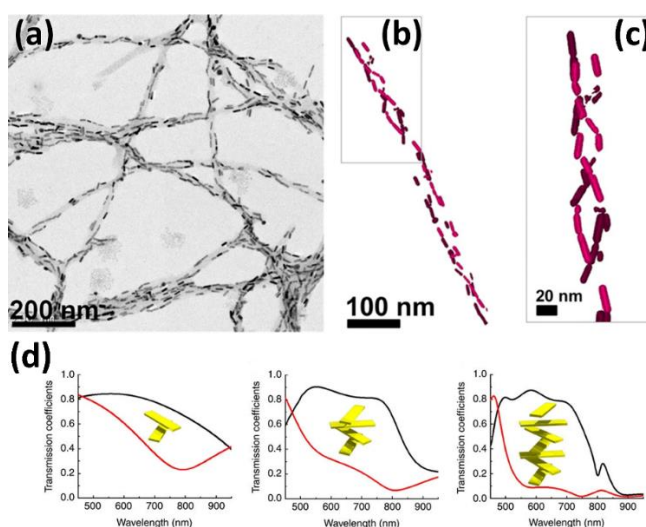
Figure 3.2 (a) TEM image of Au NRs in the presence of α-synuclein fibrils. (b) Cryo-tomography reconstruction image of a composite fiber showing the 3D chiral arrangement of Au NRs. An enlarged view of the top marked portion of the assembly is shown in (c).[174] Image is taken from open access article distributed under the terms of the Creative Commons CC BY license (Copyright © 2018 PNAS). (d) Transmission of LCP and RCP waves through a stack of rotated metasurfaces by increasing the number of layers (L=120 nm, θ=60°). From left to right, the number of layers increases from two to seven, with the insets illustrating one unit cell of the corresponding twisted metamaterial slab along the direction of propagation.[175] Reproduced with permission from Springer Nature (Copyright © 2012, Springer Nature Limited).

3.1 Facet dependent adsorption of amino acids leading to twisted morphologies

Wet chemical synthesis can be used as an efficient technique for the synthesis of chiral NPs, particularly by utilizing chiral molecules as co-surfactants during the crystal growth process. By incorporating diverse chiral molecules during the synthesis, it becomes possible to induce different types of chirality in the resulting NPs. However, the mechanisms underlying chiral growth should still be investigated in more detail. In the following sections, chiral growth in presence of different types of chiral inducers will be discussed.

Among the first experimental efforts, the synthesis of chiral Au "propellers" from achiral nanotriangles was performed using cysteine enantiomers (Figure 3.3a).[177] The following studies, performed by Nam et al,[178,179] revealed the mechanism of chiral overgrowth on cubic and octahedral Au seeds using enantiomers of amino acids and peptides, e.g. cysteine (Figure 3.3b). In more detail, the chiral growth can be explained by the formation of high-order facets, e.g., {321} at kink sites of the Au seed. The {321} facets can exist in the R (clockwise rotation, $(321)^R$) or S (anticlockwise rotation, $(321)^S$) conformations, defined by the rotational direction of the low-index planes (or microfacets) (100), (110) and (111), as represented in the Figure 3.4(a,b).[178] The type of R or S rotation is defined by the type of chiral inducer, used during the synthesis: D-cysteine molecules more likely adsorb on the right-handed $\{321\}^R$, rather than on the left-handed $\{321\}^S$ facets, which hinders the crystal growth of right-handed $\{321\}^R$, therefore resulting in the 4-fold left-handed symmetry, confined by $\{321\}^S$ facets.[178] the optimization of synthesis enabled to produce more homogeneous chiral helicoids with 432 point symmetry and improved g-factor of 0.3.[179] The study of the polarization-dependent photothermal characteristics of these structures revealed that when circularly polarized laser illumination was applied, the temperature of a chiral helicoid nanoparticle (grown in the presence of L-glutathione) exhibited a higher increase under right-polarized irradiation compared to left-polarized irradiation.[180] Starting from chiral helicoid gold NPs, K. Nam's group further developed similar structures with a rhombic dodecahedral morphology using cysteine[181] and a cube shape with protruding chiral

wings using dipeptides (γ-glutamylcysteine and cysteinylglycine).[182] In another work, N. Kotov and colleagues reported enhanced optical asymmetry properties, i.e. g-factors that reached values as high as 0.42 and 0.44 for chiral triangle-like Au particles synthesized using cysteine–phenylalanine dipeptides as chiral inducers under CPL irradiation (Figure 3.3c).[183]
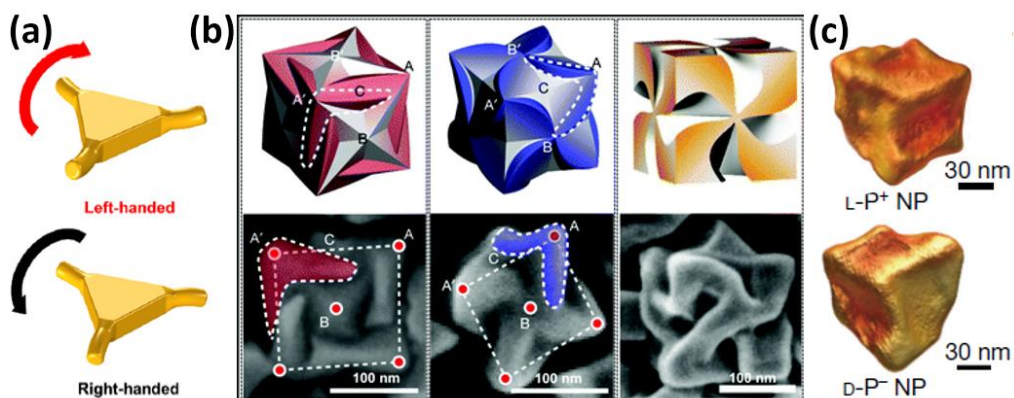
Figure 3.3 (a) Chiral Au "nanopropellers".[177] Adapted with permission from American Chemical Society (Copyright © 2020 American Chemical Society). (b) Chiral gold helicoids obtained from chiral overgrowth on cubic and octahedral seeds.[178] Reproduced with permission from Springer Nature (Copyright © 2018 Macmillan Publishers Ltd). (c) ET reconstructions of chiral triangle-like Au NPs.[183] Reproduced with permission from Springer Nature (Copyright © 2022 Springer Nature Limited).
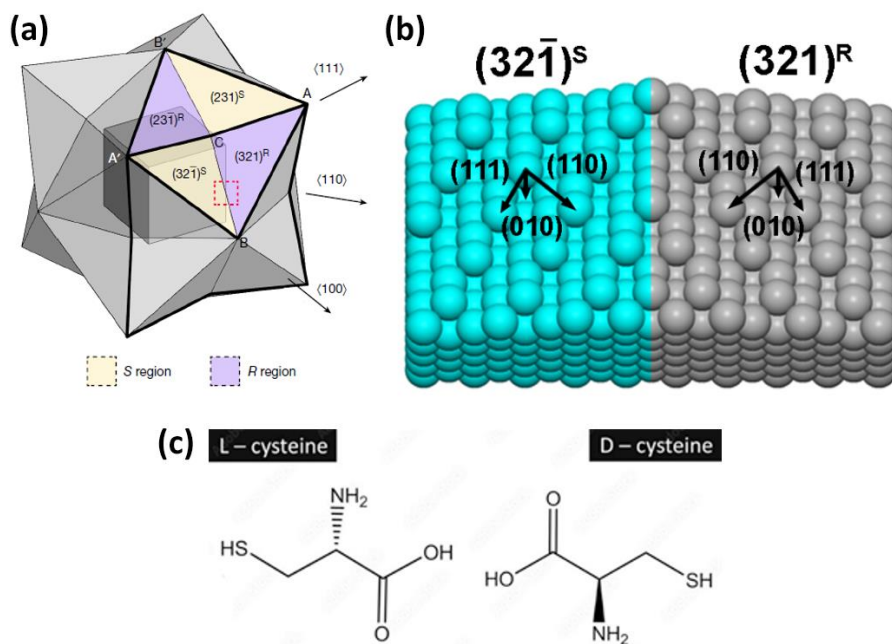
Figure 3.4 (a) Schematic of a stellated octahedron, differentiated by high-index facets consisting of {321}^{S}.[16] Reproduced with permission from Springer Nature (Copyright © 2018 Macmillan Publishers Ltd). (b) Comparison of the atomic arrangement of the (321)^R and (32-1)^S Au surfaces. (c) Schematic representation of L- and D-cysteine.

3.2 Helical CTAC-BINAMINE micelles leading to the wrinkled chiral morphology

In parallel to the use of chiral molecules selectively adsorbing on specific surface sites of NPs, another type of chiral inducer was proposed by the research group of Prof. Luis Liz-Marzán (CIC BiomaGUNE, Spain) and studied in the framework of collaboration with EMAT.[167] Namely, the ability of organic molecules with long aliphatic chains (e.g., CTAB, CTAC) to form elongated micelles in the solution at high concentration was found to be also beneficial for the chiral seeded growth. The agglomeration of CTAC and dissymmetric molecules, e.g., 1,1′-bi-2-naphthol (BINOL) or 1,1′-binaphthyl-2,2′-diamine (BINAMINE), at the relatively high concentrations leads to the formation of chiral micelles (Figure 3.5a), that can coil on the surface of Au NRs, forming quasihelical patterns (Figure 3.5b). In this manner, adsorbed micelles direct the chiral overgrowth in NRs with pronounced morphological handedness, where sharp Au

wrinkles can only grow in between the adsorbed micelles (Figure 3.5b,c).[167] The CD spectra of the resulting NRs demonstrate chiral plasmon modes with high g-factors (~0.20).[167] It is worth noting that the g-factor values obtained are higher compared to those associated with "twisted" nanoparticles (as illustrated in Figure 3.3b,c)[181,183]. Additionally, the process of micelle-mediated chiral growth offers the enhanced flexibility in synthetic parameters (e.g., the choice of chiral surfactant, the size and aspect ratio of the Au seeds).[167] This flexibility enables the adjustment of surface wrinkle sizes and, consequently, the control of g-factor values in the resulting chiral NPs.[167]
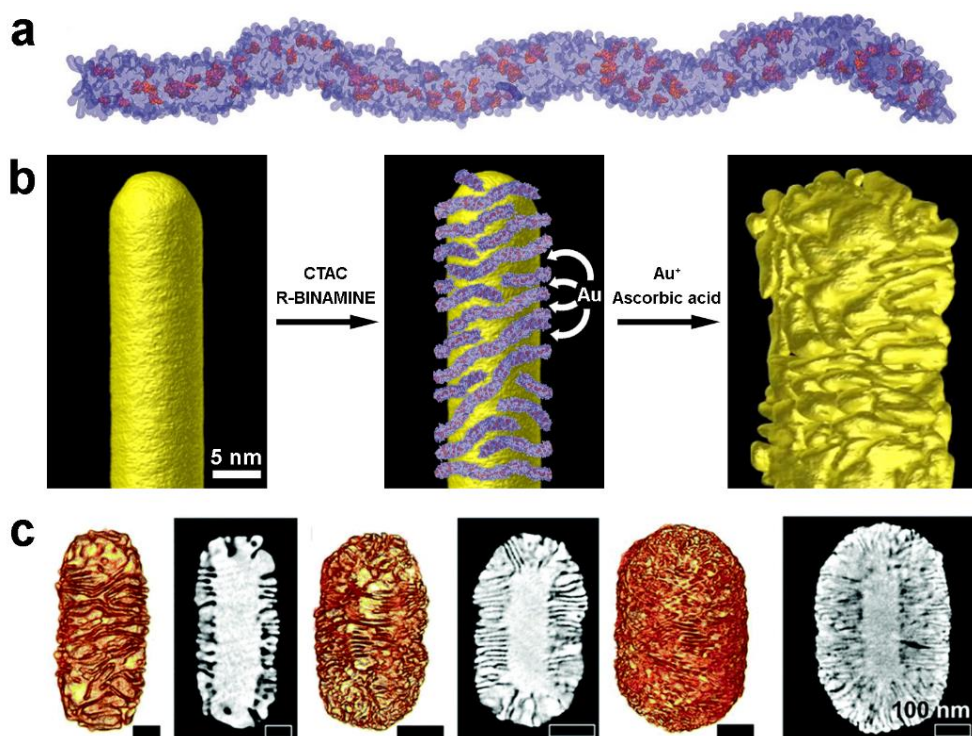
Figure 3.5 (a) Chiral CTAC-BINOL micelle. (b) Schematic representation of the micelle-mediated chiral growth of Au NPs from achiral rod-like Au seed. (C) ET visualization of wrinkled Au NPs of different dimensions.[167] Adapted under the terms of the Science Journals Default License (Copyright © 2020 American Association for the Advancement of Science).

3.3 Quantitative chirality analysis based on electron tomography

To investigate chiral NPs, traditional techniques such as CD spectroscopy provide valuable information about their chiroptical properties (see **Section 1.2**) but lack structural information due to ensemble averaging.[184] Scanning electron microscopy (SEM) can offer surface morphology information, but its resolution is typically insufficient ($\geq$1 nm) for analyzing nm-sized chiral features or atomic-level structural details (Figure 3.6a).[185] On the other hand, 2D STEM imaging can provide spatial resolution up to 50 pm, enabling structural characterization of sub-nm sized structures (Figure 3.6b). However, in case of highly asymmetric chiral NPs, single 2D projection of the studied object can be misleading (Figure 2.2). In such cases, 3D information retrieved from HAADF-STEM tomography can be explicitly used for the analysis of the chirality of individual NPs (Figure 3.6c). It should be noted, that even qualitative analysis of chirality is not straightforward based only on visual analysis of obtained 3D reconstructions, where the strong bias can be introduced due to the high irregularity of the surface features. Thus, dedicated quantification methods should be introduced to enable an accurate analysis of the chirality.
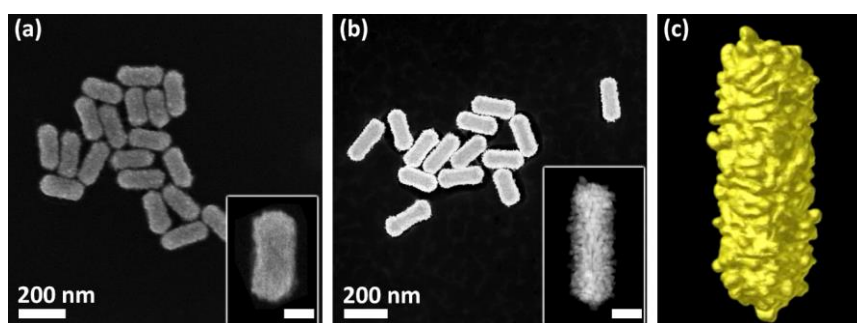
Figure 3.6 (a) SEM image of chiral Au NPs, estimated spatial resolution is approximately 4 nm. Courtesy of E. Vlasov and W. Heyvaert, EMAT. (b) HAADF-STEM image, taken at the same magnification with the spatial resolution of ~50 pm. Insets in (a,b) shows the magnified Au NPs to highlight the difference in spatial resolution between SEM and STEM. Scalebars in the insets are 50 nm. (c) The visualization of 3D reconstruction of the Au NP shown in the inset in (b).

In addition to providing only the input data for electromagnetic modeling of the optical properties described in **Section 2.5.5**, the volumetric nature of ET information can be used independently to conduct geometric analyses of the chirality of individual nanoparticles. For instance, the Hausdorff chirality measure quantifies the chirality of a geometric representation of an object by measuring the degree of coincidence of the object with its mirror image.[186,187] It is based on minimizing the "Hausdorff distance" between the object and its mirror image, where an object is represented by a set of points in 3D space.[186] The chirality measure is defined as the ratio between the minimum Hausdorff distance and the diameter of the set of points. While this method proves effective for quantitatively asessing the chirality of spherical assemblies of Au NPs,[188] it encounters limitations for relatively complex shapes. These limitations are primarily related to the extensive computational time required and the inability to differentiate between left- and right-handed chirality in intricate structures. Therefore, there is a pressing need for alternative techniques that can facilitate both qualitative and quantitative analyses of intricate chiral structures.

Inspired by diffraction investigations performed on DNA molecules, single-walled carbon nanotubes (SWNT) and twisted Cu nanowires, where the X-shaped patterns related to the helical arrangement of (surface) features in reciprocal space were observed,[189–191] 3D FFT on the reconstructions of the wrinkled NPs (Figure 3.7a) were calculated. Indeed, X-shaped patterns were obtained (Figure 3.7b). The spots in reciprocal space were linked to the corresponding features in real space by manually segmenting the 3D FFT to minimize noise (Figure 3.7c). [167] When overlaying the inverse FFT with the original reconstruction the helical features were visually highlighted.[167] Although this method does not provide a quantitative value, it provides a qualitative approach to evaluate the presence of chiral features.
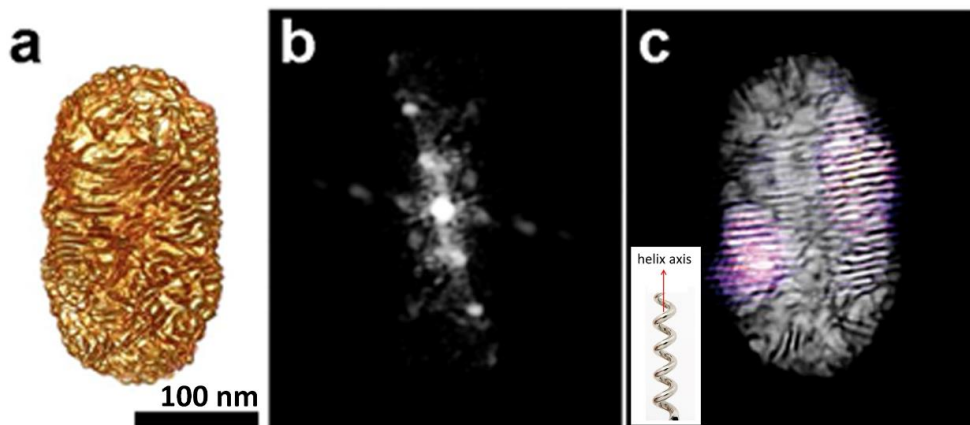
Figure 3.7 (a) Tomography reconstruction of a Au NP grown in an (R)-BINAMINE-CTAC mixture, (b) 3D FFT pattern from which the inverse FFT was computed after segmentation, (c) Inverse FFT showing the areas of the particle with chiral features (pink) overlapped with the projection of the tomography, indicating a right-handed angle. The inset shows an example of right-handed helix.[167] Adapted under the terms of the Science Journals Default License (Copyright © 2020 American Association for the Advancement of Science).

To achieve the quantitative helicity analysis of chiral NPs, a methodology based on the geometrical properties of a helix was developed at EMAT.[192] The basis of this method is strongly connected to the properties of a helix, corresponding to a central axis (z), the distance ρ between the helix and its central axis, and the angle of inclination α (Figure 3.8a). By considering a helical shape as a composition of individual helices having the same helical axis, the quantification of helicity simplifies to detecting the sum of helices. Therefore, the analysis of the 3D reconstructions is initiated by the assignment of the helical axis that should pass through the center of mass of the studied NP. The described method suits better for elongated NPs, the helical axis is considered to be parallel to their longitudinal symmetry axis. After the central axis is found, a cylindrical coordinate system can be used, where helices around the z axis correspond to straight lines. The converting of a discrete voxel grid of an ET reconstruction from Cartesian (Figure 3.8b) to cylindrical coordinates (Figure 3.8c) enables the investigation of separate concentric cylindrical 2D sections at constant ρ (red voxels, Figure 3.8c).[192]
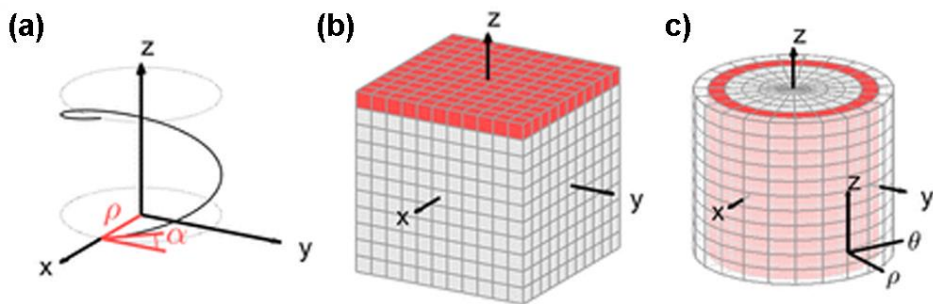
Figure 3.8 (a) A helix around the z-axis with radius ρ and inclination angle α; (b) a discrete voxel grid in Cartesian coordinates; and (c) a discrete voxel grid in cylindrical coordinates.[192] Image is adapted from open access article distributed under the terms of the Creative Commons CC BY license (Copyright © 2022 American Chemical Society).

In other words, an ET reconstruction of an elongated helical NP, can be "unwrapped" into cylindrical sections with certain distances (ρ) from the central axis (z), where each section can be considered as a sum of straight lines with certain inclination angles (α). As can be seen in case of a 3D model of a rod with a right-handed helical shell shown in Figure 3.9a, the preferred orientation of diagonal lines can be plotted and computed for different cylindrical sections through the model and further recombined into a 2D histogram (Figure 3.9b), which represents the radial spread and inclination degree of right- and left handed features (red and blue peaks). Figure 3.10c represents the helicity analysis of a ET reconstruction of the wrinkled chiral Au NP, where the interpretation of the directionally is more challenging due to the complex distribution of right- and left-handed features. To ensure an objective interpretation, the helicity function $H(\rho,\alpha)$ can be introduced as the difference between right- and left-handed bins in the directionality $D(\rho,\alpha)$:

$$H(\rho, \alpha) = D(\rho, \alpha) - D(\rho, -\alpha) \tag{3.1}$$

for $\alpha \in [0°, 90°]$. The total helicity parameter can be obtained by calculating the integral of the helicity function that can be useful to compare the degree of helicity for different NPs:

$$H_{total} = \sum_\rho \sum_\alpha H(\rho, \alpha) \Delta\rho \Delta\alpha \tag{3.2}$$

with $H_{total} \in [-1,1]$ due to the normalization of the directionality. By obtaining a positive value of H_{total}, the more abundant presence of right-handed features in the morphology of the studied NP can be quantitatively determined (Figure 3.9c). Thus, combination of the ET tomography of chiral NPs with the helicity analysis has proven itself to be a viable approach for the quantitative analysis of chiroptical properties.
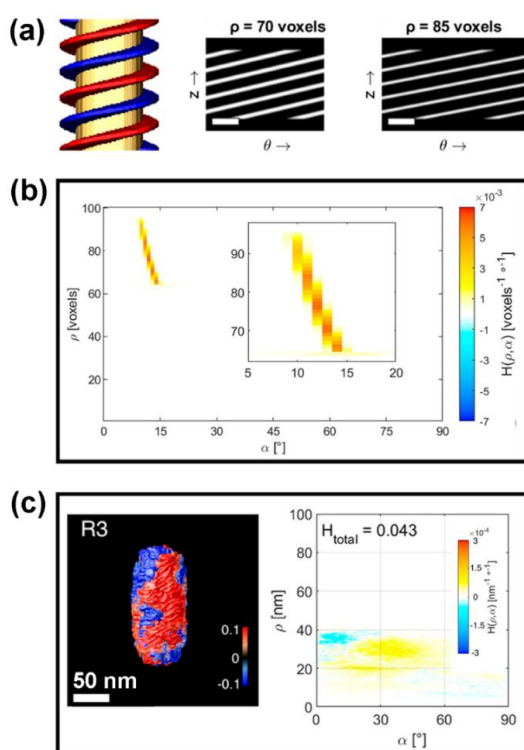
Figure 3.9 (a) A simulated helix with two of its cylindrical sections at $\rho = 70$ voxels and $\rho = 85$ voxels. The scale bars are 100 voxels wide. (b) Helicity function $H(\rho,\alpha)$ histogram and zoomed view (inset) of the peak corresponding to the helical shell of the model. (c) 3D color-coded volume renderings of the helicity maps for the chiral Au NP along with a plot of the corresponding helicity function $H(\rho,\alpha)$. The positive H_{total} value is also indicated. Red indicates right-handed helical features, blue indicates left-handedness.[192] Image is adapted from open access article distributed under the terms of the Creative Commons CC BY license (Copyright © 2022 American Chemical Society).

3.4 Facet specific adsorption of chiral surfactants leading to chiral growth

Despite the significant progress in the wet chemical synthesis of various chiral NPs and the quantitative analysis of their morphology and chiroptical properties, several questions on the growth mechanisms remain open. To be specific, a deeper understanding of the formation of twisted shapes is needed, especially the analysis of the intermediate stages and the influence of the seed faceting on the formation of specific chiral facets. For instance, in addition to the formation $\{321\}^R$ or $\{32\text{-}1\}^S$ chiral facets,[178] the synthesis of chiral trisoctahedral Au NPs was reported, where the presence of L- of D-cysteine enantiomers leads to the formation of $\{15\ \text{-}5\ 8\}^R$ or $\{\text{-}8\ 5\ 12\}^S$ chiral facets.[193] Based on these results, the conclusion regarding the potential diversity of $\{hkl\}$ chiral facets (where $h{\neq}k{\neq}l{\neq}0$) can be made, theoretically leading to a range of possible twisted morphologies. Additionally, the growth mechanism of micelle mediated growth of wrinkled NPs should be examined in more detail, e.g., the influence of the surface faceting of Au seeds on the adsorption of chiral micelles (e.g., BINAMIME-CTAC). Hereby, a thorough structural analysis of chiral seed-mediated growth should be further performed, which would allow for finer control over the chiroptical properties of both twisted and wrinkled systems.

The morphology of symmetric achiral NPs has been studied extensively, where the conclusions of the surface faceting can be made based on SEM or 2D HAADF-STEM images (Figure 3.10), where the atomic resolution and zone axis imaging may not be even necessary.[194–197] In contrast, the complex morphology of the intermediate products and final chiral NPs hinders the studies of the surface evolution during the chiral growth, due to, e.g., high curvature or irregularity of the surface.
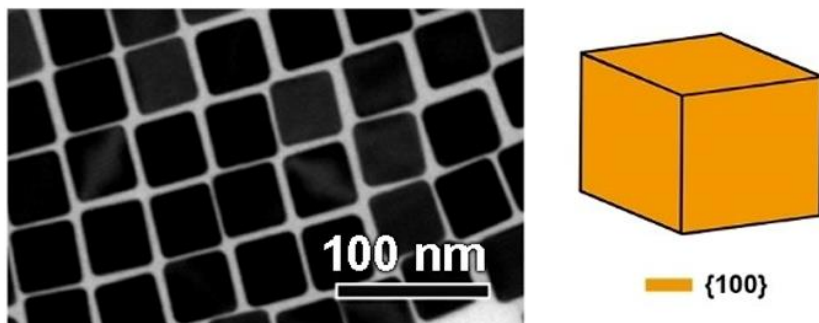
Figure 3.10 HAADF-STEM image of cubic Au NPs along with the proposed model, confined between six {100} facets.[197] Adapted with permission from Nano Letters (Copyright © 2018 American Chemical Society).

Given the highly asymmetric morphology of the studied Au NPs, where the reliable 3D information of sub-nm features or high-index faceting is required, advanced ET techniques should be implemented. In the next section I will describe several tomography approaches, that can provide us with the required information. For instance, intermediate structures obtained during the chiral growth can be examined in order to reveal the surface faceting of Au seeds and, thus, to make reliable conclusions on the interaction of the different facets with molecules of surfactant.

3.5 Atomic resolution electron tomography

In scenarios where a thorough investigation of sub-nm sized features or high-index surface facets is necessary, conventional ET techniques may fall short in providing satisfactory results. To overcome these limitations, it becomes imperative to enhance the quality of 3D reconstructions to attain atomic resolution. Remarkable progress has already been made in this area, with significant advancements achieved in pushing the resolution of 3D reconstructions to a level that allows for detailed insights into the atomic arrangement and structural characteristics of nanomaterials.[198]

One example of investigation of the characterisation of the atomic structure in 3D is a methodology capable of retrieving atomic positions using a limited number of high-

resolution HAADF-STEM images along the main crystallographic zone axis, using compressed sensing (Figure 3.11a).[64] To obtain several in zone axis projections of a particle, a dual-axis tomography holder can be used, enabling the precise planar rotation of an in-zone axis NP so that one of its principal crystallographic directions coincides with the α rotation axis, that can be performed in ±75° range with maintained microscope resolution and specimen visibility (Figure 3.12). The in-zone axis projections of a NP collected in this manner can further serve as an input for compressed sensing reconstruction. This approach allows us to obtain more reliable atomic-scale reconstruction by exploiting the sparsity of the object (and its 3D reconstruction) as prior knowledge, assuming that only a limited number of voxels contain an atom and most voxels correspond to vacuum. This technique is particularly advantageous for nanostructures sensitive to the electron beam, as the number of atomic-resolution projection images required for obtaining the 3D atomic structure is minimal. Furthermore, without assuming the positions of the atoms during tomographic reconstruction, this technique enabled the investigation of strain in the atomic lattice in Au NR through the extension of Geometrical Phase Analysis (GPA) to 3D.[64] However, acquiring a complete tomographic series at lower magnifications was still necessary to provide prior information on the morphology of the object. This step can be challenging for extremely beam-sensitive nanostructures, but advanced acquisition schemes such as fast tomography[62] and TEM tomography[199] can be advantageous for obtaining the required prior information.

Another methodology has been utilized to retrieve the 3D atomic structure of a gold nanodecahedron (Figure 3.11b).[66] In this case, atomic 3D reconstruction was obtained from a continuous tilt series of high-resolution images, assuming that the atomic potential could be modelled with 3D Gaussian spheres.[66] Consequently, the coordinates of each atom in the object were directly retrieved along with the 3D atomic structure, enabling the determination of 3D displacement maps for strain analysis. This technique does not make assumptions about the crystal lattice of the object under investigation but involves higher computational costs and complexity.
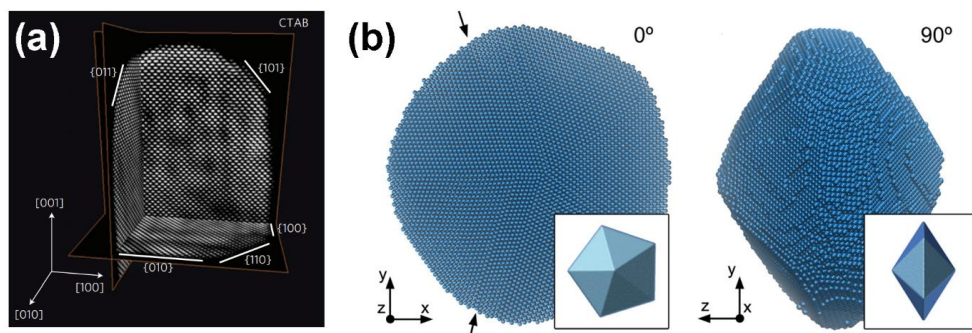
Figure 3.11 (a) Orthoslices through the 3D reconstruction of Au NP.[64] Reproduced with permission from Springer Nature (Copyright © 2012, Springer Nature Limited). (b) Front and side view of the 3D reconstruction of PT Au NP.[66] Image is adapted from open access article distributed under the terms of the Creative Commons CC BY license (Copyright © 2015 American Chemical Society).
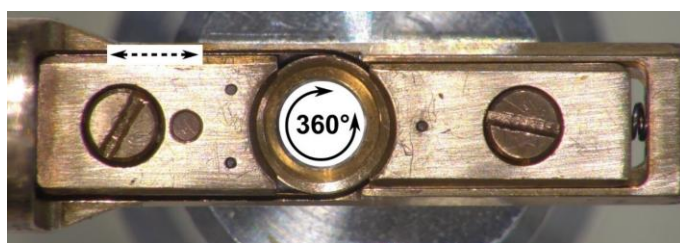
Figure 3.12 Fischione 2040 dual-axis tomography holder. Dashed arrow represents the wire that drives the 360° planar rotation of the grid (black solid arrow), maintaining the eccentricity and maximizing the specimen visibility.

Additionally, for nanomaterials with unknown defects, determining prior information can be challenging. Consequently, state-of-the-art atomic-level ET techniques cannot be routinely applied to characterize nanomaterials containing unknown structural defects. Supported by a Convolutional Neural Network (CNN)-based methodology developed at EMAT,[200] the quality of data can be augmented, providing the better input (e.g., SNR) for the following reconstruction. This 12-layered CNN is trained using several HAADF-STEM images with and without known distortions, which allows one to minimize the effects of e.g. scanning distortions, x/y jitter, dead pixels, saturation

70

account and thermal noise.[200] In experimental data, scanning distortions are typically the most profound distortions that are highly correlated along a fast-scan row, but far more varying between rows (in the slow-scan direction).[201] These distortions become worse with slower scans (longer total frame time) or faster stage drift.[201] To avoid this limitation and to ensure that the image distortions are sufficiently isotropic and unbiased repeated fast imaging is preferred over fewer slow frames.[200,201] Lower SNR of individual fast-scanning images in this case can be compensated by acquiring multiple consecutive images, followed by averaging between the acquired images based on rigid[202] or non-rigid registration.[201] To illustrate the effect of the image restoration using the described CNN, Figure 3.13 shows a single HAADF-STEM frame before and after the image restoration. It is essential to note that the utilization of neural networks in image restoration can potentially introduce artifacts. Therefore, careful analysis is necessary to prevent such artifacts from being introduced. A comprehensive comparison in high-resolution ET tomography between reconstructions obtained from raw and restored projections is advisable to ensure, for instance, that no atoms were introduced or lost during the restoration procedure.
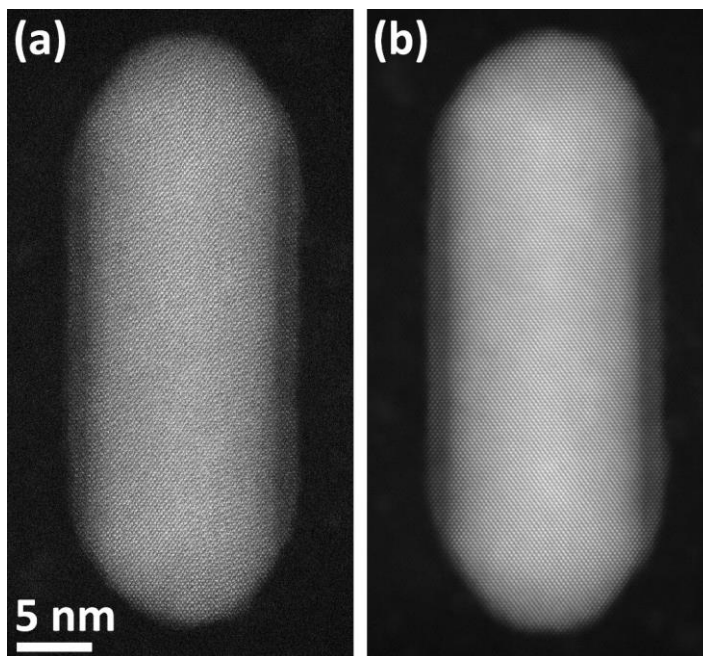
Figure 3.13 High resolution HAADF-STEM image of the Au@Ag NR (a) before and (b) after the image restoration through the CNN.

In the process of data alignment, the first step involves aligning the individual projections using cross-correlation method as described before. Following this, the alignment of the tilt axis is carried out using a specific approach: a reconstruction is created, and forward projections are calculated based on it. The next step involves computing the reprojection error, which is the mean square error between the acquired images and the corresponding forward projections. This process is repeated for various horizontal tilt axis offsets, and the offset yielding the lowest error is selected as the optimal alignment. Additionally, similar steps are taken for the rotation of the tilt axis, which involves collective in-plane rotations of the images. After the tilt series are aligned, atomic resolution 3D reconstruction is carried out using a conventional SIRT algorithm. Additionally, constraints are imposed on the grey levels in both real and reciprocal spaces within the acquired 3D volume resulting from each SIRT iteration.[203,204] Following this, to prevent alterations to the values of individual voxels during Fourier space filtering, a normalization step is executed, utilizing one projection image as a reference. This approach enabled the atomic structure of nanomaterials to be obtained without any prior knowledge of the material's structure.[200] The schematic representation of this technique is shown in Figure 3.14. An additional advantage of this technique is that the acquisition of zone axis projections is not necessary to provide the reconstruction of sufficient quality. Although the presence of precisely oriented zone-axis images increases the quality of the reconstruction, near-zone axis projections are likely to be found and acquired in typical tilting range of ±75°, that can ensure the atomic resolution in the resulting 3D reconstruction.
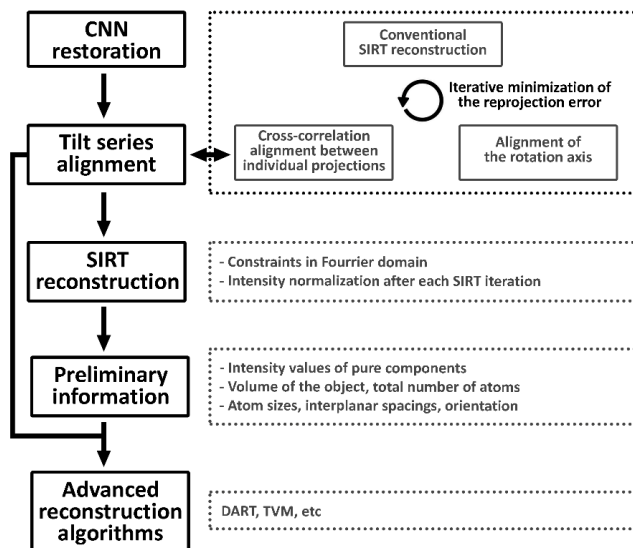
Figure 3.14 The schematic of atomic resolution 3D reconstruction algorithm.

Special attention must be paid during the selection of the experimental parameters during high resolution HAADF-STEM tomography acquisition. To ensure the collection of projections revealing atomic features, the highest feasible resolution and sufficient magnification (≥1Mx) should be employed for image registration. However, it is essential to consider that at high magnifications, the field of view is limited by the number of pixels in each image. For example, the Thermo Fisher Scientific Themis Z electron microscope at 1.8 Mx magnification can only capture a region of 52-by-52 nm (2048x2048 pixels). Consequently, the study of NPs larger than a certain size may become unfeasible via atomic resolution tomography. In such cases, one may be limited to studying only specific parts of larger particles, such as the tips of elongated NPs, or alternatively, larger image sizes can be employed (e.g., 4096x4096 pixels). In addition, it is crucial to consider the focal depth of the convergent electron beam to ensure that the entire thickness of the studied particle remains in optimal focus. The focal depth (in nm) of the convergent electron beam in HAADF-STEM is described by the following equation:

$$Focal\ depth = 1.77 * \frac{\lambda}{\alpha^2}$$ (3.3),

where λ represents the wavelength of the incident electron beam measured in pm, and α denotes the convergent semi-angle of the incident electron beam given in mrad.[205] For instance, for an accelerating voltage of 300 kV and a convergent semi-angle of 20 mrad, the depth of focus would be approximately 8.7 nm, setting the limit for the maximum thickness of the NPs that can be studied effectively.

To achieve a reliable (atomic) reconstruction, all the factors mentioned earlier should be carefully considered, in addition to the stability of the NP under electron beam exposure. To validate whether the NP remains intact and does not experience degradation or alterations in orientation during the tilt series acquisition, it is essential to acquire images both before and after the ET experiment (for more detail see Section 6.2). This practice allows for the observation of any potential morphological changes that might have occurred during the course of the experiment. By comparing pre- and post-ET images, a researcher can ascertain the structural stability of the NP and make credible conclusions regarding the reliability of the reconstruction.

In this work, I employed atomic resolution tomography to investigate the high index facets of intermediate Au chiral NPs, revealing facet-dependent adsorption of cysteine molecules on the surface of Au seed. These results will be explained in more detail in **Chapter 4**. In addition, the CNN-assisted reconstruction method also allowed me to visualise the ~2 nm thin Pd layer between the seed (core) and helical features within the wrinkled Au NPs, described in **Chapter 5**.

3.6 Combined HAADF-STEM and ED tomography

In cases where the studied particle size is relatively large, high-magnification studies of the entire particle or its part at atomic resolution might not be feasible. To be more specific, when the dimensions of the studied (chiral) NP exceed 20 nm, the typical focal depth and field of view are not sufficient for capturing tilt series data at atomic resolution. This situation commonly arises in the production of highly asymmetric chiral nanoparticles, where the size or thickness of the specimen can extend up to 100 nm.[167,181] In such situations, possessing knowledge of the true crystallographic orientation of the

3D object becomes crucial, as it allows for precise rotations to specific angles where structural features can be clearly attributed to particular facets or orientations. In such situations, a combination of conventional ET with electron diffraction tomography (3D-ED) can be employed. This approach provides information on surface features (facets) and crystallography simultaneously, enabling the investigation of initial, intermediate, and final structures of different NPs synthesized under various conditions.

With 3D-ED the 3D reciprocal space of a single crystal is reconstructed by tilting the crystal along one axis using an equidistant small step size (e.g. 1°) and acquiring an off-zone diffraction pattern at every step (Figure 3.15).[206,207] The position and amplitude of each reflection in this 3D reciprocal space is extracted and used for crystal structure and crystallographic directions determination. At every step, it should be checked if the same area of interest is illuminated to get only information of the same area. Reconstructions of obtained tilt series are performed in Pets2.0 software, that allows one to routinely perform step-by-step 3D ED reconstruction, where such steps as peak positions determination, refinement of the rotation axis, extractions of intensities can be performed automatically.[68]
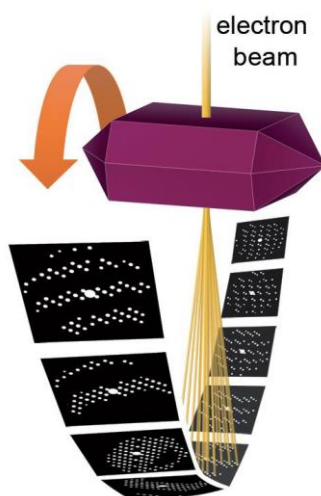
Figure 3.15 Schematics of the principle of electron diffraction tomography.[208] Reproduced with permission from the American Chemical Society (Copyright © 2018 American Chemical Society).

In this thesis, I implement the combination of ET and electron diffraction tomography to study the complex surface of the chiral Au NPs. More precisely, the ability to rotate the studied particle precisely along certain crystallographic directions allowed me to draw conclusions on the high-order surface faceting of the Au seeds during chiral overgrowth and therefore, to confirm the facet-dependent adsorption of chiral inducing surfactants. The insights gained in this manner contribute to a deeper understanding of the mechanisms involved in chiral growth and will be described in **Chapter 6** in more detail. In addition, I will provide the technical details of combined ET and 3D-ED methodology.

3.7 Different conventions for determining the handedness and types of chirality

Given the different conventions, used in the field of chirality studies, great care should be taken when working with dissymmetric systems. For example, the opposite handedness values of the circularly polarized light can be assigned by using two opposite conventions: from the point of view of the source (typically used in engineering community)[209] and from the point of view of the receiver (used in IUPAC).[210] Also, additional confusion may be caused by the switch between R/S (rectus and sinister, right and left) and D/L (dextro and levo, right and left). These notations correspond to absolute and relative configurations, where the chirality is determined by arrangement of different radical groups around the chiral center, since amino acids may contain different constituent element and radicals (-NH2, -COOH, $-CH_2-OH$, -H, etc). Consequently, R-cysteine correspond to the L-chirality, whereas the other R-aminoacids correspond to the D-form (except achiral molecule of glycine).

An additional potential source of confusion arises from the differences in 3D data representation among various software applications. For instance, while most 3D visualization and processing applications (such as Amira, Blender, Microsoft Paint 3D, CAD) adopt the (x, y, z) convention for datasets, 'volshow ' function used in MATLAB (a software specialized in matrix operations) employs a different convention with the y-axis flipped (x, -y, z). Consequently, performing visualization of the datasets in different

software applications can introduce the errors in the analysis of the handedness of the studied object (Figure 3.16). To ensure reliable 3D reconstructions, great care should be taken to verify that data are not flipped at any stage of ET reconstruction. Initially, HAADF-STEM projections should accurately correspond to the actual position and shape of the studied objects, which can be assessed using an asymmetric grid. Figure 3.17 demonstrates that the top view onto the grid matches the HAADF-STEM image obtained from the same grid. Given the potential sources of confusion, it is crucial to meticulously verify the ET results and conventions used at each stage of the reconstruction, especially when providing the 3D reconstruction as an output for electromagnetic modeling of optical properties, for instance.
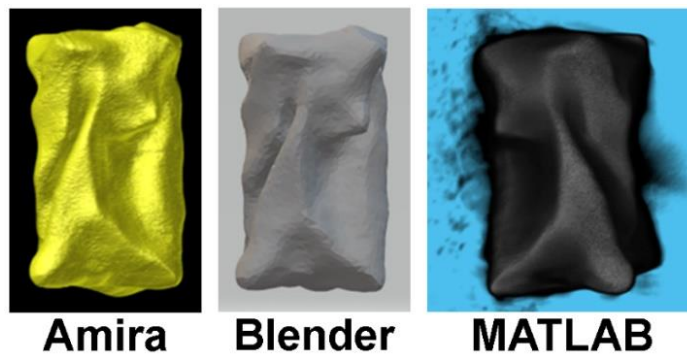
Figure 3.16 The representation of the ET reconstruction in different software applications. It should be noted that MATLAB software shows the opposite handedness to other programs.
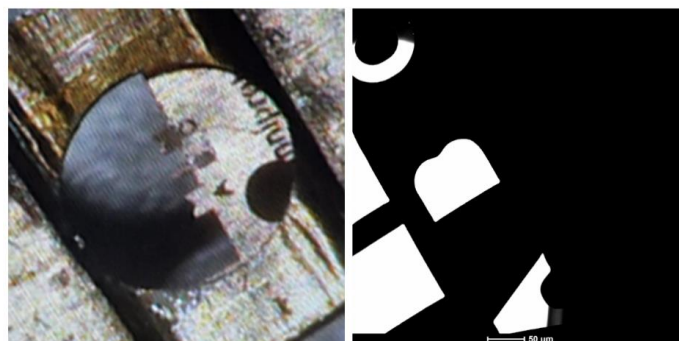
Figure 3.17 The top view onto the lamella grid made in light microscope (left panel) and in STEM (right panel).

Chapter 4. Mechanisms of cysteine mediated chiral growth on single-crystalline and pentatwinned Au seeds

This chapter is based on:

Synthesis of the samples was carried out at CIC BiomaGUNE in Donostia-San Sebastián, Spain; at the University of Konstanz, Physical Chemistry Department in Konstanz, Germany; and at University of Vigo, Department of Physical Chemistry in Vigo, Spain.

Density functional theory (DFT) calculations were performed at the Institute of Chemical Research of Catalonia in Tarragona, Spain.

Electromagnetic modelling of optical properties was performed at the Department of Sustainable Energy Materials, AMOLF in Amsterdam, Netherlands and at EM3WORKS, Spin-off of the University of Vigo and the University of Extremadura, Spain.

TEM characterization was carried out at the research group for electron microscopy for materials science (EMAT) at the University of Antwerp. I was responsible for all TEM acquisition, ET reconstructions and analysis. Helicity analysis was performed by W. Heyvaert.

This study aimed to validate the hypothesis that various high-index facets can serve as the starting point for chiral crystal growth of Au NPs (**Sections 3.1, 3.4**). Furthermore, in contrast to previous findings involving cube-like structures,[211,212] this study was focused on rod-like structures. These rod-like structures exhibit helical features and, consequently, chiroptical properties that can be theoretically adjusted by, for example, varying the AR of the resulting chiral Au NRs. Specifically, enantiomers of cysteine (Cys) were used as a chiral inducer to generate elongated twisted Au NPs with strong chiroptical properties. Given the complex resulting morphology, HAADF-STEM tomography was essential for examining the morphology of the synthesized chiral NPs and confirming their helical structure. Moreover, a thorough investigation into the mechanism of chiral growth was carried out. To be more precise, the proposed facet-dependent adsorption of chiral inducer molecules was substantiated through meticulous analysis of the initial and intermediate Au structures formed during the synthesis. This analysis was made possible by implementing atomic resolution ET, which provided insights into the formation of {520} facets during the cysteine-assisted chiral growth of elongated SC Au NPs. These {520} facets can subsequently serve as the starting point for the formation of {521} chiral facets. The results obtained from atomic resolution ET were further corroborated by DFT calculations, demonstrating the preferential adsorption of cysteine on the {520} facets rather than on low-index achiral facets.

4.1 Synthesis of fourfold twisted Au nanoparticles

Inspired by the dissymmetric growth of cubic Au NPs,[213] the potential use of Cys as a chiral ligand to direct dissymmetric growth on pre-formed Au NRs is investigated. As described elsewhere, a single-crystalline Au NR ideally has a 4/mmm symmetry.[64,215] A similar transformation as that described in Figure 4.1a for nanocubes, can be expected to lead to twisted rodlike structures, which should have different structural features (Figure 4.1b). It should be emphasized, that during the transformation from achiral to chiral structures only rotational axis symmetry operations can remain, such as the 2-fold and 4-fold rotation axes (illustrated as C2 and C4 in Figure 4.1). Simultaneously, symmetry planes (2/m and 4/m in Figure 4.1) must vanish during the transition to chiral

structures. This is due to the inherent absence of mirror symmetry in chiral/helical structures, as discussed in **Section 1.2**.
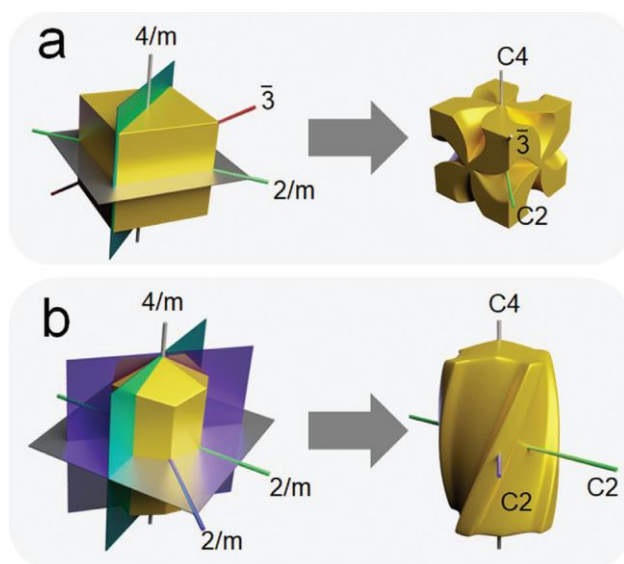
Figure 4.1 Symmetry analysis of different NP morphologies, where the main symmetry elements (rotation axes and mirror planes) are labelled. a) According to the Hermann–Mauguin notation, a cubic shape has symmetry of $\frac{4}{m}\overline{4}\frac{2}{m}$. When all mirror planes are removed, a 432 symmetry is obtained. b) The single crystal Au NR in this image (with octagonal cross-section) has a symmetry of 4/mmm. The rod axis is along the <001> direction, and therefore only C4 symmetry can be found in the primary direction. When all mirror planes are removed from the 4/mmm symmetry, a 422 symmetry may be obtained, as in the twisted rod.

The selected growth conditions in this study were similar to those typically used in the standard seed-mediated growth of Au NRs.[179] By controlling the growth parameters, NRs with a twisted morphology and high chiral optical activity were obtained. Although twisted Au NRs can be readily obtained through a single seeded-growth step, both morphological and optical chirality were significantly enhanced by implementing a multistep protocol involving repeated additions of the metal precursor in small aliquots.

The morphology could be additionally tuned through variations in Cys concentration, and growth temperature, as well as through the size and aspect ratio of the Au NR seeds.

Preliminary 2D HAADF-STEM analysis shows the formation of twisted structures upon successive $HAuCl_4$ additions in presence of L-Cys (Figure 4.2). HAADF-STEM images show an initial increase of rod width and sharpening of tip corners after the first $HAuCl_4$ additions (Figure 4.4b,c), whereas twisted structures became apparent after 5 $HAuCl_4$ additions (Figure 4.2d) and subsequent additions reinforced the twisted appearance of the obtained NPs (Figure 4.2e–g). Apparently, similar twisted structures were obtained by using D-Cys as the chiral inducer (Figure 4.3). The obtained results allows us to measure the size and AR changes, which was confirmed with Vis-NIR spectroscopy measurements of synthesized samples.

It should be noted, however, that given the complex morphology, one cannot conclude on the actual shape and, therefore, handedness of the studied particles based only on 2D HAADF-STEM images. To obtain reliable information about the 3D shape of twisted Au NPs, which can be also used as input for the analysis of chiroptical properties, ET in HAADF-STEM mode is performed (inset in Figure 4.2g). The experimental conditions for electron ET acquisition are detailed in Table 4.1. These conditions were carefully chosen to attain an optimal balance between resolution, acquisition time, electron dose, and mass-thickness contrast. Additionally, the obtained 3D information can be directly used for the helicity analysis, explained in more detail in **Section 3.5**. The helicity measurements obtained with this approach can be subsequently correlated to CD spectroscopy measurements, where opposite CD signs were obtained for the samples produced either with L or D-Cys.
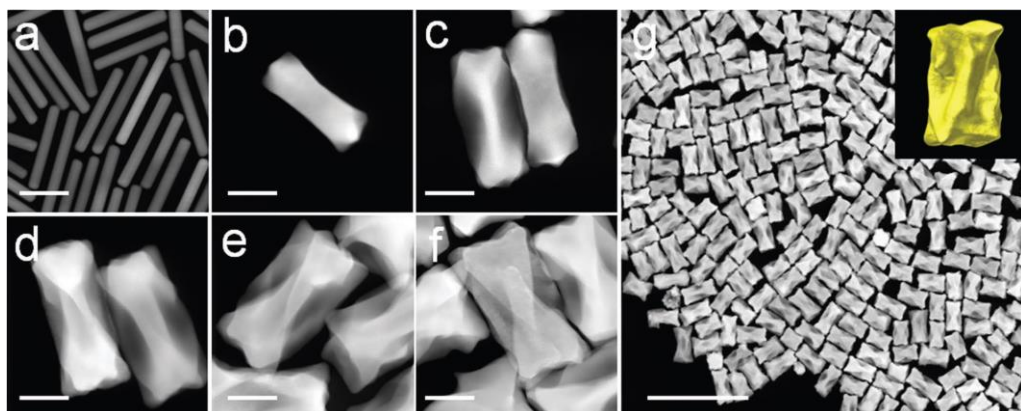
Figure 4.2 Evolution of twisted morphology during Au NR growth with an L-Cys concentration of 75 nM. a) STEM image of Au NRs used as seeds. b–f) HAADF-STEM images of the products after 1 (b), 3 (c), 5 (d), 7 (e), and 9 (f) $HAuCl_4$ additions. g) Low-magnification HAADF-STEM image of twisted Au NRs obtained after 9 $HAuCl_4$ additions. The inset shows the electron tomography reconstruction of a single chiral Au NR. Scale bars: 50 nm (a–f) and 500 nm (g).
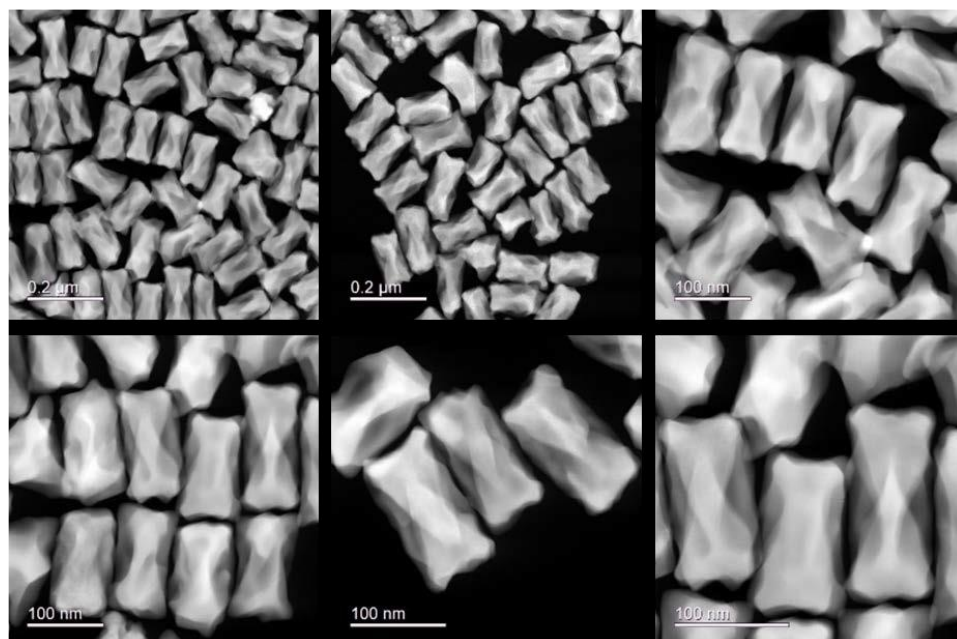
Figure 4.3 Representative STEM images, at different magnifications, of 4-fold twisted Au NRs grown using D-Cys (75 nM) as the chiral inducer.

Table 4.1 Overview of the experimental parameters used for the investigation of chiral NPs, shown in Figure 4.2g.

Sample preparation	Drop casting of the aqueous solution
TEM grids	Conventional carbon coated Cu grids
TEM	Thermo Fisher Scientific Themis Z
Voltage	300 kV
Imaging mode	HAADF-STEM (1024x1024)
Detector collection angle	50 – 200 mrad
Magnification	320 kx
Screen current	50 pA
Sample holder	Fischione 2022 tomography holder
Angular range/increment	-75° : 3° : 75° (51 projections)

The helicity analysis, described in **Section 3.3**, is employed to quantify the total helicity from electron tomography reconstructions and thereby gain insight into the chiral nature of nanoparticles (Figure 4.4).[193] As expected, the results show mainly right-handed structures, with only one exception among 10 randomly selected NRs. The helicity of these particles is described by steep helical features, as indicated by helical inclination angles between 45 and 90°. The 3D reconstructions revealed a fourfold twisted structure along the NR length (Figure 4.5), in which 4 tilted ridges are obvious. If the surface roughness is not considered, this particle can be described by an ideal model that features a 422 symmetry (Figure 4.1b). It should be noted that no helicity was observed closer than 20 nm to the helical axis, which demonstrates that the cores are not helical. Therefore, it can be concluded that the observed right-handed helicity originates from the 4 tilted ridges, ensuring the local helicity of the studied samples (i.e., helicity within each individual NPs). The 3D objects retrieved from electron tomography reconstructions are reliable models that can be used directly as the input morphologies for detailed electromagnetic simulations based on the boundary element method.[216] In this manner, the simulated g-factor plots for several tomography reconstructions

supported the hypothesis that the twisted structure is responsible for the recorded optical activity.
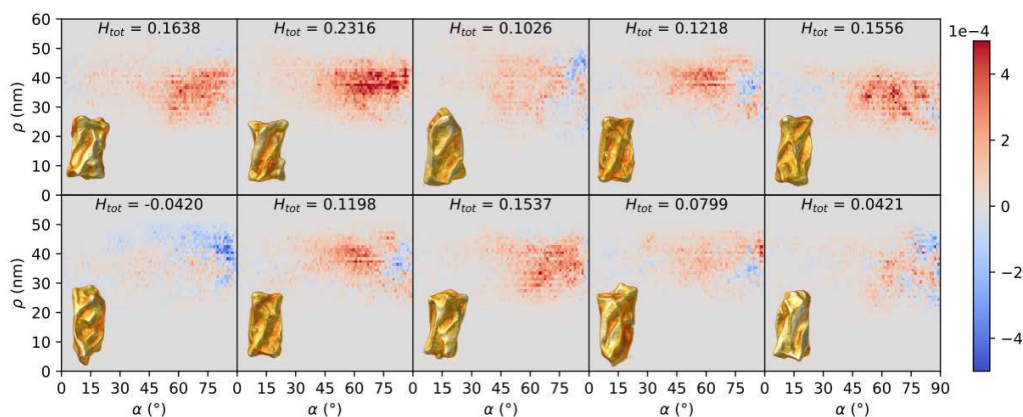
Figure 4.4 Geometrical helicity analysis of the twisted Au NP obtained with L-cysteine. The helicity function and total helicity derived from tomography reconstructions of 10 randomly selected NRs are plotted. Individual reconstructions corresponding to each result are shown as insets. The color bar indicates righthanded (red) and left-handed (blue) signals. Most particles exhibit a right-handed helical signal, with steep inclination angles α between 45° and 90°, accompanied by a positive (right-handed) total helicity H_{tot}. Only one particle was found to have negative total helicity, which can be attributed to lack of perfect uniformity in the sample.
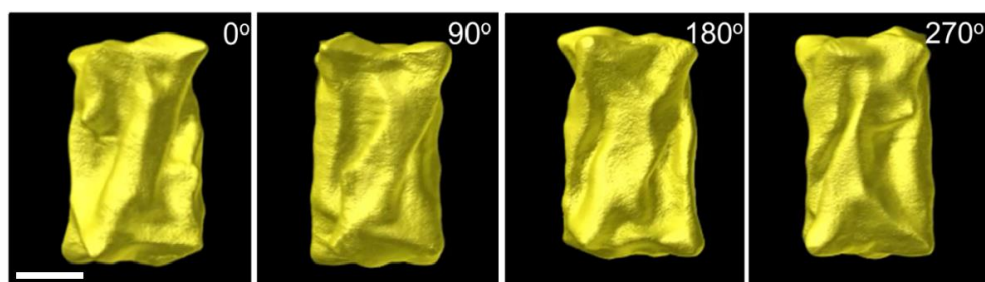
Figure 4.5 3D render of the ET reconstruction: snapshots of the twisted Au NP taken at different rotation angles (vertical axis). Scalebar is 50 nm.

Prior to the facet analysis of the intermediate stages, which could explain the mechanism of the Cys-mediated chiral growth, the crystallinity of the studied particles should be

examined. First, the absence of crystal defects should be proven to eliminate the influence of the alternative sources that could result in the observed chirality of the produced particles. For instance, the formation of spiral Au nanostructures was shown to occur due to sequentially occurring symmetry-breaking events, e.g. the formation of stacking faults (planar defects).[217] Secondly, the single-crystalline structure of the twisted NPs can serve as an additional proof that the synthesis of an individual NP proceeds through the seed-mediated growth, where the chirality cannot be caused, for instance, by specific agglomeration of several seeds or intermediate products. By acquiring the high resolution HAADF-STEM images with ronchigrams from different parts (similar to Convergence Beam Electron Diffraction, CBED) of the same particle, the single-crystalline nature of the studied particles is confirmed, where no indication of linear or planar defects was observed, as shown in Figure 4.6.
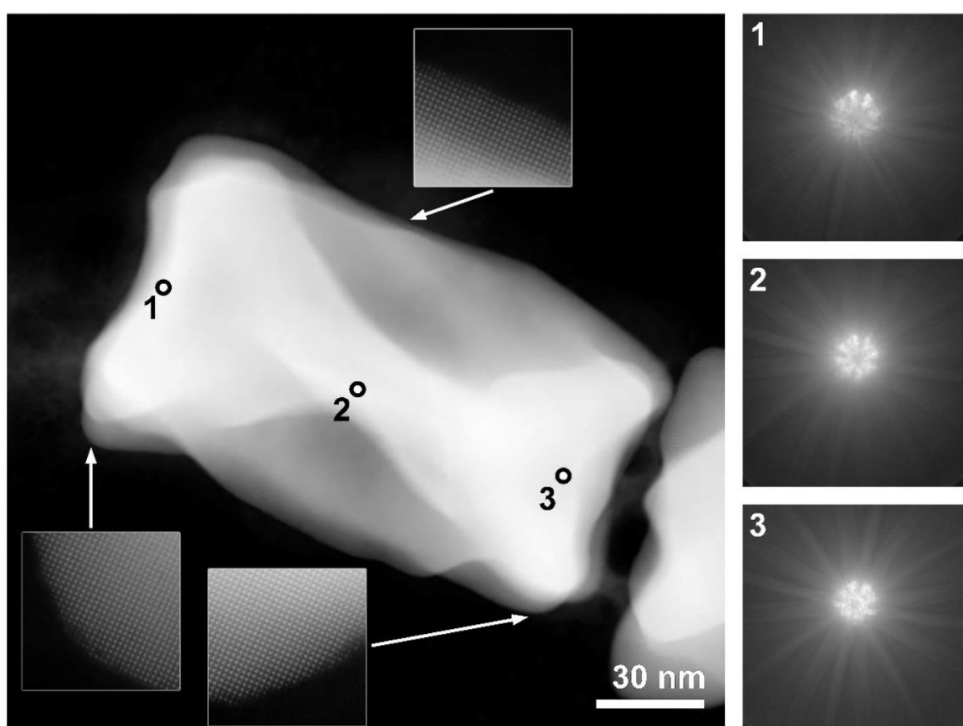
Figure 4.6 HAADF-STEM image of the twisted Au NP taken [100]. HR insets show the identical atomic arrangement at the different sides of the particle. (1-3) The ronchigrams on the right are taken from the beam positions indicated by black circles and show the identical Kikuchi pattern, corresponding to [100] zone axis.

Upon closer examination of the twisted structures formed upon successive $HAuCl_4$ additions (Figure 4.2b-d), the presence of twin boundaries within their structure becomes evident even in HAADF-STEM regime, where the contribution of strong diffraction contrast can be seen at high detector collection angles when using smaller camera lengths (Figure 4.7a-c, marked by white arrows). It is noteworthy that single and multi-step twin boundaries can occur irregularly, and they may be found at one or both tips of the chiral NPs. Additionally, it should be mentioned that the overall morphology of particles containing twin boundaries appears similar to "single-crystalline" NPs. Interestingly, the chirality of the final products of the chiral growth remains preserved even in cases where twin boundaries are not observed (Figure 4.6). From these observations, it can be inferred that the presence of twin boundaries does not significantly influence the formation of twisted structures. However, the occurrence of twins on the most densely packed {111} planes in <110> directions within the *fcc* lattice of Au[218] can be considered as evidence of fast crystal growth along the corresponding directions,[219] responsible for the formation of 4-fold spike arrangement at the both tips. Notably, within the studied samples, it was observed that certain particles exhibited one or more prominently pronounced branches, in contrast to their counterparts, which displayed comparatively smoother surface characteristics. (Figure 4.7d).
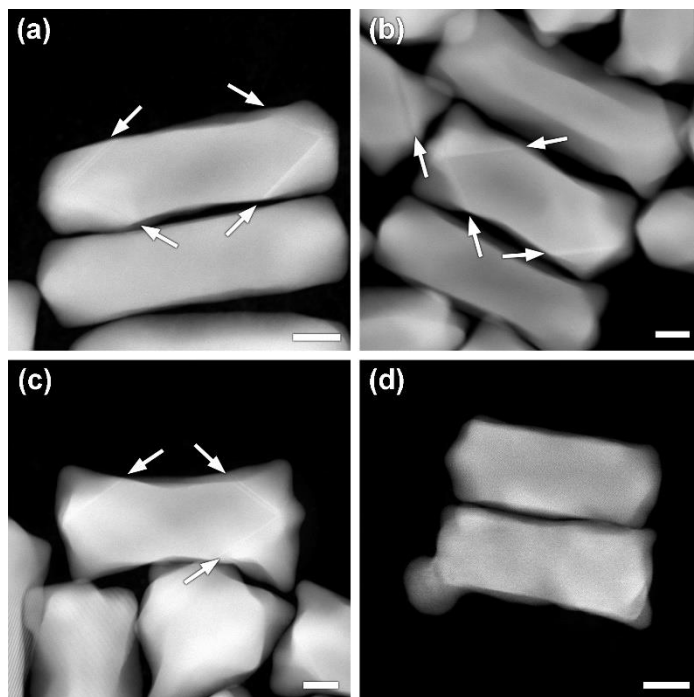
Figure 4.7 HAADF-STEM images of the products obtained during Au NR growth with an L-Cys concentration of 75 nM after 1 (a), 3 (b), 5 (c) HAuCl$_4$ additions. (d) HAADF-STEM image indicating the simultaneous presence of relatively smooth and spikey particles within the same sample (75 nM L-Cys, 1 HAuCl$_4$ addition). White arrows indicate the presence of twin defects. Scare bars are 20 nm.

To confirm whether the observed branches are grown due to the TB formation, Multimode ET (described in more detail in **Section 2.4.1**, experimental parameters are shown in Table 4.2)[220] was implemented to study the branched NP in both HAADF and LAADF regimes (Figure 4.8a,b). Indeed, the diffraction contrast corresponding to twin boundaries can be seen from LAADF-STEM projections (Figure 4.8b, white arrows). After the full tilt series were acquired in both regimes simultaneously, SIRT reconstruction was performed based on the thickness contrast, obtained from HAADF data (Figure 4.8c). The positions of TB was determined by the manual segmentation of LAADF-STEM reconstruction and shown to be in the base of branched feature at the tips and within its volume (Figure 4.8d). The provided results support the hypothesis on

the TB-induced nature of irregular branched features at the tips of the investigate NPs, that, however, are not responsible for the final chiral morphology.

Table 4.2 Overview of the experimental parameters used for the investigation of chiral Au NPs, shown in Figure 4.9.

Sample preparation	Drop casting of the aqueous solution	
TEM grids	Conventional carbon coated Cu grids	
TEM	Thermo Fisher Scientific Themis Z	
Voltage	300 kV	
Imaging mode	HAADF-STEM	LAADF-STEM
Detector collection angle	100 – 200 mrad	13 – 26 mrad
Magnification	640 kx	
Screen current	50 pA	
Sample holder	Fischione 2022 tomography holder	
Angular range/increment	-75° : 3° : 75° (51 projections)	
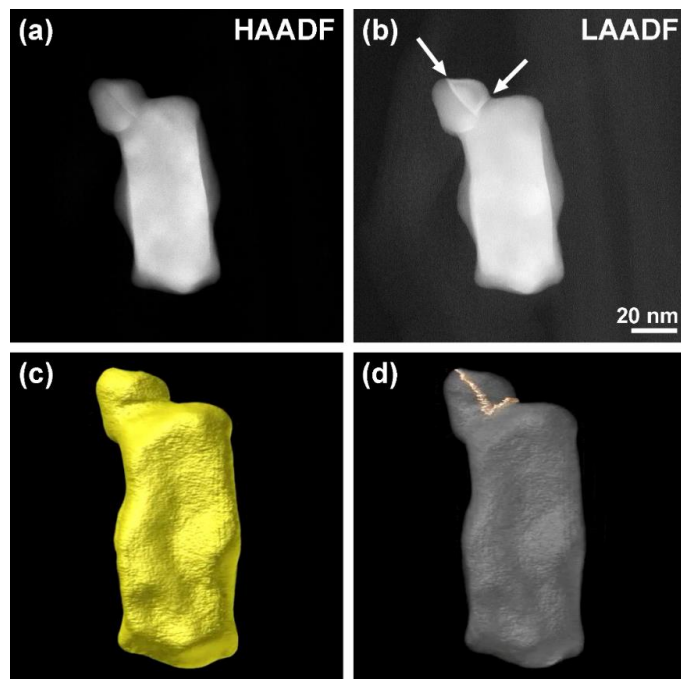
Figure 4.8 (a,b) HAADF and LAADF-STEM projections of the chiral Au NP (75 nM L-Cys, 1 HAuCl₄ addition). White arrows show the positions of TBs; (c) 3D render of the HAADF-STEM reconstruction; (d) the segmented TBs (light-yellow), obtained from 3D LAADF-STEM reconstructions superimposed with the volume shown in (c).

An additional ET analysis (same experimental conditions as in Table 4.1) was carried out for Au NPs obtained with racemic D/L-Cys mixture as the additive in the growth solution (Figure 4.9a). The resulting products also show preferential growth at tips and caves at the sides (Figure 4.9b). In addition, achiral 4/mmm symmetry is apparent from electron tomography analysis, which is consistent with noise-level circular dichroism spectra (Figure 4.9c). Based on these results, it can be concluded that using an achiral racemic D/L-Cys mixture as co-surfactant results in the achiral morphology of synthesized Au NPs (Figure 4.9d). This fact can serve as an additional indirect proof of the selective adsorption of D- and L-Cys molecules on corresponding chiral facets forming during the crystal growth and, thus, resulting in final morphologies. In the case of a racemic mixture where both enantiomers are present in equal concentrations, there is no preferential growth of either left or right-handed features.
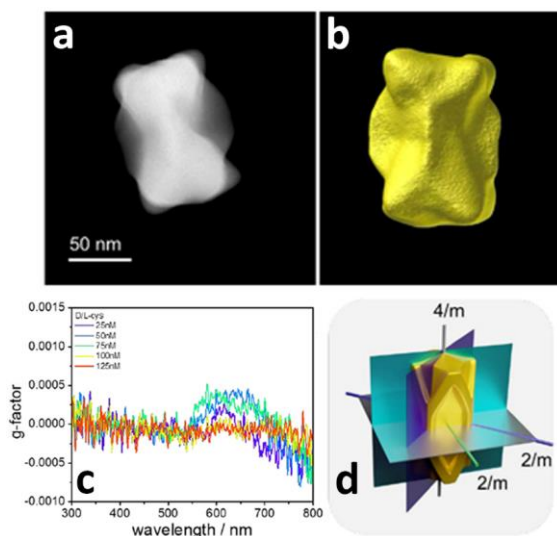
Figure 4.9 (a) HAADF-STEM image and (b) ET reconstruction of a NP obtained by the multi-step seeded-growth in the presence of a racemic mixture of D-Cys and L-Cys. (c) Optical activity (g-factor) and UV-Vis-NIR spectra for Au NRs obtained with different D/L-Cys concentrations. (d) The idealized the particle with a 4/mmm symmetry.

4.2 The mechanism of chiral growth via the structural investigation of intermediate structures

Given the expected formation of high index facets and, thus, final twisted morphology, the analysis of 2D projections or "low" resolution 3D reconstructions is not sufficient to determine the order of surface faceting. In this case, the 3D information with atomic resolution is necessary to analyse highly asymmetric arrangement of surface atoms. To obtain such information, I hereby implemented HR tomography that enables accurate determination of low and high index surface faceting of initial and intermediate Au NPs, that will be further used for the analysis of the interaction of chiral molecules with the surface of the studied NPs. Due to the relatively large particle size and complex twisted morphology of the obtained nanostructures, it is not straightforward to determine the local crystallographic nature of their surface facets. Therefore, the structures at early

stages, such as the seeds (Figure 4.2a) and the samples obtained after the first chiral growth step (Figure 4.2b), were selected for careful ET analysis.

It should be noted, that initial Au NRs undergo noticeable shape deformation after long beam exposure, which hinders the acquisition of full tomography dataset (e.g., in angular range of ±75° with 2° tilt step). Figure 4.10 exhibits a significant deformation of the Au NR following the completion of the entire ET experiment, which may be attributed to beam-induced surface diffusion of Au atoms. This deformation can potentially modify the morphology of the investigated NP, leading to unreliable conclusions regarding its surface faceting. To address this issue, alternative ET techniques based on lower electron doses were considered, as they may mitigate the observed deformation and provide more accurate surface information.
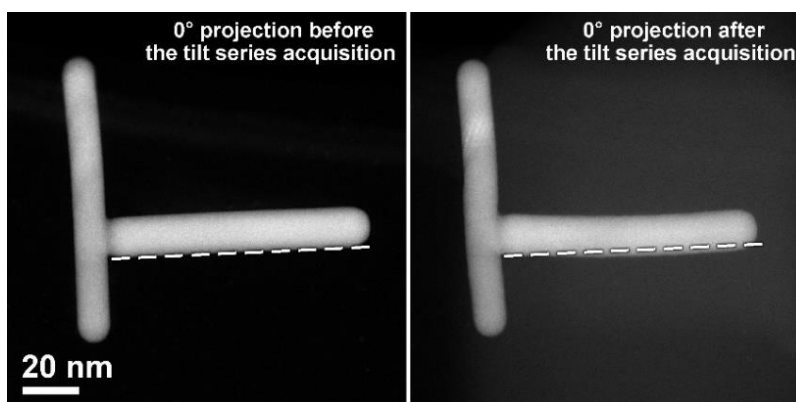
Figure 4.10 0° HAADF-STEM projections, taken before and after the full tilt series acquisition (in angular range of ±75° with 2° tilt step, 76 projections in total).

Therefore, to avoid the morphological transformations of the studied particle during the tomography experiment the total electron dose should be significantly reduced. To achieve this goal, compressive sensing 3D reconstruction[221] was performed based on a limited set of zone axis projections (see the detailed description in **Section 3.5**). For the studied NP, only three zone axis projections were acquired along the [100], [110] and [010] orientations (Experimental conditions are shown in Table 4.3). To ensure the ability to achieve several zone axis projections of the same particle, a dual axis

tomography holder was used (see Table 4.3). The 3D reconstruction results suggest that the initial Au NRs used as seeds are enclosed by {111}, {110}, and {100} facets at the tips, whereas the lateral facets are a mixture of different facets resulting in rounded rods (Figure 4.11). The presence of {111} facets is in agreement with the previous conclusion, based on the formation of irregular TBs during the chiral growth (Figure 4.7). To reduce the missing wedge caused by a high amount of missing data, a full tilt-series acquisition at "low"-resolution was performed for the same particles (similar to the magnification shown in Figure 4.9) and further implemented in compressed sensing reconstruction.[64] However, during the acquisition of tilt series for the studied Au NR taken in ±75° with 3° increment, change of the surface morphology of the studied particle was observed (Figure 4.12). Thus, the obtained "low"-resolution reconstruction cannot be used as a reliable volume input for the compressed sensing algorithm. This limitation hampered the reduction of the large missing wedge artifact in the resulting HR reconstruction.

Table 4.3 Overview of the experimental parameters used for the investigation of Au NR, shown in Figure 4.10.

Sample preparation	Drop casting of the aqueous solution
TEM grids	Conventional carbon coated Cu grids
TEM	Thermo Fisher QU-Ant-EM
Voltage	300 kV
Imaging mode	HAADF-STEM (2048x2048)
Detector collection angle	50 – 200 mrad
Magnification	2.55 Mx
Spatial resolution	70 pm
Screen current	50 pA
Sample holder	Fischione 2040 dual-axis tomography holder
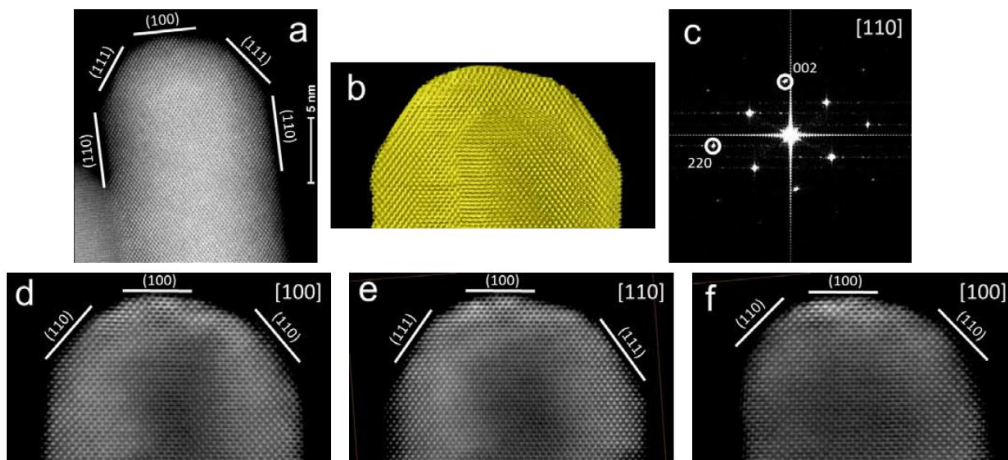
Figure 4.11 Atomic resolution analysis of the initial Au NR seed. (a) In zone axis HAADF-STEM projection (0°). (b) A snapshot of the tomography reconstruction along the 0° direction. (c) FFT taken along 0° projection. (d-f) Oblique slices through the 3D reconstruction, parallel to the rotation axis and taken from the middle of the NP.
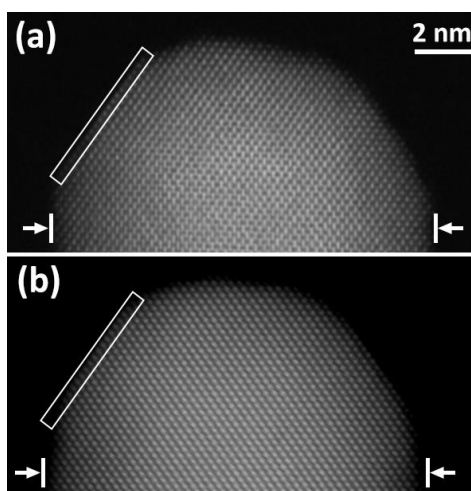
Figure 4.12 Atomic resolution HAADF-STEM images of Au NR seed shown in Figure 4.10: (a) [110] projection taken (a) before and (c) after the acquisition of high and low resolution tilt series. White arrows represent the altered thickness of the samples, whereas the white rectangles highlight the difference between {111} facets at the tip. These morphological changes confirm the low stability of the studied Au NR under the long electron beam exposure.

After the information about the surface faceting of the initial seeds was obtained, the analysis of NPs after the first growth step was performed. In this case, the stability of the NPs under the electron beam exposure was significantly higher and no indication of reshaping or internal deformation was found. This is related to the formation of rigid C layer on the surface on the studied NPs, originated due to the pyrolysis of remaining surfactants (Cys, CTAC) under the electron beam irradiation (Figure 4.13). It was previously already shown that the formation of protective C layer significantly improves the thermal stability of Au NRs.[222]
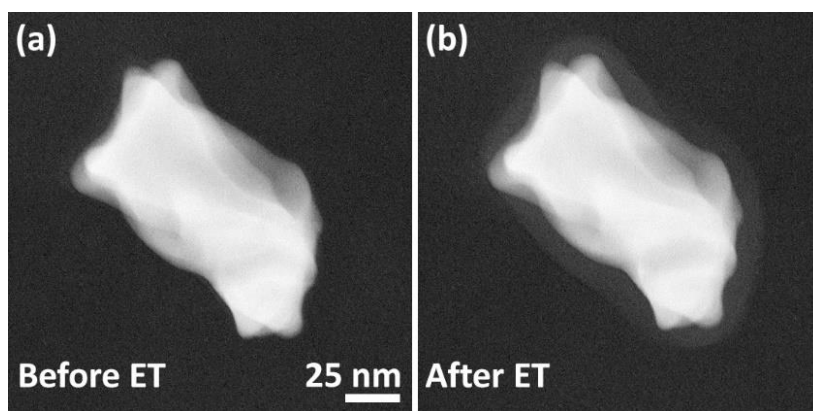
Figure 4.13 LAADF-STEM projections of chiral Au NP (a) before and (b) after the tilt-series acquisition, showing the formation of C layer at the surface.

Thus, HR tomography of the NP after the first growth step is performed using a single tilt tomography holder, and continuous tilt series were acquired over ±75° with 2° tilt step (all experimental parameters can be found in Table 4.4). 3D reconstruction is performed using the CNN-supported method described in **Section 3.5**,[201] and the obtained result indicates that the exposed facets changes drastically (Figure 4.14). Accurately analyzing the surface facets of a particle can be achieved by rotating the particle to a zone-axis direction, carefully chosen so that the facet of interest aligns parallel to the direction of view. This approach allows us to measure the orientation of the specific facet in relation to known facets. For example, when observing along the [100] direction, the crystallographic angle between (010) and (025) facets in the face-centered cubic (*fcc*) lattice of gold (Au) is equal to 21.8°. This type of analysis is

feasible when the rotation to arbitrary crystallographic orientations is possible, coupled with the ability to precisely visualize the surface of the particle. This underscores the significance of atomic resolution ET, as it provides information about the orientation of the NPs and the actual atomic arrangement at the surface. As an example, this analysis was conducted along the [100] direction, where two flat surfaces parallel to the viewing direction were observed on either side of the NP's tip (as depicted in Figure 4.14a and c). Based on the atomic arrangement, the (010) facet was determined to be oriented vertically and at an approximate angle of ~22° relative to its neighboring facet, which was consequently assigned as (025). By analysing different orthoslices through the 3D reconstruction of the structure obtained after one growth step, we conclude that the lateral facets correspond to {110} planes, in agreement with the fourfold symmetry of the final products. Moreover, there are 8 (520) facets at each tip (4 bigger facets closer to the lateral sides, 4 smaller facets at the very tip). The 4 protrusions at each tip coincide with the [111] direction and are limited by the {520}-like facets. After subsequent growth steps, these structures would evolve into fourfold twisted structures.
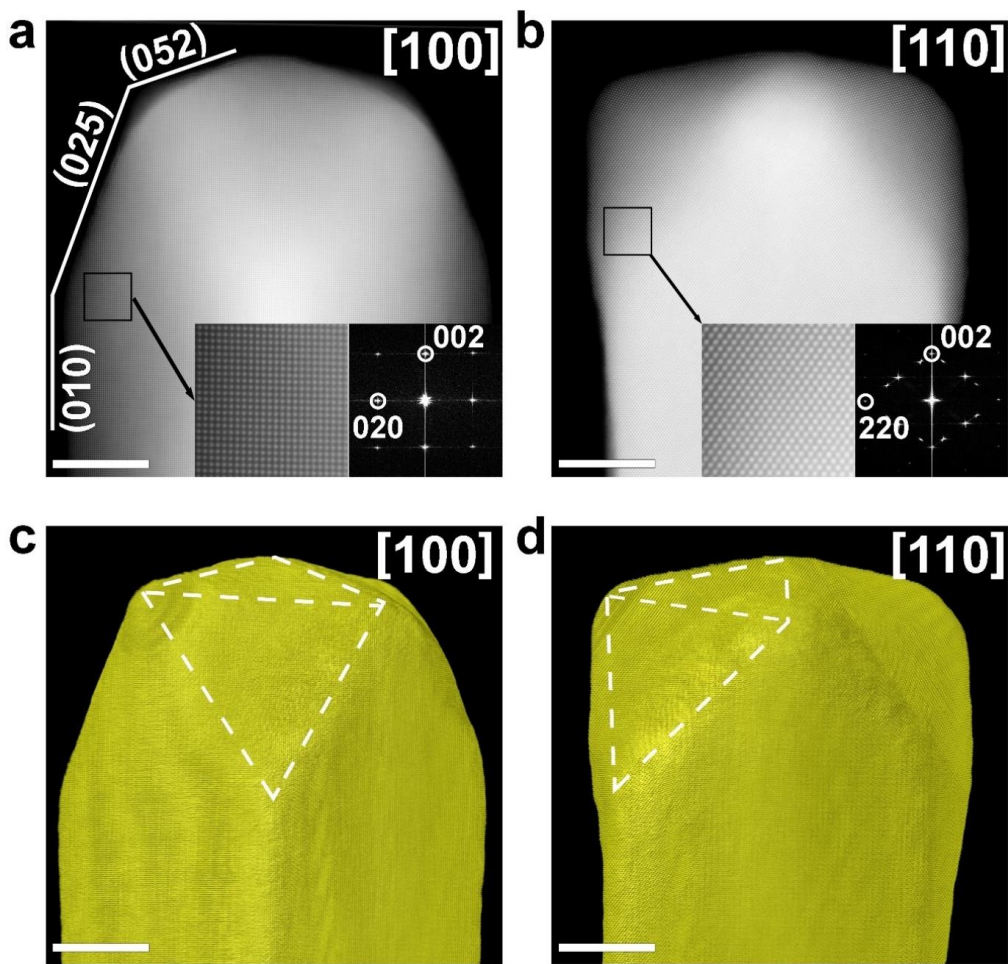
Figure 4.14 Atomic-resolution ET characterization of an Au NR obtained after one chiral growth step. (a,b) HAADF-STEM projections taken along [100] and [110] directions. Magnified regions showing atomic columns and corresponding Fourier transform patterns are presented as insets and indexed according to the Au *fcc* lattice. The white lines indicate the expected position of {010} and {520} types of facets (perpendicular to the projection plane). (c,d) Visualization of the 3D reconstruction, taken along the indicated orientations. The white dashed lines indicate the position of {520} facets. All scale bars are 10 nm.

Table 4.4 Overview of the experimental parameters used for the investigation of Au NP, shown in Figure 4.13.

Sample preparation	Drop casting of the aqueous solution
TEM grids	Conventional carbon coated Cu grids
TEM	Thermo Fisher Scientific Themis Z
Voltage	300 kV
Imaging mode	HAADF-STEM (2048x2048)
Detector collection angle	50 – 200 mrad
Magnification	1.8 Mx
Spatial resolution	60 pm
Screen current	50 pA
Sample holder	Fischione 2022 tomography holder
Angular range/increment	-75° : 2° : 75° (76 projections)

This shape is used as the intermediate structure to understand how the mirror planes of the particle can be removed. Similar to the Au NR seed, as discussed above and presented in Figure 4.1b, the intermediate structure showed a symmetry close to 4/mmm, whereas the idealized twisted NR has a symmetry of 422. The transition from 4/mmm to 422, implying the removal of mirror symmetry, can be hypothesized to occur through the enantioselective development of chiral facets. As proposed by Sholl et al., chiral facets are high-index facets with Miller indices such that $h \neq k \neq l$ and $h \times k \times l \neq 0$, in an *fcc* lattice.[223] Such chiral facets, e.g., $(521)^S$ planes, can be theoretically seen as a combination of lower microfacets or terraces, and their handedness (R- or S-type facet) is decided by their arrangement.[224] Moreover, chirality at the atomic level could help remove the mirror planes of the particle at the nanoscale. Since the {521} facets are quite close to the {520} facets, here the chiral {521} facets are used as an example to illustrate how to achieve the symmetry descent from 4/mmm to 422. In the NR obtained after the first growth step, the four achiral {520} facets at the tips closer to the lateral sides can evolve into chiral {521} facets. Each achiral facet would equally diverge into one R and one S facet if the growth is not enantioselective, thereby leading to achiral

particles with a 4/mmm symmetry (Figure 4.15). However, if the process is enantioselective, the overexpression of R or S facets would help remove the mirror planes of the particle to obtain a 422 symmetry. The reason behind enantioselectivity appears thus to be related to the preferential binding of Cys molecules, which may promote the growth of one of the enantiomeric facets, for example, $(521)^S$ versus $(52-1)^R$.
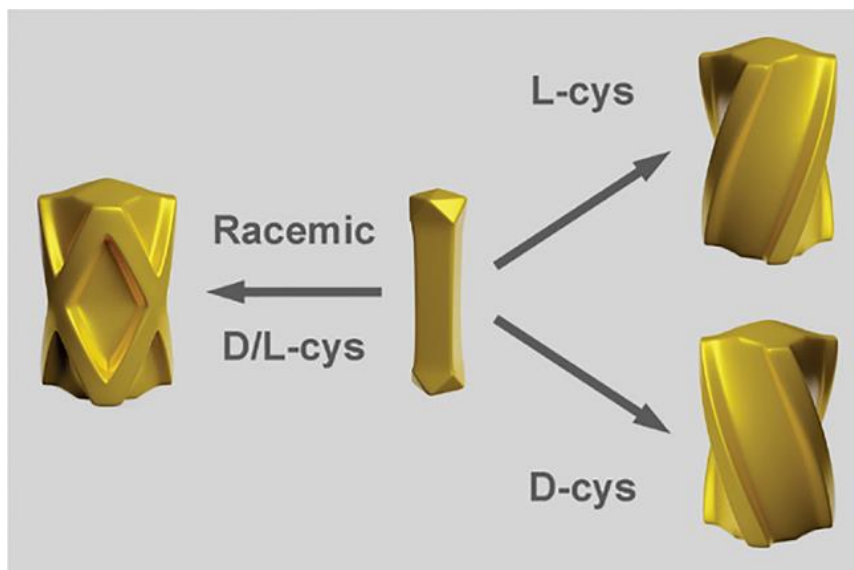
Figure 4.15 Schematic representation of enantioselective (using D- or L-cysteine) and non-enantioselective (using racemic D/L-cysteine) structural evolution of an Au NR after the first growth step.

To support this hypothesis, DFT simulations[225] were employed to investigate the role of Cys in the symmetry descent of Au NRs during seeded growth. Based on the results of the ET tomography, this studies were concentrated on the configurational space of adsorbed L-Cys on achiral low index facets and (520) facets, which are present in single-crystal Au NRs, as well as chiral $(521)^S$ and $(52-1)^R$ facets, as examples of S- and R-type surfaces, respectively (Figure 4.16a). The adsorption energies (E_{ads}) for different L-Cys conformations were computed (Figure 4.16b). Surface concentrations used in these simulations were smaller (low coverage regime) than experimental estimates because the experimental value is an upper limit assuming all molecules being adsorbed

on the metal surface, whereas an equilibrium between Cys in solution and adsorbed on the surface would be a much more realistic scenario. At low coverage, E_{ads} was found to be more exothermic on chiral than on achiral facets, adsorption on an S-type surface being favored by 0.14 eV over that on an R-type surface. Consequently, more development of $\{521\}^S$ facets or even other S-type facets (with different indexes) would result in a 4-fold twisted structure according to the lattice and seed symmetry. These results are in an excellent agreement with the conclusions made from ET tomography studies. Thereby, the hypothesis of facet-specific adsorption of chiral inducer molecules during the crystal growth is strenghtened.
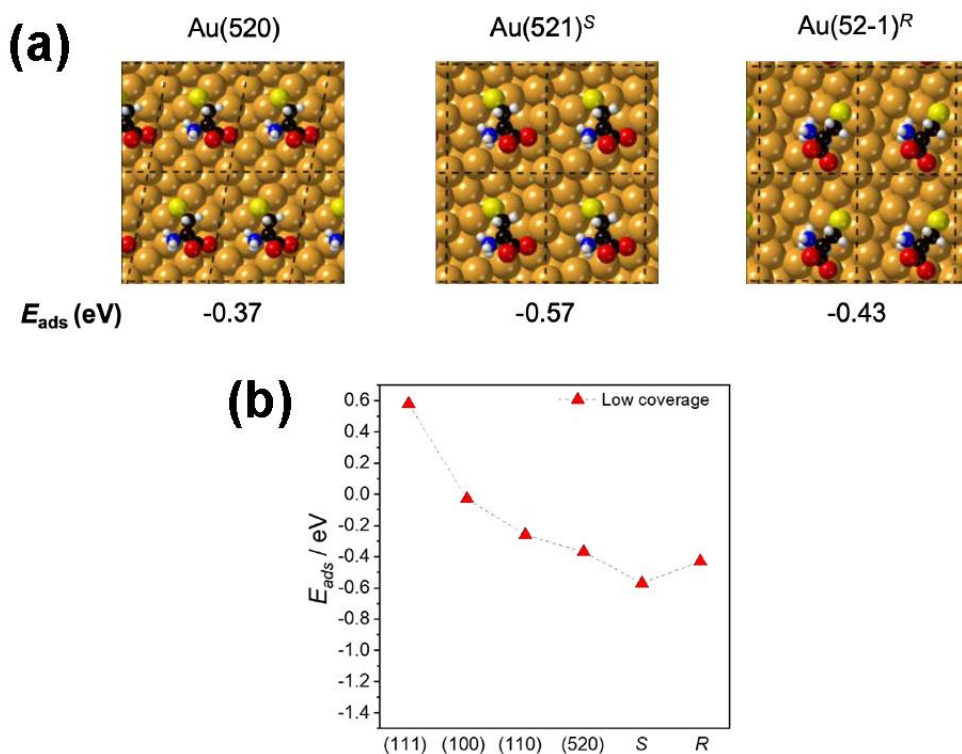
Figure 4.16 (a) Most stable L-Cys adsorption conformations and E_{ads} (eV) on (520), $(521)^S$, and $(52\text{-}1)^R$ facets at low-coverage. Atom legend: Au = pale orange, S = yellow, O = red, N = blue, C = black, and H = white. (b) Adsorption energy (E_{ads}) of L-Cys on different surfaces.

4.3 Stereochemical processes in the formation of helical penta-twinned Au nanorods

During the examination of the 4-fold twisted NPs, discussed in section 4.1, the irregular presence of twin-boundaries was observed, resulting in the formation of branched features that could potentially influence the chirality of produced particles (see an example in Figure 4.9). Based on SC NPs, where no indication of TB was found and the helicity was well preserved, the formation of twins was excluded from the potential sources of chiral growth. However, a systematic study should be conducted to assess the impact of the twin boundaries on the chiral crystal growth. To be more precise, the main aim of this section is to analyze the faceting of the intermediate structures, leading to the formation of the final chiral morphology, and the determination of the helicity of the PT Au NPs.

In this study, the synthetic protocol is similar to that used in **Section 4.1**, however in this case PT Au NRs were used as seeds for chiral growth. The 5-fold symmetry of PT seeds, as well as the presence of twin boundaries, may play a significant role during chiral growth, thus, resulting in different morphologies of final chiral NPs compared to SC counterparts (typically with 4-fold symmetry). By using the successive $HAuCl_4$ additions, to mimic the stages of crystal growth reaction, the dissymmetric growth process of PT chiral Au NPs was studied using ET (see experimental details in Table 4.6). Figure 4.17 shows the HAADF-STEM overview and 3D reconstructions of 2 different NPs for the samples, obtained after (a) 1 and (b) 9 successive $HAuCl_4$ additions. As can be seen, the overall morphology of the samples becomes more intricate during the growth reaction, where the 5-fold symmetry of initial Au PT seeds disappears and both left right handed features can be seen at the later stage in Figure 4.17a,b(ii). To determine the overall handedness of the studied particles, helicity measurements were conducted based on the obtained reconstructions (as described in section 3.3) and the results are shown in Figure 4.17a,b(iii). From these plots, the simultaneous presence of both left and right-handed features can be seen, resulting in the negligible total helicity in both cases (H_{tot} = -0.02). In comparison, the formation of well-pronounced right-handed helical NPs was observed during chiral growth of SC Au

NPs when using L-Cys as a surfactant, that can already indicate the different mechanism of the chiral growth in case of PT Au seeds. These observations are supported by CD spectrometry of PT chiral NPs, showing weak chiroptical response.

Table 4.6 Overview of the experimental parameters used for the investigation of PT Au NR, shown in Figure 4.16.

Sample preparation	Drop casting of the aqueous solution
TEM grids	Conventional carbon coated Cu grids
TEM	Thermo Fisher Scientific Themis Z
Voltage	300 kV
Imaging mode	HAADF-STEM
Detector collection angle	100 – 200 mrad
Magnification	450 kx
Screen current	50 pA
Sample holder	Fischione 2022 tomography holder
Angular range/increment	-75° : 3° : 75° (51 projections)

Figure 4.17 The products obtained after different chiral growth conditions: (a)1 and (b) 9 chiral growth steps; (i) HAADF-STEM overview and (ii) the ET reconstructions of two different particles, (iii) the helicity analysis of corresponding the particle from (ii), demonstrating the simultaneous presence of left-handed (blue) and right-handed (red) features. Scalebars are 50 nm.

It is worth mentioning, however, that the studied samples lack of any uniform or characteristic morphology. Of course, one can validly argue, that (S)TEM studies are rarely statistically meaningful due to the limited number of the studied particles, however the seed-mediated colloidal technique has proven itself to be able to produce highly homogeneous NPs which can be reliably shown using (S)TEM techniques, e.g. for chiral Au NPs studied in **Section 4.1**. The observed shape irregularity may be explained by the fast growth kinetics, where the thermodynamically governed site-specific adsorption of surfactant molecules does not play the determining role in the formation of chiral surfaces. In addition, atomic resolution ET can still be used to obtain information about the faceting and twinning in the studied NPs. In this manner, a Au NP obtained after 1 growth step was studied using conventional and atomic resolution ET technique (Figure 4.18). Experimental details are presented in Table 4.7. Helicity analysis was also performed for this particle, where the total helicity H_{tot} was found to be equal to -0.02, in agreement with the results for the particles in Figure 4.17a,b(iii).
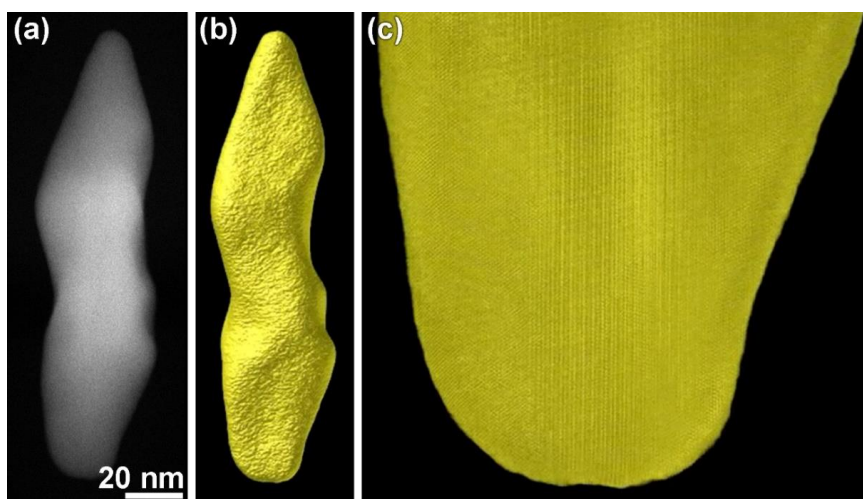
Figure 4.18 (a) HAADF-STEM projection and (b) 3D reconstruction of a PT Au NP obtained after 1 growth step; (c) Atomic resolution 3D reconstruction of the bottom tip.[201]

Table 4.7 Overview of the experimental parameters used for the investigation of PT Au NR, shown in Figure 4.17.

Sample preparation	Drop casting of the aqueous solution	
TEM grids	Conventional carbon coated Cu grids	
TEM	Thermo Fisher Scientific Themis Z	
Voltage	300 kV	
Imaging mode	HAADF-STEM	
Detector collection angle	100 – 200 mrad	
ET technique	Conventional	High resolution
Magnification	450 kx	1.8 MX
Screen current	50 pA	
Spatial resolution	50 pm	
Sample holder	Fischione 2022 tomography holder	
Angular range/increment	-75° : 3° : 75° (51 projections)	-75° : 2° : 75° (76 projections)

A detailed analysis was carried out, where the central slices through the obtained reconstruction (Figure 4.18c) were taken perpendicularly to the relatively flat surface features, from which the surface facets can be determined through their relative orientation to the known crystallographic orientations (e.g., angle between the measured and known facets, Figure 4.19a) or by the arrangement of atoms at the surface (Figure 4.19b,c). However, one should be careful with angular measurements, especially in case of high index facets, where the difference between two planes can be smaller than 3°. In case of the studied NP, where the flat surface regions (facets) are not always obvious, "low" index facets can be determined with a certain degree of confidence. At the same time, when having the uncertainty between two possible types of faceting, it is reasonable to choose the faces with the smallest sum of *hkl* indexes. Interestingly, (-1 2 3)^S and (132)^R facets were observed in this case, thereby, supporting the simultaneous formation of left and right handed features, observed from the helicity analysis.
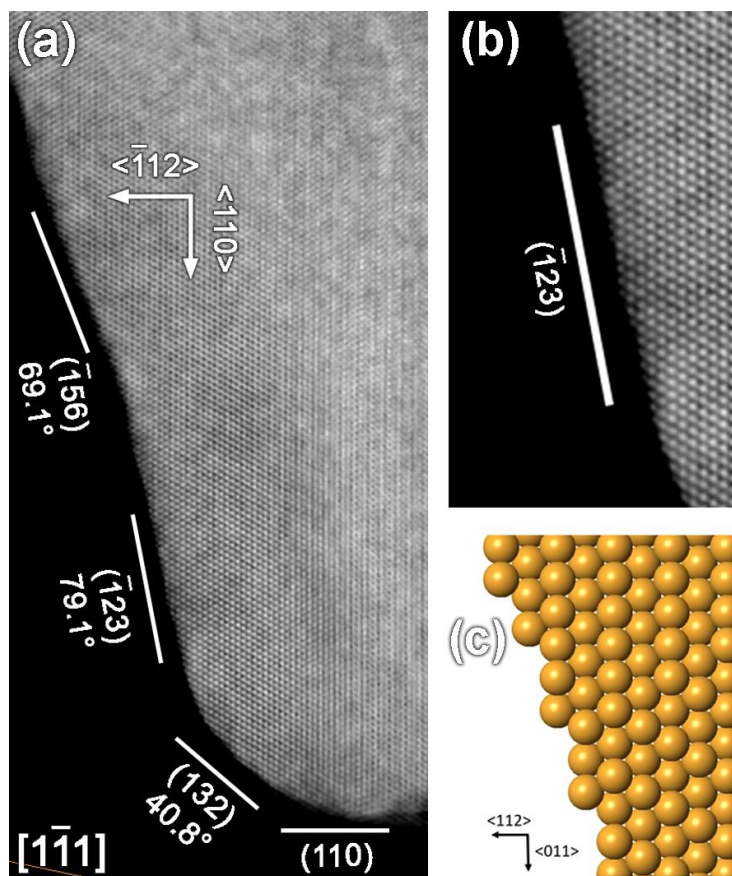
Figure 4.19 (a) Central slice through the atomic resolution 3D reconstruction taken along the [1 -1 1] direction. (b) Magnified region of (a), corresponding to (-1 2 3) facet. (c) schematic view of the {-1 2 3} facet, taken along [1 -1 1] orientation if *fcc* lattice of Au.

Based on the obtained results, we can assume, that TBs can serve as a starting point for a rapid crystal growth, similar to the formation of the branched features in the case of SC chiral Au NPs (Figure 4.8), breaking the chiral morphology of the produced NPs. Besides, fast kinetics of the growth prevail over the thermodynamics of the interaction between the surface facets and chiral inducer molecules, where the certain degree of equilibrium (e.g., of the preferential adsorption)[226] should be reached. Albeit certain chiral facets and features were observed in PT chiral Au NPs, the fast growth disregards the formation of certain shapes, leading to highly irregular morphologies.

To have additional evidence that kinetics plays a crucial role, the synthesis at different temperatures to assess the possibility of obtaining other potential shapes using ET (same experimental settings as in Table 4.6) was conducted. The previous discussion primarily focused on particles obtained with the initial 5 steps at 25°C, followed by 4 steps at 16°C (Figure 4.20a). When the synthesis was conducted purely at (5×25°C + 4×16°C), the resulting products exhibit more intricate shapes, where the chiral features still can be discerned. With higher growth temperatures, the surface became smoother. Nevertheless, the products obtained at (5×25+4×30) still exhibited helical features (Figure 4.20b). Finally, the products obtained at (5×25+4×35) displayed an even smoother surface (Figure 4.20c), with the helical structures becoming less discernible. Given the faster rate of the chemical reaction at higher temperatures, it can be assumed that the contribution of kinetics will also increase during the NPs growth. In this case, the trend for smoother surfaces (due to the facilitated atom diffusion) and less pronounced chiral features can serve as an additional proof of prevailing contribution of kinetics over the thermodynamics during the Cys-mediated chiral growth of PT Au NPs.
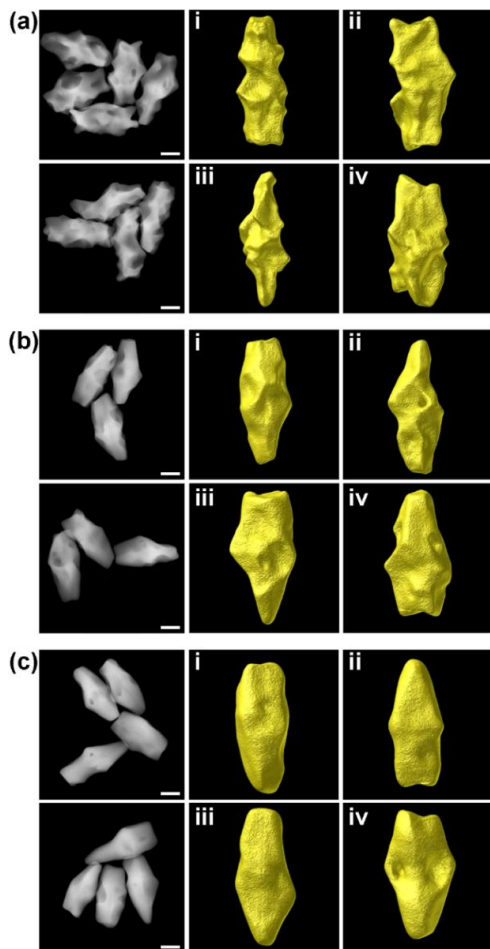
Figure 4.20 PT chiral Au particles obtained at different reaction temperatures. (a) (5×25°C +4×16°C); (b) (5×25°C +4×30°C); (c) (5×25°C +4×35°C). (i-iv) 3D ET reconstructions of the NPs from the corresponding samples. All scalebars are 50 nm.

4.4 Conclusions

In this chapter, I implemented conventional, multimode and high resolution ET techniques to perform the detailed study of the Au NPs produced by cysteine assisted chiral growth. To be more specific, the 4-fold twisted morphology of the resulting individual Au NPs was demonstrated in 3D. Based on the obtained 3D reconstruction, the helicity measurements were conducted revealing the well-pronounced handedness depending on the enantiomer of cysteine, used during the synthesis. Additionally,

achiral structures were observed after the synthesis in the presence of racemic (D/L) mixture of cysteine, that was further confirmed with CD-spectrometry measurements. Based on these findings, the formation of chiral $\{521\}^S$ or $\{52\text{-}1\}^R$ surface facets during the chiral growth was hypothesized depending on the (L-) or (D-) enantiomers of cys used. This hypothesis was further confirmed by the atomic resolution studies in 3D, revealing the evolution of initial $\{100\}$, $\{110\}$ and $\{111\}$ facets intrinsic for initial Au seeds into $\{520\}$ facets demonstrated for intermediate Au structures. Supported by DFT calculations, it was concluded that achiral $\{520\}$ may promote the growth of one of the enantiomeric facets, for example, $(521)^S$ versus $(52-1)^R$.

The observed twisted Au NPs (**Section 4.1**) are single-crystalline in their nature, which enabled me to exclude the influence of crystal defects formation on the final helicity of the studied samples. However, in some individual NPs (approximately in 10% of the observed particles) the irregular presence of twin boundaries was also observed at the tips of the particles, leading to more complex branched structures. To study the influence of twinning on chiral growth in a more systematic manner, I performed the ET characterization of PT Au NPs obtained by Cys-mediated chiral overgrowth of PT Au seeds. Highly irregular nonhomogeneous morphologies were observed after every stage of the chiral growth, resulting in the negligible total helicity of the studied particles. This can be explained by the prevailing contribution of kinetics over the thermodynamics of the chiral growth reaction of PT Au NPs, where the selective interaction of Cys molecules with the chiral surface facets could not be reached. Atomic resolution ET tomography analysis of the intermediate NP demonstrated the simultaneous presence of both left- and right-handed facets, e.g. $(-1\ 2\ 3)^S$ and $(132)^R$. Additionally, the synthesis at higher temperatures can also indicate the growing contribution of the kinetic to the crystal growth, leading to smoother surfaces, where less chiral features can be observed.

Chapter 5. Morphological transitions during micelle-seeded chiral growth on Au nanorods

This part is based on:

The synthesis of the samples and spectral characterization analysis was carried out at CIC BiomaGUNE in Donostia-San Sebastián, Spain.

Electromagnetic modelling of optical properties was performed at EM3WORKS, Spin-off of the University of Vigo and the University of Extremadura, Spain.

TEM characterization was carried out at the research group for electron microscopy for materials science (EMAT) at the University of Antwerp. I was responsible for all TEM acquisition, ET reconstructions and analysis. Helicity analysis was performed by W. Heyvaert.

This chapter discusses the mechanism of the micelle-mediated growth of chiral Au NPs. More specifically, high-resolution HAADF-STEM and ET techniques was implemented to study the shape evolution of the corresponding nanoparticles obtained at the different stages of synthesis. Obtained results enabled a careful investigation of initial, intermediate and final morphologies, that were also correlated to the chiroptical properties of the studied samples. Additionally, the thin Pd layer incorporated between the Au core and surface[227] wrinkles was visualized by 3D HAADF-STEM, allowing to analyse the interface between the core and the wrinkled shell of the studied NPs and, thus, to draw conclusions on the surface-dependent adsorption of chiral micelles.

5.1 Different stages of the synthesis of helical nanoparticles

To carry out a systematic study towards a better understanding of micelle-directed seeded growth, from achiral single-crystal Au NRs into chiral Au NRs (rod-shaped structures with helical wrinkles), 3D characterization of intermediate states during synthesis is necessary. Under the recently reported synthetic conditions,[168] the achiral-to-chiral transition is found to occur around minute 1 of the seeded-growth reaction. Due to the fast reaction rate, it is challenging to monitor the growth process by detaining the reaction instantaneously at different stages and studying the corresponding morphological changes. Therefore, an alternative method to mimic the reaction progress around minute 1 was used by carrying out a series of syntheses in which the seed concentration ($[Au^0]/[Au^+]$ ratio) is varied for chiral overgrowth. In this manner, control over the growth of the helical wrinkles could be achieved, enabling one to mimick initial stages of the achiral-to-chiral transition (Figure 5.1). To investigate the intricate morphological evolution expected for this process, the different samples were analysed by HAADF-STEM tomography. The experimental parameters used for ET studies are shown in Table 5.1. I applied this technique to the achiral Au NR seeds and representative Au NRs overgrown at different $[Au^0]/[Au^+]$ ratios, to reconstruct their 3D morphologies using EM reconstruction algorithm, as explained in **Section 2.5.3** (Figure 5.1A−D).
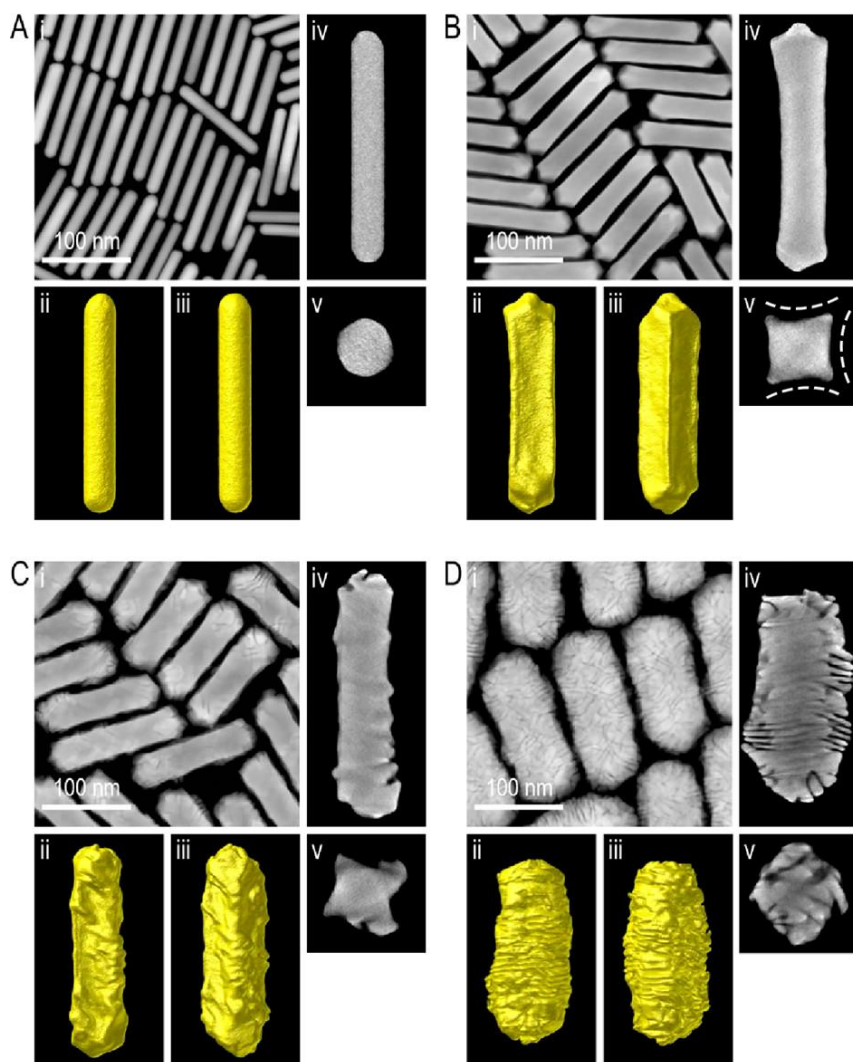
Figure 5.1 Morphological characterization of Au NRs obtained by varying seed concentration in chiral overgrowth. (A) HAADF-STEM image, tomography reconstruction, and selected orthoslices of single-crystalline seed Au NRs. (B−D) Morphology of Au NRs grown with decreasing seed concentration, i.e., decreasing $[Au^0]/[Au^+]$ ratio between seed and growth solution (B: 0.31; C: 0.13; D: 0.03). The morphological characterization for each sample includes (i) HAADF-STEM image, (ii, iii) 3D reconstructions along different viewing angles, (iv, v) selected orthoslices perpendicular to the longitudinal and transverse axes at the center of the NRs. Dashed curved lines highlight the concave lateral sides of NP shown in (B).

Table 5.1 Overview of the experimental parameters used for the investigation of chiral Au NR, shown in Figure 5.1.

Sample preparation	Drop casting of the aqueous solution
TEM grids	Conventional carbon coated Cu grids
TEM	Thermo Fisher Scientific Themis Z
Voltage	300 kV
Imaging mode	HAADF-STEM
Detector collection angle	100 – 200 mrad
Magnification	450 kx
Screen current	50 pA
Sample holder	Fischione 2022 tomography holder
Angular range/increment	-75° : 3° : 75° (51 projections)

As shown in Figure 5.1A, the seeding Au NRs are single-crystalline with a rounded octagonal cross-section, which has been reported to comprise alternating {100}, {520}, and {110} facets.[64] Upon overgrowth with an [Au^0]/[Au$^+$] ratio of 0.31 (Figures 5.1B and 5.2), a transition into a four-fold symmetric shape with square cross-section and pyramidal tips, i.e., an elongated octahedral shape, is observed. According to previous studies, four-fold symmetric Au NRs may exist as different geometrically allowed structures, comprising lateral sides enclosed by {100}, {110}, or {111} facets.[228–230] I carried out high resolution HAADF-STEM measurements along different directions, which revealed four lateral {110} facets (Figure 5.2A). According to the 3D reconstruction and longitudinal orthoslices, the square cross-section shows a rotation of 45° from one end to the center along the Au NR longitudinal axis (Figure 5.2B). Moreover, the angle between an end facet and a lateral edge was measured to be 135°, whereas the tip angle at different views was measured as either 109° or 90° (Figure 6.2C), all of which are characteristic angles of *fcc* crystals with adjacent {110} facets. We can conclude that the four-fold symmetric Au NR is enclosed by 12 {110} facets, including the four lateral sides and four smaller facets at each end (Figure 5.2D). It is also worth noting that all facets are slightly concave (as indicated by dashed lines in

Figure 5.1Biv), which likely indicates a precursor state to the subsequently emerging wrinkles. When the seed concentration ($[Au^0]/[Au^+]$) ratio was reduced to 0.13, the obtained Au NRs already displayed helical wrinkles on the surface, albeit short and rather disordered (Figure 5.1C). Well-defined chiral Au NRs with rich helical wrinkles were obtained with a significantly lower $[Au^0]/[Au^+]$ ratio of 0.03 (Figure 5.1D). Interestingly, both of the orthoslices in Figures 5.1C,D also display a quasi-square cross-section, similar to that in Figure 5.1B, but with additional protrusions at the edges and corners. With the aim of better understanding the morphology of the different samples, a methodology to quantify the helical morphology of NRs was applied, which is based on the analysis of electron tomography reconstructions (for more detail see Section 3.3).[193] These results indicate an increase in left-handed total helicity during the gradual formation of helical wrinkles (Figure 5.3). Although both left- and right-handed local helical features can be recognized in all of the overgrown Au NRs, the relative amount of left-handed features increases as helical wrinkles are more clearly distinguished, in agreement with an achiral-to-chiral transition. It is interesting to note that the inclination angles (the position of blue features in the plots shown in Figure 5.3) of early-stage helical wrinkles (75−90°, Figure 5.3A,B) are steeper than those for well-defined helical structures (<45°, Figure 5.3C). This agrees with the earlier observation that the inclination angles of helical wrinkles depend on the thickness of the helical shell.[193]
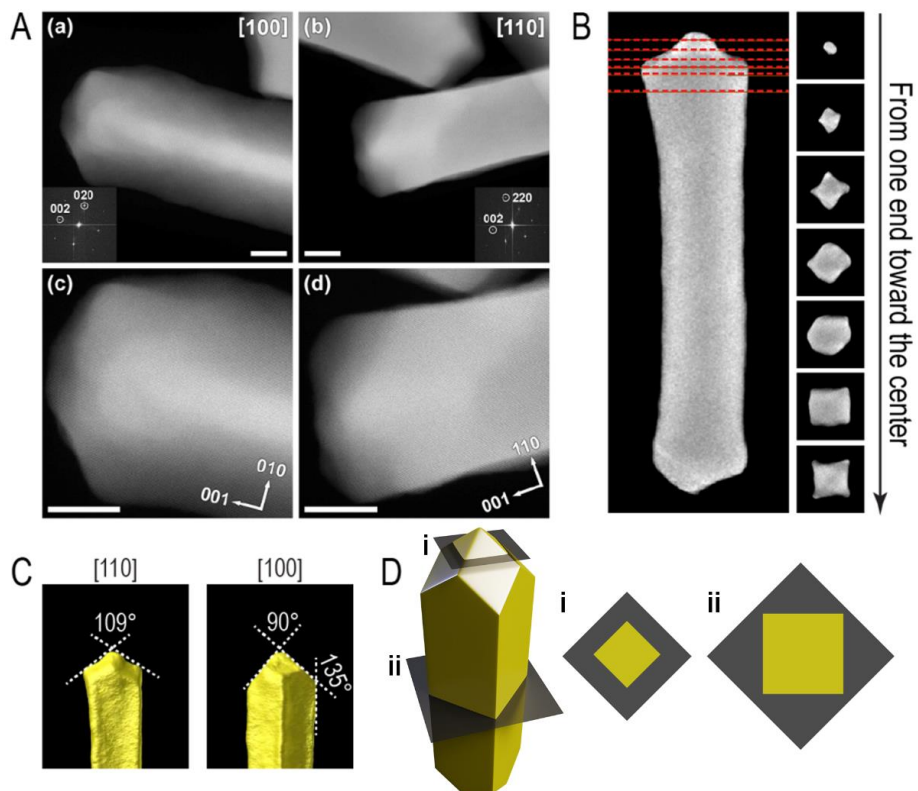
Figure 5.2 (A) (a,b) HAADF-STEM images and (c,d) high-resolution HAADF-STEM images of an Au NR (similar to that in Figure 6.1B), taken along [110] and [100] zone axis. The insets in (a) and (b) show fast Fourier transform (FFT) patterns along [110] and [100] directions for the *fcc* lattice of Au, which indicate that the lateral sides are enclosed by {110} facets. Scale bars: 10 nm. (B) Selected orthoslices through the 3D reconstruction (Figure 6.2Bii), showing a quasi-square cross-section, from the central part to one end of the Au NR. The red dashed lines in the left image indicate the positions of the orthoslices. Rotation of the square pattern near the end of the Au NR helps determine the nanocrystal structure. (C) Angles between edges and facets measured from the 3D reconstruction, viewed in [110] and [100] directions (perpendicular to the image plane). (D) 3D render of a rod enclosed only by {110} facets. The 109°, 90°, and 135° are some characteristic angles between specific edges and facets. In (i,ii) slices taken through 3D model are shown, indicating 45° rotation of square cross-section, similar to what is observed in (B).
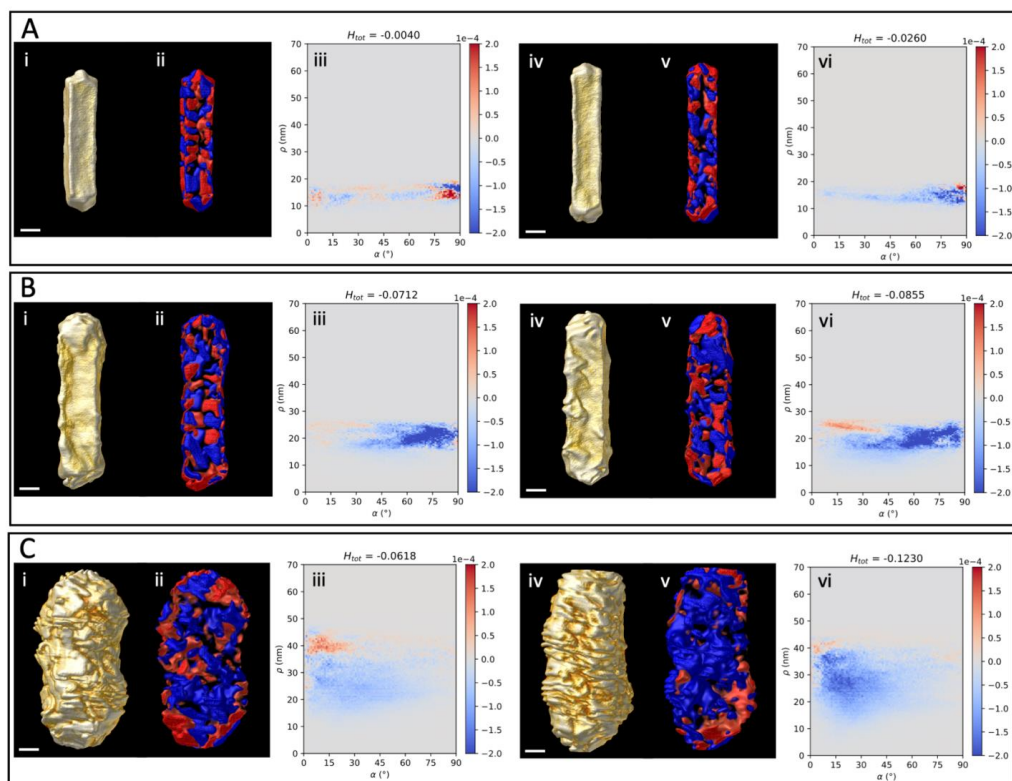
Figure 5.3 Isosurface visualizations of the 3D reconstructions (i, iv) for six Au NRs at different growth stages ($[Au^0]/[Au^+]$ ratios). Two individual NRs were measured from each of the samples shown in Figures 5.2B (A), 2C (B), and 2D (C). The corresponding local geometrical helicity map (ii,v; red: right-handed; blue: left-handed) and a plot of the corresponding helicity function (iii, vi) are provided for each 3D reconstruction.

Assuming that the analysis reflects the behavior during direct chiral overgrowth, the existence of two main stages during growth was proposed: first, preferential Au deposition on high-index {520} facets until the formation of slightly twisted elongated octahedra, followed by the formation of helical wrinkles, which are likely directed by adsorbed BINAMINE-CTAC micelles. These results suggest that the formation of a quasi-square cross-section may play a crucial role in the achiral-to-chiral transition of Au NRs.

5.2 Faceting of intermediate stages and seed position visualization

As additional evidence to verify the formation of a quasi-square cross-section, quasi-cuboid achiral Au NRs were prepared.[231] Such Au quasi-cuboids (QCBs) are reported to display well-defined {100} facets, which could be coated by a thin layer of Pd (Figures 5.5A,B and 5.5A,B). The synthesized Au@Pd QCBs were used as seeds under the conditions previously identified to generate chiral Au NRs, i.e., following the same incubation and chiral overgrowth procedures. It should be noted that Au QCBs were prepared in the absence of any chiral molecules that might influence the early growth transition. As a result, chiral wrinkles were grown on nonchiral Au QCB, ultimately displaying a chiroptical response (Figure 5.5C,D).

Most interestingly, the Pd layer can be used to identify the boundary between the achiral QCB cores and the chiral features in the final Au NRs (Figure 5.5E). Multimode ET can be used, where the information collected at the different scattering angles can be used to highlight the different elements with the certain difference in the atomic number (for mre detail see **Section 2.4.1**).[220] However, due to the significant difference in atomic numbers of Au and Pd (Z_{Au} = 79, Z_{Pd} = 46), the mass-thickness contrast of HAADF-STEM tomography and resolution of modern EM techniques should be sufficient to visualize these elements separately while detecting only the electrons, scattered at high angles ($\geq$50 mrad). To achieve reliable results, acquisition of projections at the highest attainable resolution is essential, necessitating careful alignment of projections and rotation axes at the pixel level. In this study involving Au-Pd NPs, an optimal magnification of 620 kx was employed in the HAADF-STEM regime, capturing projections of 1024x1024 size with a pixel size of 0.15 nm. It should be noted that a misalignment of even a few pixels can impede the resolution of nm-sized features. Utilizing conventional tomography reconstruction algorithms, such as those offered by the Tomohawk scripts package and ASTRA Toolbox,[232] may lead to inadequate tilt series alignment, resulting in a loss of significant information (Figure 5.7b). In order to ensure an optimal alignment of tilt series and obtain reliable information regarding sub-

nm-sized structural features, the SIRT algorithm is used in this work (Figure 5.7c), including the projection alignment as described in Figure 3.14.[201]

In this manner, the thin Pd (~1 nm) layer was visualized, that can be distinguished from the contrast difference in the orthoslices of the HAADF-STEM tomography reconstruction (Figure 5.5E, iii and iv and Figure 5.6C,D), showing that helical wrinkles can grow directly on the Pd-covered surface of achiral QCBs, and thereby confirming the role of the quasi square intermediate morphology in the achiral-to-chiral transition. It should be noted that, although both these QCBs and the elongated octahedra identified as intermediates display a quasi-square cross-section, their structure differs in the crystallographic index of their facets ({100} vs. {110}) and their tip morphologies (flat vs. pointed). It is therefore concluded that the crystalline nature of lateral facets does not play a major role in chiral growth, again supporting the micelle-templating hypothesis.
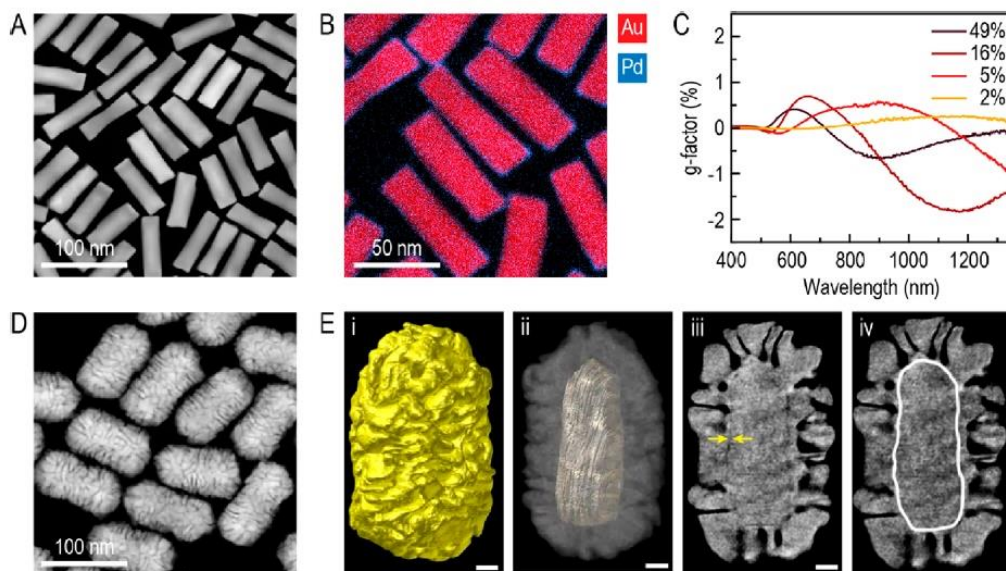
Figure 5.5 Chiral overgrowth using Au@Pd quasi-cuboids (QCBs) as seeds. (A) HAADF-STEM image of Au@Pd QCBs. (B) Elemental EDX mapping of Au@Pd QCBs (red, Au; blue, Pd) showing a Pd thin layer coating the surface of Au QCBs. (C) g-factor spectra of chiral Au NRs using different concentrations of QCB seeds. (D) HAADF-STEM image of the QCB-directed chiral Au NRs ($[Au^0]/[Au^+] = 0.16$). (E) Tomography reconstruction of a QCB-seeded chiral Au NR. (i) 3D visualization of the external Au surface; (ii) 3D visualization of the Pd−Au interface; (iii, iv) orthoslice perpendicular to the transverse axis, where the Pd layer can be seen as a thin, darker line surrounding the core, as indicated by the yellow arrows in (iii) and white outline in (iv). Scale bars: 10 nm. An orthoslice perpendicular to the longitudinal axis of the QCB-directed chiral Au NR is shown in Figure 5.6C,D.
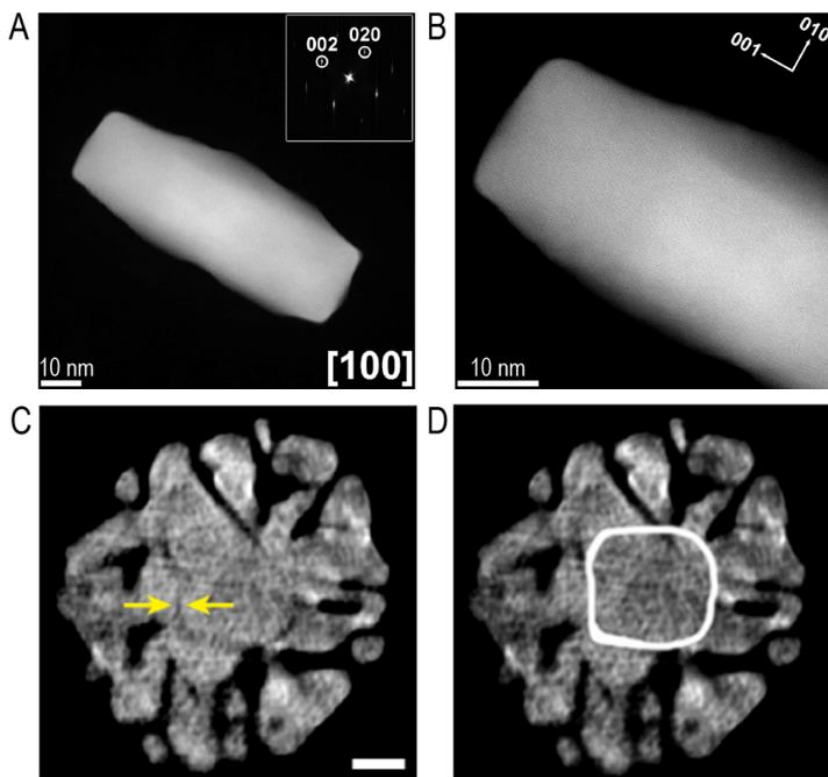
Figure 5.6 (A) HAADF-STEM image and (B) high-resolution HAADF-STEM images
of an Au quasi-cuboid (QCB) from the sample shown in Figure 5.5A. The inset in (A)
shows an FFT pattern along the [100] direction for the *fcc* Au lattice, indicating that the
lateral sides are enclosed by {100} facets; crystalline directions are indicated in (B). (C,
D) Selected orthoslice perpendicular to the longitudinal axis of the QCB-directed chiral
Au NR in Figure 5.5E. The Pd layer can be seen as a thin, dark line surrounding the
core, as indicated by the yellow arrows in (C) and white outline in (D). Scale bar: 10
nm.
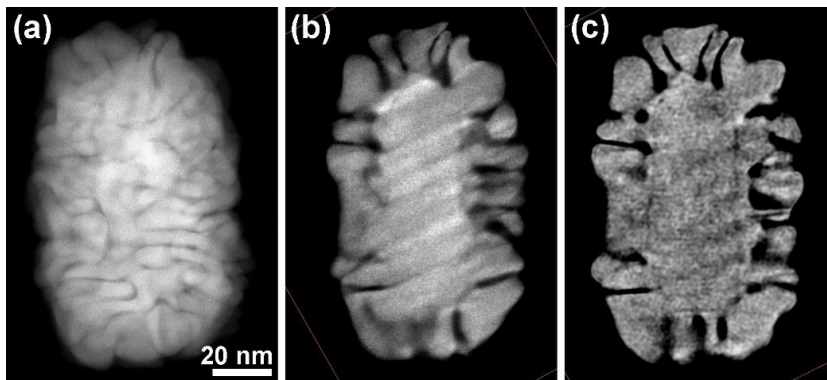
Figure 5.7 (a) HAADF-STEM projection of the QCB seeded chiral Au NR, used in Figure 5.5E; (b) The central slices through the 3D reconstruction performed with the Tomohawk scripts package. The presence of oblique diagonal lines indicates improper tilt-series alignment, leading to inconsistencies in the thickness observed between the reconstructed NP and its projections at different tilt angles; (c) The central slices through the 3D reconstruction performed with the CNN-assisted ET algorithm. In this case, the more precise alignment of the projections and rotation axis allows the analysis, performed in Figure 5.5E(iii,iv).

To summarize, it was concluded that the formation of the elongated octahedral structures at the intermediate stages might be most efficient at accommodating helical micelle adsorption. However, the actual mechanism behind the preferential adsorption to such surfaces remains unclear, requiring detailed examination of the interaction of chiral micelles with the surface (facets) of Au seeds. Direct electron microscopy studies currently do not allow us to investigate the actual distribution of chiral micelles on the surface of studied NPs due to the low contrast and the electron beam damage, leading to the decomposition of organic-based micelles. Additionally, most (S)TEM experiments are conducted in high vacuum, where the conformation of dried samples can strongly differ from the actual synthetic condition, performed, e.g. in water solutions. The combination of low beam-damage imaging techniques with liquid holders or liquid encapsulation[233] should be developed and implemented to study the adsorption of chiral micelles in more detail. The preliminary efforts to perform graphene liquid cell encapsulation of Au NRs are discussed in **Section 9.2.1.**

5.3 Conclusions

In this chapter, the shape evolution of Au NPs during the micelle-mediated chiral growth was studied using ET. The morphological transition of {100}, {520}, and {110} facetted Au elongated seeds with a rounded octagonal cross-section into elongated intermediate octahedral shapes, enclosed by 12 {110} facets. The overgrowth of the chiral wrinkles was shown to occur at resulting four-fold symmetric shape with square cross-section, that was confirmed by the visualisation of thin Pd layer incorporated between the Au core and Au helical wrinkles.

Thus, a key turning point of the achiral-to-chiral transition has been hypothesized to be an intermediate elongated octahedral structure, which might be most efficient at accommodating helical micelle adsorption. Unfortunately, this hypothesis cannot be confirmed by using conventional ET techniques due to the beam-sensitivity of organic micelles under the electron beam irradiation and vacuum conditions. Nevertheless, this limitations are opening promising prospects for the development of liquid encapsulation techniques, that can be combined with the low-electron dose techniques. These investigation would allow us to examine actual adsorption of chiral micelles on the surface of chiral Au NPs, thus, leading to a fundamental understanding of micelle-mediated growth processes at nanoscale.

Chapter 6. Tuning the growth of chiral Au nanoparticles through rational design of a chiral molecular inducer

This part is based on:

The synthesis of chiral inducers was done at CICA, University of A Coruña in A Coruña, Spain. The synthesis and spectral characterization of chiral Au NPs was carried out at CIC BiomaGUNE in Donostia-San Sebastián, Spain.

Electromagnetic modelling of optical properties was performed at EM3Works, Spin-off of the University of Vigo and the University of Extremadura, Vigo, Spain.

TEM characterization was carried out at the research group for electron microscopy for materials science (EMAT) at the University of Antwerp. I was responsible for all TEM acquisition, ET reconstructions and analysis. Helicity measurements were performed by W. Heyvaert.

In this chapter, I discuss the synthesis of chiral Au NPs using LipoCYS – a novel type of chiral inducer combining both the properties of cysteine and chiral micelles. In more detail, I employed the ET technique to investigate the different structures, obtained depending on the concentration of LipoCYS. Supported by CD spectrometry and electromagnetic simulations, the ability to synthesize both twisted and wrinkled morphologies with strong chiroptical properties is demonstrated.

Additionally, the combination of HAADF-STEM and ED tomography was introduced, which allowed me to conduct a thorough faceting characterization of the resulting twisted shapes, hereby, unravelling the site-specific adsorption of LipoCYS with the surface of studied NPs. The technical details of combined HAADF-STEM and ED tomography were also demonstrated.

6.1 Chiral morphology types controlled by modified surfactants

According to **Chapters 3,4** and **5**, chiral-seeded growth on AuNRs can be achieved through two alternative paths, according to the morphology of the chiral NRs and the chemical nature of the molecular inducer of dissymmetry. One synthetic path results in the formation of plasmonic nanorods with twisted geometry using amino acids (such as cysteine) or short peptides containing the same amino acid, as the dissymmetry inducers (Figure 6.1a).[234] The second synthetic protocol is known as micelle-directed chiral growth,[168,235] through which plasmonic nanoparticles are grown as a dense array of quasi-helical wrinkles around a central NR (Figure 6.1b). Using this methodology, a co-surfactant with axial chirality, such as BINAMINE, is applied together with the main surfactant (often CTAC), to induce chiral seeded-growth (Figure 6.1b). The aliphatic tails of LipoCYS are hypothesized to serve as anchor points for the LipoCYS-CTAC micelles. Therefore, when the surface coverage of LipoCYS is below a certain threshold, the micelles do not serve as templates for the growth of wrinkles and LipoCYS plays a similar role as that of cysteine, inducing chiral growth via the mechanism described in **Section 3.1**. In contrast, high concentrations of LipoCYS lead to the formation of NPs with well-defined helical wrinkles, typically obtained through micelle-directed growth, as discussed in **Section 3.2**.
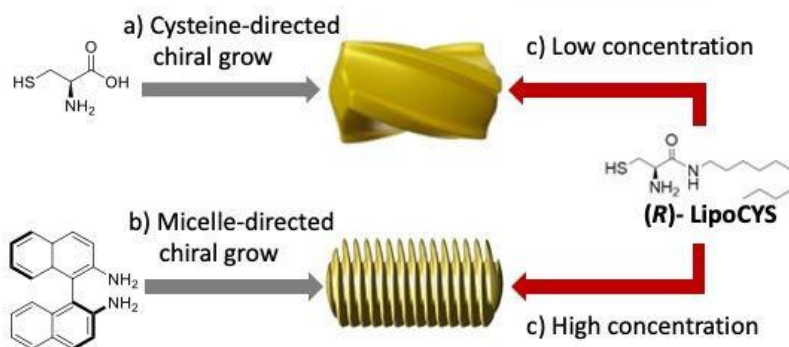
Figure 6.1 Schematic view of the mechanisms for seeded growth of chiral nanorods. a) Cysteine as chirality inducer, resulting in twisted NRs. b) Chiral growth directed by micelles containing BINAMINE as co-surfactant, resulting in a wrinkled particle structure. The use of LipoCYS (c) is proposed to bridge both growth mechanisms.

This chapter describes the role of a purposely devised chiral molecule consisting of a modified cysteine, (R)-2-amino-N-decyl-3-mercaptopropanamide (R)-LipoCYS (Figure 6.1c), as the chiral inducer for the seeded growth of gold nanorods. The presence of a cysteine-like head group and a longer hydrophobic tail was foreseen to provide a dual function, allowing high affinity for both the gold surface and the micellar system. LipoCYS is a versatile inducer that can produce both twisted and wrinkled chiral plasmonic nanoparticles as described above, depending on its concentration.

6.2 The gradual evolution from twisted to wrinkled morphology

To evaluate the performance of LipoCYS as a chiral inducer, the chiral growth of Au nanorod seeds is implemented experimentally. To characterize surface wrinkles and other geometrical features of resulting samples, ET is used to investigate the morphology and structural features in 3D, which can hardly be discerned in conventional 2D HAADF-STEM images. Experimental parameters of ET analysis can be found in Table 6.1. In this manner, by monitoring the resulting structural evolution of the particles obtained using different concentrations of LipoCys, the maximization of the dissymmetry factor (g-factor) becomes possible. The results of ET used for a

quantitative helicity analysis[193] (Figure 6.2) confirm the direct correlation between the handedness of studied NPs and the type of enantiomer used during the synthesis. These results are also supported with the dissymmetry factor (g-factor) values obtained from CD spectroscopy and electromagnetic simulations based on the obtained 3D reconstructions (Figure 6.3).
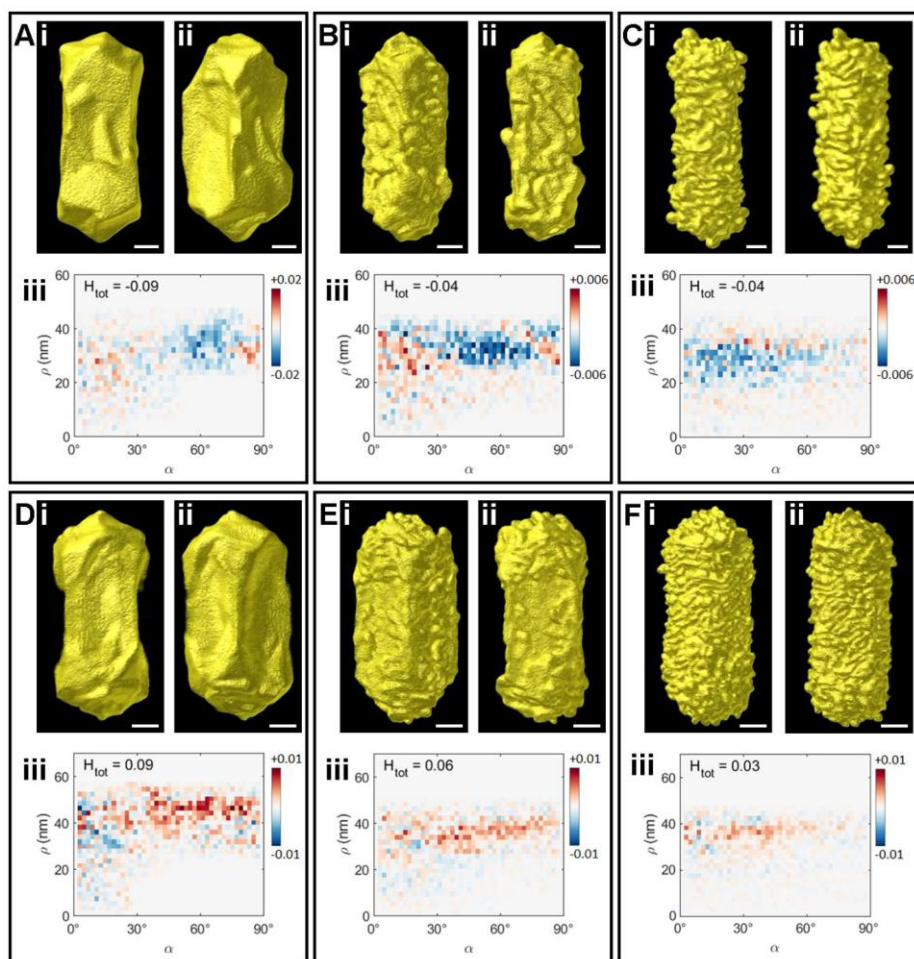
Figure 6.2 Isosurface visualizations of the 3D reconstructions (i, ii) for Au NRs obtained using different concentrations of (S)-LipoCYS (top) and (R)-LipoCYS (bottom) (A,D: 20 μM; B,E: 45 μM; C,F: 90 μM). Presented images are made along different viewing angles (oriented 45° relatively to each other) for each particle. Plots of the corresponding helicity function (iii; red: right-handed; blue: left-handed) are provided for each 3D reconstruction. All scale bars are 25 nm.

Table 6.1 Overview of the experimental parameters used for the investigation of chiral Au NR, shown in Figures 6.1 and 6.4.

Sample preparation	Drop casting of the aqueous solution
TEM grids	Conventional carbon coated Cu grids
TEM	Thermo Fisher Scientific Themis Z
Voltage	300 kV
Imaging mode	HAADF-STEM
Detector collection angle	100 – 200 mrad
Magnification	320 kx
Screen current	50 pA
Sample holder	Fischione 2022 tomography holder
Angular range/increment	-75° : 3° : 75° (51 projections)

Figure 6.3. A,B: Circular dichroism (g-factor) spectra (A) and absorbance spectra (B) for chiral Au NR colloids prepared using different concentrations of LipoCYS, as labelled. Solid and dashed lines correspond to results from particles synthesized with the (R) and (S) enantiomers of LipoCYS, respectively. The determination of g-factor is explained in more detail in **Section 1.2**. C,D: Simulated circular dichroism (C) and extinction (D) spectra for three models resembling the morphology of selected experimental samples (as indicated by the color code). Simulations were based on SIE-MoM (see **Section 2.5.5** for details).

It should be noted, that Au (chiral) nanostructures may be subject to degradation by electron beam irradiation at high dose typically used in ET studies. To verify that the optimized electron dose utilized during the tilt series acquisition did not damage the sample, compare projections taken at the same tilt angle before and after the acquisition of the full tilt series was compared for each studied particle. From the comparison shown in Figures 6.4a and 6.4b, no changes are obvious. To demonstrate the stability, the projections should carefully aligned be and subtracted corresponding pixel intensity values. The difference values are assigned to a representative color scale (e.g., magenta-green). The result is presented in Figure 6.4c, indicating no significant changes before and after the tilt series. Intentional color oversaturation of Figure 6.4c was performed to highlight minor differences (Figure 6.4d) that remain at the noise level.
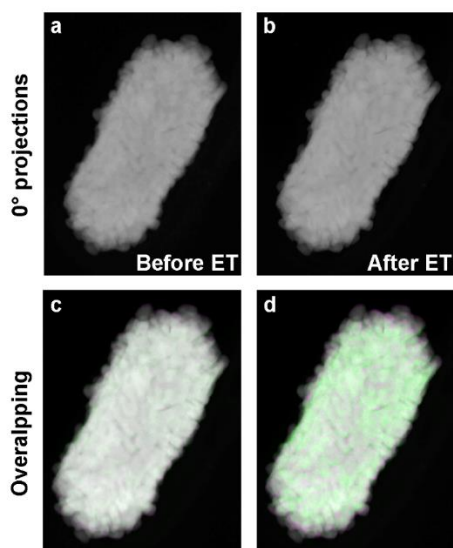
Figure 6.4 0° projections of chiral the Au NP taken (a) before and (b) after the tomography series acquisition. (c) The overlapping result of two projections and (d) its color saturation, showing no indication of morphological changes.

To gain further insight into the influence of LipoCYS concentration on the mechanism of chiral growth, I performed a detailed analysis of the morphology of the produced particles using HAADF-STEM tomography for both enantiomers, e.g., for (R)-LypoCys in Figure 6.5. Three-dimensional reconstructions of the NPs indicate an

evolution from relatively smooth surfaces at low LipoCYS concentration to densely wrinkled shapes at high LipoCYS content. For higher concentrations of LipoCYS, the average length of the wrinkles (~22 nm) and the distance between them (~2 nm) remain the same, regardless of LipoCYS concentration. At the same time, the average thickness of well-pronounced wrinkles slightly decreases (from ~7 nm to ~4 nm) when increasing the concentration of LipoCYS (examples are present in Figure 6.6). These values were obtained by manually measuring the parameters of the distinct wrinkles in the presented 3D reconstructions. Measured values were further averaged over a number of measured wrinkles. The obtained differences between the wrinkles parameters can be related to the formation and adsorption of LipoCYS-CTAC micelles on the surface of Au seeds: a higher amount of strongly bound micelles on the surface decreases the free area available for crystal growth. This observation is in excellent agreement with the hypothesis concentration dependent role LipoCYS during the chiral growth, proposed in **Section 6.1**.
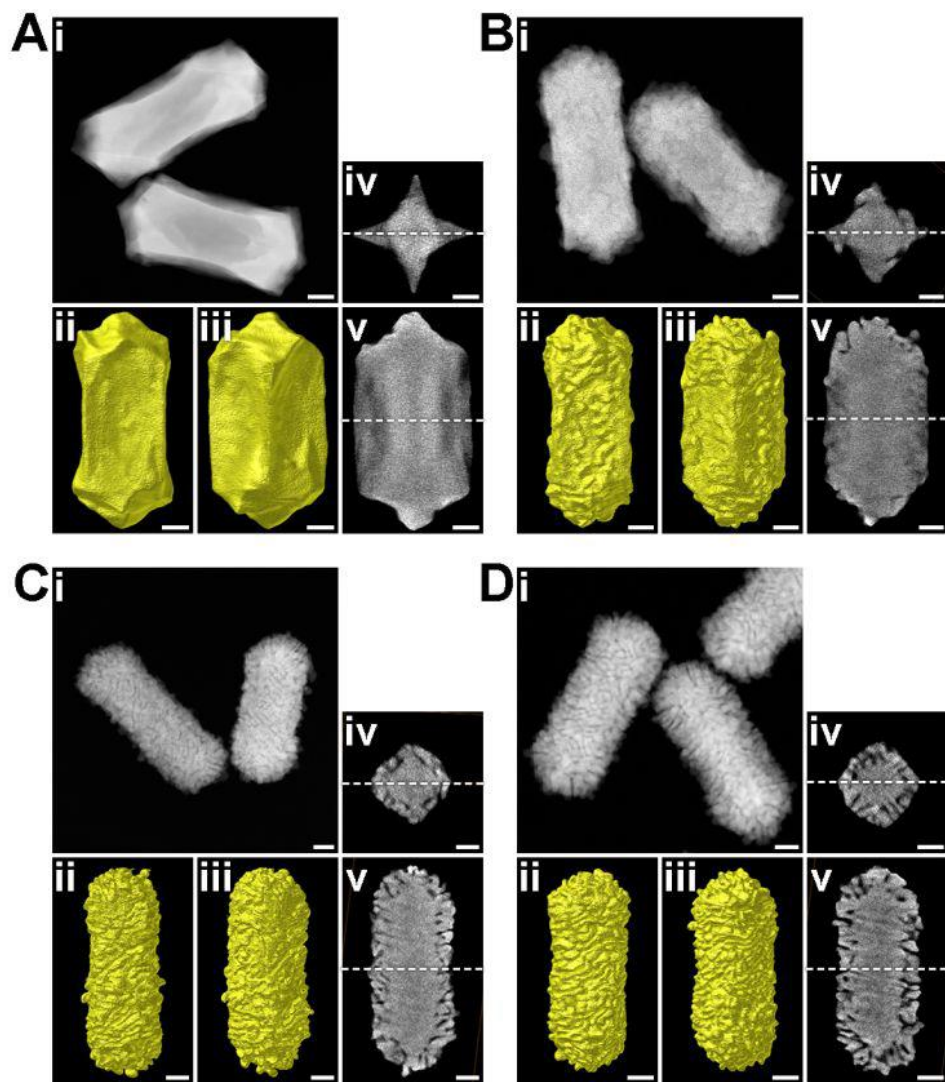
Figure 6.5 Morphological characterization of Au NPs obtained by increasing the concentration of (R)-LipoCYS (A: 20 μM, B: 45 μM, C: 75 μM, D: 90 μM) during chiral overgrowth. The morphological characterization for each sample includes: (i) HAADF-STEM image of several representative nanoparticles; (ii, iii) Visualizations of the 3D reconstructions, presented along different viewing angles (oriented 45° relative to each other); (iv, v) selected orthoslices extracted from the 3D reconstructions, perpendicular to the longitudinal and transverse axes, at the center of the NRs. White dashed lines represent the relative positions of slices shown in (iv) and (v). All scale bars are 25 nm.
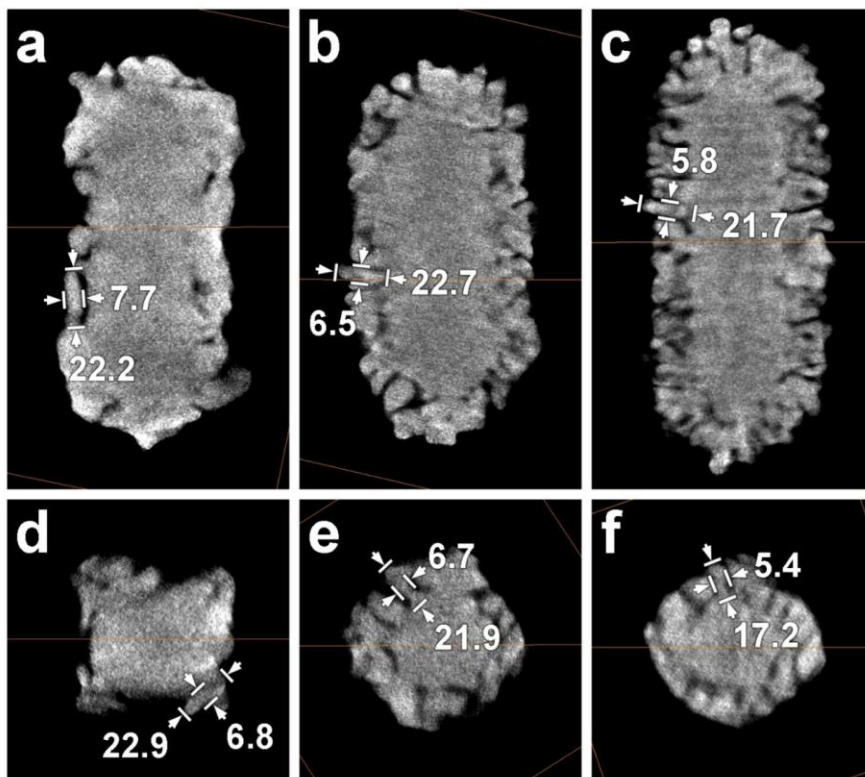
Figure 6.5 The evolution of the wrinkles parameters during chiral overgrowth: Selected orthoslices extracted from the 3D reconstructions, perpendicular to the longitudinal and transverse axes, at the center of the NRs (A,D: 45 μM, B,E: 75 μM, C,F: 90 μM of (R)-LipoCYS). All values are given in nm.

6.3 Growth mechanism dependence on the chiral inducer concentration

To further investigate the chiral growth mechanism for low LipoCYS concentration, the thorough analysis of the surface faceting is required. However, the relatively big size of the particles does not allow us to perform HR tomography experiment due to a limited field of view of the scanning engine of STEM, where only a small fraction of the studied particle can be seen at the sufficient magnification required for HR imaging. In addition, the depth of focus of a convergent electron beam is typically smaller than 10 nm, whereas the studied particles are approximately 50 nm thick. 2D HRTEM imaging

(Figure 6.7) enabled the approximate estimation of the crystallographic orientation of the studied particle, but fails to determine high index facets, e.g. {520}, even when combined with "low" resolution ET.
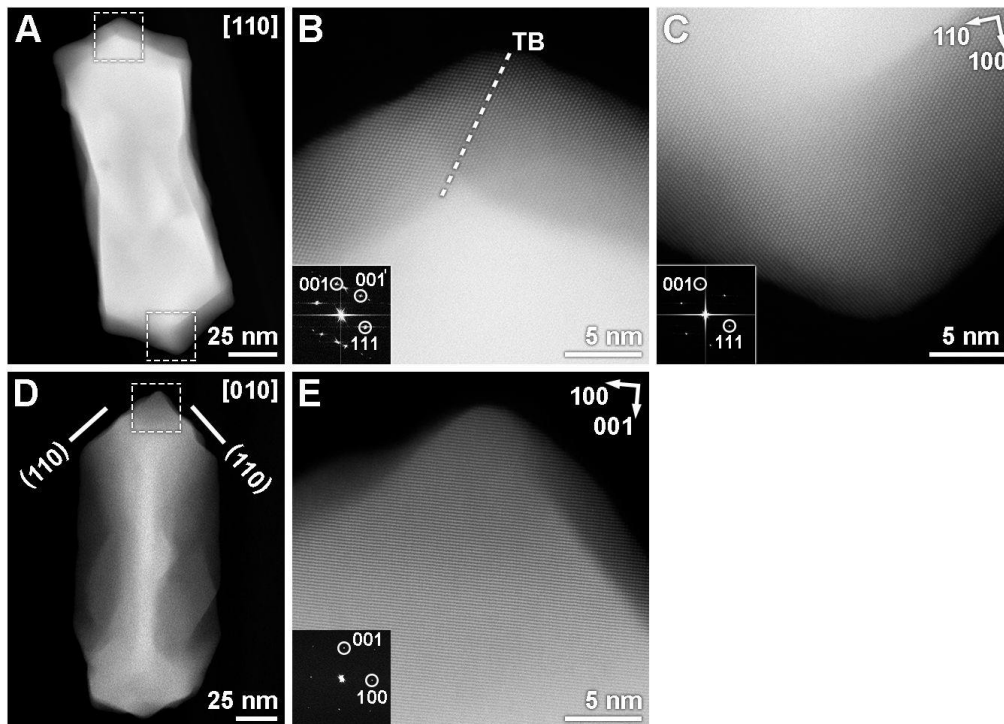
Figure 6.7 (A,D) HAADF-STEM images and (B,C,E) high-resolution HAADF-STEM images of a chiral Au NR prepared with (R)-LipoCYS (similar to that in Figure 6.4A), taken along [110] and [100] zone axis. The insets in (B), (C) and (E) show fast Fourier transform (FFT) patterns along [110] and [100] directions for the *fcc* lattice of Au, which indicate that the tips are enclosed by {110} facets.

To overcome this challenge, the combination of HAADF-STEM tomography and ED tomography was proposed to retrieve the information about the actual morphology of the studied particle together with the actual knowledge about its crystallographic orientation. Prior to tilt series acquisition, the surrounding of the particle chosen for the characterization should be examined so that it is distant from other particles. The required distance from the crystalline neighbours is determined by the diameter of the

selected area aperture (typically ~10 μm), that defines the beam size under the parallel beam conditions used in TEM. This ensures further acquisition of correct SAED projections, where the Bragg diffraction only occurs from the studied particle. Additionally, only single crystalline particles can be studied by these approach, since presence of such defects as twin boundaries will introduce additional uninterpretable reflexes to the obtained ED patterns. Eventually, the particle should be visible in as wide angular range as possible to reduce the missing wedge artifacts in both reconstructions.

After the appropriate Au NP was found, the experiment started by conventional HAADF-STEM tilt series acquisition using the experimental parameters, identical to those presented in Table 6.1. The reconstruction of HAADF-STEM tilt series was performed using EM reconstruction algorithm described in more detail in **Section 2.5.3**. The next step was the ED tilt series acquisition, that was performed by switching in TEM regime (diffraction mode). It should be noted that the tilt-step appropriate for a reliable 3D-ED reconstruction is typically lower than 1°, which significantly complicates the manual acquisition of tilt series.[68] Therefore, the automated continuous tilting of the stage was used. The speed of the rotation (~0.5°/s) was optimized with the integration time of the CCD (charge-coupled device) camera (1 s, 1024x1024 projections) to obtain consecutive ED projections at each 0.5°. After tilt-series were acquired they were used as an input for 3D-ED reconstructions performed in PETS2.0 software (see more details in **Section 3.6**). The next step was the careful alignment of HAADF-STEM and 3D-ED reconstructions in Amira software, that enabled the further analysis of the surface faceting. First, the relative orientation of 0° projections (Figure 6.8a,d) should be carefully checked. Due to the possible difference in configurations of used detectors (HAADF-STEM detector and CCD-camera in this case), the projections can be by rotated by 90° (or any other angle) with respect to each other. This can be checked by acquisition of the atomic resolution image and its comparison with corresponding SAED pattern. After the 0° projections were aligned, they were used to confirm correct relative orientation of central slices through both reconstructions (Figure 6.8b,e), followed by the final overlapping of both reconstructions (Figure 6.8c,f) as shown in Figure 6.8B.
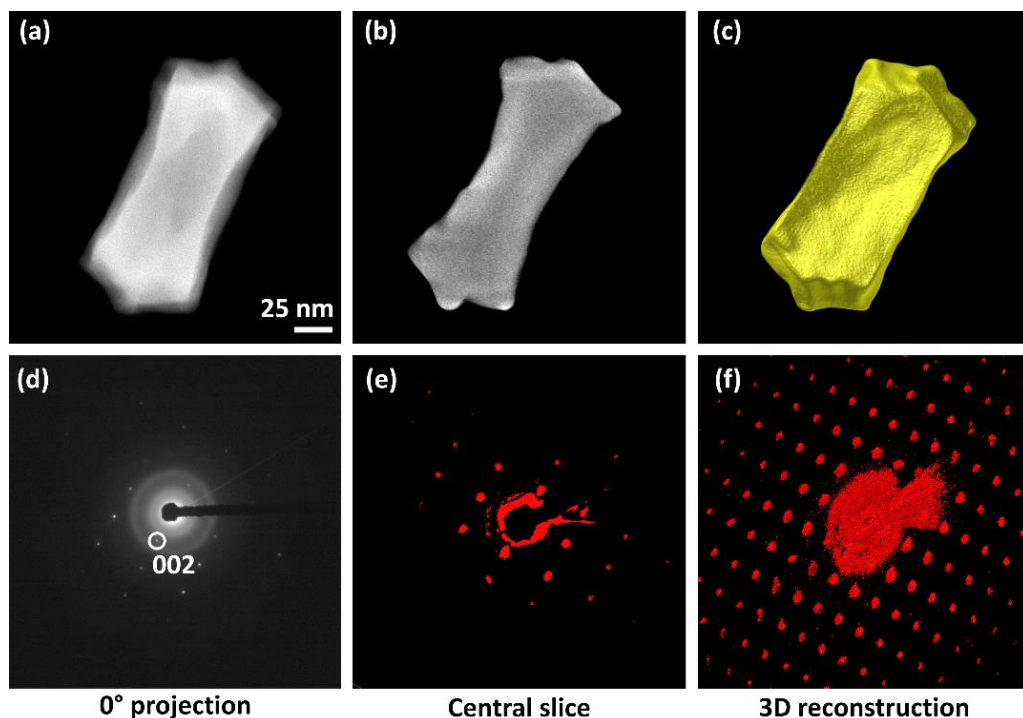
Figure 6.8 HAADF-STEM tomography and ED tomography of chiral Au NPs: (a,d) 0° projection, (b,e) central slice through the 3D reconstruction, (c,f) 3D reconstruction.

In this manner, it becomes possible to rotate the studied particle along the certain (especially high-index) zone axis orientations precisely and, therefore, to extract reliable data on the faceting of the features of interest. Orthoslices orthogonal to the [001] direction (Figure 6.9A) of the HAADF-STEM reconstruction indicate that the particle has a square-like cross-section, albeit with concave faces. Combination of tomography reconstructions in real and reciprocal space enables a detailed analysis of the various facets in the NP, by orienting it precisely along a given zone axis and inspecting the corresponding part of the NP surface perpendicular to that direction (Figure 6.9B). For instance, when orienting the particle along [520] as shown in Figure 6.9b (second image from the left) the vertical facets, parallel to the direction of view, will be perpendicular to <250> (similar to the purple facet from Figure 6.10a) and, thus, this facet is assigned to {250} family. Through this analysis, it can be concluded that the observed concave faces mainly consist of two facets belonging to the {520} family (Figure 6.9A).

Correspondingly, an idealized morphology is shown in Figure 6.9C. Further inspection of the orthoslices near the NP tips (Figure 6.9Ai,iii) indicates selective overgrowth at the corners of the two-sided faces (indicated by white arrows), resulting in a seemingly twisted structure. In the case of (R)-LipoCYS, this selective over-growth occurs on the top left and bottom right corners of each concave face, as also illustrated in the idealized model (Figure 6.9C). The concavity of the NR morphology in these regions can be expected to lead to local {521} facets at the top left and bottom right corners of the lateral facets and {52-1} facets at the top right and bottom left corners. Since these are chiral facets, the mechanism resulting in the final morphology would, therefore, be similar to that described in chapter 4. Finally, an inspection of the <111> and <011> corners (Figure 6.10b) indicates that they are twisted in a similar manner as the helicoids reported by Lee et al.,[214] likely intertwined with the presence of chiral facets. These observations prove the facet-dependent adsorption of LipoCYS at low concentrations, leading to twisted Au structures. The model particle form Figure 6.9C was also used as an input structure for electromagnetic simulations of chiroptical properties (inset in 6.3D), that were in an excellent agreement with CD-spectrometry results.
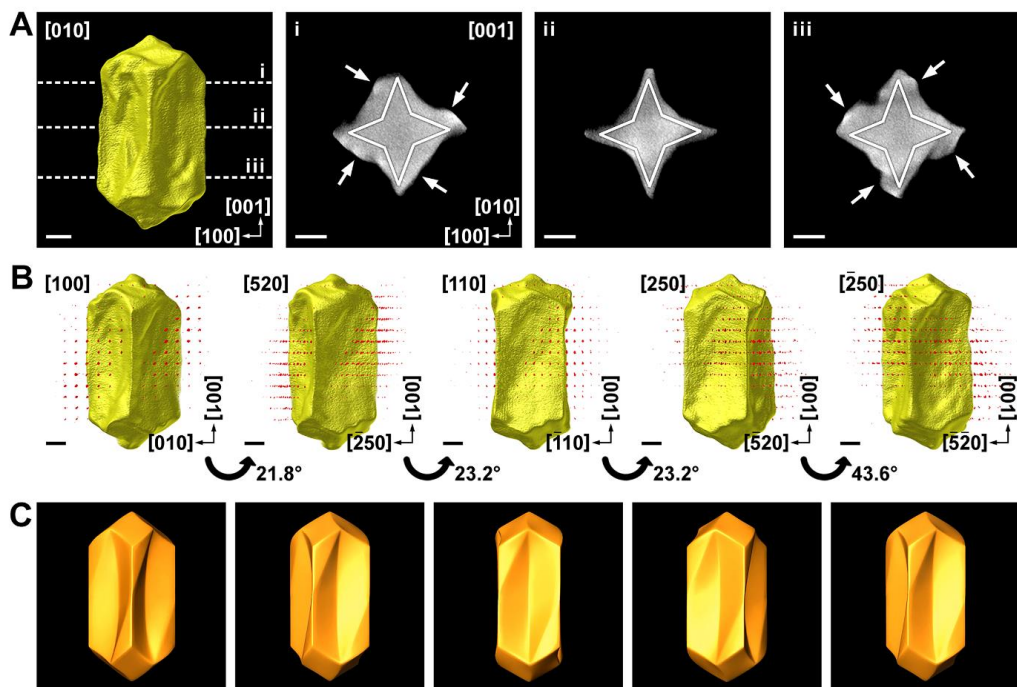
Figure 6.9 (A) 3D reconstruction and selected orthoslices of a twisted Au NR, obtained using 20 µM (R)-LipoCYS during chiral overgrowth, solid white lines indicate the expected crystallographic orientations of {520} facets. White arrows indicate positions where chiral overgrowth occurs. (B) Combined HAADF-STEM tomography (real space) and electron diffraction tomography (reciprocal space) reconstructions of the same particle oriented along [100], [520], [110], [250], and [–250], rotation angles as indicated. (C) Idealized chiral model of the same nanoparticle, oriented along the same directions as the corresponding panels in (B). All scale bars correspond to 25 nm.
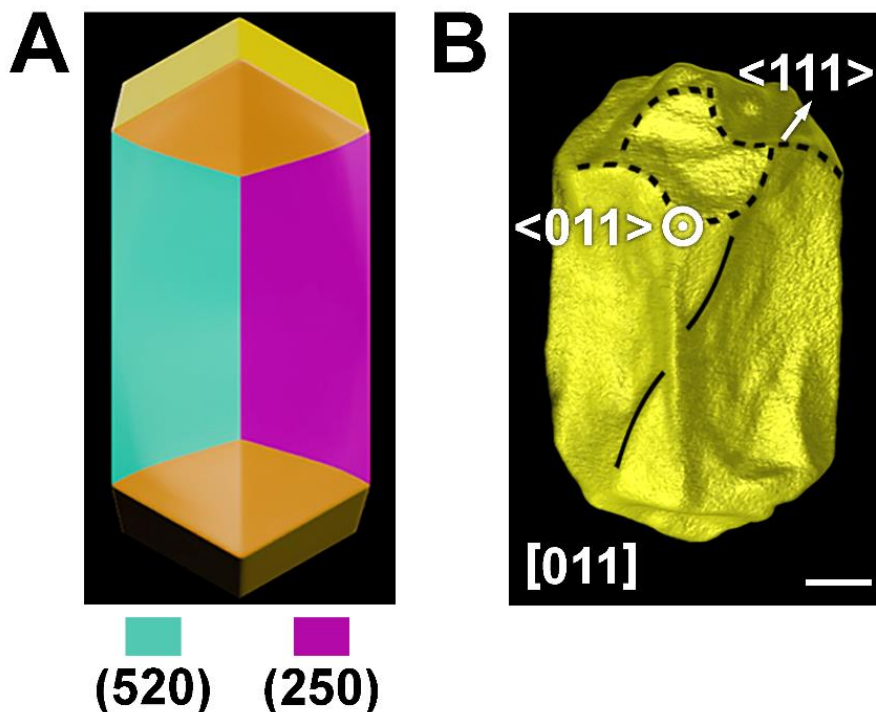
Figure 6.10 (A) Idealized model of achiral concave NP with 8 lateral {520} facets. (B) 3D reconstruction of a twisted Au NR, obtained using 20 µM (R)-LipoCYS during chiral overgrowth, shown along [011]. Solid and dashed lines highlight the presence of the twisted features at the lateral sites and at the tips. Scale bar is 25 nm.

It is worth mentioning that careful crystallographic analysis using 3D-ED, e.g. lattice parameter measurements, may require smaller tilt steps than used in this work (up to 0.1°/s), which was out of the scope of this work, where the study was performed on well-known crystal lattice of Au. However, in scope of future application of combined HAADF-STEM tomography and 3D-ED, the ability to precisely determine the lattice parameters of studied NPs along with the information about their morphology open promising prospects for, e.g. the investigation of phase transitions in nanomaterials.

6.4 Conclusions

This work demonstrates the chiral growth of Au NPs in presence of a novel chirality inducer – LipoCYS, combining both the properties of cysteine and chiral micelles. ET studies reveal the intricate morphologies of the produced particles and the transition for twisted structures into wrinked shapes when the concentration of LipoCYS increasing. This was explained by the certain threshold in the coverage of the surface of Au NPs, when the facet dependent adsorption of chiral amino group in the molecule of LipoCYS is supressed by the formation of chiral micelles. The helicity measurements performed on obtained 3D reconstructions are in an agreement with CD-spectroscopy analysis.

Additionally, the combination of HAADF-STEM tomography and ED tomography was implemented to confirm the formation of {520} facets for the particles obtained at low concentrations of cysteine. This is an additional proof of facet-specific adsorption of the chital amino group, included in the long aliphatic chain of LipoCYS. Information about the surface faceting obtained from the combined 3D reconstructions entitled the creation of the model structure, that was further used in electromagnetic simulations of the optical properties.

Another valuable outcome of this work is the demonstration of the capabilities, albeit only partial, of the combined HAADF-STEM and ED tomography. Due to the displayed ability to rotate the studied NP along arbitrary crystallographic directions, it is feasible make a reliable characterization of the surface features based on the reconstruction in the real space. Nevertheless, alternative application of this approach can be envisioned, e.g. the *in-situ* tomography instigations of phase transitions accompanied or induced by morphological changes at nanoscale.

Part 2

Thermal stability of Au@Ag core-shell nanoparticles.

Chapter 7. In situ heating 3D investigations of mono and bimetallic nanoparticles

One of the limitations during the ET investigation of mono and bimetallic NPs and their stability is the relatively long data acquisition (~1 hour per tilt series). Moreover, *in situ* heating investigations of such systems require the acquisition of several tilt series of same NPs after different heating steps. In addition, for better reliability, several particles deposited on the same heating chip should be studied during one experiment to ensure the same heating condition for all studied particles. In this manner, examining N particles after M distinct heating steps will necessitate capturing a total of (N×M) tilt-series. Multiplied by the acquisition time of a single tomography dataset, it becomes challenging for one to conduct the proposed experiment during one microscopy session. Therefore, one of the main aims of my PhD research was to reduce the time required to acquire ET dataset, which in turn allowed me to investigate the effect of different morphological parameters on heat induced alloying in Au@Ag NPs. In this chapter, I will illustrate the combination of fast tomography with *in situ* heating tomography holders, allowing for in-depth investigations of heat induced processes in different monometallic and bimetallic NPs.

7.1 Fast electron tomography

The recently developed approach for acquiring a tomographic series within much reduced time windows involves continuously rotating the sample holder while recording images of the studied object.[62] Unlike conventional tomographic acquisitions where the stage is manually re-centered in all directions before capturing a new projection image, fast tomography involves simultaneous image acquisition and stage adjustment, entailing the acquisition of hundreds of frames during the rotation process. The rotation speed of the goniometer is carefully selected to find an optimal balance between speed and image quality. Compared to conventional acquisition techniques, the total acquisition time for a tomographic series can be significantly reduced from around 1

hour to just 6 minutes when employing fast acquisition schemes.[62] The individual acquisition time for each frame in the tomographic series is typically short, around 1 second per frame. The decreased acquisition time enables the recording of more tomographic series within a one-hour timeframe, resulting in higher throughput for nanomaterial characterization.

However, fast tomography presents challenges related to tracking and refocusing the nanoparticle during the acquisition process.[62] When the goniometer is tilted, the particle experiences displacements in the x, y, and z directions of the stage. Consequently, motion-blurring artifacts may be present in some frames of the tomographic series (Figure 7.1a). These artefacts appeared as a directional band of frequencies in Fourier space (Figure 7.1b). Thus, they could be corrected for by applying a low pass filter within Fourier space (Figure 7.1c), resulting in improved image quality (Figure 7.2d). Projection images that were heavily affected by blurring or motion effects were afterwards excluded. However, these frames with motion artifacts only represent a fraction of the total number of projection images (e.g., 50 out of 360 frames) and their removal prior to tomographic reconstruction does not compromise the final result's quality.[62]
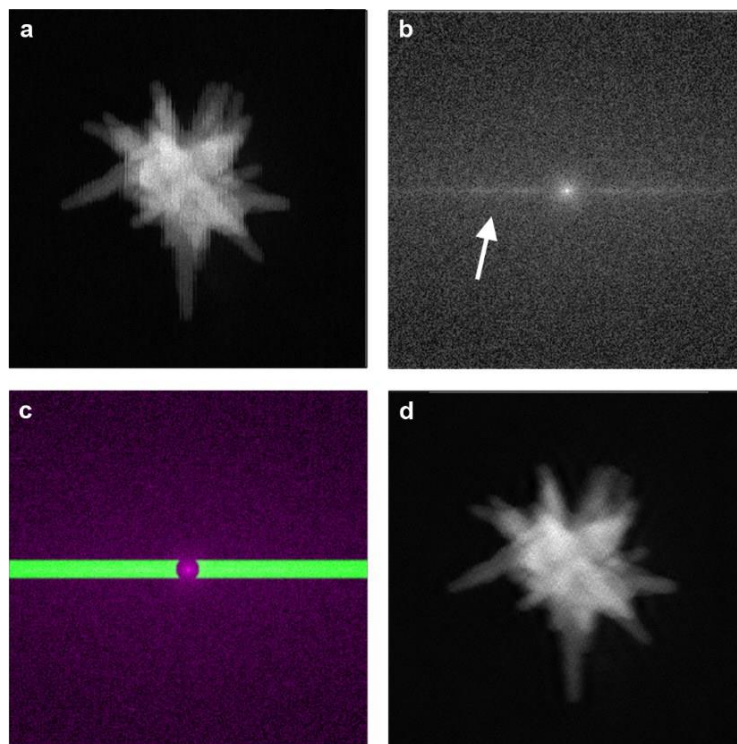
Figure 7.1 (a) HAADF-STEM image obtained during the fast acquisition of a single NS, revealing noise in the direction of scanning. (b) The amplitude of the Fourier transform of (a). The white arrow indicates the presence of directional noise at higher frequencies. In order to correct the projection images a dedicated low pass filter was used (c) to remove these higher frequencies and restore the projection image (d).[62] Image is taken from open access article distributed under the terms of the Creative Commons CC BY license (Copyright © 2018 The Royal Society of Chemistry).

To further improve the approach, e.g. to reduce motion-blurring artifacts, the concept of fast tomography was modified, resulting in so-called incremental tomography (See schematic representation in Figure 7.2). Specifically, a specially designed Python script is used to control the microscope stage and the HAADF-STEM detection system. This allows for continuous registration of all HAADF-STEM images while the script automatically tilts the sample holder in incremental steps (2-3° with a 5-10 second pause after each tilting step) across the entire range of tilt angles. The incremental approach requires slightly longer acquisition times (around 6-8 minutes), but the pause between

140

tilting steps allows the stage to stabilize and the microscopist can track the particle and adjust its position and focus to the optimal settings. This results in higher-quality data and reconstructions compared to the continuous approach. For instance, several NPs were studied employing both techniques using the same experimental conditions, where incremental approach showed lower volume error values compared to continuous counterpart, which is related to the blurring of projections caused by continuous movement of the stage.[236] An argument can be made that the sample focusing during the pause between automated tilting steps, as utilized in the incremental approach, along with subsequent exclusion of 'bad' projections, introduces a manual aspect, potentially leading to biased outcomes. This focusing process resembles that of conventional ET, where each projection is manually acquired. However, in numerous scenarios, this technique may be preferable over continuous tilting, which unavoidably leads to projection blurring due to mechanical stage vibrations. Achieving unbiased incremental ET acquisition necessitates the automation of all imaging steps, encompassing the tracking of the studied NP and its automatic focus. Regrettably, the advancement of this process is impeded by stage instabilities, particularly inconsistent shifts at different angles, where the particle drift during tilting cannot be accurately correlated with specific angular ranges. It should be also noted that the reduced acquisition time offered by fast tomography makes it particularly suitable for beam-sensitive materials, as it minimizes the total beam exposure (approximately by a factor of 10).

Continuous projections registration in preview mode (1 frame/~1.3 s, 1024 x 1024 pixels)
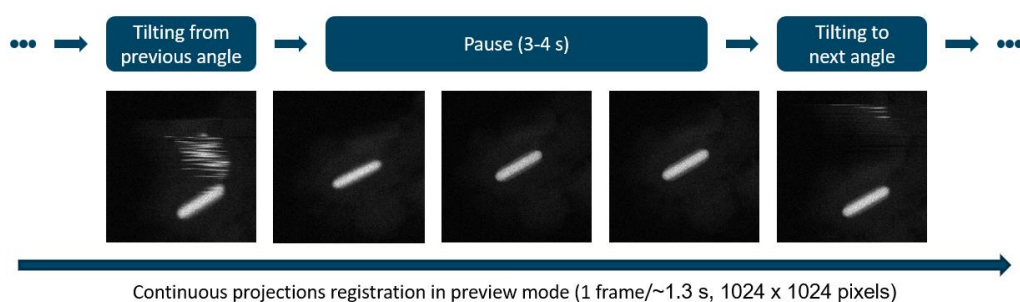
Figure 7.2 Schematic representation of incremental tomography approach.

Furthermore, the ability to capture the entire tilt series in approximately 8 minutes without significant information loss has enabled us to perform *in situ* alloying

experiments on multiple Au@Ag particles simultaneously within a single experiment, which is described in more detail in the **Chapter 8**. This advancement significantly increased the capability of *in situ* ET investigations of various complex nanomaterials at the nanoscale, which was one of the main goals of the REALNANO project (granted by European Research Council, ERC) provided the essential financial support for this work.

7.2 In situ heating tomography studies

To enable 3D *in situ* investigations on NPs, a MEMS-based DENSsolutions Wildfire heating holder optimized for ET can be utilized (Figure 7.3). This holder, combined with a tilting range of ±70°, enables heating the specimen from room temperature up to 1100 °C with a precision of less than 1°C. With these capabilities, detailed 3D *in situ* heating investigations of reshaping processes in Au[62] and Au-Pd [237] systems became possible, as well as alloying phenomena in Au@Ag NPs.[44] **Chapter 8** of my research work will extensively discuss the integration of the *in situ* heating holder with fast tomography techniques and atomic resolution tomography.

Figure 7.3 Heating tomography holder and schematics of the heating chip. Images are taken from DENSSolutions Wildfire Brochure (https://denssolutions.com).

The combination of fast ET with *in situ* heating tomography holders applied in EMAT has already enabled the 3D characterization of heat-induced morphological changes of highly asymmetric Au nanostars, which was further employed to investigate to influence of reshaping on the nanostars' plasmonic properties (Figure 7.4a).[62] In the following study, fast *in situ* heating ET was used to demonstrate the enhanced thermal stability of

Pd doped Au NPs even at 450 °C in a vacuum (Figure 7.4b).[237] Another particular example of the *in situ* heating investigation of Au@Pt NPs, was also conducted at EMAT, enabled the thorough analysis of the diffusion of Au and Pt in this system, where the redistribution of Au atoms form the core to the surface was shown to enhance the stability of the particles (Figure 7.4c).[147] It should be noted, however, that HAADF-STEM is a Z-contrast technique, which does not allow to distinguish between Au and Pt ($Z_{Au} = 79$, $Z_{Pt} = 78$), thus hindering the implementation of HAADF-STEM-based ET techniques to the investigation of heat-induced processes in Au-Pt systems. These results clearly demonstrate the capability to combine the *in situ* heating holders with (fast) ET techniques, thus, obtaining valuable information about the processes taking place in individual NPs
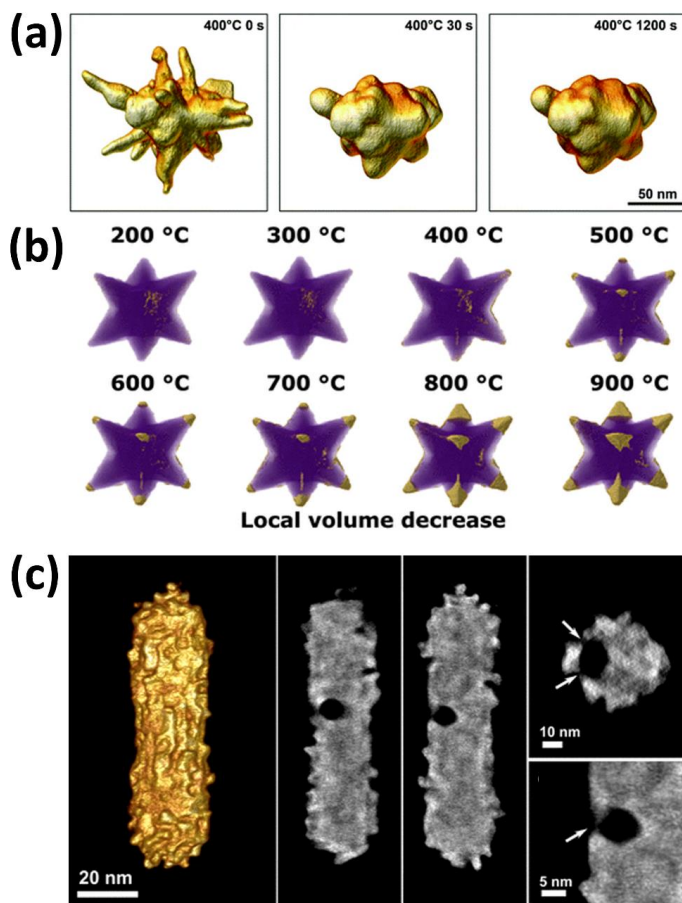
Figure 7.4 (a) 3D visualizations, using fast tomography, of an Au NS before and after heating for 30 and 1200 s at 400 °C.[62] Image is taken from open access article distributed under the terms of the Creative Commons CC BY license (Copyright © 2018 The Royal Society of Chemistry). (b) Volume redistribution of the heated Au-Pd octopod: 3D visualizations of local volume decreases (golden color) at different heating temperatures superimposed with the initial octopod morphology (purple).[237] Adapted with permission from ACS Nano (Copyright © 2019 American Chemical Society). (c) 3D reconstruction and orthoslises of Au@Pt NR after heating at 200 °C. Orthoslices through the 3D reconstruction show the presence of diffusion pathways for Au atoms (marked by white arrows) from the core on the surface, leading to a formation of voids within the volume of the NP.[147] Adapted with permission from ACS Nano (Copyright © 2022 American Chemical Society).

144

7.3 3D in situ heating investigations of alloying in Au@Ag NPs

The next effort to investigate the thermal properties of bimetallic NPs at EMAT was made for the alloying of Au@Ag NPs.[44] Based on the significant difference in atomic weights of Au and Ag, a methodology based on HAADF-STEM ET was proposed,[44] enabling to distinguish between these elements without using additional analytical techniques, e.g. EDX. In this manner, by implementing fast ET the heat induced elemental redistribution was observed in 3D for different individual Au@Ag NPs. Moreover the diffusion simulation method was proposed, allowing to investigate the alloying in quantitative manner.

The approach to obtain quantitative 3D compositional information at different time steps in the alloying process[44] is illustrated in Figure 7.5 and proceeds as follows: first a 3D HAADF-STEM reconstruction is obtained for an object where the constituting elements are not mixed, for example, a Au–Ag core–shell nanorod. After reconstructing the 3D distribution of the HAADF-STEM signal and thus removing the contribution of the projected thickness to the contrast, the remaining intensities in the 3D reconstruction only correspond to local elemental compositions inside the object (Figure 7.5a). Hence, the histogram of intensities inside the particle reconstruction shows a clear bimodal distribution in the case of a two-element system (Figure 7.5b), where maxima correspond to the expected intensity values for each element. Since Ag has a lower atomic number than Au, voxel intensities at the lower maximum and below can be attributed to pure Ag, whereas voxel intensities at the higher maximum and above correspond to pure Au. Furthermore, the intensities lying between the maxima are related to the elemental composition of corresponding voxels by the following relation (see the Supporting Information for derivation):

$$\omega_{Au} = \frac{I - I_{Ag}}{I - I_{Au}} \tag{7.1}$$

where I is the intensity of the voxel, ω_{Au} is the relative atomic content of Au in the voxel, and I_{Au} and I_{Ag} are intensities corresponding to pure Au and Ag, respectively. Figure 8.5c shows a slice through the 3D elemental distribution for the initial state of the Au–

Ag nanorod, obtained in this way, where red corresponds to pure Au and green to pure Ag. As can be seen, the resulting map clearly reflects the expected core–shell morphology of the particle. Equation 7.1 can now be used to estimate the local elemental compositions in the 3D reconstructions of the imaged object during the entire alloying process, provided that the imaging conditions were kept the same. Slices through the quantified 3D results for the nanorod after heating at 450 °C for 0, 60, 150, and 300 s are displayed in Figure 7.5d using the same red–green color map. The obtained elemental distribution maps display the expected gradual transition of the core–shell morphology of the nanorod into a homogeneous elemental distribution upon alloying. The dynamics of particles alloying can be directly followed from the histograms showing the intensities inside the volume of a nanoparticle. The two peaks, corresponding to the separate phases of Ag and Au for the initial core-shell particles (Figure 7.5b), gradually merge together until complete homogeneity is reached (one single peak in the histogram) at the end of alloying. Thus, the spread of the distribution in the histograms can be used to quantify the alloying progress. Here, degree of alloying was related to the standard deviation of the distributions in the histograms. After scaling the standard deviations between 0% for the initial core-shell state and 100% for the completely homogeneous material, this approach was used to compare the dynamics of the alloying process between different particles.[44]
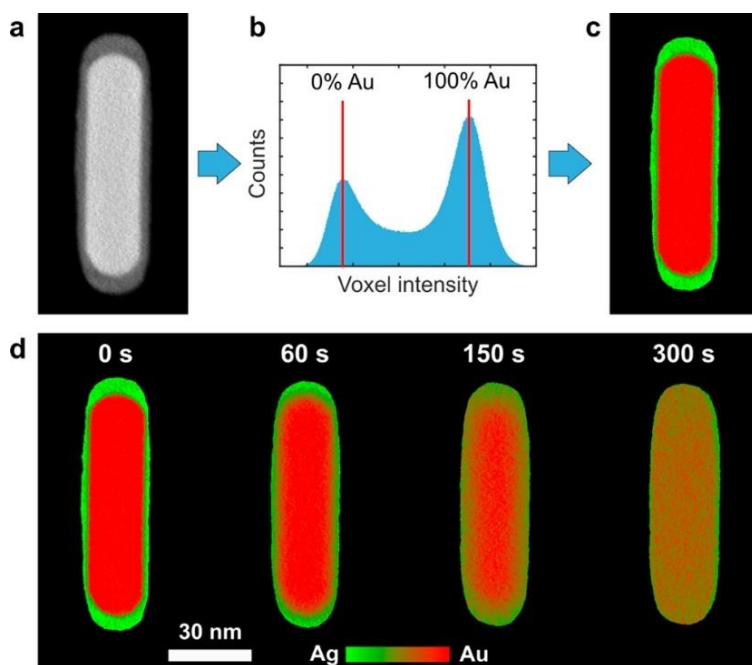
Figure 7.5 Schematic of the approach used to reconstruct the 3D elemental distribution inside nanoparticles upon heating. (a) Slice through the HAADF-STEM reconstruction of the Au@Ag core–shell nanorod. (b) Histogram of voxel intensities inside the particle; estimated intensity values for pure Ag and pure Au are indicated by red vertical bars. (c) Color map of the elemental distribution inside the slice of the nanorod before heating, where red corresponds to pure Au and green to pure Ag. (d) Slices through 3D compositional distributions inside the same particle at different stages of alloying upon heating at 450 °C.[44] Adapted with permission from ACS Nano (Copyright © 2019 American Chemical Society).

To gain more insight into the alloying process and diffusion dynamics in the studied NPs, experimental results were compared with 3D diffusion simulations. The simulations of elemental redistribution were based on a finite-difference approximation of Fick's second law, using a forward-time central-space (FTCS) method. The elemental distribution was defined on a uniform cubical grid derived from 3D reconstructions of the particles (voxel grid). Equation 7.1 enabled determining the Au-Ag ratio from voxel

intensity values. Fick's second law was approximated using the following convolution operation (Equation 7.2):

$$\frac{dC}{dt} = D \cdot (\Delta * C),\tag{7.2}$$

where $C = C(x, y, z, t)$ is 3D elemental distribution evolving in time, D is the diffusion coefficient, $*$ is a spatial convolution operation, Δ – discrete Laplace operator, defined as a 3D array Δ_{ijk} (Equation 7.3): [44]

$$\Delta_{ij1} = \begin{bmatrix} 0 & 0 & 0 \\ 0 & 1 & 0 \\ 0 & 0 & 0 \end{bmatrix}, \ \Delta_{ij2} = \begin{bmatrix} 0 & 1 & 0 \\ 1 & -6 & 1 \\ 0 & 1 & 0 \end{bmatrix}, \ \Delta_{ij3} = \begin{bmatrix} 0 & 0 & 0 \\ 0 & 1 & 0 \\ 0 & 0 & 0 \end{bmatrix}$$

$$\tag{7.3}$$

The elemental distribution was updated iteratively using Euler's method (Equation 7.4), starting from an initial state:

$$C(t + \Delta t) = C(t) + \frac{dC}{dt}(t) \cdot \Delta t\tag{7.4}$$

The time step Δt was set to be small enough to ensure the method convergence. A no-flow condition was imposed on the particle boundary at each time step. At all time steps a no flow condition was imposed on the boundary of the particle by locally setting the appropriate coefficients of the Δ operator to zero. The boundary was estimated in the same manner as the vacuum mask described in the elemental quantification procedure. All the described computations were conducted in the Matlab programming environment. [44]

The starting elemental distribution for simulations originated from particle reconstructions at initial time steps. The shape of the Au core was obtained by using $\frac{I_{Ag}+I_{Au}}{2}$ intensity as a threshold, whereas for the outer shape of the particle $\frac{I_{Ag}}{2}$ threshold was used. Edges of both masks were smoothed by applying a 3D morphological closing with a radius of 5 pixels. The Au content was set to 100% within the core and 0% between the core and outer shell. [44]

When obtaining the alloying curves based on the diffusion simulations results, the effects of limited projection angles and blurring were incorporated at each time step of the simulation. Next, the spread of voxel intensities was calculated and normalized between the values for the core-shell and the perfectly alloyed state of the particles using the same procedure as for the experimental data. [44]

This work has proposed the powerful approach for the investigation of heat-induced processes in Au@Ag, although systematic study of the parameters affecting alloying dynamics lied beyond the scope of this work.[44] Thus, in the next part of my thesis I aimed to conduct a more detailed examination of various structural and morphological parameters affecting the diffusion dynamics and, therefore the stability and properties of Au@Ag NPs.

Chapter 8. The influence of size, shape, and twin boundaries on heat-induced alloying in individual Au@Ag core–shell nanoparticles

This part is based on:

The synthesis of the samples was carried out at CIC BiomaGUNE in Donostia-San Sebastián, Spain.

I was responsible for fast *in situ* heating tomography experiments, data analysis and diffusion simulations.

The dynamics and mechanism of interdiffusion in bimetallic systems strongly depend on various aspects, e.g. NP composition,[47,48,238] size[46,238] or shape.[44,49] Additionally, a difference in core-shell interface[49] or the presence of twin boundaries, such as those in PT NPs, may also play a role.[50,51] Despite recent progress concerning the investigation of bimetallic systems using various experimental and simulation techniques, understanding of the mechanisms behind atomic diffusion at the single NP level is still far from complete. In fact, the diffusion dynamics are expected to be different at the nanoscale compared to the bulk, as indicated by orders of magnitude enhanced diffusion coefficients for Au-Ag NPs with sizes smaller than 5 nm, compared to bulk coefficients.[58] This phenomenon may be attributed to the inherently higher surface-to-volume ratio of nanomaterials in contrast to bulk materials. In nanomaterials, surface atoms exhibit increased mobility owing to the presence of uncompensated lattice bonds at the surface. Thus, a detailed understanding of nano-alloying processes and their dependence on relevant external stimuli and NP parameters is crucial for further improvement of NP properties and applications.

Because of its high spatial resolution, fast HAADF-STEM tomography has several advantages in comparison to ensemble-based techniques, such as Vis-IR spectroscopy [222] or extended X-ray absorption fine structure (EXAFS). [239] Since ET enables the investigation in 3D (over the volume of the NP), this approach is also superior to conventional two-dimensional (2D) (S)TEM techniques. [43,58] Major drawbacks of the techniques mentioned above, such as averaging of data over a large number of particles or the inability of performing *in situ* investigations in 3D, may result in discrepancies between different studies, especially for objects with complex morphologies. For example, significant divergence in alloying temperatures [43,55] or disagreement in diffusion speeds [43,44,46] for Au@Ag NPs of similar compositions and sizes have been reported.
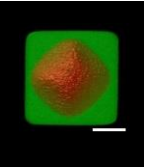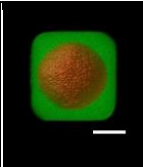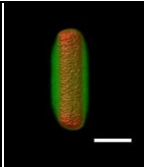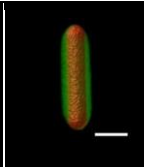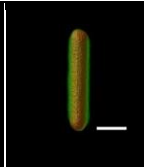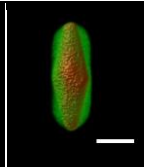
In this chapter, I use fast ET to perform 3D *in situ* heating investigations of different NPs under heating at 450 °C. I focused on SC and PT Au@Ag core-shell NPs with different sizes, aspect ratios and overall shapes. By characterizing NPs with a different core morphology, the effect of the type of interfacial facets could also be investigated.

A careful comparison enabled me to study the influence of each isolated factor on the alloying kinetics. For all of these systems, the diffusion dynamics was quantified by comparing experimental data to finite difference diffusion simulations based on Fick's law. These experiments yield novel insights on how parameters such as size, aspect ratio, core shape and the presence of twin boundaries influence heat-induced alloying in bimetallic core-shell NPs.

8.1 Experimental aspects of fast *in situ* heating tomography used in this work

Au-Ag NPs are ideal for the investigation of interdiffusion dynamics, since Au and Ag both crystallize in the *fcc* crystal lattice with almost identical lattice constants (0.408 nm for Au and 0.409 nm for Ag). This makes the elements completely intermixable, without significant lattice strain, and allows them to form alloys in the whole range of concentrations. Moreover, Au@Ag NPs are relatively stable under beam exposure in a TEM, while the significant difference in atomic number Z enables one to reveal Au and Ag distributions using HAADF-STEM. Previously, a fast HAADF-STEM tomography approach was implemented, which allowed authors to perform a quantitative analysis of the elemental redistribution in 3D for Au@Ag core-shell nanorods and nanotriangles.[44] Although these experiments served as a proof of principle of the technique, detailed understanding of key influences in the elemental redistribution process of nanomaterials is still lacking. Here, the analysis of elemental redistribution in Au@Ag NPs is extended to investigate the effects of size, aspect ratio, overall morphology, shape of the core and the presence of twin boundaries. The main focus was aimed at Au@Ag NPs with the following morphologies: SC Ag NC with either octahedral (OCT) or spherical (SP) Au cores, SC Ag NRs with Au NR cores and PT Ag NRs with NR or bipyramid (BP) Au cores. An overview of the investigated systems is provided in Table 8.1, where representative 3D visualizations of the corresponding tomography reconstructions for all NP types in their initial (room temperature) state are also included.

Table 8.1 Selected parameters of the investigated Au@Ag@m-SiO$_2$ NPs. The following abbreviations are used to describe the different types of NPs: SC – single-crystalline, PT – pentatwinned, NC – nanocube, NR – nanorod, BP – bipyramid, OCT – octahedron, SP – sphere. Volumes and AR values were extracted from 3D reconstructions of the initial (RT) state for all presented Au@Ag NPs, excluding the m-SiO$_2$ shell. Scale bars are 20 nm.

NPs						
	NC1	NC2	NR1	NR2	NR3	NR4
Au core	SC-OCT	SC-SP	SC-NR	SC-NR	PT-NR	PT-BP
Ag shell	SC-NC	SC-NC	SC-NR	SC-NR	PT-NR	PT-NR
Volume [10^3 nm^3]	195	148	14.1	24.7	17.5	27.5
AR	1	1	2.3	3.7	4.1	3.1
Au : Ag [at. %]	22 : 78	24 : 76	43 : 57	46 : 54	43 : 57	44 : 56

It should be noted that, thermodynamically driven reshaping of anisotropic morphologies due to atomic redistribution at the NP surface may hinder the interpretation of alloying experiments and even alter the mechanism of elemental redistribution.[49,62,240,241] Moreover, because of the lower activation energies, surface diffusion is typically faster in comparison to volume diffusion. To minimize reshaping of the NPs upon heating, all particles studied in this work were coated by a 20 nm thick mesoporous silica-shell (m-SiO$_2$).[242]

Prior to the actual alloying experiments, I carefully determined the most suitable experimental conditions to be used during *in situ* heating investigations. For example, reported alloying temperatures for Au@Ag core-shell NPs with sizes comparable to

those used in this paper range between 350 and 450 °C.[55,238] In order to determine an optimal alloying temperature, a preliminary *in situ* heating experiment was carried out. Relevant particles were hereby deposited from a colloidal dispersion on a MEMS-based heating chip and heated *in situ* heating from 20 up to 500 °C, in steps of 50 °C (the schematics of the experiment is presented in Figure 8.1a). The NPs were kept at the selected temperature for 5 minutes and the system was subsequently cooled down to room temperature. 2D HAADF-STEM images were acquired after every heating step for an overall visualization of the elemental redistribution and potential reshaping (Figure 8.1b). A slight reshaping, possibly due to a certain degree of flexibility of the mesoporous silica shell, was indeed observed around the tip of Au@Ag NRs at 250 °C, as marked by white arrows in Figure 8.1b. However, the overall shape of the NRs was preserved, even at longer heating steps and higher temperatures. From Figure 8.1 it is furthermore clear that alloying started to occur within the temperature range of 300-350 °C. For all subsequent experiments, we selected an operating temperature of 450 °C, which provided optimal alloying kinetics to track the most pronounced elemental redistribution during the first heating steps, while ensuring complete alloying within a time period of a few minutes.
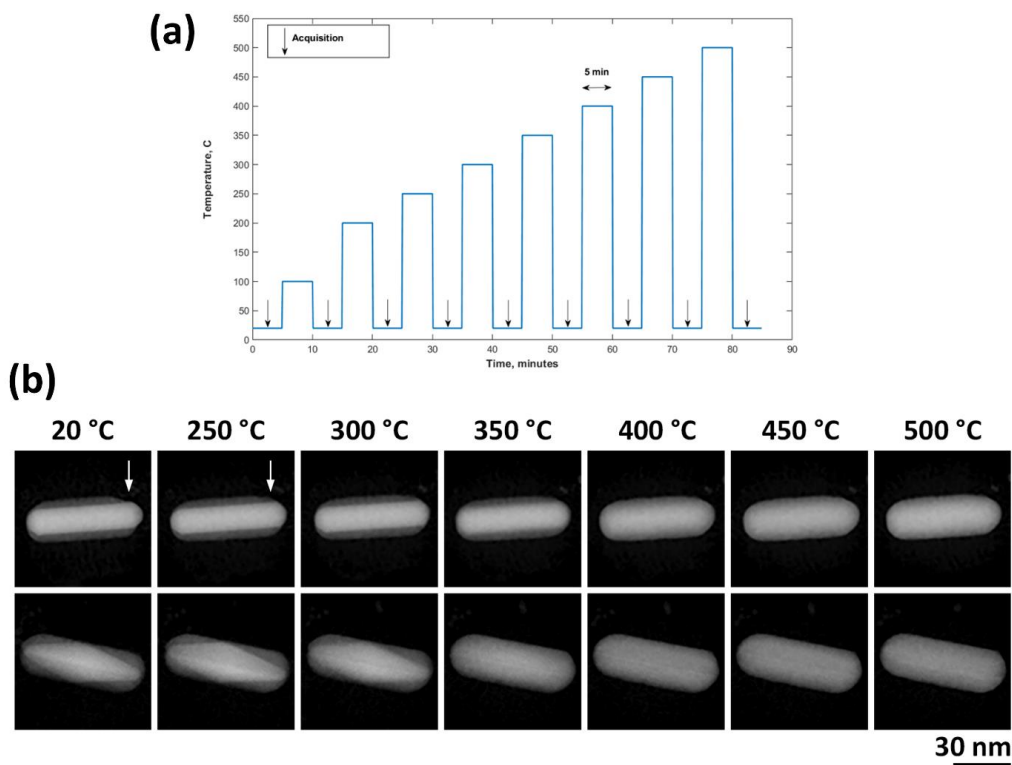
Figure 8.1 (a) The schematic representation of the preliminary *in situ* heating experiment. (b) HAADF-STEM images of the atomic redistribution inside an Au@Ag SC-NR (upper row) and an Au PT-NBP@Ag PT-NR (lower row), acquired at room temperature after heating for 5 minutes at the indicated temperature. In this additional experiment, SC-NR and PT-NR with sizes and composition similar to NR2 and NR4 were chosen, which allowed us to estimate 450 C as an optimal temperature for our alloying experiment.

In situ 3D investigation of heat-induced metal redistribution in individual Au@Ag core-shell NPs was performed by HAADF-STEM tomography using a DENSsolutions Wildfire MEMS-based heating sample holder, optimized for electron tomography. To induce alloying, all particles were heated at 450 °C for a total of 600 seconds. EDX mapping was performed for each particle before (0 seconds) and after heating (600 seconds) to confirm complete and uniform alloying at the final stage (Figures 8.2, 8.3). To investigate intermediate states, the heating process was interrupted after 15, 30, 45,

60, 90, 120, 180, 300 and 600 seconds by fast cooling (within less than 1 second), down to room temperature. Microscopic dimensions of the heating setup allowed rapid cooling by merely discontinuing the application of heat. This swift heat dissipation was made possible by the relatively massive metal components of the holder, which acted as efficient heat conductors. After every heating interval, a fast tilt series for tomography was acquired (experimental parameters can be seen in Table 8.2). From the 3D reconstructions, retrieved from every tilt series, the volumes of the investigated NPs were calculated. In this manner, I confirmed that the volume did not change for any of the studied NPs during heating. An example for NC2 is shown in Figure 8.3e. Given that both the volume and composition of all investigated NPs remained constant, it can be concluded that both Au and Ag redistributed only at the surface and within the volume of the presented NPs.
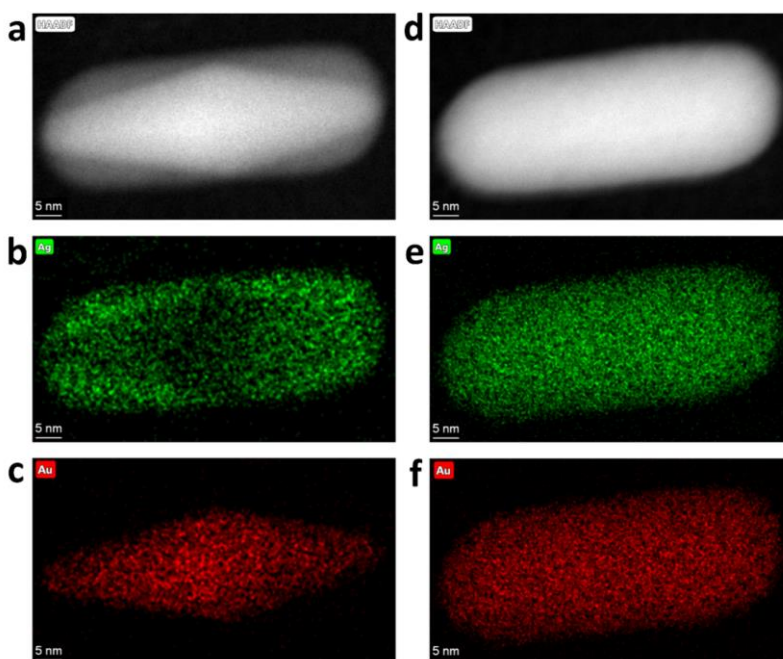
Figure 8.2 2D EDX mapping of NR4 before (a-c) and after heating for 600 seconds at 450 °C (d-f).
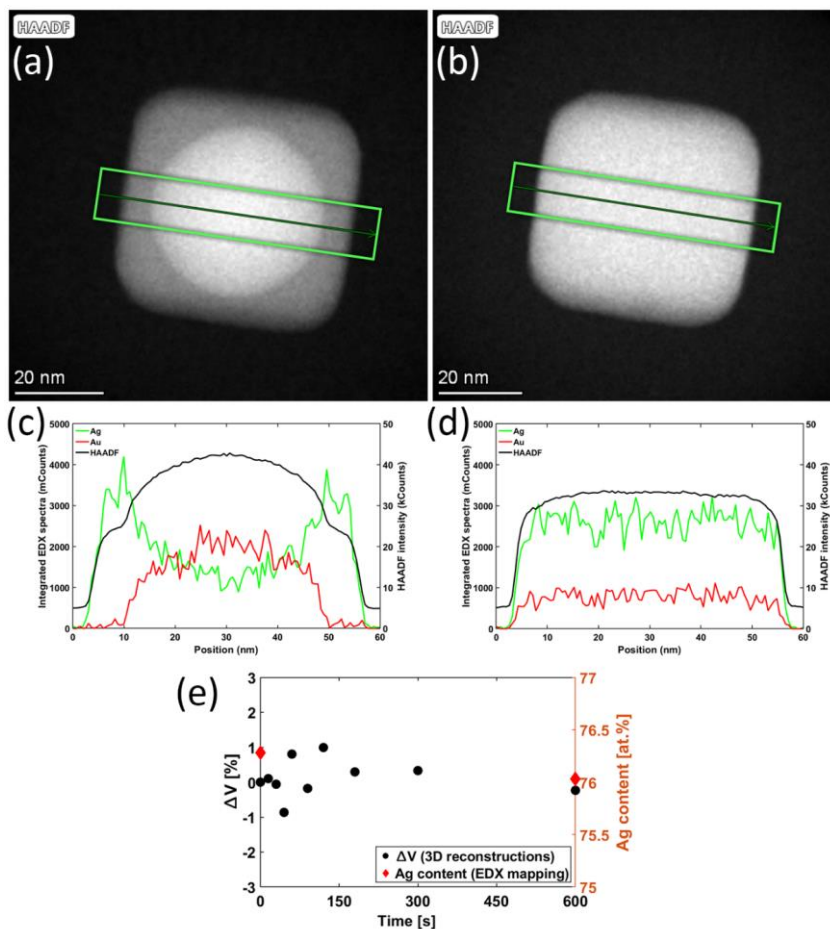
Figure 8.3 (a,b) HAADF image of NC2 acquired after 0 seconds (a) and 600 seconds (b) of heating. (c,d) Comparison between integrated line profiles based on the same region (green rectangle) of the 2D EDX elemental mapping before (c) and after (d) alloying. (e) Relative volume change (black circles) calculated from 3D reconstructions, and Ag content values (red diamonds) retrieved from EDX mapping before heating (0 s) and after the last heating step (600 s).

Table 8.2 Overview of the experimental parameters which are used for the fast *in situ* heating tomography investigation of Au@Ag NPs.

Sample preparation	Drop casting of the aqueous solution
TEM grids	Si_3N_4-based Wildfire chips
TEM	Thermo Fisher Scientific Themis Z
Voltage	300 kV
Imaging mode	STEM, (1024x1024)
Detector	HAADF, EDX
HAADF frame time	~1.3 s
Screen current	50 pA
Sample holder	DENSsolutions Wildfire heating tomography holder
ET mode	Incremental tomography
Angular range/tilt increment	-70° : 2 : 70°
Pause between tilt steps	7 s

8.2 Diffusion in Au@Ag nanoparticles

In this work, I first applied the quantification of alloying degree (see details in **Section 7.3**) to NCs with different shapes for the core: a slightly truncated octahedron for NC1 and a sphere for NC2 (Figure 8.4a and Table 8.1). The Au octahedral core for particles such as NC1 is mostly confined by (111) facets, whereas the Au sphere surface is formed by a wide variety of higher order facets.[243] In both NC1 and NC2, the Au cores were encapsulated by an Ag cube. By comparing the different types of NC, it is possible to obtain a comprehensive understanding of diffusion processes across different interfacial planes and along different axes in a single-crystalline structure. It is worth noting that no twin boundaries were observed in either NC1 or NC2 during the rapid ET acquisition.

Figures 8.4b and 8.4c illustrate the outcome of our experiments by showing slices through the 3D HAADF-STEM reconstructions along the [100] and [110] zone axes.

Since the intensity in HAADF-STEM images scales with the atomic number Z of the elements that are present, these 3D reconstructions could be translated into compositions by using a quantitative methodology described in section 8.3.[44] From the slices in Figures 8.4b and 8.4c, the redistribution of Au and Ag along different directions and after every heating interval at 450 °C can be readily monitored. It can be seen that alloying proceeds uniformly in all directions. These findings are in good agreement with existing literature, where it has been reported that the extent and frequency of atomic exchange events are expected to be the same for all directions in close-packed structures, as is the case for the *fcc* crystalline cell of both Au and Ag.[244]

However, one can notice a faster alloying rate for NC2 (Figure 8.4c) as compared to NC1 (Figure 8.4b), which may be related to the slightly smaller volume of NC2 (Table 8.1) and therefore, shorter distances for atoms to diffuse until alloying is completed. It is important to note that, on the basis of this qualitative comparison only, it is impossible to determine if the volume or the different morphology of the core and therefore different interfacial facets are responsible for the differences in the alloying behaviour.
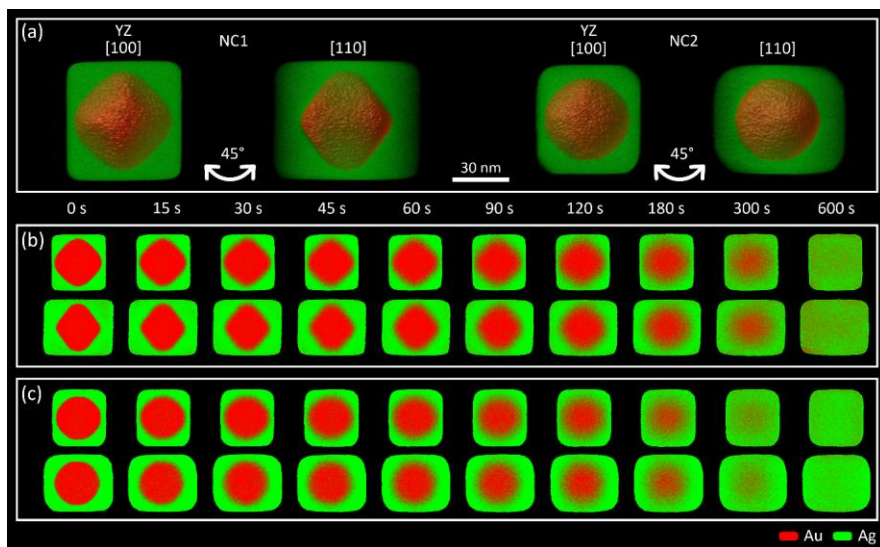
Figure 8.4 (a) Visualization of 3D reconstructions for NC1 and NC2, presented along [100] and [110] directions. (b,c) Corresponding slices through the 3D reconstructions, yielding the elemental distributions in NC1 (b) and NC2 (c), at different stages during alloying at 450 °C.

Based on the 3D reconstructions, I could quantify the degree of alloying after each heating interval (Figure 8.5a). The quantification procedure is based on the spread in the voxel intensity histogram (detailed description in **Section 7.3**).[44] In agreement with the visual interpretation from Figure 8.4, Figure 8.5a confirmed the slightly slower alloying of NC1 compared to NC2. It should be also noted that the influence of the missing wedge was clearly visible on the orthoslices in the XY-direction, manifesting itself as apparent Ag-rich regions along the vertical direction. This emphasizes the importance of including the missing wedge artifact in the diffusion simulation for accurate retrieval of the diffusion coefficients.

In order to eliminate the influence of NC volume and to enable a direct comparison between NC1 and NC2, I performed 3D diffusion simulations based on a finite-difference approximation of Fick's law using the tomography reconstruction at room temperature for each particle as an input (as discussed in **Section 7.3**).[44] In this thesis, the effect of Poisson noise on the spread of intensities was additionally incorporated in the simulations and implemented an automated fitting procedure to more accurately retrieve the value for the diffusion coefficient from experimental data. The amount of noise in the experimental reconstructions was estimated using the reconstructions of the particles in the fully alloyed state. To exclude the influence of artifacts coming from the limited tilt range of the sample holder, a central slice is used through the reconstruction in the direction perpendicular to the "missing wedge" of projections. Since the elemental distribution in this case is expected to be completely homogeneous, the remaining intensity variations in the reconstruction can be attributed purely to noise. The scale of noise was estimated by calculating the standard deviation of intensities within the particle mask. Fitting of the simulated alloying curve to experimental metrics was performed by numerical minimization of the mean squared difference between the experimental and simulated data as a function of diffusion coefficient using Brent's algorithm[245] implemented in MATLAB. The uncertainty of the diffusion coefficient fitting was calculated using the finite-difference approximation of Fisher information at the optimal point of the fitting.

During our experiments, it was observed that both particles underwent minor reshaping during heating, leading to slightly more rounded vertices and edges, which should be considered for a more accurate quantitative description.[44] Hence, the observed reshaping was included in the simulations by applying a mask, corresponding to the deformed shell of the NP, to the reconstruction obtained at room temperature. The resulting morphology was then used as an input for diffusion simulations. Moreover, missing wedge artifacts together with Poisson noise were also included in the simulations to make a more accurate comparison with the experimental results. By fitting the outcome of the simulations using different diffusion coefficients to our experimental observations, I was able to determine the best match for this coefficient, as shown in Figures 8.5b and 8.5c. The optimal fit corresponds to the blue dashed lines with diffusion coefficients of $(2.7 \pm 0.1) \times 10^{-19}$ m^{2}s^{-1} for NC1 and $(2.4 \pm 0.2) \times 10^{-19}$ m^{2}s^{-1} for NC2. Figures 8.5d and 8.5e show slices through the experimental 3D reconstructions and the corresponding simulations along the [100] direction. This conclude that the diffusion coefficients for NC1 and NC2, which are not influenced by differences in NC volume, have comparable values. These results therefore indicate that the interdiffusion kinetics at high temperature in isotropic single-crystalline Au@Ag NPs do not appreciably depend on the details of the Au-Ag interface.

Figure 8.5 (a) Comparison of the alloying progress for NC1 and NC2. (b,c) Comparison of the experimental results to the diffusion simulations performed for different diffusion coefficients. The degree of alloying was quantified from the experimental data (black circles) for NC1 and NC2, respectively. The blue dashed curves correspond to the best fit of simulations to the experiments for diffusion coefficients of 2.7×10^{-19} m^{2}s^{-1} for NC1 (b) and 2.4×10^{-19} m^{2}s^{-1} for NC2 (c). For both NCs, the red curves correspond to simulations based on a diffusion coefficient of 10×10^{-19} m^{2}s^{-1}, whereas the green curves were obtained using a diffusion coefficient of 1.0×10^{-19} m^{2}s^{-1}. These values were chosen to demonstrate the influence of diffusion coefficient value on the alloying kinetics; (d,e) The upper rows show slices through the experimentally determined 3D elemental distribution in NC1 and NC2, respectively, at different stages of alloying. The lower rows display slices through the simulated 3D elemental distributions using the optimal diffusion coefficient.

8.3 Shape and twin boundaries effects on elemental redistribution

To investigate the effect of aspect ratio, presence of twin boundaries and core shape during heat-induced alloying, four different types of Au@Ag NRs with similar compositions were studied (Table 8.1: NR1-4 and Figure 8.6a). For comparison, I selected pairs of NRs, which differ in only one parameter: aspect ratio in the case of NR1 and NR2, absence or presence of twin planes and a different shape of the core for NR2 and NR3. Finally, NR3 and NR4 were also compared, both PT-NRs, but with a PT-NR and a PT-BP core, respectively. For each comparison, the other parameters had similar values, which enabled the investigation of the separate influence of each factor on the alloying dynamics. Any dependence on volume could again be eliminated by comparing the extracted diffusion coefficients.

Figure 8.6b,c shows the experimental results for all four NRs. Similar to the NCs, elemental diffusion proceeded uniformly in all directions. In addition, for the larger PT-BPs (NR4) a darker and hence seemingly greener region in the YZ orthoslices in the middle of the particle could be observed. We attribute this effect to remaining diffraction contrast due to the pentatwinned structure.
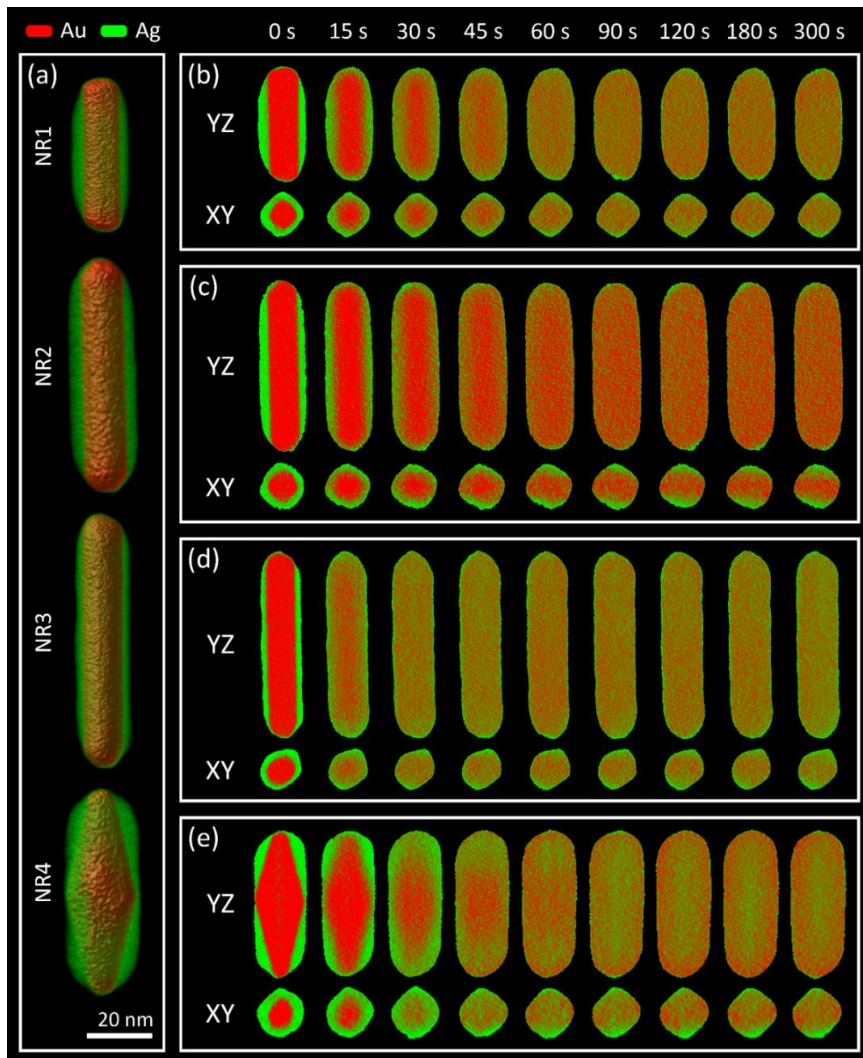
Figure 8.6 (a) Visualization of 3D reconstructions for NR1, NR2, NR3, and NR4. (b-e) YZ- and XY- slices through the 3D reconstructions of elemental distributions at different stages of alloying at 450 °C.

The degrees of alloying for all NRs were calculated from 3D reconstructions after each heating interval, in the same manner as described above for NCs, and the results are presented in Figure 8.7a. The best fits of the 3D diffusion simulations to the experimental data are summarized in Figure 8.7b-e. The corresponding fitted diffusion coefficients are listed in Table 8.3, together with values for NC1 and NC2, as a

reference. YZ-slices through the 3D simulated reconstructions after each heating step, as well as the corresponding experimental YZ-slices, are presented in Figure 8.7f-i for all NRs. Also for NRs, fitting of the simulated diffusion curves resulted in good agreement with the experimental data, confirming the appropriate performance of our simulation model, which results in reliable diffusion coefficients. However, a slight difference in apparent composition between simulations and experimental results could be observed during the latter heating steps (Figure 8.7f-i). This cannot be related to actual differences in composition, which are the same for the experiments and simulations and stayed constant over the course of the experiment. It is also worth noting, that diffraction contrast due to the presence of twin boundaries was observed in PT NPs after each heating step.

Table 8.3 Values for diffusion coefficients, obtained by 3D diffusion simulations and comparison to experimental data. Uncertainties for the diffusion coefficients were estimated by fitting the experimental data with simulated alloying curves and correspond to the standard deviation of this parameter.

Particle	Defect structure	Core-Shell morphology	Volume [10^3 nm^3]	AR	Au : Ag [at.%]	D [10^{-19} m^{2}s^{-1}]
NC1	SC	OCT @ NC	195	1	22 : 78	2.7 ± 0.2
NC2	SC	SP @ NC	148	1	24 : 76	2.4 ± 0.3
NR1	SC	NR @ NR	14.1	2.3	43 : 57	3.4 ± 0.4
NR2	SC	NR @ NR	24.7	3.7	46 : 54	2.9 ± 0.2
NR3	PT	NR @ NR	17.5	4.1	43 : 57	6.0 ± 0.2
NR4	PT	NBP @ NR	27.5	3.1	44 : 56	6.3 ± 0.4

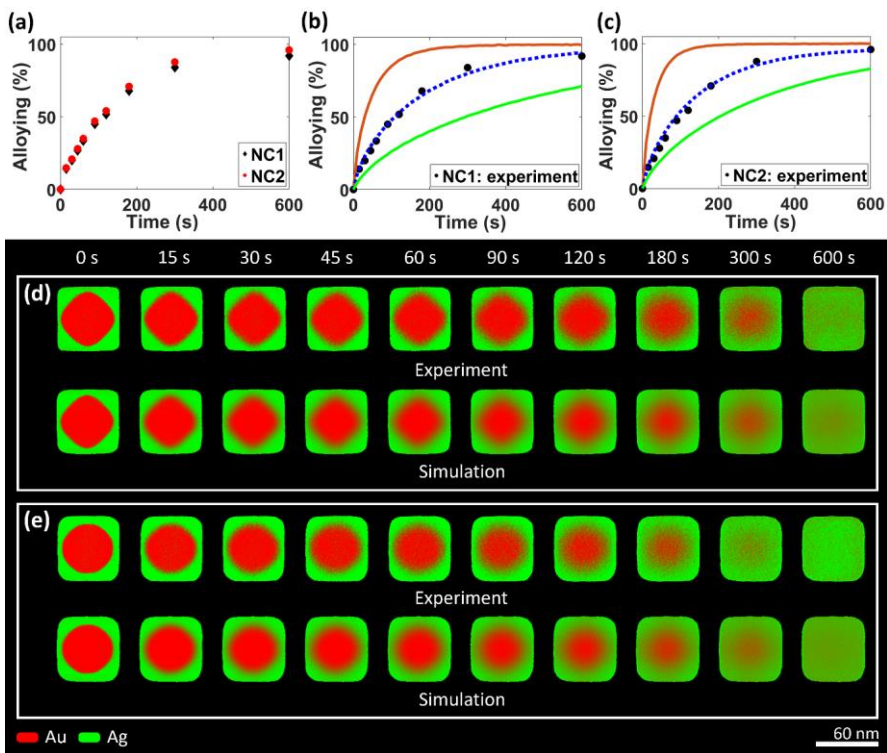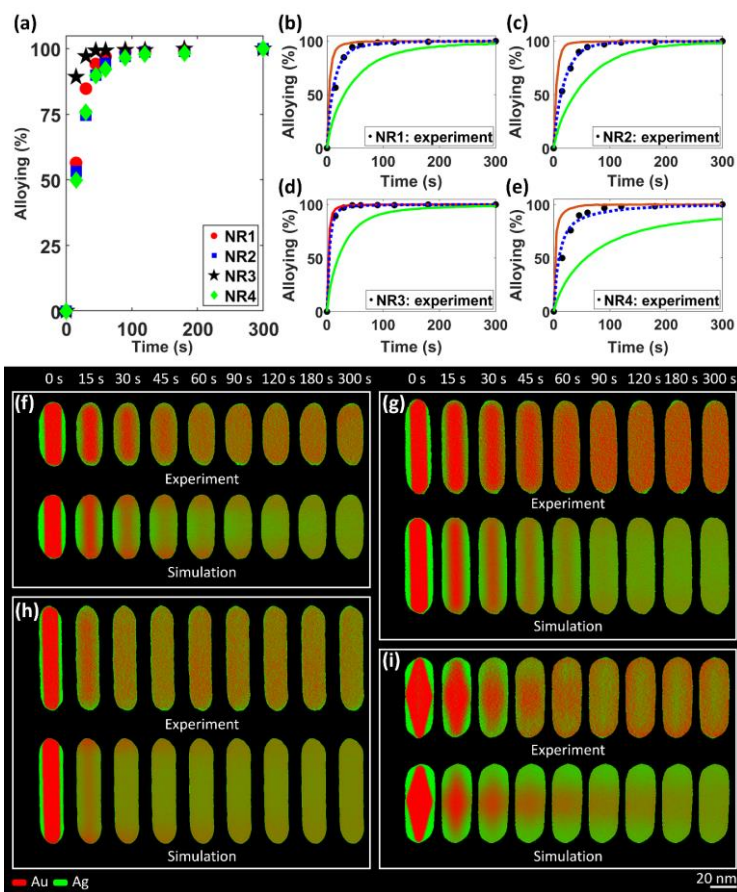**Figure 8.7** (a) Comparison of the alloying progress for NR1-4; (b–e) Comparison of the experimental results and diffusion simulations performed for different diffusion coefficients. The degree of alloying was quantified from the corresponding experimental data (black circles) for NR1-4. The blue dashed curves correspond to the best fit of simulations to experiments for diffusion coefficients of 3.4×10^{-19} m^{2}s^{-1} (b), 2.9×10^{-19} m^{2}s^{-1} (c), 6.0×10^{-19} m^{2}s^{-1} (d), and 6.3×10^{-19} m^{2}s^{-1} (e), for NR1-4 respectively. For all NRs, the red curves correspond to simulations based on a diffusion coefficient of 10×10^{-19} m^{2}s^{-1}, whereas the green curves were obtained using a diffusion coefficient of 1.0×10^{-19} m^{2}s^{-1}. These values were chosen to demonstrate the influence of diffusion coefficient value on the alloying kinetics; (f–i) The upper rows display slices through the experimentally determined 3D elemental distribution for the various NRs at different stages of alloying. The lower rows display slices through the simulated 3D elemental distribution using the optimal diffusion coefficients.

From Table 8.3, it can be concluded that the obtained values of diffusion coefficients for all NPs investigated in this work are of the same order of magnitude as those reported for Au and Ag interdiffusion in bulk Au-Ag solid solutions and for single-crystalline Au/Ag thin films.[246,247] This suggests that the difference in the volumes of the NPs at the investigated length scale does not affect the alloying dynamics significantly. A slightly higher diffusion coefficient can be observed for SC-NRs when compared to SC-NCs. In this case, the difference in composition (~45 at.% of Au for NR1 and NR2, ~23 at.% of Au for NC1 and NC2) plays a role in the alloying dynamics, due to the different mobility of Ag and Au atoms. Indeed, for particles with a higher Ag content, relatively slow Au atoms limit the alloying rate, since they require longer times to diffuse over longer distances and to get uniformly redistributed within the volume of the particle. A composition-dependent behavior of alloying in Au@Ag NPs of comparable sizes has been reported elsewhere.[44,238]

Interestingly, about twice higher diffusion coefficients were obtained for PT-NRs (6.0×10^{-19} m^{2}s^{-1} for NR3 and 6.3×10^{-19} m^{2}s^{-1} for NR4) in comparison to SC-NRs (3.4×10^{-19} m^{2}s^{-1} for NR1 and 2.9×10^{-19} m^{2}s^{-1} for NR2). The faster diffusion observed for PT-NRs can likely be attributed to a faster atomic transport due to distortions in the crystal lattice, caused by defects. The boundary between two twin planes may contain a higher amount of vacant sites and longer distances between neighbouring sites, thereby creating pathways for faster and easier atomic transport along these boundaries. A similar enhancement of diffusion kinetics due to the presence of twin boundaries has been previously suggested in the literature,[244] whereas the presence of lattice vacancies was shown to significantly increase diffusion dynamics in bimetallic NPs.[46] As an additional proof of the faster diffusion in the presence of twin boundaries, it should be noted from 8.1b that the starting alloying temperature for PT-NRs (~300 °C) is lower than that for SC-NRs of comparable volume (~350 °C).

Based on the comparable values of the diffusion coefficients for NR1 and NR2, it can be seen that a difference in AR (2.3 vs. 3.7) in rod-like Au@Ag NPs did not affect the diffusion dynamics significantly. Along with the difference in AR, NR3 (AR=4.1) and NR4 (AR=3.1) also displayed a different morphology for the Au core (PT-NR and PT-BP), leading to different interfacial facets. Still, these NRs yielded comparable diffusion

coefficients. Together with the results obtained for NC1 and NC2, this allows me to conclude that the kinetics of alloying in isotropic and anisotropic Au@Ag NPs do neither depend on the direction of diffusion inside the lattice cell nor on the difference in the type of Au-Ag interfacial facets. Interestingly, these findings are not in agreement with the alloying behaviour reported for Pd@Pt NPs, where a lower temperature threshold for core-shell interdiffusion was observed for octahedral core-shell NPs in comparison to cubic core-shell NPs.[49] This was explained by a higher tendency for subsurface Pt vacancy formation in octahedra than in cubes, which governs interdiffusion of atoms between core and shell of the NP.[49] Enhanced diffusion kinetics in the presence of vacancies in the vicinity of the bimetallic interface was observed for Au@Ag NPs.[46] However, these investigations were performed for spherical NPs, where no information about the influence of Au-Ag boundary faceting could be extracted.

Since all NP systems described so far yielded diffusion coefficients comparable to the bulk scale, I investigated an even smaller nanorod (SR), with aspect ratio and composition similar to NR1, but with significantly (~10 times) smaller volume (Figure 8.8). From a visual inspection, the SR appeared to be fully alloyed after a short heating time between 5 and 10 seconds. Despite the presence of a mesoporous-silica shell and shorter heating times, a significant reshaping of the SR is observed, meaning that at this scale surface diffusion, or even local melting, dominated over lattice diffusion. The main reason for the lower stability of the SRs is the significantly higher fraction of active and mobile surface Ag atoms, which can be estimated from the surface-to-volume ratio of these NPs: 0.49 nm^{-1} for the SR vs. 0.26 nm^{-1} for NR1. Still, the value of the diffusion coefficient for the selected SR can be approximately estimated by performing 3D simulations of elemental diffusion, using the initial shape and elemental distribution from experimental data in the same manner as explained above. As can be seen from the simulations for different diffusion coefficients in Figure 8.9, the SR would be fully alloyed after 5 seconds if $D = 10 \times 10^{-19}$ m^{2}s^{-1}. For simulations performed using $D = 1 \times 10^{-19}$ m^{2}s^{-1}, incomplete alloying was obtained after 10 seconds. Since the experimental data (Figure 8.8) show that the SR was not completely alloyed after 5 seconds of heating at 450 °C, we can assume that the value of the diffusion coefficient for this SR is within the same order of magnitude as those obtained for the larger NRs

(between 1×10^{-19} m^{2}s^{-1} and 10×10^{-19} m^{2}s^{-1}). In the literature, very fast diffusion rates (D ~ 10^{-14} m^{2}s^{-1}) have been reported for 5 nm Au@Ag spherical NPs at even lower temperatures.[58] Therefore, we could expect that below a certain NP volume, alloying dynamics drastically increase possibly due to size confinement effects, e.g. higher ratio of mobile surface atoms. However, these observations were made from images in 2D rather than in 3D. Therefore, a more accurate evaluation of the diffusion dynamics in 3D is important to gain a more detailed understanding of the nature of alloying for such small NRs. However, for this to be achieved with our current method, more elaborate simulations of surface diffusion or alternative synthetic techniques are needed, which would prevent interfering surface diffusion, for example, by encapsulation of NPs with a more rigid shell, e.g. a thin amorphous carbon layer.[61,248]
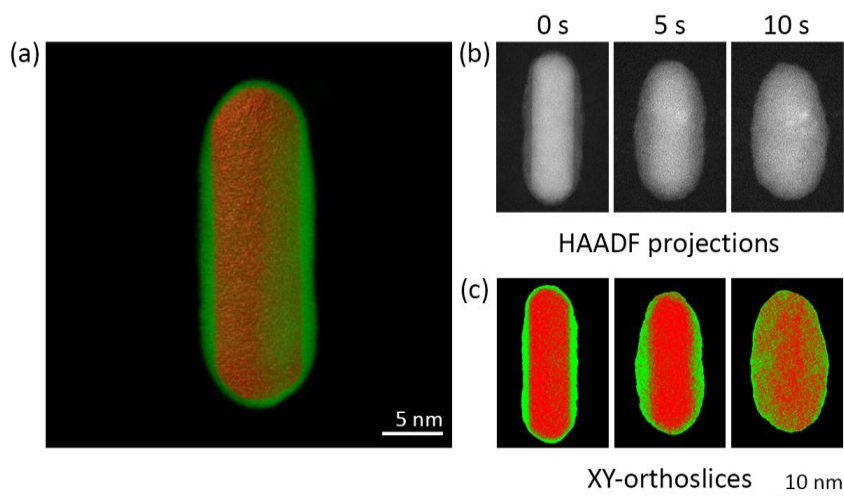
Figure 8.8 (a) 3D visualization of an Au@Ag small nanorod (SR) with volume ~$1.8*10^3$ nm^3, AR = 2.4, and Au:Ag=56:44 at.%; (b) HAADF projections of SR acquired after 0, 5, 10 seconds of heating at 450 °C; (c) YZ-orthoslices through quantified 3D-reconstructions after 0, 5, 10 seconds of heating at 450 °C. The low stability of the particle hinders a quantitative assessment of alloying kinetics.
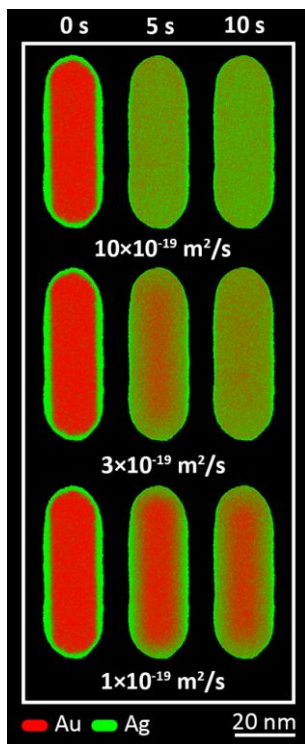
Figure 8.9 Slices through the 3D diffusion simulations for SR calculated for different values of the diffusion coefficients: 10×10^{-19} m^{2}s^{-1} (upper row), 3×10^{-19} m^{2}s^{-1} (middle row), 1×10^{-19} m^{2}s^{-1} (lower row).

It is important to note that both experimental ET results and diffusion simulation analyses employed in this study operate solely within voxel grid systems, lacking atomic-scale information. Within these systems, each voxel comprises multiple atoms. Consequently, the analyses allow for determination only of local Au/Ag ratios, while critical structural details, such as lattice distortions near twin boundaries, which hypothetically correlate with enhanced atomic diffusion along specific directions, remain largely unexplored at the atomic level.

170

8.4 High resolution in situ heating tomography of single-crystalline and pentatwinned Au@Ag NRs

In the previous sections, I demonstrate the enhanced diffusion kinetics due to the presence of lattice distortions in the vicinity of twin boundaries facilitating atomic transport in Au-Ag NPs. However, there is no clear evidence proving this hypothesis and revealing the mechanisms of diffusion at the atomic scale. In this part, I performed an additional *in situ* heating tomography experiment where the main aim was to investigate alloying processes with atomic resolution. Therefore, I obtained high-resolution HAADF-STEM tilt series of single-crystalline and pentatwinned Au@Ag nanorods at different stages of alloying, that were further reconstructed using advanced HR reconstruction techniques, allowing to perform a correlation between the observed elemental redistribution and the relative displacement of atomic positions, caused by the presence of twin boundaries.

In order to investigate the influence of twin boundaries on the alloying dynamics, I focused on two NRs: SC Au NR @ Ag NR and PT Au BP @ Ag NR (Figure 8.10a,b, SC-NR and PT-NR). *In situ* heating 3D investigation of heat-induced metal redistribution in selected Au@Ag core-shell NPs was performed by high resolution HAADF-STEM ET using a DENSsolutions Wildfire MEMS-based heating sample holder, optimized for electron tomography. To induce alloying, all particles were heated at 450 °C for a total of 30 seconds. EDX mapping was performed for each particle before (0 seconds) and after heating (30 seconds) to confirm complete and uniform alloying at the final stage (Figure 8.11 for PT-NR). To investigate intermediate states, the heating process was interrupted after 10, 20 and 30 seconds by fast cooling (within less than 1 second), down to room temperature. After every heating interval, a high resolution HAADF-STEM tilt series for tomography was acquired (Figure 8.10c, Table 8.4). From the 3D reconstructions, retrieved from every tilt series, the volumes of the investigated NPs were calculated. In this manner, we confirmed that the volume did not change for both of the studied NPs during heating (Figure 8.12). Given that both the volume and composition of all investigated NPs remained constant, it can be assumed that both Au and Ag redistributed only at the surface and within the volume of the presented NPs. To

minimize reshaping of the NPs upon heating, all particles studied in this work were coated by a 20 nm thick mesoporous silica-shell (m-SiO$_2$).[242]
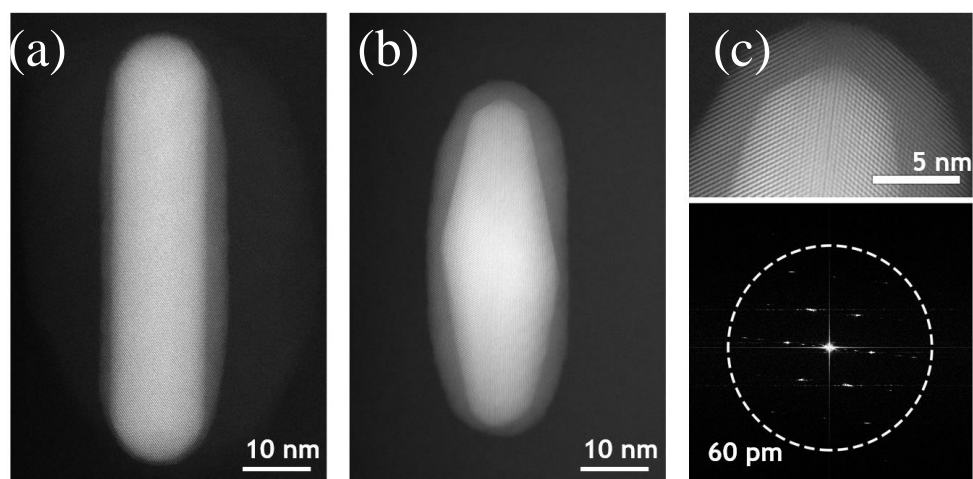
Figure 8.10 (a) SC AuNR @ AgNR and (b) PT AuBP @ AgNR studied during *in situ* heating experiment. (c) The magnified part of the NR2: HRSTEM and corresponding FFT demonstrating the achieved spatial resolution of ~60 pm.
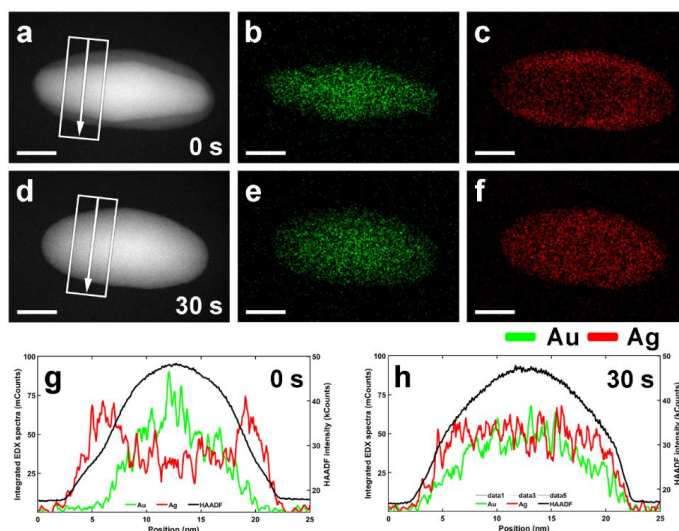
Figure 8.11 2D EDX mapping of NR2 before (a-c) and after heating for 600 seconds at 450 °C (d-f). (g,h) Comparison between integrated line profiles based on the same region (green rectangle) of the 2D EDX elemental mapping before and after alloying. All scale bars are 10 nm.

Table 8.4 Overview of the experimental parameters which are used for high resolution *in situ* heating tomography investigation of Au@Ag NPs.

Sample preparation	Drop casting of the aqueous solution
TEM grids	Si_3N_4-based Wildfire chips
TEM	Thermo Fisher Scientific Themis Z
Voltage	300 kV
Imaging mode	STEM, (2048×2048)
Detector	HAADF, EDX
HAADF frame time	~10 s
Screen current	50 pA
Sample holder	DENSsolutions Wildfire heating tomography holder
ET mode	Incremental tomography
Angular range/tilt increment	-70° : 2 : 70°
Spatial resolution	~60 pm
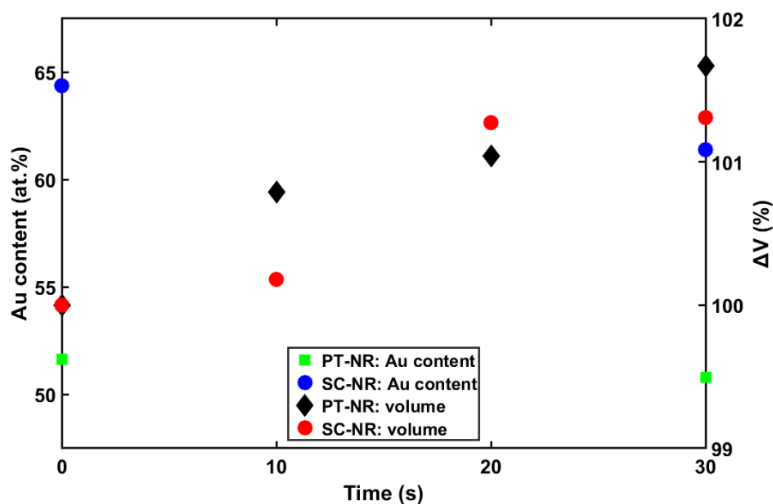
Figure 8.12 Relative volume change (red circles for NR1 and black diamonds for NR2) calculated from 3D reconstructions, and Au content values (blue circles for NR1 and green squares for NR2)

It is interesting to emphasize in Figure 8.13 that both particles slightly alter their orientations after each heating step (rotation by approximately 2°) and undergo subtle deformation. This phenomenon is most likely caused by the slight reshaping, e.g. shrinking, of m-silica shell, surrounding the studied particles. The slight reshaping of the particles studied in **Sections 8.2** and **8.3** also serves as a proof of the certain flexibility of m-SiO_2 under heating, allowing the Au and Ag atoms to participate in the surface diffusion. Due to the possible re-orientation of NPs during the heating, 2D high resolution HAADF-STEM or atomic resolution ET studies based on the limited in zone-axis projections[64] can become unfeasible if a single-tilt tomography holder is used. In this case, the reconstruction algorithm, described in more detail in Figure 3.14,[201] can be used, since it does not necessitate the acquisition of the carefully oriented zone-axis projections. This will be discussed further in more detail.
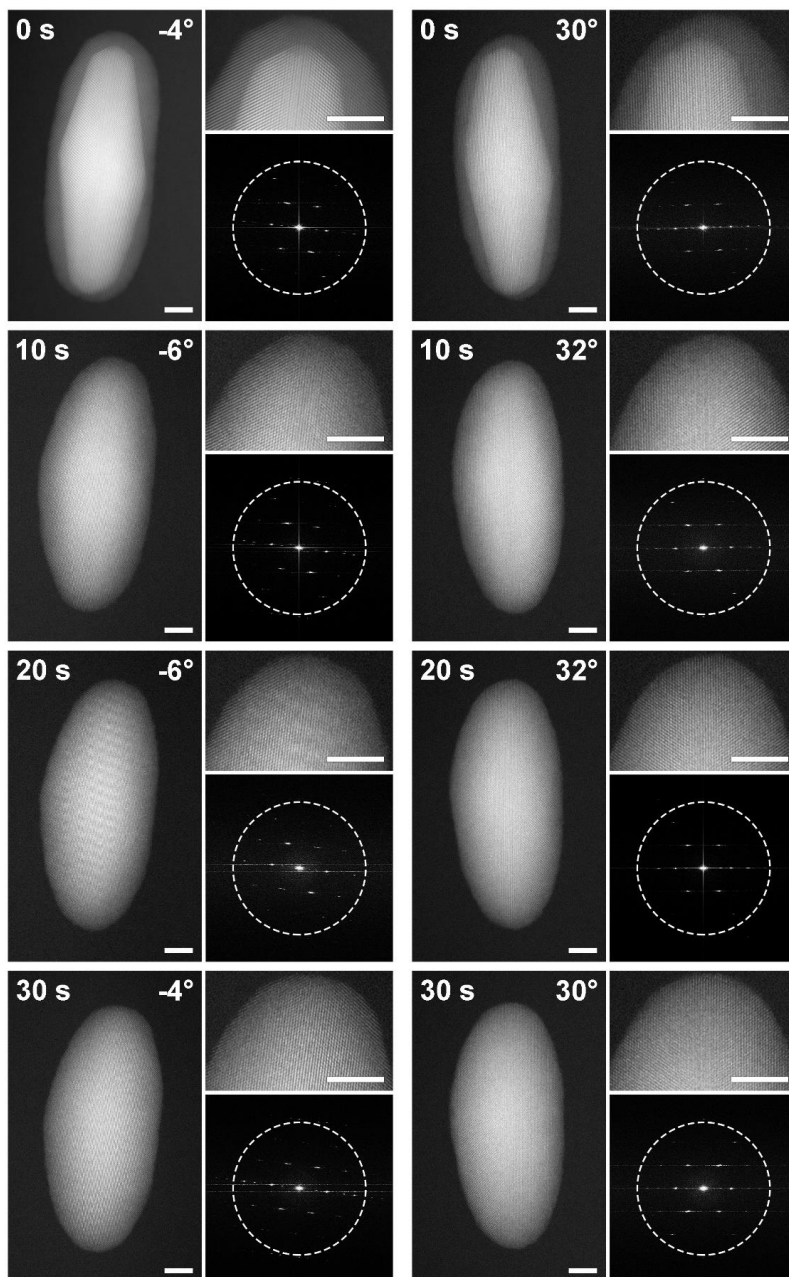
Figure 8.13 The HAADF-STEM projections of NR2 taken along two different crystallographic directions (left and right columns) after each heating step. It should be noted, that while the HRSTEM insets and corresponding FFT show the similar orientation within each column, the projections are taken at slightly different tilt angles (±2°). Scale bars are 5 nm.

Following the restoration of the initial projections using CNN[201] and careful alignment of each tilt series, all obtained tomography datasets were employed for conventional SIRT algorithm to monitor the diffusion of Au and Ag. This approach enabled me to discern individual atomic columns at various heating steps, as illustrated in Figures 8.14a-c and 8.15a-d. It is important to note that the overall crystalline structure of both investigated NRs remained intact throughout the entire heating process. No lattice defects formed in NR1, and twin boundaries remained in both Au core and Ag shell of NR2. This observation led to the conclusion that no phase transitions, such as melting, occurred in the Au-Ag system at the temperatures used in this study. Furthermore, the ability to distinguish between the core and shell of the NRs allowed for the determination of the initial Au-Ag interface boundaries, as explained in **Section 4.2**. Upon closer examination of the Au core in NR1, it was observed that it is primarily surrounded by eight {520} lateral facets, accompanied by lower index facets at the tips, such as {100} and {110}, as depicted in Figure 8.16a and c. Likewise, the Au bipyramid in NR2 exhibited mainly {111} and {711} type faceting before heating, as shown in Figure 8.16b and d.
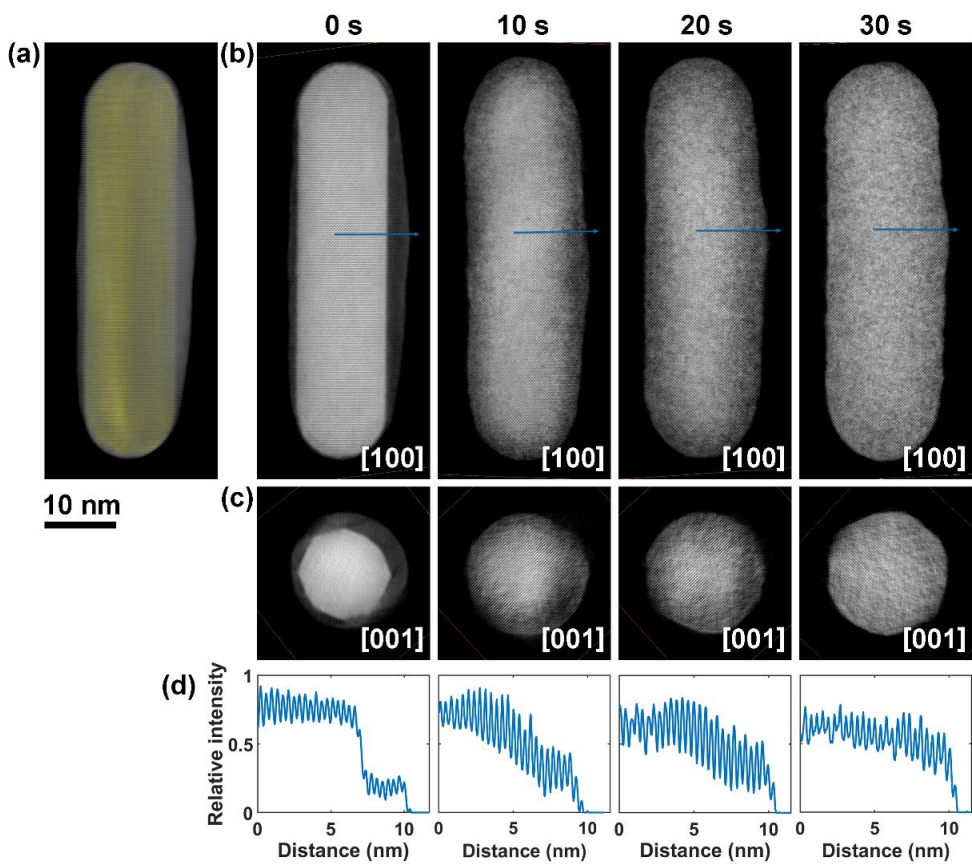
Figure 8.14 (a) 3D render of initial SC-NR, (b,c) central slices along [100] and [001] through the reconstruction after all heating steps. Individual atoms can be resolved at every heating time. (d) Linear intensity profiles corresponding to the blue arrows in (b).
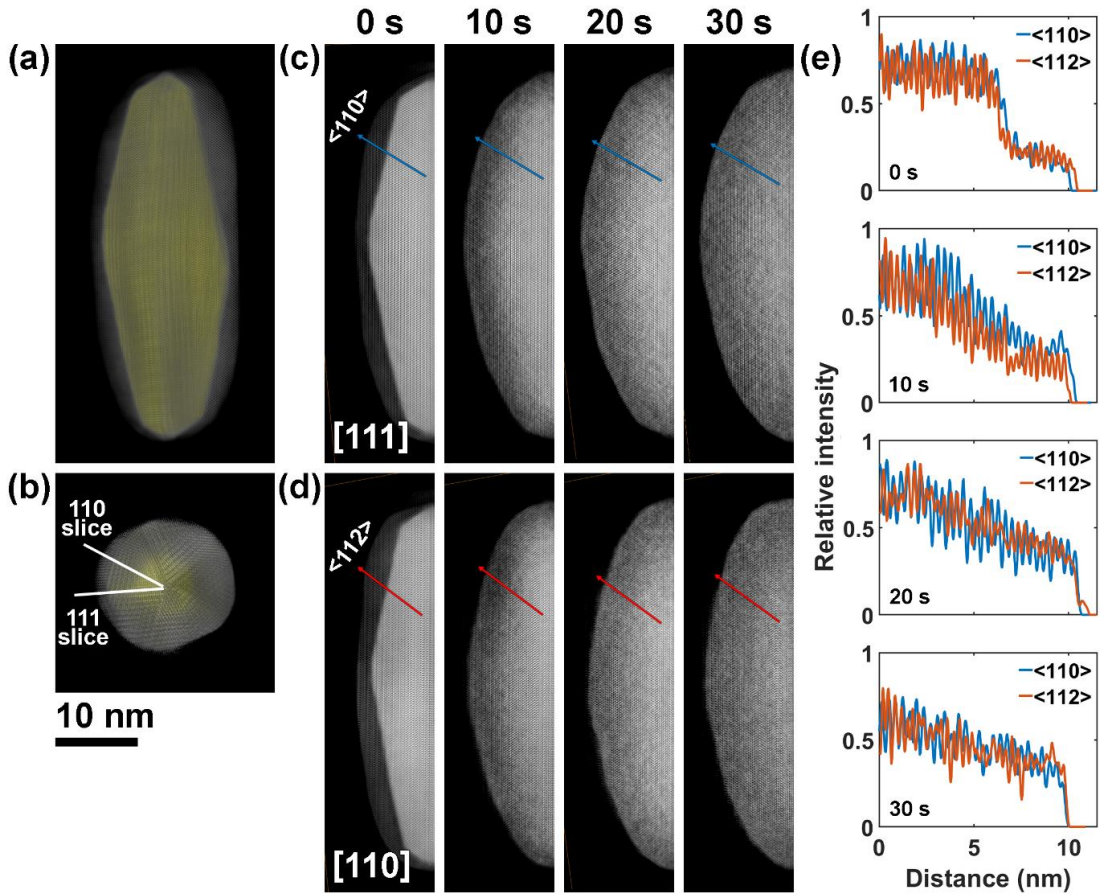
Figure 8.15 (a,b) Side and top view on 3D render of initial PT-NR, (b,c) central slices along [111] and [110] through the reconstruction after all heating steps. Individual atoms can be resolved after every heating step. (e) Linear intensity profiles corresponding to the blue and red arrows in (c,d).
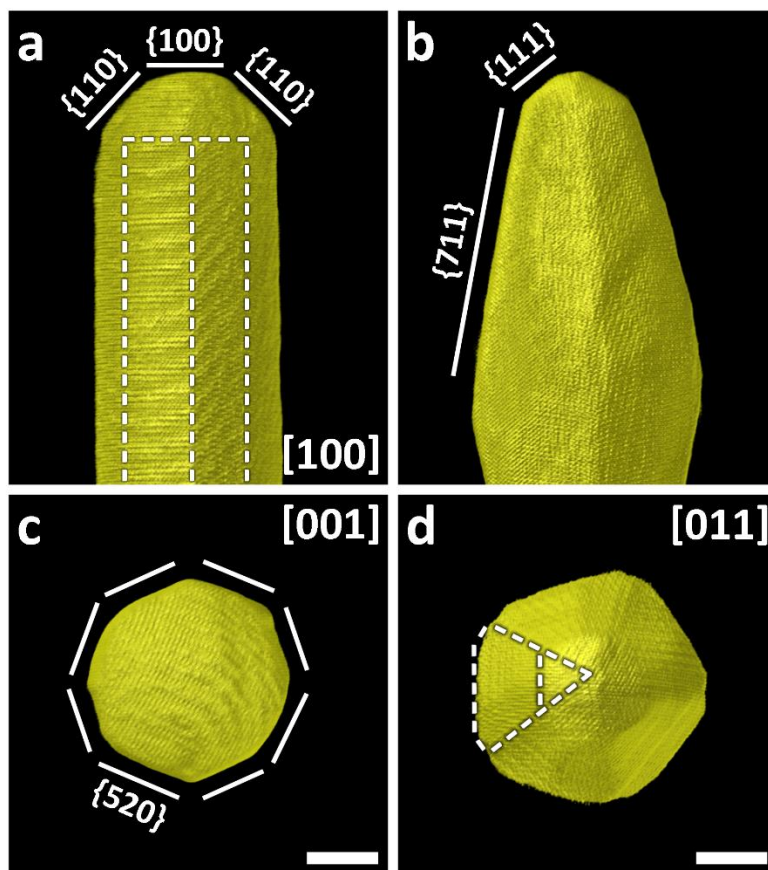
Figure 8.16 Side and top view on 3D render of segmented Au core in (a,c) SC-NR and (b,d) PT-NR before heating. The solid white lines correspond to the determined surface facets, whereas the dashed white lines in (a,d) highlight the position of {520}, {111} and {711} facets shown in (c,b). All scalebars are 5 nm.

The described observations of the initial arrangement of elements and the presence or absence of lattice defects can serve as a foundation for the analysis of atomic redistribution based on crystallographic orientations and lattice dimensions. However, there are several limitations that impede further analysis. First, the conventional SIRT algorithm can effectively distinguish between core (Au) and shell (Ag) atoms only for the initial state of SC-NR and PT-NR. When alloying occurs, regions where Au and Ag are randomly intermixed contain atoms with intensity values falling between those corresponding to pure Au or Ag (as seen in Figure 8.14d and 8.15e). This apparent

reconstruction artifact can be caused by the insufficient data (missing wedge of 40°, 2° tilt step, experimental noise and sub-pixel misalignment between projections), where the huge number of two types of atoms should be resolved ($>10^5$ atoms). This artifact hinders a quantitative analysis of elemental diffusion and, thus, further analysis of diffusion processes at the nanoscale. To address these limitations, more advanced tomography reconstruction methods, for instance Sparse Sphere Reconstruction (SSR),[66] was employed.

In SSR, atoms are represented as 3D Gaussians, allowing for the direct estimation of atomic positions from the Radon transform of the tilt-series images.[249,250] Known atomic sizes ($r_{Au} \approx r_{Ag} \approx 0.145$ nm) can be expressed in pixels based on the experimental settings (such as the pixel size of the original projections). This approach eliminates the need for intermediate scattering potential calculations, which are often susceptible to noise and artifacts. To maintain the physical integrity of the reconstructed atomic structure, a regularization component is integrated into the optimization process.[251] This component ensures that the intensity of each voxel is contributed by only one atom, penalizing atomic collisions and preventing unrealistic atomic configurations. Furthermore, relative intensity values of Au and Ag atoms can be derived from SIRT reconstructions of the initial SC-NR and PT-NR and used as input for SSR reconstructions. However, it's important to note that SSR faces challenges in multi-material or alloyed systems due to the difficulty in distinguishing atoms of different materials at boundaries. To address these complexities, an intermediate phantom material was introduced, having intensity values between those of Au and Ag (Figure 8.17a,c), to account for uncertain atomic states (Figure 8.17b). Additionally, due to the size of the obtained datasets (2048x2048 pixel projections), the computational cost of the proposed technique may be prohibitive for full 3D reconstructions with the initial resolution using an average user's PC. In this work, the original projections were downscaled by a factor of 2, resulting in the reconstruction of only half of the volumes of SC-NR or PT-NR. The main drawback of downscaling is a reduction in the accuracy of atomic position determination, consequently limiting the ability to determine all atom positions in the studied nanoparticles. From Figure 8.17 it can be clearly seen that proposed approach could not resolve all atomic positions even in the initial core-shell Au@Ag PT-NR, where the

boundary between Au and Ag is most distinct. To enhance SSR reconstructions, upscaling of the initial grid can be employed, for example, by 5-times subsampling of the original data. This enhances the accuracy of atom position determination to about (60/5) picometers accuracy. This approach also improves the alignment between projections, enabling more accurate 3D reconstructions. However, it comes at the cost of increased computational demands, requiring the use of computer clusters or supercomputers.
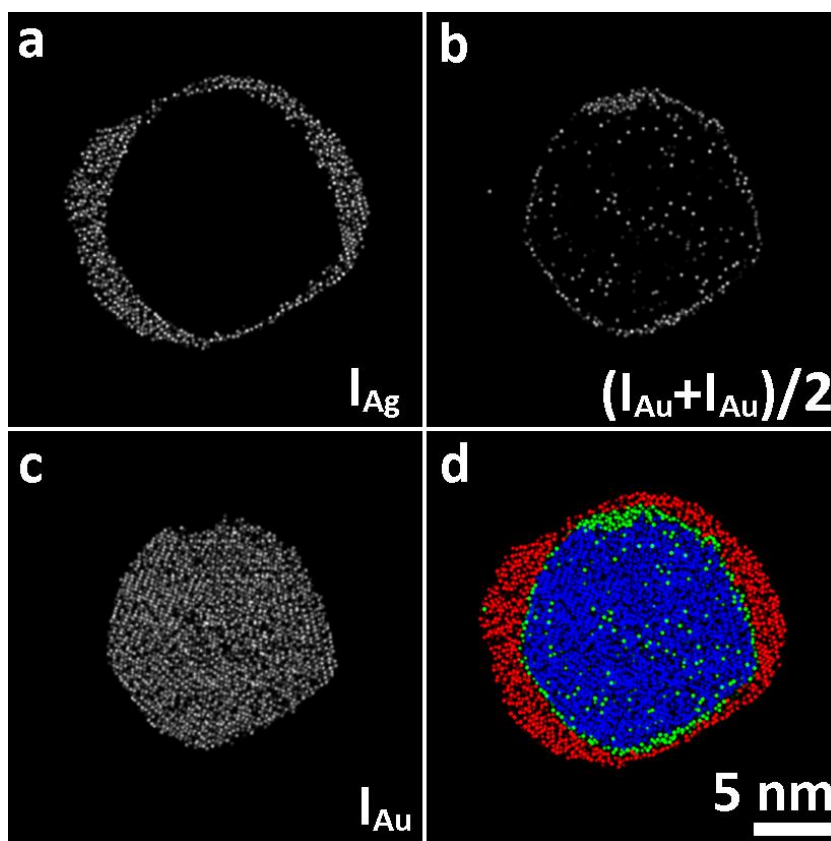
Figure 8.17 Slice taken from SSR reconstruction along [011] zone axis showing determined (a,b,c) Ag, phantom and Au atoms positions. (d) Overlapping of the atoms shown in (a,b,c). Red, green and red colour correspond to Ag, phantom and Au atoms.

8.5 Conclusions

By combining fast electron tomography with an *in situ* heating holder and elemental diffusion simulations, I was able to quantitatively investigate the influence of size, aspect ratio, core morphology and the presence of twin boundaries on the dynamics of alloying of Au@Ag core-shell NPs in 3D. I observed that the diffusion dynamics do not depend on the crystallographic direction and type of interfacial facets between Au and Ag in an *fcc* lattice. On the other hand, I obtained evidence showing that the presence of twin boundaries significantly increased the value of the atomic diffusion coefficient, presumably due to the formation of distortions and vacant sites in the crystal lattice, facilitating the diffusion of atoms. In contrast, the specific details of interfacial crystal planes did not appear to make a big difference in the diffusion coefficient. It is also concluded that the values of the obtained diffusion coefficients are in the same range as tabulated values for bulk materials, which indicates a minor influence of particle volume on the alloying kinetics of NPs. Finally, for small nanorods, with a diameter of 10 nm, surface effects were observed to dominate over elemental diffusion.

To establish a direct correlation between diffusion dynamics and the presence of twin boundaries, high resolution HAADF-STEM ET was employed for SC and PT Au@Ag nanorods. More specifically, the goal of this work is to visualize the difference in the kinetics of the volume diffusion depending on the local lattice distortions, e.g. in the vicinity of twin boundaries vs. the single-crystalline regions. While this technique can clearly visualize individual atoms at each heating step, conventional algorithms, such as SIRT, struggle to distinguish between Au and Ag in the later stages of alloying. These limitations pose challenges for further analysis of heat-induced elemental redistribution at the atomic scale. Therefore, future work will leverage advanced reconstruction algorithms, such as SSR. However, it's important to note that the computational cost of these algorithms is high, requiring the utilization of computer clusters or supercomputers.

Chapter 9. General conclusions and outlook

In this chapter, a general conclusion is drawn regarding the methodologies and insights presented in this thesis. It also entails a discussion of future perspectives for the research presented in this thesis, along with the demonstration of promising results that will motivate further exploration.

9.1 Conclusions

As indicated in the title of this thesis, the primary objectives of my research were to gain a deeper understanding of the growth mechanisms of various chiral Au NPs and to examine the thermal stability of Au@Ag NPs. I demonstrate that ET serves as a powerful and versatile set of methods for conducting comprehensive compositional and morphological analysis of such nanomaterials in 3D. The complex nature of the morphologies under investigation and the redistribution of constituent elements necessitated the application of the following ET techniques:

- Conventional HAADF-STEM ET
- Multimode ET
- Atomic resolution ET
- Combined HAADF-STEM ET and 3D-ED
- Fast *in situ* heating ET

In the first part of my doctoral research I was able to trace morphological evolution of Au NPs during chiral crystal growth in the presence of different chirality inducing surfactants. First, intrinsic chirality of produced NPs was observed and quantified in 3D. The obtained results were in an excellent agreement with optical spectroscopy measurements and electromagnetic simulations of chiroptical properties. In addition, I performed facet analysis of intermediate structures to validate the hypothesis that chiral growth is ensured by site specific adsorption of organic surfactant, thus, controlling the formation of certain chiral features. In that manner, it is illustrated that controlling the

synthetic conditions, e.g. type and concentration of surfactant, allows to produce various chiral Au NPs.

The second part of my thesis is devoted to the investigation of the thermal stability of Au@Ag NPs. Studying individual NPs in 3D after several heating steps allowed me to draw several conclusions regarding the elemental redistribution at the nanoscale. First, it was demonstrated that volume diffusion has dynamics similar to that in bulk materials and is not dependent on the morphology and the type of Au-Ag interface in the studied NPs. However, faster diffusion is observed in the presence of twin boundaries, which may be related to the presence of lattice distortions that facilitate atomic transport within the *fcc* lattice of Au and Ag.

9.2 Outlook

There are several directions for further development of the methods proposed in this thesis that remain to be explored. Promising advancements for the research presented in this thesis can be categorized into three main topics discussed further.

9.2.1 Visualization of surfactant molecules in TEM

The major drawback of (S)TEM studies when investigating the interaction of metallic NPs with organic molecules during crystal growth is that most of these studies are conducted under high vacuum conditions. In such cases, the arrangement of surfactant molecules on the surface of NPs in a dried-out state can significantly differ from their deposition under actual synthetic conditions, e.g. in water solutions. One approach to overcome this constraint is to utilize environmental cells that contain a sealed reservoir with a viewing window fabricated from Si_3N_4 or SiO_2.[252–254] While these liquid cells have facilitated the study of nanoscale phenomena, their relatively thick (up to 100 nm) and relatively high atomic number (Z) element windows result in poor electron transmittance, leading to reduced sensitivity and a resolution that falls short of true atomic-resolution imaging. Moreover, the design of liquid holders restricts the tilting range of the sample, which is insufficient for ET studies. To address this limitation, a

solution can be found in the use of graphene encapsulation. This high-resolution liquid cell is prepared by encapsulating a solution between two laminated graphene layers suspended over holes in a conventional TEM grid (see Figure 9.1).[255,256]
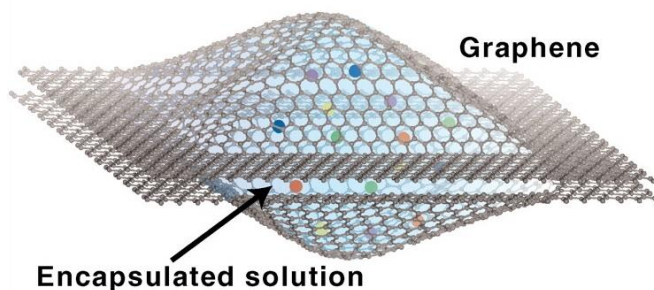
Figure 9.1 Idealized illustration of local graphene liquid cell encapsulating growth solution of ~4 nm Pt NPs.[255] Adapted under the terms of the Science Journals Default License (Copyright © 2012, American Association for the Advancement of Science).

While the preparation of specimens in this method presents challenges and requires further optimization, it offers the advantage of capturing the studied solution within two atomic-thick layers of C, ensuring optimal electron transmittance. In this way, I conducted a preliminary experiment where the liquid graphene encapsulation of Au NRs@CTAC solution was successfully achieved. In Figure 9.2a,b, the hole in the quantifoil Cu grid is shown containing the solution with Au NRs enclosed by two layers of graphene. The double layer of graphene is confirmed with SAED, revealing two patterns corresponding to graphene layers slightly rotated in respect to each other (Figure 9.2c). It's worth noting that (S)TEM studies often involve high electron doses, which can lead to the decomposition of beam-sensitive organic molecules, e.g. surfactants. However, careful selection of experimental parameters can still allow for the visualization of organic ligands, as demonstrated in the case of nicotinamide adenine dinucleotide (NADH) molecules adsorbed on the surface of Au NRs.[257] These results were obtained by acquiring a series of high-resolution TEM images, followed by an exit wave reconstruction (EWR).[258] Hence, it can be concluded that the combination of graphene liquid encapsulation with EWR studies holds the potential for deeper insights

into the adsorption of helical micelles on the surface of metallic NPs during the chiral growth and can be explored in the near future.
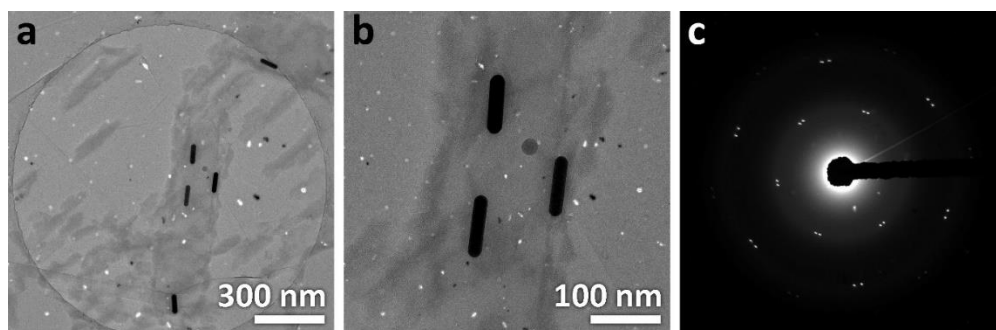
Figure 9.2 (a,b) BF-TEM images of Au NR@CTAC solution, encapsulated between two graphene layers on a quantifoil Cu grid. (c) SAED pattern taken from left top corner in (a), where only the double layer of graphene is expected. ED pattern corresponding to two graphene layers slightly rotated in respect to each other was observed.

9.2.2 Investigation of various chiral nanomaterials

Chapter 6 of this thesis highlights the potential of simultaneously examining highly asymmetric nanoparticles in both real (ET) and reciprocal (3D-ED) space, enabling the correlation between surface features, such as surface facets, and the actual crystallographic orientations of the studied crystals. Nevertheless, several improvements are needed to broaden the potential applications of this approach in the near future. To ensure the reliable investigation of crystal structures with unknown structural parameters, it is essential to carefully calibrate both HAADF-STEM and SAED measurements. It is worth noting that the studies in this thesis focused on Au or Au-Ag NPs with a well-known *fcc* crystal lattice, and, therefore, the calibration of ED datasets lied out of the scope of this work. Additionally, manual alignment between HAADF-STEM and ED reconstructions was necessary due to the misalignment of original datasets obtained with different detectors (HAADF-STEM detector and CCD camera). Therefore, automating the alignment of 3D reconstructions is imperative to allow for more precise analysis of the morphology and crystal structure of the studied nanomaterials.

With these improvements, the utilization of combined HAADF-STEM ET and 3D-ED can be extended to other types of nanomaterials. For example, a more detailed examination of the crystal structure and shape of chiral Te NPs[259,260] can be conducted simultaneously. Figure 9.3 illustrates the screw dislocation-mediated formation of left and right-handed Te NPs,[260] although 3D level information is lacking. In such cases, the suggested method will facilitate a clear and direct correlation between the crystal structure and the intricate morphologies of the studied nanomaterials.
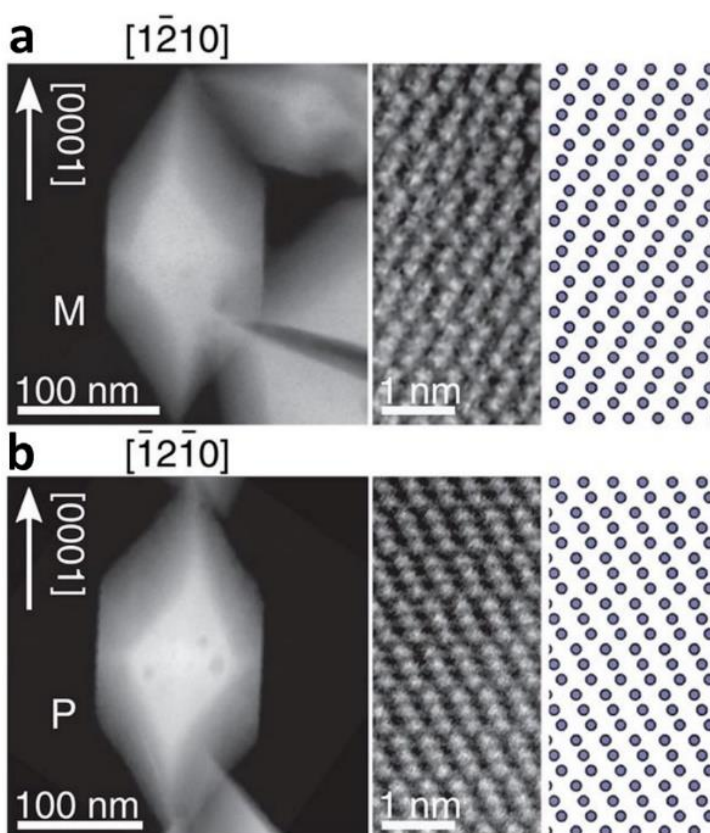
Figure 9.3 Determination of crystal structure and shape handedness of (a) Left-handed (M, *P3221* space group) and (b) right-handed (P, *P3121* space group) Te nanocrystals: (Left) Low-resolution, (middle) high-resolution HAADF-STEM images and (right) a corresponding atomistic model observed along the (a) and (b) zone axes.[260] Adapted under the terms of the Science Journals Default License (Copyright © 2021 American Association for the Advancement of Science).

9.2.3 Advanced reconstruction algorithms for high resolution ET of complex NPs

In addition to the utilization of powerful computing facilities, the attainment of atomic resolution in ET can be progressively augmented through the continuous advancement and refinement of (S)TEM correctors, detection devices, and investigative techniques, such as 4D-STEM or iDPC. Moreover, several data acquisition modes can be employed to increase the volume and quality of input data for tomography reconstruction, as is the case with multimode ET. Consequently, I hold a strong belief that, in the future, we will be capable of conducting atomic resolution investigations on multicomponent nanomaterials, which would not only enable the visualization of heavy elements but also allow for the precise determination of light elements and even crystal lattice vacancies. The presence of vacant sites in the crystal lattice significantly reduces the activation energy for atomic transport, thereby facilitating volume diffusion. Thus, the ability to visualize vacancies will also be useful for diffusion studies.

Summary

Nanomaterials play a crucial role in diverse scientific and technological domains owing to their distinctive optical and catalytic properties derived from their elevated surface-to-volume ratio and dimensional constraints, which are characteristics that are not inherent in bulk materials.[261–263] Achieving optimized control over their unique properties necessitates meticulous tuning of the size, shape, and composition of nanomaterials.[264] Such tuning became feasible by the rapid advancements in synthetic methodologies, such as wet colloidal synthesis.[265,266] Furthermore, alongside the synthesis of diverse nanomaterials, a comprehensive characterization of the resultant structures enabled unveiling the true morphology and elemental distribution. Electron tomography (ET) has hereby merged as a robust and versatile technique for investigating nanomaterials in three dimensions (3D), offering high chemical sensitivity and spatial resolution.[101,105,135]

The need of ET investigations has increasingly grown with the rapid advancement of synthetic techniques, facilitating the production of monometallic and bimetallic nanoparticles (NPs) with diverse sizes and complex structures.[25] In many cases, extracting 3D atomic-level information is of crucial importance, particularly when studying sub-nanometer features and crystal defects. Furthermore, only visualization of the morphology of synthesized NPs is often not sufficient, and a detailed analysis of the growth mechanisms is necessary to achieve a precise control over the synthesized particles parameters, as well as to connect their e.g. optical properties to the 3D structure. Such studies will be increasingly more challenging for more complex morphologies such as, e.g., chiral NPs that are highly promising because of their chiroptical properties. It is important to note that NPs carefully synthesized to yield specific properties may undergo degradation during their application, leading to changes in their useful properties and applicability. To elucidate the relationship between structure and stability, *in situ* ET experiments should be conducted to investigate the influence of external stimuli on the NP structure and properties.

In the following sections, I will outline the efforts undertaken in my PhD project to enhance different ET techniques and to perform a quantitative 3D analysis of various NPs.

The **first chapter** of this thesis provides an introduction to plasmonic NPs, including their properties and applications. Next, the chapter delves into the concept of highly asymmetric chiral NPs, followed by an overview of bimetallic NPs together with a discussion of their thermal stability. Finally, the necessity of advanced ET characterization for both types of NPs is discussed.

Chapter 2 offers a detailed description of ET for 3D characterization of nanomaterials. It focuses on High-Angle Annular Dark Field Scanning Transmission Electron Microscopy (HAADF-STEM) as the basis for ET and provides an in-depth explanation of the technique. Then the thesis will continue with the original contribution, discussed in **2 parts**.

Part 1 of my thesis is dedicated to the application of advanced ET techniques for the comprehensive characterization of various chiral nanostructures. Both qualitative and quantitative analyses of Au NPs morphology are conducted, considering different asymmetric inducers that result in various chiral morphologies.

The aim of **Chapter 3** is to provide an overview of the chiral growth mechanisms of various NPs, that are currently understood. In continuation, I introduce advanced ET approaches that can enhance further understanding.

In **Chapter 4,** atomic resolution ET is employed to investigate the role of the surface facets of single-crystalline (SC) and pentatwinned (PT) Au seeds during chiral nanocrystal growth using enantiomers of cysteine as a surfactant.

Chapter 5 demonstrates the use of HAADF-STEM tomography for the visualization of a symmetric Au core within the overgrown chiral features, obtained by helical CTAC-BINAMINE micelles.

Chapter 6 introduces the combination of HAADF-STEM tomography with electron diffraction (ED) tomography to simultaneously provide information on surface faceting and crystallography of the studied NPs during chiral growth.

Part 2 focuses on investigating the stability of core-shell Au@Ag NPs with varying shapes, sizes, compositions, and defect structures under heating conditions.

In **Chapter 7** I discuss the development of fast ET and its combination with *in situ* heating holders, optimized for *in situ* heating tomography.

In **Chapter 8**, fast tomography is combined with an *in situ* heating holder to analyze heat-induced interdiffusion processes in various Au@Ag NPs in 3D. In addition, atomic resolution *in situ* heating tomography is performed to examine enhanced diffusion phenomena in the presence of twin boundaries.

In the **Conclusions and Outlook** section, I present the overall outcomes of this thesis and provide a perspective on the future application of the developed techniques for characterizing novel nanomaterials.

Samenvating

Nanomaterialen spelen een cruciale rol in verschillende wetenschappelijke en technologische domeinen vanwege hun specifieke optische en katalytische eigenschappen. De eigenschappen van de nanomaterialen verschillen sterk van het bulk materiaal en hangen sterk samen met de oppervlakte/volume verhouding.[261–263] Om deze unieke eigenschappen te bestuderen moet de grootte, vorm en samenstelling van nanomaterialen worden bepaald.[264] Het verfijnen van deze parameters is mogelijk door de snelle vooruitgang in verschillende synthese methodes, waarvan colloïdale synthese en voorbeeld is.[265,266] Daarnaast is een uitgebreide karakterisering noodzakelijk om de ware morfologie en elementaire distributie van de nanodeeltjes te onderzoeken. Elektronentomografie (ET) is een robuuste en veelzijdige techniek die gebruikt wordt om nanomaterialen in drie dimensies (3D), met een hoge chemische gevoeligheid en ruimtelijke resolutie te onderzoeken.[101,105,135]

ET wordt steeds belangrijker in het onderzoek naar nanodeeltjes door de snelle vooruitgang van synthese methodes. Deze methodes maken het mogelijk om monometallische en bimetallische nanodeeltjes (NDs) met verschillende afmetingen en complexe structuren te produceren.[25] Het verkrijgen van 3D informatie op atomair niveau is voor deze NDs van cruciaal belang, vooral bij het bestuderen van kristaldefecten en kenmerken met subnanometer grootte. Echter, de visualisatie van de 3D morfologie van gesynthetiseerde NDs is vaak onvoldoende. Een gedetailleerde analyse van de groeimechanismen is noodzakelijk om een nauwkeurige controle over de parameters van de nanodeeltjes te verkrijgen en om hun optische eigenschappen te linken aan de 3D structuur. Dergelijke studies worden nog uitdagender voor complexe structuren zoals chirale NDs. Deze zijn veelbelovend vanwege hun chiroptische eigenschappen. Het is belangrijk op te merken dat NDs tijdens hun toepassing structurele degradatie kunnen ondergaan, wat kan leiden tot veranderingen in hun nuttige eigenschappen. Om de relatie tussen structuur en stabiliteit te verduidelijken, moeten *in situ* ET experimenten worden uitgevoerd om de invloed van externe stimuli op de ND structuur en hun eigenschappen te onderzoeken.

In de volgende secties licht ik toe welke stappen ik ondernomen heb in mijn PhD project om verschillende ET technieken te verbeteren en om een kwantitatieve 3D analyse van verschillende NDs uit te voeren.

In het **eerste hoofdstuk** van dit proefschrift wordt een inleiding over plasmonische NDs, inclusief hun eigenschappen en toepassingen gegeven. Vervolgens wordt dieper ingegaan op het concept van asymmetrische chirale NDs, gevolgd door een overzicht van bimetallische NDs en een bespreking van hun thermische stabiliteit. Tenslotte wordt de noodzaak van geavanceerde ET karakterisering voor beide types NDs besproken.

Hoofdstuk 2 bevat een gedetailleerde beschrijving van ET voor de 3D karakterisering van nanomaterialen. Er wordt gefocust op hoge hoek verstrooide ringvormige donkerveld raster transmissie elektronen microscopie (*High-Angle Annular Dark Field Scanning Transmission Electron Microscopy,* HAADF-STEM) als basis voor ET. Vervolgens wordt de thesis opgesplitst in **2 delen**.

Deel 1 van mijn thesis is gewijd aan de toepassing van geavanceerde ET technieken voor de uitgebreide karakterisering van verschillende chirale nanostructuren. Zowel kwalitatieve als kwantitatieve analyses van de morfologie van Au NDs worden uitgevoerd, rekening houdend met verschillende asymmetrische inductoren die leiden tot verschillende chirale vormen.

Hoofdstuk 3 geeft een overzicht van de chirale groei mechanismen bij verschillende gekende NDs. Om deze groeimechanismen beter te begrijpen introduceer ik vervolgens geavanceerde ET benaderingen.

In **Hoofdstuk 4** wordt atomaire resolutie ET gebruikt om de rol van facetten te bestuderen aan het oppervlak van eenkristallen (*single-crystalline*, SC) en bij vijfvoudige tweelingvlakken begrensde (*pentatwinned*, PT) Au zaden. Dit doe ik tijdens de groei van deze chirale nanokristallen met behulp van eantiomeren van cysteine als oppervlakte-actieve stof.

Hoofdstuk 5 demonstreert het gebruik van HAADF-STEM tomografie door het visualiseren van een symmetrische Au kern die overgroeid is met chirale structuren.

Deze is verkregen met helische CTAC-BINAMINE micellen als oppervlakte-actieve stof.

Hoofdstuk 6 introduceert de combinatie van HAADF-STEM tomografie met elektronendiffractie (ED) tomografie om gelijktijdig de facetten aan het oppervlak en de kristallografie van NDs te bestuderen, tijdens de chirale groei.

Deel 2 focust op het onderzoek van de stabiliteit van kern-schil Au@Ag NPs met verschillende vorm, grootte, samenstelling en defecten tijdens opwarming.

In **Hoofdstuk 7** bespreek ik de ontwikkeling van snelle ET en de combinatie met *in situ* opwarming houders, geoptimaliseerd voor *in situ* tomografie.

In **Hoofdstuk 8** wordt snelle tomografie gecombineerd met de *in situ* opwarming houder om interdiffusie processen geïntroduceerd door warmte te bestuderen voor verschillende Au@Ag NDs. Daarnaast wordt atomaire resolutie *in situ* tomografie uitgevoerd om verbeterde diffusiefenomenen in de aanwezigheid van tweelinggrenzen te onderzoeken.

In de **Conclusie** en **Vooruitzichten** secties, presenteer ik de algemene resultaten van dit proefschrift en bespreek ik mogelijke toekomstige toepassingen voor de ontwikkelde technieken voor het karakteriseren van nieuwe nanomaterialen.

List of scientific contributions

Peer-Reviewed Publications:

o   Van Gordon K.*, Baúlde S.*, <u>Mychinko M.</u>*, Heyvaert W., Obelleiro-Liz M., Criado A., Bals S., Liz-Marzán L.M, Mosquera J., *Tuning the Growth of Chiral Gold Nanoparticles Through Rational Design of a Chiral Molecular Inducer*, Nano Lett. 2023, 23, 21, 9880–9886. DOI: 10.1021/acs.nanolett.3c02800

* Equal contribution to the published work

o   Zhuo X., <u>Mychinko M.</u>, Heyvaert W., Larios D., Obelleiro-Liz M., Taboada J.M., Bals S., and Liz-Marzán L.M., *Morphological and Optical Transitions during Micelle-Seeded Chiral Growth on Gold Nanorods*, ACS Nano 2022, 16 (11), 19281. DOI: 10.1021/acsnano.2c08668

o   Ni B., <u>Mychinko M.</u>, Gómez-Graña S., Morales-Vidal J., Obelleiro-Liz M., Heyvaert W., Vila-Liarte D., Zhuo X., Albrecht W., Zheng G., González-Rubio G., Taboada J.M., Obelleiro F., López N., Pérez-Juste J., Pastoriza-Santos I., Cölfen H., Bals S., and Liz-Marzán L.M., *Chiral Seeded Growth of Gold Nanorods Into Fourfold Twisted Nanoparticles with Plasmonic Optical Activity*, Adv. Mater. 2023, 35, 2208299. DOI: 10.1002/adma.202208299

o   Renero-Lecuna C., Herrero A., Jimenez de Aberasturi D., Martínez-Flórez M., Valiente R., <u>Mychinko M.</u>, Bals S., Liz-Marzán L.M., *Nd^{3+}-Doped Lanthanum Oxychloride Nanocrystals as Nanothermometers*, J. Phys. Chem. C 2021, 125, 36, 19887–19896. DOI: 10.1021/acs.jpcc.1c05828

o   <u>Mychinko M.</u>, Skorikov A., Albrecht W., Sánchez Iglesias A., Zhuo X., Kumar V., Liz-Marzán L.M. and Bals S., *The Influence of Size, Shape, and Twin Boundaries on Heat-induced Alloying in Individual Au@Ag Core-Shell Nanoparticles*, Small 2021, 17, 2102348. DOI: 10.1002/smll.202102348

o   Mychinko M., Kadu A.A., De Backer A., Sánchez Iglesias A., Liz-Marzán L.M., Van Aert S., Bals S., *Unraveling the diffusion at the atomic scale in 3D: heat-induced alloying in single-crystalline and pentatwinned Au@Ag nanoparticles*. In preparation.

Oral and Poster Presentations:

o   Mychinko M., Zhuo X., Ni B., Wouter Heyvaert W., González-Rubio G., Cölfen H., Liz-Marzán L.M., Bals S. *Electron tomography: a powerful method for the characterization of Au chiral nanoparticles.* E-MRS 2023 Spring Meeting, Strasbourg (France), May 29 – June 2,2023. (Poster)

o   Mychinko M., Skorikov A., Albrecht W., Kumar V., Zhuo X., Irmak E.A., De Backer A., Kadu A.A., Sànchez-Iglesias A., Liz-Marzán L.M., Van Aert S., Bals S. *Unraveling the diffusion at the atomic scale in 3D: heat-induced alloying in single-crystalline and pentatwinned Au@Ag nanoparticles*. E-MRS 2023 Spring Meeting, Strasbourg (France), May 29 – June 2,2023. (Talk)

o   Mychinko M., Skorikov A., Albrecht W., Kumar V., Zhuo X., Irmak E.A., De Backer A., Kadu A.A., Sànchez-Iglesias A., Liz-Marzán L.M., Van Aert S., Bals S. *Heat-induced alloying in individual Au@Ag core-shell nanoparticles as a function of size, shape, and presence of defects.* Microscopy Conference (MC 2023), Darmstadt (Germany), February 26 – March 2, 2023. (Talk)

o   Mychinko M., Skorikov A., Albrecht W., Kumar V., Zhuo X., Sánchez Iglesias A., Liz-Marzán L.M., Bals S. *The influence of size, shape, and defects on heat-induced alloying in individual Au@Ag core-shell nanoparticles.* ChemCYS, Blankenberge (Belgium), October 12-14, 2022. (Poster)

o   Mychinko M., Skorikov A., Albrecht W., Zhuo X., Sánchez Iglesias A., Liz-Marzán L.M., Bals S. *The influence of size, shape, and defects on heat-induced alloying in individual Au@Ag core-shell nanoparticles.* Microscopy Conference (MC 2021), online, August 22-26, 2021. (Talk)

Acknowledgements

Conducting my PhD research at EMAT presented challenges in both predictable and unexpected ways. The former involved a steep learning curve on both professional and personal levels, as well as adapting to the high expectations set for every EMAT member. While it was challenging at times, it provided a valuable perspective on how genuine success is achieved and maintained. EMAT had already established itself as a prominent name in the world of electron microscopy and material science long before I joined, and I hope my contributions have been sufficient to maintain its well-deserved reputation.

First and foremost, I would like to express my gratitude to my scientific supervisor, Prof. Dr. Sara Bals, for granting me the opportunity to work in such a wonderful and professional team. You are both an exemplary supervisor and scientist, effectively managing numerous responsibilities and keeping our research at the cutting edge of science. I greatly appreciate your feedback on my reports, presentations, and drafts, especially the critical ones, which contributed the most to my growth. I am particularly grateful for your understanding and patience during challenging times.

I would also like to thank all my colleagues with whom I had the honour of working during these years. We supported and assisted one another, readily sharing knowledge and experience to achieve the best possible results. We also had a lot of fun discussing non-work-related matters, which is just as important for fostering proper team spirit as our work results. Whether you are still at EMAT or have embarked on new adventures elsewhere, please know that you can always contact me, and I will be happy to help you right away!

Special acknowledgment is due to our collaborators, particularly the team led by Prof. Liz-Marzán, for their exceptional work in preparing the samples investigated in this study. A great deal of credit also goes to the brainstorming sessions, where numerous bright ideas were conceived and materialized. Each image and conclusion underwent meticulous examination and received valuable scientific criticism. I have gained

invaluable knowledge from this experience and wish everyone continued success in fostering fruitful collaborations and pioneering studies.

A brief word of appreciation should also be extended to my non-work friends, mainly from our volleyball games. You, too, have contributed to this work, helping keep me in good mental and physical shape with your support and friendly competition.

Ну и напоследок, хочется поблагодарить моих родителей и друзей за всю ту поддержку и те уроки, благодаря которым я оказался там, где я есть. Спасибо преподавателям и коллегам с Химического Факультета за весь пригодившийся опыт и знания!

Спасибо моей супруге, партнеру и другу в одном лице за постоянную поддержку, понимание, мотивацию и заботу. Ну и конечно за самый главный подарок в моей жизни. Ева, ты сейчас едва начала улыбаться и общаться с нами. И возможно ты прочитаешь это только лет через 20. Просто знай, что с момента твоего рождения я делал все возможное для тебя и для твоей мамы!

References

(1)   Feynman, R. P. Plenty of Room at the Bottom. *Calif Inst Technol Eng Sci Mag* **1960**.

(2)   Herzog F.; Clift M.; Piccapietra F.; Behra R., Schmid O.; Petri-Fink A.; Rothen-Rutishauser B. Exposure of silver-nanoparticles and silver-ions to lung cells in vitro at the air-liquid interface. *Part Fibre Toxicol* **2013**, 10, 11. https://doi.org/10.1186/1743-8977-10-11.

(3)   Radetić, M. Functionalization of Textile Materials with Silver Nanoparticles. *J Mater Sci*. **2013**, 95–107. https://doi.org/10.1007/s10853-012-6677-7.

(4)   Fernandes, M.; Padrão, J.; Ribeiro, A. I.; Fernandes, R. D. V.; Melro, L.; Nicolau, T.; Mehravani, B.; Alves, C.; Rodrigues, R.; Zille, A. Polysaccharides and Metal Nanoparticles for Functional Textiles: A Review. *Nanomaterials* **2022**, *12* (6), 1006. https://doi.org/10.3390/nano12061006.

(5)   Petryayeva, E.; Krull, U. J. Localized Surface Plasmon Resonance: Nanostructures, Bioassays and Biosensing-A Review. *Anal Chim Acta* **2011**, *706* (1), 8–24. https://doi.org/10.1016/j.aca.2011.08.020.

(6)   Baffou, G.; Quidant, R. Nanoplasmonics for Chemistry. *Chem Soc Rev* **2014**, *43* (11), 3898–3907. https://doi.org/10.1039/c3cs60364d.

(7)   Erwin, W. R.; Zarick, H. F.; Talbert, E. M.; Bardhan, R. Light Trapping in Mesoporous Solar Cells with Plasmonic Nanostructures. *Energy Environ Sci* **2016**, *9* (5), 1577–1601. https://doi.org/10.1039/c5ee03847b.

(8)   Paul, KK.; Giri, P. K. Plasmonic Metal and Semiconductor Nanoparticle Decorated TiO2-Based Photocatalysts for Solar Light Driven Photocatalysis. In *Encyclopedia of Interfacial Chemistry*; Elsevier, **2018**, 786–794. https://doi.org/10.1016/B978-0-12-409547-2.13176-2.

(9)   Choi, Y.; Kang, T.; Lee, L. P. Plasmon Resonance Energy Transfer (PRET)-Based Molecular Imaging of Cytochrome C in Living Cells. *Nano Lett* **2009**, *9* (1), 85–90. https://doi.org/10.1021/nl802511z.

(10)   Reguera, J.; Langer, J.; Jiménez De Aberasturi, D.; Liz-Marzán, L. M. Anisotropic Metal Nanoparticles for Surface Enhanced Raman Scattering. *Chem Soc Rev* **2017**, *46* (13), 3866–3885. https://doi.org/10.1039/c7cs00158d.

(11)   Zijlstra, P.; Chon, J. W. M.; Gu, M. Five-Dimensional Optical Recording Mediated by Surface Plasmons in Gold Nanorods. *Nature* **2009**, *459* (7245), 410–413. https://doi.org/10.1038/nature08053.

(12)   Linic, S.; Christopher, P.; Ingram, D. B. Plasmonic-Metal Nanostructures for Efficient Conversion of Solar to Chemical Energy. *Nat Mater* **2011**, *10* (12), 911–921. https://doi.org/10.1038/nmat3151.

(13)   Li, X.; Jia, C.; Ma, B.; Wang, W.; Fang, Z.; Zhang, G.; Guo, X. Substrate-Induced Interfacial Plasmonics for Photovoltaic Conversion. *Sci Rep* **2015**, *5*, 1–10. https://doi.org/10.1038/srep14497.

(14)   Stern, J. M.; Stanfield, J.; Kabbani, W.; Hsieh, J. T.; Cadeddu, J. A. Selective Prostate Cancer Thermal Ablation with Laser Activated Gold Nanoshells. *J Urol* **2008**, *179* (2), 748–753. https://doi.org/10.1016/j.juro.2007.09.018.

(15)   Liang, R.; Xie, J.; Li, J.; Wang, K.; Liu, L.; Gao, Y.; Hussain, M.; Shen, G.; Zhu, J.; Tao, J. Liposomes-Coated Gold Nanocages with Antigens and Adjuvants Targeted Delivery to Dendritic Cells for Enhancing Antitumor Immune Response. *Biomater* **2017**, *149*, 41–50. https://doi.org/10.1016/j.biomaterials.2017.09.029.

(16)   Kim, M.; Lee, J. H.; Nam, J. M. Plasmonic Photothermal Nanoparticles for Biomedical Applications. *Adv Sci* **2019**, *6* (17). https://doi.org/10.1002/advs.201900471.

(17)   Wu, Y.; Jiang, P.; Jiang, M.; Wang, T. W.; Guo, C. F.; Xie, S. S.; Wang, Z. L. The Shape Evolution of Gold Seeds and Gold@silver Core-Shell Nanostructures. *Nanotechnology* **2009**, *20* (30). https://doi.org/10.1088/0957-4484/20/30/305602.

(18)   Cao, Y.; Jin, R.; Mirkin, C. A. DNA-Modified Core-Shell Ag/Au Nanoparticles. *J Am Chem Soc* **2001**, *123* (32), 7961–7962. https://doi.org/10.1021/ja011342n.

(19)   Chen, H.; Kou, X.; Yang, Z.; Ni, W.; Wang, J. Shape- and Size-Dependent Refractive Index Sensitivity of Gold Nanoparticles. *Langmuir* **2008**, *24* (10), 5233–5237. https://doi.org/10.1021/la800305j.

(20)   Vinnacombe-Willson, G. A.; Conti, Y.; Stefancu, A.; Weiss, P. S.; Cortés, E.; Scarabelli, L. Direct Bottom-Up *In Situ* Growth: A Paradigm Shift for Studies in Wet-Chemical Synthesis of Gold Nanoparticles. *Chem Rev* **2023**. https://doi.org/10.1021/acs.chemrev.2c00914.

(21)   Ahmed, W.; Bhatti, A. S.; van Ruitenbeek, J. M. Efficient Seed-
        Mediated Method for the Large-Scale Synthesis of Au Nanorods. *J
        Nanoparticle Res* **2017**, *19* (3). https://doi.org/10.1007/s11051-017-
        3815-9.

(22)   Sánchez-Iglesias, A.; Winckelmans, N.; Altantzis, T.; Bals, S.;
        Grzelczak, M.; Liz-Marzán, L. M. High-Yield Seeded Growth of
        Monodisperse Pentatwinned Gold Nanoparticles Through Thermally-
        Induced Seed Twinning; *J Am Chem Soc* **2016**, 139, 1, 107–110.
        https://doi.org/10.1021/jacs.6b12143.

(23)   Liz-Marzán, L. M.; Grzelczak, M. Growing Anisotropic Crystals at the
        Nanoscale. *Science* **2017**, *356* (6343), 1120–1121.
        https://doi.org/10.1126/science.aam8774.

(24)   Meena, S. K.; Celiksoy, S.; Schäfer, P.; Henkel, A.; Sönnichsen, C.;
        Sulpizi, M. The Role of Halide Ions in the Anisotropic Growth of Gold
        Nanoparticles: A Microscopic, Atomistic Perspective. *Phys Chem Chem
        Phys* **2016**, *18* (19), 13246–13254. https://doi.org/10.1039/c6cp01076h.

(25)   Min, Y.; Wang, Y. Manipulating Bimetallic Nanostructures With
        Tunable Localized Surface Plasmon Resonance and Their Applications
        for Sensing. *Front Chem* **2020**, *8*.
        https://doi.org/10.3389/fchem.2020.00411.

(26)   Ito, T.; Ando, H.; Imamura, Y.; Yamaguchi, Y.; Handa, H.; Suzuki, T.;
        Ogura, T.; Hotta, K. Identification of a Primary Target of Thalidomide
        Teratogenicity. *Science* **2010**, 327, 1345-1345.
        https://doi.org/10.1126/science.1177319

(27)   Leitereg T.J.; Guadagni D.G. ; Harris J.; Mon T.R.; Teranishi R.
        Chemical and sensory data supporting the difference between the odors
        of the enantiomeric carvones *J Agric Food Chem* **1971** *19* (4), 785-787.
        https://doi.org/10.1021/jf60176a035

(28)   Baker, B. R.; Garrell, R. L. G-Factor Analysis of Protein Secondary
        Structure in Solutions and Thin Films. *Faraday Discuss* **2004**, *126*, 209.
        https://doi.org/10.1039/b305291e.

(29)   Wakabayashi, M.; Yokojima, S.; Fukaminato, T.; Shiino, K.; Irie, M.;
        Nakamura, S. Anisotropic Dissymmetry Factor, *g* : Theoretical
        Investigation on Single Molecule Chiroptical Spectroscopy. *J Phys
        Chem A* **2014**, *118* (27), 5046–5057. https://doi.org/10.1021/jp409559t.

(30)   Ben-Moshe, A.; Maoz, B. M.; Govorov, A. O.; Markovich, G. Chirality
        and Chiroptical Effects in Inorganic Nanocrystal Systems with Plasmon

and Exciton Resonances. *Chem Soc Rev* **2013**, *42* (16), 7028–7041. https://doi.org/10.1039/c3cs60139k.

(31)   Zhuang, T. T.; Li, Y.; Gao, X.; Wei, M.; García de Arquer, F. P.; Todorović, P.; Tian, J.; Li, G.; Zhang, C.; Li, X.; Dong, L.; Song, Y.; Lu, Y.; Yang, X.; Zhang, L.; Fan, F.; Kelley, S. O.; Yu, S. H.; Tang, Z.; Sargent, E. H. Regioselective Magnetization in Semiconducting Nanorods. *Nature Nanotechnology*, **2020**, 192–197. https://doi.org/10.1038/s41565-019-0606-8.

(32)   West, P. R.; Ishii, S.; Naik, G. V.; Emani, N. K.; Shalaev, V. M.; Boltasseva, A. Searching for Better Plasmonic Materials. *Laser Photonics Rev*, **2010**, 795–808. https://doi.org/10.1002/lpor.200900055.

(33)   Lu, L.; Burkey, G.; Halaciuga, I.; Goia, D. V. Core-Shell Gold/Silver Nanoparticles: Synthesis and Optical Properties. *J Colloid Interface Sci* **2013**, *392* (1), 90–95. https://doi.org/10.1016/j.jcis.2012.09.057.

(34)   Harish, S.; Sabarinathan, R.; Joseph, J.; Phani, K. L. N. Role of PH in the Synthesis of 3-Aminopropyl Trimethoxysilane Stabilized Colloidal Gold/Silver and Their Alloy Sols and Their Application to Catalysis. *Mater Chem Phys* **2011**, *127* (1–2), 203–207. https://doi.org/10.1016/j.matchemphys.2011.01.060.

(35)   Pal, A.; Shah, S.; Devi, S. Preparation of Silver, Gold and Silver-Gold Bimetallic Nanoparticles in w/o Microemulsion Containing TritonX-100. *Colloids Surf A Physicochem Eng Asp* **2007**, *302* (1–3), 483–487. https://doi.org/10.1016/j.colsurfa.2007.03.032.

(36)   Ji, Y.; Yang, S.; Guo, S.; Song, X.; Ding, B.; Yang, Z. Bimetallic Ag/Au Nanoparticles: A Low Temperature Ripening Strategy in Aqueous Solution. *Colloids Surf A Physicochem Eng Asp* **2010**, *372* (1–3), 204–209. https://doi.org/10.1016/j.colsurfa.2010.10.028.

(37)   Mahmoud, M. A.; El-Sayed, M. A. Different Plasmon Sensing Behavior of Silver and Gold Nanorods. *J Phys Chem Lett* **2013**, *4* (9), 1541–1545. https://doi.org/10.1021/jz4005015.

(38)   Verbruggen, S. W.; Keulemans, M.; Goris, B.; Blommaerts, N.; Bals, S.; Martens, J. A.; Lenaerts, S. Plasmonic "rainbow" Photocatalyst with Broadband Solar Light Response for Environmental Applications. *Appl Catal B* **2016**, *188*, 147–153. https://doi.org/10.1016/j.apcatb.2016.02.002.

(39)   Ristig, S.; Chernousova, S.; Meyer-Zaika, W.; Epple, M. Synthesis, Characterization and in Vitro Effects of 7 Nm Alloyed Silver-Gold

Nanoparticles. *Beilstein Journal of Nanotechnology* **2015**, *6* (1), 1212–1220. https://doi.org/10.3762/bjnano.6.124.

(40) Gonzalez, C. M.; Liu, Y.; Scaiano, J. C. Photochemical Strategies for the Facile Synthesis of Gold-Silver Alloy and Core-Shell Bimetallic Nanoparticles. *Journal of Physical Chemistry C* **2009**, *113* (27), 11861–11867. https://doi.org/10.1021/jp902061v.

(41) Uppal, M. A.; Ewing, M. B.; Parkin, I. P. One-Pot Synthesis of Core-Shell Silver-Gold Nanoparticle Solutions and Their Interaction with Methylene Blue Dye. *Eur J Inorg Chem* **2011**, No. 29, 4534–4544. https://doi.org/10.1002/ejic.201100536.

(42) Borah, R.; Verbruggen, S. W. Silver-Gold Bimetallic Alloy versus Core-Shell Nanoparticles: Implications for Plasmonic Enhancement and Photothermal Applications. *J Phys Chem C* **2020**, 124 (22), 12081–12094. https://doi.org/10.1021/acs.jpcc.0c02630.

(43) Van Der Hoeven, J. E. S.; Welling, T. A. J.; Silva, T. A. G.; Van Den Reijen, J. E.; La Fontaine, C.; Carrier, X.; Louis, C.; Van Blaaderen, A.; De Jongh, P. E. In Situ Observation of Atomic Redistribution in Alloying Gold-Silver Nanorods. *ACS Nano* **2018**, *12* (8), 8467–8476. https://doi.org/10.1021/acsnano.8b03978.

(44) Skorikov, A.; Albrecht, W.; Bladt, E.; Xie, X.; Van Der Hoeven, J. E. S.; Van Blaaderen, A.; Van Aert, S.; Bals, S. Quantitative 3D Characterization of Elemental Diffusion Dynamics in Individual Ag@Au Nanoparticles with Different Shapes. *ACS Nano* **2019**, *13* (11), 13421–13429. https://doi.org/10.1021/acsnano.9b06848.

(45) Balogh, Z.; Schmitz, G. Diffusion in Metals and Alloys. *Physical Metallurgy: Fifth Edition* **2014**; 1, 387–559. https://doi.org/10.1016/B978-0-444-53770-6.00005-8.

(46) Shibata, T.; Bunker, B. A.; Zhang, Z.; Meisel, D.; Vardeman, C. F.; Gezelter, J. D. Size-Dependent Spontaneous Alloying of Au-Ag Nanoparticles. *J Am Chem Soc* **2002**, *124* (40), 11989–11996. https://doi.org/10.1021/ja026764r.

(47) González, E.; Arbiol, J.; Puntes, V. F. Carving at the Nanoscale: Sequential Galvanic Exchange and Kirkendall Growth at Room Temperature. *Science (1979)* **2011**, *334* (6061), 1377–1380. https://doi.org/10.1126/science.1212822.

(48) Chee, S. W.; Wong, Z. M.; Baraissov, Z.; Tan, S. F.; Tan, T. L.; Mirsaidov, U. Interface-Mediated Kirkendall Effect and Nanoscale Void Migration in Bimetallic Nanoparticles during Interdiffusion. *Nat*

Commun **2019**, *10* (1), 1–12. https://doi.org/10.1038/s41467-019-10623-0.

(49)   Vara, M.; Roling, L. T.; Wang, X.; Elnabawy, A. O.; Hood, Z. D.; Chi, M.; Mavrikakis, M.; Xia, Y. Understanding the Thermal Stability of Palladium-Platinum Core-Shell Nanocrystals by in Situ Transmission Electron Microscopy and Density Functional Theory. *ACS Nano* **2017**, *11* (5), 4571–4581. https://doi.org/10.1021/acsnano.6b08692.

(50)   Huang, R.; Wen, Y. H.; Shao, G. F.; Zhu, Z. Z.; Sun, S. G. Single-Crystalline and Multiple-Twinned Gold Nanoparticles: An Atomistic Perspective on Structural and Thermal Stabilities. *RSC Adv* **2014**, *4* (15), 7528–7537. https://doi.org/10.1039/c3ra46631k.

(51)   Huang, J.; Yan, Y.; Li, X.; Qiao, X.; Wu, X.; Li, J.; Shen, R.; Yang, D.; Zhang, H. Unexpected Kirkendall Effect in Twinned Icosahedral Nanocrystals Driven by Strain Gradient. *Nano Res* **2020**, *13* (10), 2641–2649. https://doi.org/10.1007/s12274-020-2903-9.

(52)   Wiebke Albrecht W.; van der Hoeven J.E.S.; Deng T-S.; de Jonghb P.E.; van Blaaderen A. Fully Alloyed Metal Nanorods with Highly Tunable Properties. *Nanoscale* **2017**, *9*, 2845–2851. https://doi.org/10.1039/b000000x.

(53)   González-Rubio, G.; Díaz-Núñez, P.; Rivera, A.; Prada, A.; Tardajos, G.; González-Izquierdo, J.; Bañares, L.; Llombart, P.; Macdowell, L. G.; Palafox, M. A.; Liz-Marzán, L. M.; Peña-Rodríguez, O.; Guerrero-Martínez, A. Femtosecond Laser Reshaping Yields Gold Nanorods with Ultranarrow Surface Plasmon Resonances. *Science (1979)* **2017**, *358* (6363), 640–644. https://doi.org/10.1126/science.aan8478.

(54)   Chen, P. C.; Liu, G.; Zhou, Y.; Brown, K. A.; Chernyak, N.; Hedrick, J. L.; He, S.; Xie, Z.; Lin, Q. Y.; Dravid, V. P.; O'Neill-Slawecki, S. A.; Mirkin, C. A. Tip-Directed Synthesis of Multimetallic Nanoparticles. *J Am Chem Soc* **2015**, *137* (28), 9167–9173. https://doi.org/10.1021/jacs.5b05139.

(55)   Ni, Y.; Kan, C.; He, L.; Zhu, X.; Jiang, M.; Shi, D. Alloyed Au-Ag Nanorods with Desired Plasmonic Properties and Stability in Harsh Environments. *Photonics Res* **2019**, *7* (5), 558. https://doi.org/10.1364/prj.7.000558.

(56)   Wang, X.; Kan, C.; Xu, J.; Zhu, X.; Jiang, M.; Ni, Y. Gold Nanobipyramid Enveloped in Alloyed Nanoshell for Stable Plasmonic Sensors. *J Phys D Appl Phys* **2020**, *53* (29). https://doi.org/10.1088/1361-6463/ab86e4.

(57)   Bai, Y.; Gao, C.; Yin, Y. Fully Alloyed Ag/Au Nanorods with Tunable Surface Plasmon Resonance and High Chemical Stability. *Nanoscale* **2017**, *9* (39), 14875–14880. https://doi.org/10.1039/c7nr06002e.

(58)   Lasserus, M.; Schnedlitz, M.; Knez, D.; Messner, R.; Schiffmann, A.; Lackner, F.; Hauser, A. W.; Hofer, F.; Ernst, W. E. Thermally Induced Alloying Processes in a Bimetallic System at the Nanoscale: AgAu Sub-5 Nm Core-Shell Particles Studied at Atomic Resolution. *Nanoscale* **2018**, *10* (4), 2017–2024. https://doi.org/10.1039/c7nr07286d.

(59)   Spannhake, J.; Schulz, O.; Helwig, A.; Krenkow, A.; Müller, G.; Doll, T. High-Temperature MEMS Heater Platforms: Long-Term Performance of Metal and Semiconductor Heater Materials. *Sensors* **2006**, 6(4), 405-419; https://doi.org/10.3390/s6040405.

(60)   Cho, H.; Shin, J. W.; Ryoo, R. Atomic Scale Mechanisms Underlying Thermal Reshaping of Anisotropic Gold Nanocrystals Revealed by in Situ Electron Microscopy. *J. Phys. Chem. C* **2020**, *124* (23), 12855–12863. https://doi.org/10.1021/acs.jpcc.0c04281.

(61)   Albrecht, W.; van de Glind, A.; Yoshida, H.; Isozaki, Y.; Imhof, A.; van Blaaderen, A.; de Jongh, P. E.; de Jong, K. P.; Zečević, J.; Takeda, S. Impact of the Electron Beam on the Thermal Stability of Gold Nanorods Studied by Environmental Transmission Electron Microscopy. *Ultramicroscopy* **2018**, *193*, 97–103. https://doi.org/10.1016/j.ultramic.2018.05.006.

(62)   Vanrompay, H.; Bladt, E.; Albrecht, W.; Béché, A.; Zakhozheva, M.; Sánchez-Iglesias, A.; Liz-Marzán, L. M.; Bals, S. 3D Characterization of Heat-Induced Morphological Changes of Au Nanostars by Fast: In Situ Electron Tomography. *Nanoscale* **2018**, *10* (48), 22792–22801. https://doi.org/10.1039/c8nr08376b.

(63)   Pastoriza-Santos, I.; Liz-Marzán, L. M. Reliable Methods for Silica Coating of Au Nanoparticles. *Methods Mol. Biol.* **2013**, *1025*, 75–93. https://doi.org/10.1007/978-1-62703-462-3_6.

(64)   Goris, B.; Bals, S.; Van Den Broek, W.; Carbó-Argibay, E.; Gómez-Graña, S.; Liz-Marzán, L. M.; Van Tendeloo, G. Atomic-Scale Determination of Surface Facets in Gold Nanorods. *Nat Mater* **2012**, *11* (11), 930–935. https://doi.org/10.1038/nmat3462.

(65)   Bals, S.; Goris, B.; De Backer, A.; Van Aert, S.; Van Tendeloo, G. Atomic Resolution Electron Tomography. *MRS Bull* **2016**, *41* (7), 525–530. https://doi.org/10.1557/mrs.2016.138.

(66) Goris, B.; De Beenhouwer, J.; De Backer, A.; Zanaga, D.; Batenburg, K. J.; Sánchez-Iglesias, A.; Liz-Marzán, L. M.; Van Aert, S.; Bals, S.; Sijbers, J.; Van Tendeloo, G. Measuring Lattice Strain in Three Dimensions through Electron Microscopy. *Nano Lett* **2015**, *15* (10), 6996–7001. https://doi.org/10.1021/acs.nanolett.5b03008.

(67) Tang, Y.; Ouyang, M. Tailoring Properties and Functionalities of Metal Nanoparticles through Crystallinity Engineering. *Nat Mater* **2007**, *6* (10), 754–759. https://doi.org/10.1038/nmat1982.

(68) Palatinus, L.; Brázda, P.; Jelínek, M.; Hrdá, J.; Steciuk, G.; Klementová, M. Specifics of the Data Processing of Precession Electron Diffraction Tomography Data and Their Implementation in the Program PETS2.0. *Acta Crystallogr B Struct Sci Cryst Eng Mater* **2019**, *75*, 512–522. https://doi.org/10.1107/S2052520619007534.

(69) Link, S.; El-Sayed, M. A. Size and Temperature Dependence of the Plasmon Absorption of Colloidal Gold Nanoparticles. *Journal of Physical Chemistry B* **1999**, *103* (21), 4212–4217. https://doi.org/10.1021/jp984796o.

(70) Lee, J. D.; Jishkariani, D.; Zhao, Y.; Najmr, S.; Rosen, D.; Kikkawa, J. M.; Stach, E. A.; Murray, C. B. Tuning the Electrocatalytic Oxygen Reduction Reaction Activity of Pt-Co Nanocrystals by Cobalt Concentration with Atomic-Scale Understanding. *ACS Appl Mater Interfaces* **2019**, *11* (30), 26789–26797. https://doi.org/10.1021/acsami.9b06346.

(71) Gustafsson, M. G. L. Surpassing the Lateral Resolution Limit by a Factor of Two Using Structured Illumination Microscopy. *J Microsc* **2000**, *198* (2), 82–87. https://doi.org/10.1046/j.1365-2818.2000.00710.x.

(72) Egerton, R. F. Electron Energy-Loss Spectroscopy in the TEM. *Rep Prog Phys* **2009**, *72* (1), 016502. https://doi.org/10.1088/0034-4885/72/1/016502.

(73) Ruska, E. The Development of the Electron Microscope and of Electron Microscopy. *Biosci Rep* **1987**, *7* (8), 607–629. https://doi.org/10.1007/BF01127674.

(74) Krivanek, O. L.; Lovejoy, T. C.; Dellby, N. Aberration-Corrected STEM for Atomic-Resolution Imaging and Analysis. *J Microsc* **2015**, *259* (3), 165–172. https://doi.org/10.1111/jmi.12254.

(75) Crewe, A. V.; Wall, J.; Langmore, J. Visibility of Single Atoms. *Science (1979)* **1970**, *168* (3937), 1338–1340. https://doi.org/10.1126/science.168.3937.1338.

(76) Haider, M.; Rose, H.; Uhlemann, S.; Kabius, B.; Urban, K. Towards 0.1 Nm Resolution with the First Spherically Corrected Transmission Electron Microscope. *J Electron Microsc (Tokyo)* **1998**, *47* (5), 395–405. https://doi.org/10.1093/oxfordjournals.jmicro.a023610.

(77) Haider, M.; Hartel, P.; Müller, H.; Uhlemann, S.; Zach, J. Current and Future Aberration Correctors for the Improvement of Resolution in Electron Microscopy. *Philos. Trans. R. Soc. A* **2009**, *367* (1903), 3665–3682. https://doi.org/10.1098/rsta.2009.0121.

(78) Liu, J. (Jimmy). Advances and Applications of Atomic-Resolution Scanning Transmission Electron Microscopy. *Microsc. and Microanal.* **2021**, *27* (5), 943–995. https://doi.org/10.1017/S1431927621012125.

(79) Winckelmans, N. Advanced electron tomography to investigate the growth of homogeneous and heterogeneous nanoparticles *Ph.D. Dissertation*, University of Antwerpen, Antwerpen, Belgium, **2018**.

(80) *Transmission Electron Energy Loss Spectrometry in Materials Science and The EELS Atlas*; Ahn, C. C., Ed.; Wiley, **2004**. https://doi.org/10.1002/3527605495.

(81) Egerton, R. F. Electron Energy-Loss Spectroscopy in the TEM. *Rep Prog Phys* **2009**, *72* (1), 016502. https://doi.org/10.1088/0034-4885/72/1/016502.

(82) Kimoto, K. Practical Aspects of Monochromators Developed for Transmission Electron Microscopy. *Microscopy* **2014**, *63* (5), 337–344. https://doi.org/10.1093/jmicro/dfu027.

(83) Lopatin, S.; Cheng, B.; Liu, W.-T.; Tsai, M.-L.; He, J.-H.; Chuvilin, A. Optimization of Monochromated TEM for Ultimate Resolution Imaging and Ultrahigh Resolution Electron Energy Loss Spectroscopy. *Ultramicroscopy* **2018**, *184*, 109–115. https://doi.org/10.1016/j.ultramic.2017.08.016.

(84) Krivanek, O. L.; Dellby, N.; Hachtel, J. A.; Idrobo, J.-C.; Hotz, M. T.; Plotkin-Swing, B.; Bacon, N. J.; Bleloch, A. L.; Corbin, G. J.; Hoffman, M. V.; Meyer, C. E.; Lovejoy, T. C. Progress in Ultrahigh Energy Resolution EELS. *Ultramicroscopy* **2019**, *203*, 60–67. https://doi.org/10.1016/j.ultramic.2018.12.006.

(85)   Cherqui, C.; Thakkar, N.; Li, G.; Camden, J. P.; Masiello, D. J. Characterizing Localized Surface Plasmons Using Electron Energy-Loss Spectroscopy. *Annu Rev Phys Chem* **2016**, *67* (1), 331–357. https://doi.org/10.1146/annurev-physchem-040214-121612.

(86)   Koh, A. L.; Bao, K.; Khan, I.; Smith, W. E.; Kothleitner, G.; Nordlander, P.; Maier, S. A.; McComb, D. W. Electron Energy-Loss Spectroscopy (EELS) of Surface Plasmons in Single Silver Nanoparticles and Dimers: Influence of Beam Damage and Mapping of Dark Modes. *ACS Nano* **2009**, *3* (10), 3015–3022. https://doi.org/10.1021/nn900922z.

(87)   Ophus, C. Four-Dimensional Scanning Transmission Electron Microscopy (4D-STEM): From Scanning Nanodiffraction to Ptychography and Beyond. *Microscopy and Microanalysis* **2019**, *25* (3), 563–582. https://doi.org/10.1017/S1431927619000497.

(88)   Bustillo, K. C.; Zeltmann, S. E.; Chen, M.; Donohue, J.; Ciston, J.; Ophus, C.; Minor, A. M. 4D-STEM of Beam-Sensitive Materials. *Acc Chem Res* **2021**, *54* (11), 2543–2551. https://doi.org/10.1021/acs.accounts.1c00073.

(89)   Li, G.; Zhang, H.; Han, Y. 4D-STEM Ptychography for Electron-Beam-Sensitive Materials. *ACS Cent Sci* **2022**, *8* (12), 1579–1588. https://doi.org/10.1021/acscentsci.2c01137.

(90)   Levin B.D.A.; Zhang, C.; Bammes, B.; Voyles, P. M.; Bilhorn, R. B. 4D STEM with a Direct Electron Detector. **2020** https://doi.org/10.1002/was.00010003.

(91)   Lazić, I.; Bosch, E. G. T. Analytical Review of Direct Stem Imaging Techniques for Thin Samples; **2017**; 75–184. https://doi.org/10.1016/bs.aiep.2017.01.006.

(92)   Li, Z.; Biskupek, J.; Kaiser, U.; Rose, H. Integrated Differential Phase Contrast (IDPC)-STEM Utilizing a Multi-Sector Detector for Imaging Thick Samples. *Microscopy and Microanalysis* **2022**, *28* (3), 611–621. https://doi.org/10.1017/S1431927622000289.

(93)   Yücelen, E.; Lazić, I.; Bosch, E. G. T. Phase Contrast Scanning Transmission Electron Microscopy Imaging of Light and Heavy Atoms at the Limit of Contrast and Resolution. *Sci Rep* **2018**, *8* (1), 2676. https://doi.org/10.1038/s41598-018-20377-2.

(94)   Lazić, I.; Bosch, E. G. T.; Lazar, S. Phase Contrast STEM for Thin Samples: Integrated Differential Phase Contrast. *Ultramicroscopy* **2016**, *160*, 265–280. https://doi.org/10.1016/j.ultramic.2015.10.011.

(95)	Lazić, I.; Wirix, M.; Leidl, M. L.; de Haas, F.; Mann, D.; Beckers, M.; Pechnikova, E. V.; Müller-Caspary, K.; Egoavil, R.; Bosch, E. G. T.; Sachse, C. Single-Particle Cryo-EM Structures from IDPC–STEM at near-Atomic Resolution. *Nat Methods* **2022**, *19* (9), 1126–1136. https://doi.org/10.1038/s41592-022-01586-0.

(96)	J. Radon. Über Die Bestimmung von Funktionen Durch Ihre Integralwerte Längs Gewisser Mannigfaltigkeiten. *Ber. über Verh. Königlich-Sächsischen Ges. Wiss. Leipzig* **1917**, *69*, 262–277.

(97)	Winckelmans, N. Advanced electron tomography to investigate the growth of homogeneous and heterogeneous nanoparticles *Ph.D. Dissertation*, University of Antwerpen, Antwerpen, Belgium, **2018**.

(98)	Smith, P. R.; Peters, T. M.; Bates, R. H. T. Image Reconstruction from Finite Numbers of Projections. *Journal of Physics A: Mathematical, Nuclear and General* **1973**, *6* (3), 361–382. https://doi.org/10.1088/0305-4470/6/3/011.

(99)	Kirkland, A. I., Haigh, S. J., Eds.; *Nanocharacterisation*; The Royal Society of Chemistry*, **2015**. https://doi.org/10.1039/9781782621867.

(100)	Shepp, L. A.; Logan, B. F. The Fourier Reconstruction of a Head Section. *IEEE Trans Nucl Sci* **1974**, *21* (3), 21–43. https://doi.org/10.1109/TNS.1974.6499235.

(101)	Midgley, P. A.; Bals, S. Electron Tomography. In *Handbook of Nanoscopy*; Wiley, **2012**; 253–279. https://doi.org/10.1002/9783527641864.ch7.

(102)	Koster, A. J.; Ziese, U.; Verkleij, A. J.; Janssen, A. H.; de Jong, K. P. Three-Dimensional Transmission Electron Microscopy: A Novel Imaging and Characterization Technique with Nanometer Scale Resolution for Materials Science. *J Phys Chem B* **2000**, *104* (40), 9368–9370. https://doi.org/10.1021/jp0015628.

(103)	Bárcena, M.; Koster, A. J. Electron Tomography in Life Science. *Semin Cell Dev Biol* **2009**, *20* (8), 920–930. https://doi.org/10.1016/j.semcdb.2009.07.008.

(104)	Bals, S.; Kabius, B.; Haider, M.; Radmilovic, V.; Kisielowski, C. Annular Dark Field Imaging in a TEM. *Solid State Commun* **2004**, *130* (10), 675–680. https://doi.org/10.1016/j.ssc.2004.03.035.

(105)	Weyland, M.; Midgley, P. A. Electron Tomography. *Materials Today* **2004**, *7* (12), 32–40. https://doi.org/10.1016/S1369-7021(04)00569-3.

(106) Winckelmans, N.; Altantzis, T.; Grzelczak, M.; Sánchez-Iglesias, A.; Liz-Marzán, L. M.; Bals, S. Multimode Electron Tomography as a Tool to Characterize the Internal Structure and Morphology of Gold Nanoparticles. *J Phys Chem C* **2018**, *122* (25), 13522–13528. https://doi.org/10.1021/acs.jpcc.7b12379.

(107) Goris, B.; Polavarapu, L.; Bals, S.; Van Tendeloo, G.; Liz-Marzán, L. M. Monitoring Galvanic Replacement Through Three-Dimensional Morphological and Chemical Mapping. *Nano Lett* **2014**, *14* (6), 3220–3226. https://doi.org/10.1021/nl500593j.

(108) Liakakos, N.; Gatel, C.; Blon, T.; Altantzis, T.; Lentijo-Mozo, S.; Garcia-Marcelot, C.; Lacroix, L.-M.; Respaud, M.; Bals, S.; Van Tendeloo, G.; Soulantica, K. Co–Fe Nanodumbbells: Synthesis, Structure, and Magnetic Properties. *Nano Lett* **2014**, *14* (5), 2747–2754. https://doi.org/10.1021/nl500734k.

(109) Zanaga, D.; Altantzis, T.; Polavarapu, L.; Liz-Marzán, L. M.; Freitag, B.; Bals, S. A New Method for Quantitative XEDS Tomography of Complex Heteronanostructures. *Part Part Syst Charact* **2016**, *33* (7), 396–403. https://doi.org/10.1002/ppsc.201600021.

(110) Williams, D. B.; Carter, C. B. *Transmission Electron Microscopy*; Springer US: Boston, MA, **1996**. https://doi.org/10.1007/978-1-4757-2519-3.

(111) *ChemiSTEM Technology: A Revolution in EDX Analytics*. Application brochure, FEI **2013**.

(112) Thomas, J.; Gemming, T. *Analytical Transmission Electron Microscopy*; Springer Netherlands: Dordrecht, **2014**. https://doi.org/10.1007/978-94-017-8601-0.

(113) Brydson. *Aberration-Corrected Analytical Transmission Electron Microscopy*; Brydson, R., Ed.; Wiley, **2011**. https://doi.org/10.1002/9781119978848.

(114) Watanabe, M.; Williams, D. B. The Quantitative Analysis of Thin Specimens: A Review of Progress from the Cliff-Lorimer to the New Zeta-Factor Methods. *J Microsc* **2006**, *221* (2), 89–109. https://doi.org/10.1111/j.1365-2818.2006.01549.x.

(115) Schlossmacher P.; Klenov D.O.; Freitag B.; von Harrach S.; Steinbac A. Nanoscale Chemical Compositional Analysis with an Innovative S/TEM-EDX System **2010**.

(116) Zhong, Z.; Goris, B.; Schoenmakers, R.; Bals, S.; Batenburg, K. J. A Bimodal Tomographic Reconstruction Technique Combining EDS-STEM and HAADF-STEM. *Ultramicroscopy* **2017**, *174*, 35–45. https://doi.org/10.1016/j.ultramic.2016.12.008.

(117) Zanaga, D.; Altantzis, T.; Sanctorum, J.; Freitag, B.; Bals, S. An Alternative Approach for ζ-Factor Measurement Using Pure Element Nanoparticles. *Ultramicroscopy* **2016**, *164*, 11–16. https://doi.org/10.1016/j.ultramic.2016.03.002.

(118) Watanabe, M.; Williams, D. B. The Quantitative Analysis of Thin Specimens: A Review of Progress from the Cliff-Lorimer to the New Zeta-Factor Methods. *J Microsc* **2006**, *221* (2), 89–109. https://doi.org/10.1111/j.1365-2818.2006.01549.x.

(119) Parisini, A.; Frabboni, S.; Gazzadi, G. C.; Rosa, R.; Armigliato, A. Comparison of Cliff–Lorimer-Based Methods of Scanning Transmission Electron Microscopy (STEM) Quantitative X-Ray Microanalysis for Application to Silicon Oxycarbides Thin Films. *Microsc. Microanal.* **2018**, *24* (3), 193–206. https://doi.org/10.1017/S1431927618000259.

(120) Skorikov, A.; Heyvaert, W.; Albecht, W.; Pelt, D. M.; Bals, S. Deep Learning-Based Denoising for Improved Dose Efficiency in EDX Tomography of Nanoparticles. *Nanoscale* **2021**, *13* (28), 12242–12249. https://doi.org/10.1039/D1NR03232A.

(121) Midgley, P. A. An Introduction to Off-Axis Electron Holography. *Micron* **2001**, *32* (2), 167–184. https://doi.org/10.1016/S0968-4328(99)00105-5.

(122) Midgley, P. A.; Dunin-Borkowski, R. E. Electron Tomography and Holography in Materials Science. *Nat Mater* **2009**, *8* (4), 271–280. https://doi.org/10.1038/nmat2406.

(123) Twitchett-Harrison, A. C.; Yates, T. J. V.; Newcomb, S. B.; Dunin-Borkowski, R. E.; Midgley, P. A. High-Resolution Three-Dimensional Mapping of Semiconductor Dopant Potentials. *Nano Lett* **2007**, *7* (7), 2020–2023. https://doi.org/10.1021/nl070858n.

(124) Midgley, P. A.; Weyland, M. 3D Electron Microscopy in the Physical Sciences: The Development of Z-Contrast and EFTEM Tomography. *Ultramicroscopy* **2003**, *96* (3–4), 413–431. https://doi.org/10.1016/S0304-3991(03)00105-0.

(125) Goris, B.; Bals, S.; Van den Broek, W.; Verbeeck, J.; Van Tendeloo, G. Exploring Different Inelastic Projection Mechanisms for Electron

Tomography. *Ultramicroscopy* **2011**, *111* (8), 1262–1267. https://doi.org/10.1016/j.ultramic.2011.02.007.

(126) Goris, B.; Meledina, M.; Turner, S.; Zhong, Z.; Batenburg, K. J.; Bals, S. Three Dimensional Mapping of Fe Dopants in Ceria Nanocrystals Using Direct Spectroscopic Electron Tomography. *Ultramicroscopy* **2016**, *171*, 55–62. https://doi.org/10.1016/j.ultramic.2016.08.017.

(127) Goris, B.; Turner, S.; Bals, S.; Van Tendeloo, G. Three-Dimensional Valency Mapping in Ceria Nanocrystals. *ACS Nano* **2014**, *8* (10), 10878–10884. https://doi.org/10.1021/nn5047053.

(128) Lee, J.; Lee, M.; Park, Y.; Ophus, C.; Yang, Y. High-Fidelity 3D Imaging Achieved Through Multislice Electron Tomography Using 4D-STEM. *Microsc. Microanal.* **2023**, *29* (Supplement_1), 1388–1389. https://doi.org/10.1093/micmic/ozad067.714.

(129) Lee, J.; Lee, M.; Park, Y.; Ophus, C.; Yang, Y. Multislice Electron Tomography Using Four-Dimensional Scanning Transmission Electron Microscopy. *Phys Rev Appl* **2023**, *19* (5), 054062. https://doi.org/10.1103/PhysRevApplied.19.054062.

(130) Goris, B. Advanced Electron Tomography : 3 Dimensional Structural Characterisation of Nanomaterials down to the Atomic Scale. *Ph.D. Dissertation*, University of Antwerpen, Antwerpen, Belgium, **2014**.

(131) Sugiyama, M. A Review of Focused Ion Beam Technology and Its Applications in Transmission Electron Microscopy. *J Electron Microsc* **2004**, *53* (5), 527–536. https://doi.org/10.1093/jmicro/dfh071.

(132) Kawase, N.; Kato, M.; Nishioka, H.; Jinnai, H. Transmission Electron Microtomography without the "Missing Wedge" for Quantitative Structural Analysis. *Ultramicroscopy* **2007**, *107* (1), 8–15. https://doi.org/10.1016/j.ultramic.2006.04.007.

(133) Ke, X.; Bals, S.; Cott, D.; Hantschel, T.; Bender, H.; Van Tendeloo, G. Three-Dimensional Analysis of Carbon Nanotube Networks in Interconnects by Electron Tomography without Missing Wedge Artifacts. *Microsc. Microanal.* **2010**, *16* (2), 210–217. https://doi.org/10.1017/S1431927609991371.

(134) Molina, L.; Tan, H.; Biermans, E.; Batenburg, K. J.; Verbeeck, J.; Bals, S.; Tendeloo, G. Van. Barrier Efficiency of Sponge-like $La_2Zr_2O_7$ Buffer Layers for YBCO-Coated Conductors. *Supercond Sci Technol* **2011**, *24* (6), 065019. https://doi.org/10.1088/0953-2048/24/6/065019.

(135) Bals, S.; Van Aert, S.; Van Tendeloo, G. High Resolution Electron Tomography. *Curr Opin Solid State Mater Sci* **2013**, *17* (3), 107–114. https://doi.org/10.1016/j.cossms.2013.03.001.

(136) Jarausch, K.; Leonard, D. N. Three-Dimensional Electron Microscopy of Individual Nanoparticles. *J Electron Microsc* **2009**, *58* (3), 175–183. https://doi.org/10.1093/jmicro/dfn028.

(137) Huang, X.; Tang, Y.; Kübel, C.; Wang, D. Precisely Picking Nanoparticles by a "Nano-Scalpel" for 360° Electron Tomography. *Microsc. Microanal.* **2022**, *28* (6), 1981–1988. https://doi.org/10.1017/S1431927622012247.

(138) Mezerji, H.; Van den Broek, W.; Bals, S. A Practical Method to Determine the Effective Resolution in Incoherent Experimental Electron Tomography. *Ultramicroscopy* **2011**, *111* (5), 330–336. https://doi.org/10.1016/j.ultramic.2011.01.021.

(139) Moon, T. K. The Expectation-Maximization Algorithm. *IEEE Signal Process Mag* **1996**, *13* (6), 47–60. https://doi.org/10.1109/79.543975.

(140) Gomi, T. X-Ray Digital Tomosynthesis Imaging — Comparison of Reconstruction Algorithms in Terms of a Reduction in the Exposure Dose for Arthroplasty. *Arthroplasty - A Comprehensive Review*, **2016**. https://doi.org/10.5772/60920.

(141) Batenburg, K. J.; Bals, S.; Sijbers, J.; Kübel, C.; Midgley, P. A.; Hernandez, J. C.; Kaiser, U.; Encina, E. R.; Coronado, E. A.; Van Tendeloo, G. 3D Imaging of Nanomaterials by Discrete Tomography. *Ultramicroscopy* **2009**, *109* (6), 730–740. https://doi.org/10.1016/j.ultramic.2009.01.009.

(142) Goris, B.; Van den Broek, W.; Batenburg, K. J.; Heidari Mezerji, H.; Bals, S. Electron Tomography Based on a Total Variation Minimization Reconstruction Technique. *Ultramicroscopy* **2012**, *113*, 120–130. https://doi.org/10.1016/j.ultramic.2011.11.004.

(143) Zhuge, X.; Jinnai, H.; Dunin-Borkowski, R. E.; Migunov, V.; Bals, S.; Cool, P.; Bons, A.-J.; Batenburg, K. J. Automated Discrete Electron Tomography – Towards Routine High-Fidelity Reconstruction of Nanomaterials. *Ultramicroscopy* **2017**, *175*, 87–96. https://doi.org/10.1016/j.ultramic.2017.01.009.

(144) LeSar, R. *Introduction to Computational Materials Science*; Cambridge University Press, **2013**. https://doi.org/10.1017/CBO9781139033398.

(145) Frenkel, D. ; S. B. *Understanding Molecular Simulation: From Algorithms To*; **2002**.

(146) Albrecht, W.; Arslan Irmak, E.; Altantzis, T.; Pedrazo-Tardajos, A.; Skorikov, A.; Deng, T.; van der Hoeven, J. E. S.; van Blaaderen, A.; Van Aert, S.; Bals, S. 3D Atomic-Scale Dynamics of Laser-Light-Induced Restructuring of Nanoparticles Unraveled by Electron Tomography. *Adv. Mater.* **2021**, *33* (33). https://doi.org/10.1002/adma.202100972.

(147) Pedrazo-Tardajos, A.; Irmak, E. A.; Kumar, V.; Sánchez-Iglesias, A.; Chen, Q.; Wirix, M.; Freitag, B.; Albrecht, W.; Van Aert, S.; Liz-Marzán, L. M.; Bals, S. Thermal Activation of Gold Atom Diffusion in Au@Pt Nanorods. *ACS Nano* **2022**, *16* (6), 9608–9619. https://doi.org/10.1021/acsnano.2c02889.

(148) Opletal, G.; Grochola, G.; Chui, Y. H.; Snook, I. K.; Russo, S. P. Stability and Transformations of Heated Gold Nanorods. *J. Phys. Chem. C* **2011**, *115* (11), 4375–4380. https://doi.org/10.1021/jp1074913.

(149) Wang, Y.; Teitel, S.; Dellago, C. Surface-Driven Bulk Reorganization of Gold Nanorods. *Nano Lett* **2005**, *5* (11), 2174–2178. https://doi.org/10.1021/nl051149h.

(150) Gan, Y.; Jiang, S. Ultrafast Laser-Induced Premelting and Structural Transformation of Gold Nanorod. *J. Appl. Phys.* **2013**, *113* (7). https://doi.org/10.1063/1.4792659.

(151) Patil, S. P.; Rege, A.; Sagardas; Itskov, M.; Markert, B. Mechanics of Nanostructured Porous Silica Aerogel Resulting from Molecular Dynamics Simulations. *J Phys Chem B* **2017**, *121* (22), 5660–5668. https://doi.org/10.1021/acs.jpcb.7b03184.

(152) Grochola, G.; Russo, S. P.; Snook, I. K. On Fitting a Gold Embedded Atom Method Potential Using the Force Matching Method. *J Chem Phys* **2005**, *123* (20). https://doi.org/10.1063/1.2124667.

(153) Vashishta, P.; Nakano, A.; Kalia, R. K.; Ebbsjö, I. Molecular Dynamics Simulations of Covalent Amorphous Insulators on Parallel Computers. *J Non Cryst Solids* **1995**, *182* (1–2), 59–67. https://doi.org/10.1016/0022-3093(94)00576-1.

(154) Rapaport, D. C. *The Art of Molecular Dynamics Simulation*; Cambridge University Press, **2004**. https://doi.org/10.1017/CBO9780511816581.

(155)   O'Brien, C. J.; Barr, C. M.; Price, P. M.; Hattar, K.; Foiles, S. M. Grain Boundary Phase Transformations in PtAu and Relevance to Thermal Stabilization of Bulk Nanocrystalline Metals. *J Mater Sci* **2018**, *53* (4), 2911–2927. https://doi.org/10.1007/s10853-017-1706-1.

(156)   Carbó-Argibay, E.; Rodríguez-González, B.; Gómez-Graña, S.; Guerrero-Martínez, A.; Pastoriza-Santos, I.; Pérez-Juste, J.; Liz-Marzán, L. M. The Crystalline Structure of Gold Nanorods Revisited: Evidence for Higher-Index Lateral Facets. *Angewandte Chemie International Edition* **2010**, *49* (49), 9397–9400. https://doi.org/10.1002/anie.201004910.

(157)   Hohenberg, P.; Kohn, W. Inhomogeneous Electron Gas. *Phys Rev* **1964**, *136* (3B), B864–B871. https://doi.org/10.1103/PhysRev.136.B864.

(158)   Kohn, W.; Sham, L. J. Self-Consistent Equations Including Exchange and Correlation Effects. *Phys Rev* **1965**, *140* (4A), A1133–A1138. https://doi.org/10.1103/PhysRev.140.A1133.

(159)   Aarons J. Density Functional Theory Applied to Metallic Nanoparticles; *Doctoral dissertation*, University of Southampton, UK **2018**.

(160)   Gunnarsson, O.; Lundqvist, B. I. Exchange and Correlation in Atoms, Molecules, and Solids by the Spin-Density-Functional Formalism. *Phys Rev B* **1976**, *13* (10), 4274–4298. https://doi.org/10.1103/PhysRevB.13.4274.

(161)   Perdew, J. P.; Burke, K.; Ernzerhof, M. Generalized Gradient Approximation Made Simple. *Phys Rev Lett* **1996**, *77* (18), 3865–3868. https://doi.org/10.1103/PhysRevLett.77.3865.

(162)   Rosa, M.; Corni, S.; Di Felice, R. Van Der Waals Effects at Molecule-Metal Interfaces. *Phys Rev B* **2014**, *90* (12), 125448. https://doi.org/10.1103/PhysRevB.90.125448.

(163)   Campisi, S.; Beevers, C.; Nasrallah, A.; Catlow, C. R. A.; Chan-Thaw, C. ; Manzoli, M.; Dimitratos, N.; Willock, D. J.; Roldan, A.; Villa, A. DFT-Assisted Spectroscopic Studies on the Coordination of Small Ligands to Palladium: From Isolated Ions to Nanoparticles. *J Phys Chem C* **2020**, *124* (8), 4781–4790. https://doi.org/10.1021/acs.jpcc.9b09791.

(164)   Myroshnychenko, V.; Rodríguez-Fernández, J.; Pastoriza-Santos, I.; Funston, A. M.; Novo, C.; Mulvaney, P.; Liz-Marzán, L. M.; García de Abajo, F. J. Modelling the Optical Response of Gold Nanoparticles. *Chem Soc Rev* **2008**, *37* (9), 1792. https://doi.org/10.1039/b711486a.

(165)   Draine, B. T. The Discrete-Dipole Approximation and Its Application to Interstellar Graphite Grains. *Astrophys J* **1988**, *333*, 848. https://doi.org/10.1086/166795.

(166)   Zhang, S.; Bao, K.; Halas, N. J.; Xu, H.; Nordlander, P. Substrate-Induced Fano Resonances of a Plasmonic Nanocube: A Route to Increased-Sensitivity Localized Surface Plasmon Resonance Sensors Revealed. *Nano Lett* **2011**, *11* (4), 1657–1663. https://doi.org/10.1021/nl200135r.

(167)   Solís, D. M.; Taboada, J. M.; Obelleiro, F.; Liz-Marzán, L. M.; García de Abajo, F. J. Toward Ultimate Nanoplasmonics Modeling. *ACS Nano* **2014**, *8* (8), 7559–7570. https://doi.org/10.1021/nn5037703.

(168)   González-Rubio, G.; Mosquera, J.; Kumar, V.; Pedrazo-Tardajos, A.; Llombart, P.; Solís, D. M.; Lobato, I.; Noya, E. G.; Guerrero-Martínez, A.; Taboada, J. M.; Obelleiro, F.; MacDowell, L. G.; Bals, S.; Liz-Marzán, L. M. Micelle-Directed Chiral Seeded Growth on Anisotropic Gold Nanocrystals. *Science (1979)* **2020**, *368* (6498), 1472–1477. https://doi.org/10.1126/science.aba0980.

(169)   Hentschel, M.; Schäferling, M.; Duan, X.; Giessen, H.; Liu, N.. Chiral plasmonics. *Sci Adv,* **2017***, 3(5). https://doi.org/10.1126/sciadv.1602735.

(170)   Gansel, J. K.; Thiel, M.; Rill, M. S.; Decker, M.; Bade, K.; Saile, V.; von Freymann, G.; Linden, S.; Wegener, M. Gold Helix Photonic Metamaterial as Broadband Circular Polarizer. *Science (1979)* **2009**, *325* (5947), 1513–1515. https://doi.org/10.1126/science.1177031.

(171)   Collins, J. T.; Kuppe, C.; Hooper, D. C.; Sibilia, C.; Centini, M.; Valev, V. K. Chirality and Chiroptical Effects in Metal Nanostructures: Fundamentals and Current Trends. *Advanced Optical Materials*. Wiley-VCH Verlag, **2017**. https://doi.org/10.1002/adom.201700182.

(172)   Kuppe, C.; Zheng, X.; Williams, C.; Murphy, A. W. A.; Collins, J. T.; Gordeev, S. N.; Vandenbosch, G. A. E.; Valev, V. K. Measuring Optical Activity in the Far-Field from a Racemic Nanomaterial: Diffraction Spectroscopy from Plasmonic Nanogratings. *Nanoscale Horiz* **2019**, *4* (5), 1056–1062. https://doi.org/10.1039/c9nh00067d.

(173)   Guerrero-Martínez, A.; Auguié, B.; Alonso-Gómez, J. L.; Džolič, Z.; Gómez-Graña, S.; Žinić, M.; Cid, M. M.; Liz-Marzán, L. M. Intense Optical Activity from Three-Dimensional Chiral Ordering of Plasmonic Nanoantennas. *Angewandte Chemie - International Edition* **2011**, *50* (24), 5499–5503. https://doi.org/10.1002/anie.201007536.

(174)   Golla, M.; Albert, S. K.; Atchimnaidu, S.; Perumal, D.; Krishnan, N.;
         Varghese, R. DNA-Decorated, Helically Twisted Nanoribbons: A
         Scaffold for the Fabrication of One-Dimensional, Chiral, Plasmonic
         Nanostructures. *Angewandte Chemie* **2019**, *131* (12), 3905–3909.
         https://doi.org/10.1002/ange.201813900.

(175)   Kumar, J.; Eraña, H.; López-Martínez, E.; Claes, N.; Martín, V. F.;
         Solís, D. M.; Bals, S.; Cortajarena, A. L.; Castilla, J.; Liz-Marzán, L. M.
         Detection of Amyloid Fibrils in Parkinson's Disease Using Plasmonic
         Chirality. *PNAS* **2018**, *115* (13), 3225–3230.
         https://doi.org/10.1073/pnas.1721690115.

(176)   Zhao, Y.; Belkin, M. A.; Alù, A. Twisted Optical Metamaterials for
         Planarized Ultrathin Broadband Circular Polarizers. *Nat Commun* **2012**,
         3 (1), 870. https://doi.org/10.1038/ncomms1877.

(177)   Gao, J.; Wu, W.; Lemaire, V.; Carvalho, A.; Nlate, S.; Buffeteau, T.;
         Oda, R.; Battie, Y.; Pauly, M.; Pouget, E. Tuning the Chiroptical
         Properties of Elongated Nano-Objects via Hierarchical Organization.
         ACS Nano **2020**, *14* (4), 4111–4121.
         https://doi.org/10.1021/acsnano.9b08823.

(178)   Ma, Y.; Cao, Z.; Hao, J.; Zhou, J.; Yang, Z.; Yang, Y.; Wei, J.
         Controlled Synthesis of Au Chiral Propellers from Seeded Growth of
         Au Nanoplates for Chiral Differentiation of Biomolecules. *J. Phys.
         Chem. C* **2020**, *124* (44), 24306–24314.
         https://doi.org/10.1021/acs.jpcc.0c07046.

(179)   Lee, H. E.; Ahn, H. Y.; Mun, J.; Lee, Y. Y.; Kim, M.; Cho, N. H.;
         Chang, K.; Kim, W. S.; Rho, J.; Nam, K. T. Amino-Acid- A Nd
         Peptide-Directed Synthesis of Chiral Plasmonic Gold Nanoparticles.
         Nature **2018**, *556* (7701), 360–364. https://doi.org/10.1038/s41586-018-
         0034-1.

(180)   Cho, N. H.; Byun, G. H.; Lim, Y. C.; Im, S. W.; Kim, H.; Lee, H. E.;
         Ahn, H. Y.; Nam, K. T. Uniform Chiral Gap Synthesis for High
         Dissymmetry Factor in Single Plasmonic Gold Nanoparticle. *ACS Nano*
         2020, *14* (3), 3595–3602. https://doi.org/10.1021/acsnano.9b10094.

(181)   Rafiei Miandashti, A.; Khosravi Khorashad, L.; Kordesch, M. E.;
         Govorov, A. O.; Richardson, H. H. Experimental and Theoretical
         Observation of Photothermal Chirality in Gold Nanoparticle Helicoids.
         ACS Nano **2020**, *14* (4), 4188–4195.
         https://doi.org/10.1021/acsnano.9b09062.

(182)   Lee, H. E.; Kim, R. M.; Ahn, H. Y.; Lee, Y. Y.; Byun, G. H.; Im, S. W.; Mun, J.; Rho, J.; Nam, K. T. Cysteine-Encoded Chirality Evolution in Plasmonic Rhombic Dodecahedral Gold Nanoparticles. *Nat Commun* **2020**, *11* (1). https://doi.org/10.1038/s41467-019-14117-x.

(183)   Kim, H.; Im, S. W.; Cho, N. H.; Seo, D. H.; Kim, R. M.; Lim, Y. C.; Lee, H. E.; Ahn, H. Y.; Nam, K. T. γ-Glutamylcysteine- and Cysteinylglycine-Directed Growth of Chiral Gold Nanoparticles and Their Crystallographic Analysis. *Angewandte Chemie - International Edition* **2020**, *59* (31), 12976–12983. https://doi.org/10.1002/anie.202003760.

(184)   Xu, L.; Wang, X.; Wang, W.; Sun, M.; Choi, W. J.; Kim, J. Y.; Hao, C.; Li, S.; Qu, A.; Lu, M.; Wu, X.; Colombari, F. M.; Gomes, W. R.; Blanco, A. L.; de Moura, A. F.; Guo, X.; Kuang, H.; Kotov, N. A.; Xu, C. Enantiomer-Dependent Immunological Response to Chiral Nanoparticles. *Nature* **2022**, *601* (7893), 366–373. https://doi.org/10.1038/s41586-021-04243-2.

(185)   Spaeth, P.; Adhikari, S.; Le, L.; Jollans, T.; Pud, S.; Albrecht, W.; Bauer, T.; Caldarola, M.; Kuipers, L.; Orrit, M. Circular Dichroism Measurement of Single Metal Nanoparticles Using Photothermal Imaging. *Nano Lett* **2019**, *19* (12), 8934–8940. https://doi.org/10.1021/acs.nanolett.9b03853.

(186)   Vladár, A. E.; Hodoroaba, V. D. Characterization of Nanoparticles by Scanning Electron Microscopy. In *Characterization of Nanoparticles: Measurement Processes for Nanoparticles*; Elsevier, **2019**; 7–27. https://doi.org/10.1016/B978-0-12-814182-3.00002-X.

(187)   Buda, A. B.; Mislow, K. A Hausdorff Chirality Measure. *J Am Chem Soc* **1992**, *114* (15), 6006–6012. https://doi.org/10.1021/ja00041a016.

(188)   Yewande, E. O.; Neal, M. P.; Low, R. The Hausdorff Chirality Measure and a Proposed Hausdorff Structure Measure. *Mol Phys* **2009**, *107* (3), 281–291. https://doi.org/10.1080/00268970902835611.

(189)   Kim, J.-Y.; Yeom, J.; Zhao, G.; Calcaterra, H.; Munn, J.; Zhang, P.; Kotov, N. Assembly of Gold Nanoparticles into Chiral Superstructures Driven by Circularly Polarized Light. *J Am Chem Soc* **2019**, *141* (30), 11739–11744. https://doi.org/10.1021/jacs.9b00700.

(190)   Zhu, H.; Suenaga, K.; Hashimoto, A.; Urita, K.; Hata, K.; Iijima, S. Atomic-Resolution Imaging of the Nucleation Points of Single-Walled Carbon Nanotubes. *Small* **2005**, *1* (12), 1180–1183. https://doi.org/10.1002/smll.200500200.

(191)   Gailhanou, M.; Roussel, J.-M. Diffraction from Twisted Nanowires: Helicity Revealed by Anisotropy. *J Appl Crystallogr* **2018**, *51* (6), 1586–1596. https://doi.org/10.1107/S1600576718013493.

(192)   Thompson, J.; Braun, G.; Tierney, D.; Wessels, L.; Schmitzer, H.; Rossa, B.; Wagner, H. P.; Dultz, W. Rosalind Franklin's X-Ray Photo of DNA as an Undergraduate Optical Diffraction Experiment. *Am J Phys* **2018**, *86* (2), 95–104. https://doi.org/10.1119/1.5020051.

(193)   Heyvaert, W.; Pedrazo-Tardajos, A.; Kadu, A.; Claes, N.; González-Rubio, G.; Liz-Marzán, L. M.; Albrecht, W.; Bals, S. Quantification of the Helical Morphology of Chiral Gold Nanorods. *ACS Mater Lett* **2022**, *4* (4), 642–649. https://doi.org/10.1021/acsmaterialslett.2c00055.

(194)   Wu, F.; Tian, Y.; Luan, X.; Lv, X.; Li, F.; Xu, G.; Niu, W. Synthesis of Chiral Au Nanocrystals with Precise Homochiral Facets for Enantioselective Surface Chemistry. *Nano Lett* **2022**, *22* (7), 2915–2922. https://doi.org/10.1021/acs.nanolett.2c00094.

(195)   Meena, S. K.; Lerouge, F.; Baldeck, P.; Andraud, C.; Garavelli, M.; Parola, S.; Sulpizi, M.; Rivalta, I. On the Origin of Controlled Anisotropic Growth of Monodisperse Gold Nanobipyramids. *Nanoscale* **2021**, *13* (36), 15292–15300. https://doi.org/10.1039/D1NR01768C.

(196)   González-Rubio, G.; Scarabelli, L.; Guerrero-Martínez, A.; Liz-Marzán, L. M. Surfactant-Assisted Symmetry Breaking in Colloidal Gold Nanocrystal Growth. *ChemNanoMat* **2020**, *6* (5), 698–707. https://doi.org/10.1002/cnma.201900754.

(197)   Zhou, L.; Qiu, X.; Lyu, Z.; Zhao, M.; Xia, Y. Pd–Au Asymmetric Nanopyramids: Lateral vs Vertical Growth of Au on Pd Decahedral Seeds. *Chem. Mater* **2021**, *33* (13), 5391–5400. https://doi.org/10.1021/acs.chemmater.1c01489.

(198)   Park, J.-E.; Lee, Y.; Nam, J.-M. Precisely Shaped, Uniformly Formed Gold Nanocubes with Ultrahigh Reproducibility in Single-Particle Scattering and Surface-Enhanced Raman Scattering. *Nano Lett* **2018**, *18* (10), 6475–6482. https://doi.org/10.1021/acs.nanolett.8b02973.

(199)   Chen, C. C.; Zhu, C.; White, E. R.; Chiu, C. Y.; Scott, M. C.; Regan, B. C.; Marks, L. D.; Huang, Y.; Miao, J. Three-Dimensional Imaging of Dislocations in a Nanoparticle at Atomic Resolution. *Nature* **2013**, *496* (7443), 74–77. https://doi.org/10.1038/nature12009.

(200)   Claes, N.; Asapu, R.; Blommaerts, N.; Verbruggen, S. W.; Lenaerts, S.; Bals, S. Characterization of Silver-Polymer Core–Shell Nanoparticles

Using Electron Microscopy. *Nanoscale* **2018**, *10* (19), 9186–9191. https://doi.org/10.1039/C7NR09517A.

(201)   Altantzis, T.; Lobato, I.; De Backer, A.; Béché, A.; Zhang, Y.; Basak, S.; Porcu, M.; Xu, Q.; Sánchez-Iglesias, A.; Liz-Marzán, L. M.; Van Tendeloo, G.; Van Aert, S.; Bals, S. Three-Dimensional Quantification of the Facet Evolution of Pt Nanoparticles in a Variable Gaseous Environment. *Nano Lett* **2019**, *19* (1), 477–481. https://doi.org/10.1021/acs.nanolett.8b04303.

(202)   Jones, L.; Yang, H.; Pennycook, T. J.; Marshall, M. S. J.; Van Aert, S.; Browning, N. D.; Castell, M. R.; Nellist, P. D. Smart Align—a New Tool for Robust Non-Rigid Registration of Scanning Microscope Data. *Adv Struct Chem Imaging* **2015**, *1* (1), 8. https://doi.org/10.1186/s40679-015-0008-4.

(203)   Reddy, B. S.; Chatterji, B. N. An FFT-Based Technique for Translation, Rotation, and Scale-Invariant Image Registration. *IEEE Trans. Image Process.* **1996**, *5* (8), 1266–1271. https://doi.org/10.1109/83.506761.

(204)   Huang, T.; Rinaldi, K.; Lee, H. Comparison of Phase Retrieval Algorithms. In *ICASSP '87. IEEE International Conference on Acoustics, Speech, and Signal Processing*; Institute of Electrical and Electronics Engineers; **2018**, pp 1199–1200. https://doi.org/10.1109/ICASSP.1987.1169765.

(205)   Jo, J. G.; Cho, S. J.; Park, M.-C.; Jhon, Y. M.; Ju, B.-K. Modified Hybrid Input-Output Algorithm for Phase Retrieval. In *25th International Vacuum Nanoelectronics Conference*; IEEE, **2012**; 1–2. https://doi.org/10.1109/IVNC.2012.6316827.

(206)   Kiguchi, T.; Yamaguchi, Y.; Tashiro, S.; Sato, K.; Konno, T. J. Effect of Focal Depth of HAADF-STEM Imaging on the Solute Enriched Layers in Mg Alloys. *Mater Trans* **2015**, *56* (10), 1633–1638. https://doi.org/10.2320/matertrans.MAW201505.

(207)   Kolb, U.; Gorelik, T.; Kübel, C.; Otten, M. T.; Hubert, D. Towards Automated Diffraction Tomography: Part I—Data Acquisition. *Ultramicroscopy* **2007**, *107* (6–7), 507–513. https://doi.org/10.1016/j.ultramic.2006.10.007.

(208)   Kolb, U.; Gorelik, T.; Otten, M. T. Towards Automated Diffraction Tomography. Part II—Cell Parameter Determination. *Ultramicroscopy* **2008**, *108* (8), 763–772. https://doi.org/10.1016/j.ultramic.2007.12.002.

(209)   Abakumov, A. M.; Fedotov, S. S.; Antipov, E. V.; Tarascon, J.-M. Solid State Chemistry for Developing Better Metal-Ion Batteries. *Nat*

Commun **2020**, *11* (1), 4976. https://doi.org/10.1038/s41467-020-18736-7.

(210)   IEEE Standard Test Procedures for Antennas, ANSI/IEEE Std 149-1979, **1979**, 1-144. https://doi.org/10.1109/IEEESTD.1979.120310.

(211)   Braslavsky, S. E. Glossary of Terms Used in Photochemistry, 3rd Edition (IUPAC Recommendations 2006). *Pure and Applied Chemistry* **2007**, *79* (3), 293–465. https://doi.org/10.1351/pac200779030293.

(212)   Kim, J. W.; Cho, N. H.; Lim, Y. C.; Im, S. W.; Han, J. H.; Nam, K. T.; Im, S. W. Controlling the Size and Circular Dichroism of Chiral Gold Helicoids. *Mater Adv* **2021**, *2* (21), 6988–6995. https://doi.org/10.1039/d1ma00783a.

(213)   Kim, H.; Im, S. W.; Cho, N. H.; Seo, D. H.; Kim, R. M.; Lim, Y. C.; Lee, H. E.; Ahn, H. Y.; Nam, K. T. γ-Glutamylcysteine- and Cysteinylglycine-Directed Growth of Chiral Gold Nanoparticles and Their Crystallographic Analysis. *Angewandte Chemie - International Edition* **2020**, *59* (31), 12976–12983. https://doi.org/10.1002/anie.202003760.

(214)   Lee, H. E.; Kim, R. M.; Ahn, H. Y.; Lee, Y. Y.; Byun, G. H.; Im, S. W.; Mun, J.; Rho, J.; Nam, K. T. Cysteine-Encoded Chirality Evolution in Plasmonic Rhombic Dodecahedral Gold Nanoparticles. *Nat Commun* **2020**, *11* (1). https://doi.org/10.1038/s41467-019-14117-x.

(215)   Walsh, M. J.; Tong, W.; Katz-Boon, H.; Mulvaney, P.; Etheridge, J.; Funston, A. M. A Mechanism for Symmetry Breaking and Shape Control in Single-Crystal Gold Nanorods. *Acc Chem Res* **2017**, *50* (12), 2925–2935. https://doi.org/10.1021/acs.accounts.7b00313.

(216)   Solís, D. M.; Taboada, J. M.; Obelleiro, F.; Liz-Marzán, L. M.; García De Abajo, F. J. Toward Ultimate Nanoplasmonics Modeling. *ACS Nano*. American Chemical Society August 26, 2014, pp 7559–7570. https://doi.org/10.1021/nn5037703.

(217)   Golze, S. D.; Porcu, S.; Zhu, C.; Sutter, E.; Ricci, P. C.; Kinzel, E. C.; Hughes, R. A.; Neretina, S. Sequential Symmetry-Breaking Events as a Synthetic Pathway for Chiral Gold Nanostructures with Spiral Geometries. *Nano Lett* **2021**, *21* (7), 2919–2925. https://doi.org/10.1021/acs.nanolett.0c05105.

(218)   Kutsukake, K.; Abe, T.; Usami, N.; Fujiwara, K.; Morishita, K.; Nakajima, K. Formation Mechanism of Twin Boundaries during Crystal Growth of Silicon. *Scr Mater* **2011**, *65* (6), 556–559. https://doi.org/10.1016/j.scriptamat.2011.06.028.

(219)   Weinberger, C. R.; Boyce, B. L.; Battaile, C. C. Slip Planes in Bcc Transition Metals. *Int Mater Rev* **2013**, *58* (5), 296–314. https://doi.org/10.1179/1743280412Y.0000000015.

(220)   Jenkinson K., Liz-Marzán L.M., Bals S. Multimode Electron Tomography Sheds Light on Synthesis, Structure, and Properties of Complex Metal-Based Nanoparticles. *Adv. Mater.* **2022**, 34, 2110394. https://doi.org/10.1002/adma.202110394

(221)   Goris, B.; De Backer, A.; Van Aert, S.; Gómez-Graña, S.; Liz-Marzán, L. M.; Van Tendeloo, G.; Bals, S. Three-Dimensional Elemental Mapping at the Atomic Scale in Bimetallic Nanocrystals. *Nano Lett* **2013**, *13* (9), 4236–4241. https://doi.org/10.1021/nl401945b.

(222)   Albrecht, W.; van de Glind, A.; Yoshida, H.; Isozaki, Y.; Imhof, A.; van Blaaderen, A.; de Jongh, P. E.; de Jong, K. P.; Zečević, J.; Takeda, S. Impact of the Electron Beam on the Thermal Stability of Gold Nanorods Studied by Environmental Transmission Electron Microscopy. *Ultramicroscopy* **2018**, *193*, 97–103. https://doi.org/10.1016/j.ultramic.2018.05.006.

(223)   Sholl, D. S.; Asthagiri, A.; Power, T. D. Naturally Chiral Metal Surfaces as Enantiospecific Adsorbents. *J Phys Chem B* **2002**, *105* (21), 4771–4782. https://doi.org/10.1021/jp004524x.

(224)   Shukla, N.; Gellman, A. J. Chiral Metal Surfaces for Enantioselective Processes. *Nature Materials*. Nature Research **2020**, 939–945. https://doi.org/10.1038/s41563-020-0734-4.

(225)   Morales-Vidal, J.; López, N.; Ortuño, M. A. Chirality Transfer in Gold Nanoparticles by L-Cysteine Amino Acid: A First-Principles Study. *J Phys Chem C* **2019**, *123* (22), 13758–13764. https://doi.org/10.1021/acs.jpcc.9b02918.

(226)   De Roo, J. The Surface Chemistry of Colloidal Nanocrystals Capped by Organic Ligands. *Chem. Mater.* **2023**, *35* (10), 3781–3792. https://doi.org/10.1021/acs.chemmater.3c00638.

(227)   Sun, L.; Zhang, Q.; Li, G. G.; Villarreal, E.; Fu, X.; Wang, H. Multifaceted Gold–Palladium Bimetallic Nanorods and Their Geometric, Compositional, and Catalytic Tunabilities. *ACS Nano* **2017**, *11* (3), 3213–3228. https://doi.org/10.1021/acsnano.7b00264.

(228)   Barnard, A. S.; Curtiss, L. A. Modeling the Preferred Shape, Orientation and Aspect Ratio of Gold Nanorods. *J Mater Chem* **2007**, *17* (31), 3315–3323. https://doi.org/10.1039/b704798c.

(229)   Zhang, Q.; Han, L.; Jing, H.; Blom, D. A.; Lin, Y.; Xin, H. L.; Wang, H. Facet Control of Gold Nanorods. *ACS Nano* **2016**, *10* (2), 2960–2974. https://doi.org/10.1021/acsnano.6b00258.

(230)   Wang, Q.; Wang, Z.; Li, Z.; Xiao, J.; Shan, H.; Fang, Z.; Qi, L. Controlled Growth and Shape-Directed Self-Assembly of Gold Nanoarrows; *Sci Adv* **2017,** 3,e1701183. https://doi.org/10.1126/sciadv.1701183.

(231)   Sun, L.; Zhang, Q.; Li, G. G.; Villarreal, E.; Fu, X.; Wang, H. Multifaceted Gold-Palladium Bimetallic Nanorods and Their Geometric, Compositional, and Catalytic Tunabilities. *ACS Nano* **2017**, *11* (3), 3213–3228. https://doi.org/10.1021/acsnano.7b00264.

(232)   van Aarle, W.; Palenstijn, W. J.; De Beenhouwer, J.; Altantzis, T.; Bals, S.; Batenburg, K. J.; Sijbers, J. The ASTRA Toolbox: A Platform for Advanced Algorithm Development in Electron Tomography. *Ultramicroscopy* **2015**, *157*, 35–47. https://doi.org/10.1016/j.ultramic.2015.05.002.

(233)   Pu, S.; Gong, C.; Robertson, A. W. Liquid Cell Transmission Electron Microscopy and Its Applications. *R Soc Open Sci* **2020**, *7* (1), 191204. https://doi.org/10.1098/rsos.191204.

(234)   Ni, B.; Mychinko, M.; Gómez-Graña, S.; Morales-Vidal, J.; Obelleiro-Liz, M.; Heyvaert, W.; Vila-Liarte, D.; Zhuo, X.; Albrecht, W.; Zheng, G.; González-Rubio, G.; Taboada, J. M.; Obelleiro, F.; López, N.; Pérez-Juste, J.; Pastoriza-Santos, I.; Cölfen, H.; Bals, S.; Liz-Marzán, L. M. Chiral Seeded Growth of Gold Nanorods Into 4-Fold Twisted Nanoparticles with Plasmonic Optical Activity. *Adv Mater* **2022**, 2208299. https://doi.org/10.1002/adma.202208299.

(235)   Zhuo, X.; Mychinko, M.; Heyvaert, W.; Larios, D.; Obelleiro-Liz, M.; Taboada, J. M.; Bals, S.; Liz-Marzán, L. M. Morphological and Optical Transitions during Micelle-Seeded Chiral Growth on Gold Nanorods. *ACS Nano* **2022**, *16* (11), 19281–19292. https://doi.org/10.1021/acsnano.2c08668.

(236)   Vanrompay, H.; Skorikov, A.; Bladt, E.; Béché, A.; Freitag, B.; Verbeeck, J.; Bals, S. Fast versus Conventional HAADF-STEM Tomography of Nanoparticles: Advantages and Challenges. *Ultramicroscopy* **2021**, *221*, 113191. https://doi.org/10.1016/j.ultramic.2020.113191.

(237)   Albrecht, W.; Bladt, E.; Vanrompay, H.; Smith, J. D.; Skrabalak, S. E.; Bals, S. Thermal Stability of Gold/Palladium Octopods Studied in Situ

in 3D: Understanding Design Rules for Thermally Stable Metal Nanoparticles. *ACS Nano* **2019**, *13* (6), 6522–6530. https://doi.org/10.1021/acsnano.9b00108.

(238)   van der Hoeven, J. E. S.; Welling, T. A. J.; Silva, T. A. G.; van den Reijen, J. E.; la Fontaine, C.; Carrier, X.; Louis, C.; van Blaaderen, A.; de Jongh, P. E. In Situ Observation of Atomic Redistribution in Alloying Gold-Silver Nanorods. *ACS Nano* **2018**, *12* (8), 8467–8476. https://doi.org/10.1021/acsnano.8b03978.

(239)   Frenkel, A. I. Applications of Extended X-Ray Absorption Fine-Structure Spectroscopy to Studies of Bimetallic Nanoparticle Catalysts. *Chem Soc Rev* **2012**, *41* (24), 8163–8178. https://doi.org/10.1039/c2cs35174a.

(240)   Chi, M.; Wang, C.; Lei, Y.; Wang, G.; Li, D.; More, K. L.; Lupini, A.; Allard, L. F.; Markovic, N. M.; Stamenkovic, V. R. Surface Faceting and Elemental Diffusion Behaviour at Atomic Scale for Alloy Nanoparticles during in Situ Annealing. *Nat Commun* **2015**, *6*. https://doi.org/10.1038/ncomms9925.

(241)   Petrova, H.; Juste, J. P.; Pastoriza-Santos, I.; Hartland, G. V.; Liz-Marzán, L. M.; Mulvaney, P. On the Temperature Stability of Gold Nanorods: Comparison between Thermal and Ultrafast Laser-Induced Heating. *Phys. Chem. Chem. Phys.* **2006**, *8* (7), 814–821. https://doi.org/10.1039/b514644e.

(242)   Albrecht, W.; Deng, T. S.; Goris, B.; Van Huis, M. A.; Bals, S.; Van Blaaderen, A. Single Particle Deformation and Analysis of Silica-Coated Gold Nanorods before and after Femtosecond Laser Pulse Excitation. *Nano Lett* **2016**, *16* (3), 1818–1825. https://doi.org/10.1021/acs.nanolett.5b04851.

(243)   Gómez-Graña, S.; Goris, B.; Altantzis, T.; Fernández-López, C.; Carbó-Argibay, E.; Guerrero-Martínez, A.; Almora-Barrios, N.; López, N.; Pastoriza-Santos, I.; Pérez-Juste, J.; Bals, S.; Van Tendeloo, G.; Liz-Marzán, L. M. Au@Ag Nanoparticles: Halides Stabilize {100} Facets. *J Phys Chem Lett* **2013**, *4* (13), 2209–2216. https://doi.org/10.1021/jz401269w.

(244)   Erdélyi, Z.; Beke, D. L. Nanoscale Volume Diffusion: Diffusion in Thin Films, Multilayers and Nanoobjects (Hollow Nanoparticles). *J Mater Sci*. **2011**, 6465–6483. https://doi.org/10.1007/s10853-011-5720-4.

(245)   Brent R. P., *Algorithms for Minimization without Derivatives*, Prentice-Hall, USA, **1973**, 195.

(246) Mallard W. C.; Gardner A. B.; Bass R.F.; Slifkin L.M. Self-Diffusion in Silver-Gold Solid Solutions. *Phys. Rev.* **1963**, 129, 617. https://doi.org/10.1103/PhysRev.129.617

(247) Noah, M. A.; Flötotto, D.; Wang, Z.; Mittemeijer, E. J. Interdiffusion and Stress Development in Single-Crystalline Pd/Ag Bilayers. *J Appl Phys* **2016**, *119* (14). https://doi.org/10.1063/1.4945673.

(248) Khalavka, Y.; Ohm, C.; Sun, L.; Banhart, F.; Sönnichsen, C. Enhanced Thermal Stability of Gold and Silver Nanorods by Thin Surface Layers. *J Phys Chem C* **2007**, *111* (35), 12886–12889. https://doi.org/10.1021/jp075230f.

(249) Miao, J.; Ercius, P.; Billinge, S. J. L. Atomic Electron Tomography: 3D Structures without Crystals. *Science (1979)* **2016**, *353* (6306), aaf2157–aaf2157. https://doi.org/10.1126/science.aaf2157.

(250) Xu, R.; Chen, C.-C.; Wu, L.; Scott, M. C.; Theis, W.; Ophus, C.; Bartels, M.; Yang, Y.; Ramezani-Dakhel, H.; Sawaya, M. R.; Heinz, H.; Marks, L. D.; Ercius, P.; Miao, J. Three-Dimensional Coordinates of Individual Atoms in Materials Revealed by Electron Tomography. *Nat Mater* **2015**, *14* (11), 1099–1103. https://doi.org/10.1038/nmat4426.

(251) Peter J Huber. Robust Estimation of a Location Parameter. In Breakthroughs in Statistics: Methodology and Distribution. I*Springer*; **1992**; 492–518.

(252) Williamson, M. J.; Tromp, R. M.; Vereecken, P. M.; Hull, R.; Ross, F. M. Dynamic Microscopy of Nanoscale Cluster Growth at the Solid–Liquid Interface. *Nat Mater* **2003**, *2* (8), 532–536. https://doi.org/10.1038/nmat944.

(253) Zheng, H.; Smith, R. K.; Jun, Y.; Kisielowski, C.; Dahmen, U.; Alivisatos, A. P. Observation of Single Colloidal Platinum Nanocrystal Growth Trajectories. *Science (1979)* **2009**, *324* (5932), 1309–1312. https://doi.org/10.1126/science.1172104.

(254) Evans, J. E.; Jungjohann, K. L.; Browning, N. D.; Arslan, I. Controlled Growth of Nanoparticles from Solution with In Situ Liquid Transmission Electron Microscopy. *Nano Lett* **2011**, *11* (7), 2809–2813. https://doi.org/10.1021/nl201166k.

(255) Yuk, J. M.; Park, J.; Ercius, P.; Kim, K.; Hellebusch, D. J.; Crommie, M. F.; Lee, J. Y.; Zettl, A.; Alivisatos, A. P. High-Resolution EM of Colloidal Nanocrystal Growth Using Graphene Liquid Cells. *Science (1979)* **2012**, *336* (6077), 61–64. https://doi.org/10.1126/science.1217654.

(256)   Arble, C.; Guo, H.; Matruglio, A.; Gianoncelli, A.; Vaccari, L.; Birarda, G.; Kolmakov, A. Addressable Graphene Encapsulation of Wet Specimens on a Chip for Optical, Electron, Infrared and X-Ray Based Spectromicroscopy Studies. *Lab Chip* **2021**, *21* (23), 4618–4628. https://doi.org/10.1039/D1LC00440A.

(257)   Rogolino, A.; Claes, N.; Cizaurre, J.; Marauri, A.; Jumbo-Nogales, A.; Lawera, Z.; Kruse, J.; Sanromán-Iglesias, M.; Zarketa, I.; Calvo, U.; Jimenez-Izal, E.; Rakovich, Y. P.; Bals, S.; Matxain, J. M.; Grzelczak, M. Metal–Polymer Heterojunction in Colloidal-Phase Plasmonic Catalysis. *J Phys Chem Lett* **2022**, *13* (10), 2264–2272. https://doi.org/10.1021/acs.jpclett.1c04242.

(258)   Op de Beeck, M.; Van Dyck, D. Direct Structure Reconstruction in HRTEM. *Ultramicroscopy* **1996**, *64* (1–4), 153–165. https://doi.org/10.1016/0304-3991(96)00006-X.

(259)   Niu, C.; Qiu, G.; Wang, Y.; Tan, P.; Wang, M.; Jian, J.; Wang, H.; Wu, W.; Ye, P. D. Tunable Chirality-Dependent Nonlinear Electrical Responses in 2D Tellurium. *Nano Lett* **2023**, *23* (18), 8445–8453. https://doi.org/10.1021/acs.nanolett.3c01797.

(260)   Ben-Moshe, A.; da Silva, A.; Müller, A.; Abu-Odeh, A.; Harrison, P.; Waelder, J.; Niroui, F.; Ophus, C.; Minor, A. M.; Asta, M.; Theis, W.; Ercius, P.; Alivisatos, A. P. The Chain of Chirality Transfer in Tellurium Nanocrystals. *Science (1979)* **2021**, *372* (6543), 729–733. https://doi.org/10.1126/science.abf9645.

(261)   Kokila, G. N.; Mallikarjunaswamy, C.; Ranganatha, V. L. A Review on Synthesis and Applications of Versatile Nanomaterials. *Inorg. Nano-Met. Chem.* **2022**, 1–30. https://doi.org/10.1080/24701556.2022.2081189.

(262)   Harish, V.; Tewari, D.; Gaur, M.; Yadav, A. B.; Swaroop, S.; Bechelany, M.; Barhoum, A. Review on Nanoparticles and Nanostructured Materials: Bioimaging, Biosensing, Drug Delivery, Tissue Engineering, Antimicrobial, and Agro-Food Applications. *Nanomaterials* **2022**, *12* (3), 457. https://doi.org/10.3390/nano12030457.

(263)   Kolahalam, L. A.; Kasi Viswanath, I. V.; Diwakar, B. S.; Govindh, B.; Reddy, V.; Murthy, Y. L. N. Review on Nanomaterials: Synthesis and Applications. *Mater Today Proc* **2019**, *18*, 2182–2190. https://doi.org/10.1016/j.matpr.2019.07.371.

(264)   Khan, I.; Saeed, K.; Khan, I. Nanoparticles: Properties, Applications
          and Toxicities. *Arab. J. Chem.* **2019**, *12* (7), 908–931.
          https://doi.org/10.1016/j.arabjc.2017.05.011.

(265)   Baek, W.; Chang, H.; Bootharaju, M. S.; Kim, J. H.; Park, S.; Hyeon, T.
          Recent Advances and Prospects in Colloidal Nanomaterials. *JACS Au*
          2021, *1* (11), 1849–1859. https://doi.org/10.1021/jacsau.1c00339.

(266)   *Colloidal Synthesis of Plasmonic Nanometals*; Liz-Marzán, L., Ed.;
          Jenny Stanford Publishing, **2020**.
          https://doi.org/10.1201/9780429295188.